Newcastle University
School of Engineering
Geotechnics and Structures

Investigating the Mechanical and Electrical Behaviour of Particulate Systems Using Discrete Element Method

A thesis submitted in fulfilment

of the requirements for the degree of

Doctor of Philosophy

Chao Zhang

Newcastle upon Tyne, UK

September 2024

Abstract

Electro-mechanical behaviour of granular materials represents a significant multi-physical problem, garnering considerable interest and extensive application across various industries. A multitude of experimental and discrete element method (DEM) studies have investigated the interaction mechanisms of mechanical and electrical behaviour in particulate systems from both microscopic and macroscopic perspectives. However, acquiring data at the grain-scale through experiments is challenging, and comprehensive analysis and formulation of models for overall electrical resistance between contacting objects (particle-to-particle or particle-to-wall) under mechanical loading are still needed.

This research aims to develop understanding of the interaction between mechanical and electrical behaviour in particulate systems across both micro and macro scales. An electro-mechanical contact model is developed to represent both particle-to-particle and particle-to-wall interactions, characterised by particle resistances and contact resistances in overlapping regions. The modelling of contact resistance follows Hertz and Holm's theories, while the particle resistance is estimated by considering the geometric transformations of particles under mechanical force. The model is verified and validated against analytical solutions and experimental data in the literature.

The high pressure torsion (HPT) and drained triaxial monotonic compression tests are utilised in this thesis to systematically study electrical response characteristics under different mechanical loading conditions. A DEM model of HPT test is developed to examine the effect of sand particle characteristics on tribological behaviour at the wheel-rail interface, complemented by an in-house Python code to simulate realistic fragment size distribution following particle breakage. The electro-mechanical contact model is employed in the HPT test to examine the variations in electrical resistance at the wheel-rail interface when conductive and non-conductive sands are applied individually, as well as when a mixture of both particles is utilised. Furthermore, three samples of varying inherent anisotropies are compressed under drained triaxial monotonic condition to investigate the effect of anisotropy on the electrical responses of the particulate system.

The findings indicate that the particle size and mass, the number of particles, and the fragment size distribution (FSD) have a significant effect on the tribological behaviour at the wheel-rail interface. Two commercial conductive particles can reduce HPT electrical resistance to below 10 Ω, and that mixing 5% conductive particles to silica sand dramatically drops the HPT resistance from 55 kΩ to 220 Ω. Drained triaxial monotonic compression tests on loose samples reveal that those with predominantly vertical contact orientations (*Ver_L*) show the fastest growth in deviator stress ratio (*q/p'*) and pronounced dilative behaviour, while those with predominantly horizontal contact orientations (*Hor_L*) exhibit the largest decrease in coordination number (*CN*) and minimal increase in mean contact area (*A*). Differences in bulk resistance trends across samples at small to medium strain levels converge to similar decreasing trends at residual state (45% axial strain).

Acknowledgements

Firstly, I would like to express my sincere gratitude to my academic supervisor, Dr Sadegh Nadimi, for his continuous and comprehensive support throughout my PhD. Sadegh has always been very generous in sharing his time and insights with me during supervising my PhD project. His conscientious and enthusiastic attitude towards research have always been infectious to me, which strengthened my determination to pursue academic research after graduation.

I would like to express my special appreciation to my co-supervisor Dr David Milledge for his kind support during my PhD study. I have been encouraged by his constructive support especially at the beginning of my PhD. I am also profoundly grateful to Professor Stefano Utili for his funding support during my PhD.

I would like to thank Dr Sadaf Maramizonouz, a postdoctoral research associate in Dr Nadimi's research group, for her great support and advice during my studies at Newcastle University. I would also like to thank all the technical staff in Geotechnical laboratory for their technical assistance. I especially appreciate Mr Stuart Patterson and Mr Gareth Wear for their kind help in compression tests.

My deep gratitude is expressed to Dr Masahide Otsubo from Port and Airport Research Institute, Japan, for providing valuable support for the numerical simulation of drained triaxial compression testing in Chapter 5.

I would like to thank all PhD students and academic staff who provided help and support during my PhD, especially with regards to Mr Bin Zhang. I am also thankful my friend, Mr Changrong Yang, a PhD student at Newcastle University, for his help in the development of the circuit device for measuring the resistance at metal-metal interface in Chapter 4. I would like to sincerely thank my friend, Dr Ning Wang (currently a lecturer at Nanjing Forestry University) for his collaboration with us on DEM simulation and wish him all the best.

Last but not least, I would like to thank my parents for their unconditional support. I would also like to thank my girlfriend, Miss Faye van Rotterdam, and her family; Faye is a dear friend who has enriched my life in the UK. Without their help, I could not have been so deeply involved in my PhD studies.

Table of Contents

List of Figures

List of Tables

Chapter 1 Introduction

1.1 Motivation and Background

Electro-mechanical behaviour in particulate systems is one of the current multi-physics problems of most interest, dating back to the pioneering work of Branly in the late 19th century (Branly, 1873; Falcon and Castaing, 2005; Holm, 1967; Renouf and Fillot, 2008). His observations demonstrated that in the presence of an external electric field, loose or imperfect contact between metal particles undergoes a significant electrical transition leading to the transformation of a highly resistive state into an electrically conductive state. This phenomenon was further explored by Lodge, who introduced the concept of "cohering" particles, where metal particles rearrange themselves and come into contact due to electric field, forming conductive chains that lead to a reduction in electrical resistance (Falcon and Castaing, 2005).

Despite the early excitement arising from these discoveries, the fundamental mechanisms underlying the electro-mechanical behaviour in particulate systems, such as the role of contact, particle material, and surface properties, have remained poorly understood for decades. In particular, investigations concerning the conductivity of particulate systems under external forces and the dynamic coupling of electrical and mechanical interactions have remained largely unexplored. From the beginning of the 21st century, a large number of experimental studies have been conducted to quantitatively analyse the evolution of the electrical properties of the particulate system at the macroscopic scale in response to the application of mechanical loads and identified a direct link between them (Arias-Cuevas et al., 2010a; Creyssels et al., 2017; Falcon et al., 2004; Falcon and Castaing, 2005; Lewis et al., 2014; Skipper et al., 2023). However, the relevance of electrical conduction properties at the particle-scale in relation to inter-particle contact is usually highlighted only in a qualitative manner.

The discrete element method (DEM) enables an in-depth study of the complex relationship between electrical and mechanical behaviour in particulate systems. DEM can simulate the interaction between an individual particle and its adjacent particles, thus investigating how the contact forces, particle motions and electrical properties evolve under different loading conditions. This is a major leap forward compared to the experimental limitations of the past, allowing a more detailed and systematic exploration of how mechanical loading affects the electrical behaviour of particulate systems. Although previous electrical conduction models can be employed for the study of electrical behaviour in particulate systems (Bourbatache et al., 2012; Renouf and Fillot, 2008; Reynolds et al., 2021; Sangrós Giménez et al., 2020), they still need to be refined.

On the other hand, the interaction between the mechanical and electrical behaviour of geomaterials in practical engineering applications has become one of the areas of increasing interest, and it is a challenge to apply the electro-mechanical model to it and study it accordingly. In this study, an attempt is made to comprehensively analyse and model the components of electrical resistance in particle-to-particle and particle-to-structure contacts in particulate systems; and to apply the presented electro-mechanical contact model to the practical application of geomaterials.

1.2 Aim and Objectives

The aim of the thesis is to develop understanding of interaction between mechanical response and electrical behaviour within particulate system under loading conditions. This includes establishing an electro-mechanical contact model to analyse electrical transfer in particulate systems during mechanical loading, applied to high pressure torsion (HPT) and drained triaxial compression tests. The HPT test investigates the effects of sand particle characteristics at the wheel-rail interface on tribological and electrical conduction properties, while the triaxial test examines the role of inherent anisotropy on mechanical and electrical behaviour.

The key objectives of this thesis are as below:

- **O_1:** Critically review existing models for assessing electrical transfer under mechanical loading, identify their limitations, and present new electro-mechanical model to overcome these limitations. Also verify and validate the accuracy and reliability of the model through published analytical solutions and experimental data.
- **O_2:** Simulate small-scale HPT tests to understand the key mechanisms of particle characteristics on tribological behaviour in the interface.
- **O_3:** To apply the electro-mechanical contact model to HPT test for investigating the electrical conduction properties under mechanical loading when either conductive or non-conductive particles are used alone, as well as when a mixture of both types of

particles is present at the interface.

- **O_4**: To conduct DEM simulation of drained triaxial compression test using samples with different inherent anisotropy for studying the evolution of mechanical response and electrical behaviour within particulate systems.

1.3 Outline of Thesis

This thesis contains six chapters in total. Chapter 1 introduces the research background, the aim and objectives of research, research contributions, and provides an outline of the thesis.

Chapter 2 provides the reader with basis to understand the contents of the thesis. The chapter begins with an introduction to the governing equations of particle motion, contact model, and scaling laws used in DEM simulations. It then reviews DEM studies on the mechanical response and electrical behaviour of particulate systems under loading, including the influence of anisotropy. In light of the series of studies conducted in this thesis, which focus on the sand particles acting between the wheel and the rail; the chapter also reviews the modelling of crushable materials and examines the effect of sanding on the tribological behaviour at the wheel-rail interface.

Chapter 3 develops a DEM model of the HPT test to individually investigate the effect of different particle characteristics on the tribological behaviour at wheel-rail interface. At a macroscopic level, the tribological performance of the wheel-rail contact is quantified by estimating the coefficient of traction (CoT), calculated as the ratio of shear force to normal load. At the microscopic level, the effect of fragments generated by the breakage of the sand particles during the HPT test is discussed on the tribological characteristics of the wheel-rail contact. In addition, this chapter also introduces an in-house Python code to model the sand particles as cluster particles.

Chapter 4 presents an electro-mechanical contact model to investigate the electrical response within a particulate system under mechanical loading. The model is verified and validated using previously published analytical and experimental data. The model is further applied to DEM simulations of the HPT test to investigate the electrical behaviour at the wheel-rail interface. The effects of conductive and non-conductive particles separately, as well as the impact of mixtures of conductive and non-conductive particles on electrical conduction properties at the interface are discussed. The effect of resistivity for conductive particles on the variation of electrical resistance at the interface is studied. The compression test and Scanning Electron Microscopy (SEM) are performed to examine the effect of conductive and non-conductive particles on the electrical behaviour at the interface at both the macro and micro scales.

Chapter 5 considers the inherent anisotropy of particulate system at triaxial compression tests. Three DEM samples with different initial anisotropic degrees (a_0) are generated at approximately the same initial void ratio (e_0) and initial mean coordination number (CN_0). The evolution of mechanical response and the electrical behaviour of each sample during drained monotonic loading is studied. In addition, the links between the mechanical response and electrical behaviour of these three samples under drained monotonic loading and their induced anisotropy and interparticle contact area are discussed.

Chapter 6 summarises the overall conclusions drawn at each chapter and suggests future research that might extend this study.

1.4 Contributions

This section outlines the contributions of the author to each chapter and the associated published works, where relevant. It also details the contributions made by the supervisory team, Dr Nadimi, Dr Milledge, Dr Maramizonouz and Prof. Utili, and any external collaborators.

In Chapter 3, the author developed a DEM model of the HPT test and modelled the sand particles using the bonded particle model (BPM) method. This HPT model was used to investigate the effect of sand particle characteristics on the tribological behaviour at the contact area of the wheel-rail specimen. The supervisory team and Prof. Lewis from the University of Sheffield reviewed the work and provided feedback throughout the process. This work was published in the ASME Journal of Tribology (Zhang et al., 2024a). In addition, considering the fragment size distribution (FSD) after particle fragmentation, an in-house Python code developed by Dr Nadimi's research group was utilised in this thesis to control the FSD data based on laser diffraction for sand particle modelling. The accompanying manuscript of this code was reviewed by the supervisory team and submitted to Particuology.

In Chapter 4, the author presented an electro-mechanical contact model and implemented in Altair EDEM^{TM} software package to study the change in electrical properties (e.g., electrical resistance and current) within particulate systems under mechanical loading. The simulation results by using this contact model were also verified and validated against the published analytical solutions and experimental data. The model was also applied to HPT test to investigate the effect of coated alumina particles and silica sand particles on the electrical behaviour of HPT tests when applied individually to the wheel-rail contact area. This work was reviewed by the supervisory team and published in Powder Technology (Zhang et al., 2024b). In addition, compression tests and DEM simulations of HPT were carried out by the author. The effect of mixtures of conductive coated alumina particles and silica sand particles acting at the interface on the interfacial electrical behaviour when the load is applied was investigated. As part of this, the circuit instrument used to measure the electrical resistance data during the compression tests was built in collaboration with Mr Yang, a PhD student in Electrical and Electronic Engineering at Newcastle University. This work was reviewed by the supervisory team and the accompanying manuscript was submitted to Powder Technology.

In Chapter 5, the author investigated the effect of inherent anisotropy on mechanical and electrical behaviour of particulate systems under drained triaxial compression tests. Dr Nadimi facilitated a collaboration with Dr Otsubo from Port and Airport Research Institute (PARI) in Japan to assist in this work. DEM simulations were conducted using a modified version of LAMMPS (Large-scale Atomic/Molecular Massively Parallel Simulator) (Plimpton, 1995) by Dr Otsubo. The author developed a MATLAB code that integrates the electro-mechanical contact model to calculate the electrical properties associated with the mechanical response derived from the simulation data. The author then analysed the complete dataset on mechanical and electrical behaviour and finalised the chapter. The supervisory team and Dr Otsubo reviewed this chapter and provided feedback. The corresponding manuscript is currently under review by the supervisory team and Dr Otsubo for submission to Acta Geotechnica.

This PhD thesis summarises the work completed by the author during his studies, which has contributed to a number of publications. The list of publications is as follows:

- Zhang, C., Maramizonouz, S., Milledge, D. and Nadimi, S., 2024. An electro-mechanical contact model for particulate systems. Powder Technology, 440, p.119759. https://doi.org/10.1016/j.powtec.2024.119759

- Zhang, C., Nadimi, S., Maramizonouz, S., Milledge, D., Lewis, R., 2024. A discrete element model of high-pressure torsion test to assess the effect of particle characteristics in the interface. ASME Journal of Tribology, 146, pp.081501-1. https://doi.org/10.1115/1.4065230
- Zhang, C., O'Shaughnessy, C., Maramizonouz, S., Angelidakis, V., Nadimi, S., 2025. Controlling fragment size distribution for modelling the breakage of multi-sphere particles. Particuology. https://doi.org/10.1016/j.partic.2025.01.014
- Wang, N., Zhang, C., Ma, T., Nadimi, S., Chen, F. and Ding, X., 2023. Mechanical insights into the behaviour of cement stabilized aggregates during compaction and failure using smart aggregate: Experiments and DEM simulations. Construction and Building Materials, 399, p.132504. https://doi.org/10.1016/j.conbuildmat.2023.132504
- Zhang, C., Maramizonouz, S., Yang, C.R., Milledge, D., Lewis, R., Nadimi, S., 202X. Electro-mechanical insights into the mixing of conductive and non-conductive particulate friction modifiers at an interface. (submitted to Powder Technology).

Chapter 2 Discrete Element Modelling

2.1 Introduction

This chapter provides the reader with a basis regarding the discrete element method (DEM) and a fundamental understanding of the interaction mechanisms between mechanical response and electrical behaviour in particulate systems when using DEM. Sub-chapter 2.2 introduces the key principles of DEM, including the governing equations of particle motion, the contact models for smooth surfaces, and the scaling laws for particle's material parameters. Sub-chapter 2.3 outlines various approaches commonly employed for modelling crushable materials. Sub-chapter 2.4 reviews DEM studies on the mechanical response of granular systems under load, with a particular emphasis on the effects of anisotropy. Sub-chapter 2.5 examines DEM studies focused on the electrical behaviour of particulate systems under loading, discussing several models of electrical conduction during particle contact. Sub-chapter 2.6 explores sanding as a practical application aimed at improving tribological performance at the wheel-rail interface, detailing various methods used to investigate the mechanisms of sanding action in this context.

2.2 Theoretical Background of DEM

The discrete element method (DEM), initially introduced by Cundall and Strack (1979), has since developed into a well-established and versatile numerical technique. As a powerful tool for modelling the behaviour of particle assemblies, DEM has found widespread application across various fields, including powder engineering, geotechnical engineering, food processing, pharmaceutical engineering, geophysics, and solid-state physics. Given that the detailed formulation of DEM is extensively covered in resources such as the PFC3D User Manual (Itasca, 2019) and the Altair EDEM^{TM} User Manual (EDEM, 2021), this sub-chapter will provide only a brief overview of the governing equations of particle motion, contact models for smooth surfaces. In addition, considering the scaling laws for particle material parameters as a common means of reducing computational cost, a brief overview of this is also provided.

2.2.1 Governing Equations of Particle Dynamics

DEM models the behaviour of a particulate system by considering two main step: updating positions of particle and the calculation of contact forces between particles and their neighbouring particles (Cundall and Strack, 1979; Remy et al., 2009). The translational and rotational motions of individual particle are described by Newton's second laws and Euler's law (Cundall and Strack, 1979; Thornton, 2015):

$$m_i \frac{dv_i}{dt} = \sum_{j=1, j\neq i} \left(F_{c,ij}^{n} + F_{c,ij}^{t} \right) + m_i g \tag{2.1}$$

$$I_i \frac{d\omega_i}{dt} = \sum_{j=1, j\neq i} \left(M_{R,i} + M_{r,i} \right) \tag{2.2}$$

where v_i, ω_i, m_i, I_i and r_i are defined as the translational velocity, angular velocity, mass, moment of inertia, and radius of particle i, and g is the gravitational acceleration. $F_{c,ij}^{n}$ and $F_{c,ij}^{t}$ are the normal and tangential components of the contact force, respectively, exerted by particle j on particle i. $M_{R,i}$ and $M_{r,i}$ are defined as the rolling moment and twisting moment of particle i.

Once m_i and I_i are known, the translational and rotational accelerations can be calculated using the current force and torque acting on the particle i, respectively. In order to update the particle positions and rotations at each time step, explicit time integration schemes, such as Verlet explicit integration (J. Hanley and O'Sullivan, 2017), which is a second-order approximation, are commonly employed in DEM code to maintain stability and accuracy. The critical time step in DEM simulation is usually limited by the Rayleigh wave velocity, and typically selected to be equal or smaller than 20% of Rayleigh's time step (T_R) to ensure that the numerical solution remains stable (Li et al., 2005), as expressed below:

$$T_R = \frac{\pi R_{avg}}{0.163\upsilon_m + 0.8766} \sqrt{\frac{\rho}{G}} \tag{2.3}$$

Where R_{avg}, ρ, G, and υ_m are defined as the average radius, the density, the shear modulus, and the Poisson's ratio of the particle, respectively.

In DEM simulation, rigid particles are assumed to be non-deformable and are allowed to overlap or lose contact with one another. Following the update of particle positions, the identification of particles in contact is determined. At each contact point, the normal contact force (f_n) is derived from the overlap (δ_n) between two contacting particles and the secant normal contact stiffness (k_n), which represents the spring stiffness of the contact at that point in the normal direction:

$$f_n = k_n \delta_n \tag{2.4}$$

The tangential force (f_t) at the contact point is typically computed incrementally. Once the incremental tangential contact displacement ($\Delta\delta_t$) and the incremental tangential contact stiffness (k_t) are determined, the corresponding incremental tangential contact force (Δf_t) can be calculated as below:

$$\Delta f_t = k_t \Delta \delta_t \tag{2.5}$$

In addition, if the tangential contact force exceeds the slip limit ($f_{t,max} = \mu f_n$), it is rescaled to $f_{t,max}$. When the tangential contact force is applied, the particle experiences rotational motion, with the moment being the product between the tangential contact force and the lever arm. Rotational motion occurs about three axes: two rotational degrees of freedom are within the contact plane, referred to as rolling, while the third degree of freedom is about the contact normal, referred to as twisting or spin. When rolling resistance is considered, the incremental rolling moment (ΔM_R) can be calculated using the incremental rolling angle ($\Delta\varphi_R$) and the incremental rolling stiffness (k_R). For the twisting (or spin) moment, the incremental twisting moment (ΔM_r) can be calculated through the incremental spin angle ($\Delta\varphi_r$) and the incremental twisting stiffness (k_r). The expressions for ΔM_R and ΔM_r are given below:

$$\Delta M_R = k_R \Delta \varphi_R \tag{2.6}$$

$$\Delta M_r = k_r \Delta \varphi_r \tag{2.7}$$

For spherical particles, which are commonly utilised in DEM simulations, the spin resistance has been considered by Mindlin (1949), Lubkin (1951), and Deresiewicz (1954). Furthermore, the works of Ai et al. (2011) and Huang et al. (2017) examined the influence of particle shape on rolling and spin resistance. The rolling and twisting moments behave similarly to tangential contact forces, in that they should be rescaled to $M_{R,max}$ and $M_{r,max}$, respectively, when the slip limit is reached. In Equations 2.1 and 2.2, the resultant forces and moments are utilised to update particle positions and rotations for the next time step.

2.2.2 Contact Model for Smooth Surfaces

When two particles are in contact, the interaction generates contact forces in both the normal and tangential directions due to their relative displacement. While the macroscopic stress state within a particulate system is determined by the distribution of contact forces throughout the material, the contact model significantly influences the overall response of a DEM simulation. The force-displacement behaviour at the contact points is governed by the material properties of the particles, the size of the contacting particles, and the surface conditions (Thornton, 2015). In this section, a simplified Hertz contact model that is commonly employed in micromechanical analyses and DEM is described. Apart from the normal contact force, Hertz-type contact stiffnesses in the tangential and twisting directions are also presented.

2.2.2.1 *Normal Contact*

It is well documented (Johnson, 1987) that the Hertz contact model (Hertz, 1882) is one of the most widely adopted approaches for modelling contact interactions. This model is particularly suitable for applications involving soils and has served as a starting point for understanding the relationship between soil shear modulus and confining pressure (McDowell and Bolton, 2001). The Hertz contact model is designed for smooth surfaces and yields a non-linear force-deformation relationship, despite the fact that the contacting spheres are assumed to behave as linearly elastic bodies. The normal contact force (f_n) is described below:

$$f_n = \frac{4}{3} E^* \sqrt{R^*} \delta_n^{\frac{3}{2}} \tag{2.8}$$

where E^* and R^* are defined as the equivalent Young's modulus and the equivalent radius of two contacting particles. The overlap can be calculated from the particle positions, while E^* and R^* depend on the material properties and radii of the contacting spherical particles i and j:

$$\frac{1}{E^*} = \frac{\left(1-\upsilon_{m,i}^2\right)}{E_i} + \frac{\left(1-\upsilon_{m,j}^2\right)}{E_j} \tag{2.9}$$

$$\frac{1}{R^*} = \frac{1}{R_i} + \frac{1}{R_j} \tag{2.10}$$

where $\upsilon_{m,i}$ and $\upsilon_{m,j}$ are defined as the Poisson's ratio of the particle i and particle j.

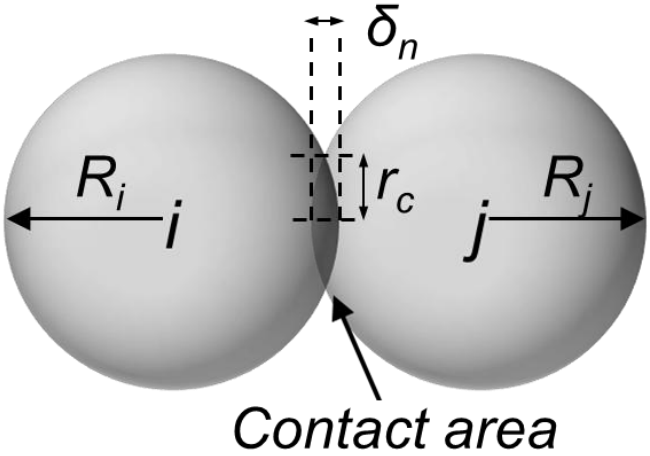

Figure 2.1. Two smooth spherical particles in contact.

As shown in Figure 2.1, the radius of the circular contact area (r_c) between two spherical particles is a function of the overlap (δ_n) and the equivalent radius (R^*). By substituting Equation 2.8 into this relationship, the radius of the circular contact area (r_c) can then be expressed as (Thornton, 2015):

$$r_c = \sqrt{R^*\delta_n} = \left(\frac{3f_nR^*}{4E^*}\right)^{\frac{1}{3}} \tag{2.11}$$

Apparently, r_c is proportional to $f_n^{1/3}$. The incremental contact stiffness in the normal direction (Δk_n) can be obtained by differentiating the normal contact force f_n in Equation 2.8 with respect to the overlap in the normal direction δ_n:

$$\Delta k_n = \frac{df_n}{d\delta_n} = 2E^*\sqrt{R^*\delta_n} = 2E^*r_c \tag{2.12}$$

It should be noted that Δk_n is the tangent (incremental) stiffness, while the secant stiffness in the normal direction k_n is expressed as:

$$k_n = \frac{f_n}{\delta_n} = \frac{4}{3}E^*\sqrt{R^*\delta_n} = \frac{4}{3}E^*r_c \tag{2.13}$$

According to Equations 2.12 and 2.13, a direct relationship between the tangent (Δk_n) and secant stiffness (k_n) can be found, i.e., $\Delta k_n = 1.5k_n$, which is valid for the non-linear Hertz contact model. For a linear Hertz contact model, the tangent (Δk_n) and secant stiffness (k_n) are identical.

2.2.2.2 Tangential Contact

Building on Hertz's (1882) foundational work, Mindlin (1949) expanded the contact model by incorporating the tangential component of particle interactions. The distributions of normal pressure (*p*) and shear stress (*τ*) along the radial distance (*r*) in a no-slip contact scenario are illustrated in Figures 2.2a and 2.2b, respectively.

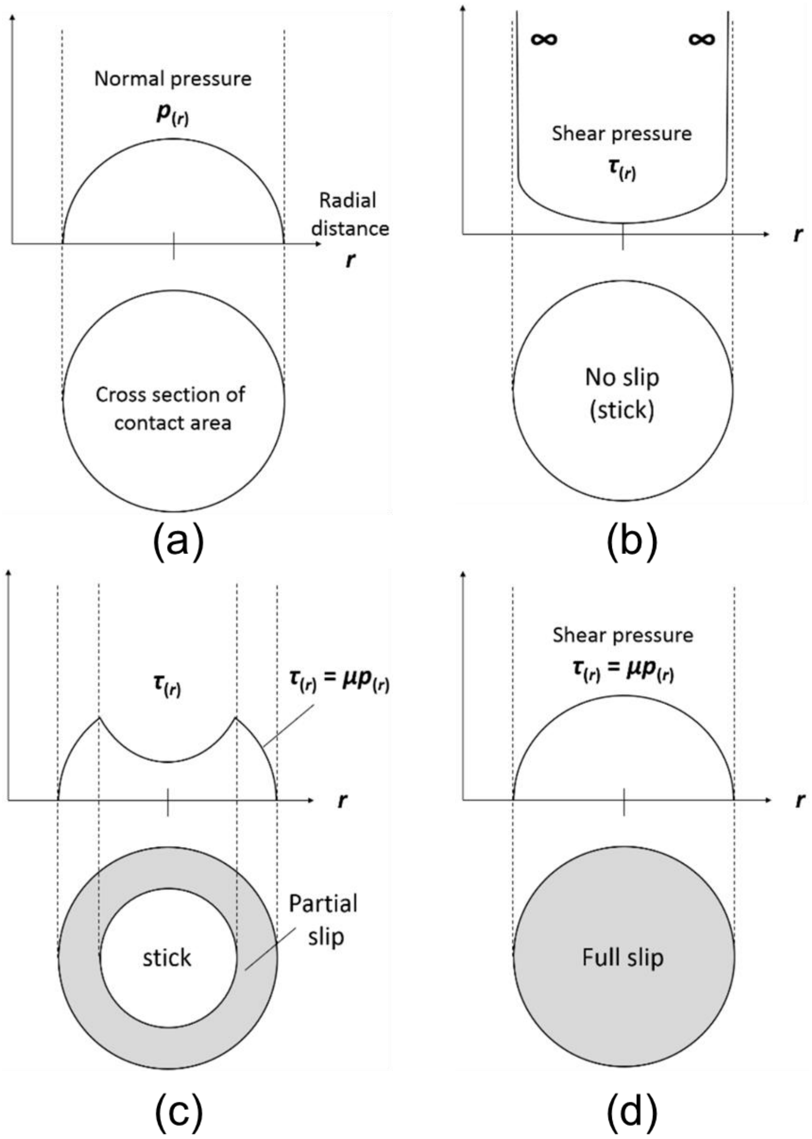

Figure 2.2. Schematics of stick and slip regions and pressure distribution along the radial distance (r) on a contact: (a) normal pressure distribution, and shear pressure distribution with (b) no-slip, (c) partial slip, and (d) full slip (Otsubo, 2016).

Mindlin (1949) formulated the incremental tangential contact stiffness (k_t) by introducing the degree of partial slip (θ) as follows:

$$k_t = 8G^* r_c \theta \tag{2.14}$$

where G^* is the equivalent shear modulus of two contacting particles given by:

$$\frac{1}{G^*} = \frac{\left(2-\upsilon_{m,i}\right)}{G_i} + \frac{\left(2-\upsilon_{m,j}\right)}{G_j} \tag{2.15}$$

Note that θ in Equation 2.14 varies for initial loading (θ^{load}), unloading (θ^{unload}), and reloading (θ^{reload}) conditions, and Mindlin (1949) expressed θ^{load} for the initial loading scenario as:

$$\theta^{load} = \left(1 - \frac{f_t}{\mu f_n}\right)^{\frac{1}{3}} \tag{2.16}$$

where μ is the coefficient of friction between particles. However, Equation 2.16 only applies to the initial loading condition in the tangential direction. The applied tangential force (f_t) decreases k_t due to partial slip before full slip at $f_t = f_t^{max}$ ($= \mu f_n$). It can be seen from Figures 2.2c and 2.2d, the area within the contact stress zone that contributes to the resultant tangential force reduces as partial slip develops, causing the outer radius of the contact annulus to shrink (Johnson, 1987).

Subsequently, Mindlin and Deresiewicz (1953) extended Mindlin's (1949) study by considering more loading scenarios. In various cases, the unloading or reloading of the tangential contact force at constant normal contact force can be represented by substituting the following expression for θ into Equation 2.14:

$$\theta^{unload} = \left(1 - \frac{f_t^{'} - f_t}{2\mu f_n}\right)^{\frac{1}{3}} \tag{2.17}$$

$$\theta^{reload} = \left(1 - \frac{f_t - f_t^{''}}{2\mu f_n}\right)^{\frac{1}{3}} \tag{2.18}$$

where $f_t^{'}$ and $f_t^{''}$ are defined as the tangential contact force at the reversal point from loading to unloading as well as from unloading to reloading, respectively. It should be noted that if $f_t = f_t^{'}$ or $f_t = f_t^{''}$ is substituted into Equations 2.17 and 2.18, then $\theta = 1$, i.e., the initial loading stiffness when $f_t = 0$. The contact model presented here is referred to the Hertz-Mindlin-Deresiewicz (HMD) model. However, as the HMD model is dependent on the loading history in both the normal and tangential directions, it presents challenges when applied in analytical or numerical models. Consequently, a simplified Hertz-Mindlin (HM) contact model is often employed, which simplifies the calculation by setting $\theta = 1$ into Equation 2.14, which can be rewritten as:

$$k_t^{HM} = 8G^* r_c \tag{2.19}$$

The HM model does not account for partial slip and remains unaffected by the sequence of loading. When $f_t = \mu f_n$, the tangential contact stiffness reduces to zero, as the contact is unable to resist any further increase in f_t, leading to a stick-slip behaviour. This simplified HM model is commonly employed in DEM simulations, such as in the commercial PFC3D code (Itasca, 2019) and the Altair EDEM$^{\text{TM}}$ software package (EDEM, 2021). A comparison of Equations 2.12 and 2.19 reveals that the ratio of tangential to normal contact stiffness for the HM model is given by:

$$\frac{k_t^{HM}}{\Delta k_n} = \frac{2(1-\upsilon_m)}{2-\upsilon_m} \tag{2.20}$$

When the Poisson's ratio υ_m of the particles (usually considered to be soil grains) is 0.2, the ratio of tangential to normal contact stiffness obtained from Equation 2.20 is 0.8889, while the ratio decreases as f_t increases regarding the HMD contact model.

2.2.2.3 Twisting Couple

Twisting resistance occurs when two contacting particles undergo relative rotational motion around the axis passing through their contact centre, as depicted in Figure 2.3.

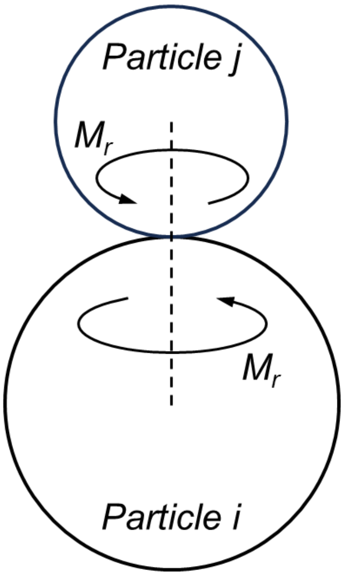

Figure 2.3. Twisting moment applied at two contacting smooth spherical particles.

The incorporation of twisting contact interactions in DEM studies has been relatively rare, and the influence of twisting coupling on the overall response of particulate system has not been extensively investigated in the literature. Lubkin (1951) built upon Mindlin's (1949) work by addressing the twisting coupling issue alongside a tangential contact model, and subsequently derived the twisting contact stiffness (k_r) for a frictionally smooth sphere as follows:

$$k_r = \frac{16}{3} G^* r_c^3 \theta_r \tag{2.21}$$

where θ_r is different for initial loading (θ_r^{load}), unloading (θ_r^{unload}), and reloading (θ_r^{reload}) of torsional moment, and Mindlin (1949) expressed the initial loading case (θ_r^{load}) as follows:

$$\theta_r^{load} = \left[2\left(1 - \frac{3}{2}\frac{M_r}{\mu f_n r_c}\right)^{-\frac{1}{2}} - 1 \right]^{-1} \tag{2.22}$$

where M_r is the twisting contact moment. As the twisting contact moment increases, the twisting contact stiffness (k_r) decreases due to partial slip in the direction of rotation. Deresiewicz (1954) discussed the more general scenarios of torsional loading in a similar manner to Mindlin and Deresiewicz (1953) who discussed tangential stiffness. Unloading and reloading for torsional loading are given as follows:

$$\theta_r^{unload} = \left[2\left(1 - \frac{3}{2}\frac{M_r' - M_r}{2\mu f_n r_c}\right)^{-\frac{1}{2}} - 1 \right]^{-1} \tag{2.23}$$

$$\theta_r^{reload} = \left[2\left(1 - \frac{3}{2}\frac{M_r - M_r''}{2\mu f_n r_c}\right)^{-\frac{1}{2}} - 1 \right]^{-1} \tag{2.24}$$

where M_r' and M_r'' are defined as the twisting contact moment at the reversal point from loading to unloading as well as from unloading to reloading, respectively. Partial slip and counter slip for spinning motion are considered in Equations 2.22 to 2.24. The associated contact model is referred to as HMDT model mentioned in Otsubo (2016). The relevant contact model is referred to as HMDT in this study. The maximum twisting moment that the contact can sustain is:

$$M_r^{\max} = \frac{3}{16} \pi \mu f_n r_c \tag{2.25}$$

When full slip occurs, the twisting contact stiffness k_r becomes zero. The expressions in Equations 2.22 to 2.24 are approximated using the first two terms of a Taylor series, and the accuracy decreases as twisting contact moment M_r approaches M_r^{max}. For instance, substituting Equation 2.25 into Equation 2.22 (with $M_r = M_r^{max}$) does not yield $\theta_r^{load} = 0$ precisely, resulting in an error of 6.1% compared to the analytical solution reported by Deresiewicz (1954). To reduce the error to within 1% or 2%, the ratio M_r / M_r^{max} should be less than 0.3 or 0.5, respectively (Otsubo, 2016). In addition, when partial slip in the tangential contact direction is not considered (i.e., the HM model), the full expression of the twisting model, which takes into account partial slip, is not appropriate. Alternatively, a simplified twisting contact model (here named HMT) can be used (Otsubo, 2016), in which partial slip in the twisting motion is not considered, with a similar approach to the HM model (i.e., $\theta_r = 1$):

$$k_r^{HMT} = \frac{16}{3} G^* r_c^3 \tag{2.26}$$

Section 2.2.2 outlined three modes of interaction between two contacting smooth particles and discussed four distinct contact models: HM, HMD, HMT, and HMDT. The selection of the appropriate contact model is determined by whether partial slip is considered and whether twisting resistance to rotational motion is included. All of these models are founded on Hertz contact mechanics, and the normal contact interactions remain consistent across each case.

2.2.3 Adjustment of Computational Time

The computational time required for DEM simulations is one of the critical challenge, especially when applied to large-scale systems involving fine particles. (Thakur et al., 2016; Wang et al., 2022). In DEM simulations, the particle positions and contact forces of inter-particles must be updated at each time step. Due to the constraints imposed by physical laws and the need to maintain numerical accuracy, the time step for the integration of the equations of particle dynamic must be sufficiently small. Cundall and Strack (1979) first noted that the time step must be smaller than the critical contact time to avoid instability in simulations. The simulate time step is usually to be equal or smaller than 20% of Rayleigh’s time step (Li et al., 2005). However, 20% of Rayleigh’s time step in DEM simulation would be too small due to the mass, size and stiffness of the fine particles.

2.2.3.1 Mass Scaling

To reduce the computational cost, a common strategy is to scale up or down certain parameters of the particles. One of the approaches is mass (density) scaling. The critical time step in DEM is directly proportional to particle mass, meaning that by artificially increasing the particle mass, and thereby increasing the critical time step, simulations can be made to obtain results within a reasonable computational time (O'Sullivan, 2011). Belytschko et al. (2000) examined the mass scaling technique from the perspective of general computational mechanics, advocating its use in scenarios where high-frequency effects are not of primary concern. When employing mass scaling, it is generally assumed that the system's response is largely unaffected by inertial effects. Thornton and Antony (2000) implemented mass scaling by adjusting the particle densities to ensure that a quasi-static deformation state could be achieved within a reasonable simulation time. Although this approach alters both velocity and acceleration, the quasi-static nature of the simulation, coupled with the absence of body forces, meant that the contact forces and displacements remained largely unaffected by the modified density values. In addition, this approach was used to investigate the correlation between the micro properties of the particles and the macro mechanical response of the particulate system during powder compaction (Sheng et al., 2004), as well as the effect of the density scale factor on the gas-solid flow (Mori et al., 2020). Overall, caution is warranted when employing density scaling in DEM simulations. To reduce simulation run times effectively, it is important to maximise the rate of deformation while ensuring that the simulation remains quasi-static. This can be achieved by closely monitoring the applied and internal stresses within the specimen, ensuring that the simulation does not deviate from the quasi-static regime.

2.2.3.2 Particle Stiffness Scaling

Stiffness scaling in DEM is also a technique used to reduce computational time by decreasing particle stiffness, which allows for a larger critical time step in the numerical integration process. This approach is widely employed for dry and relatively coarse particles that only contact force between particles is dominant (Washino et al., 2018). For example, in systems such as fluidised beds and mixers, the overall motion of particles is often relatively insensitive to particle stiffness. In these cases, reducing the particle stiffness in DEM simulations can still yield accurate representations of powder flow, with simulation results showing good agreement with experimental observations (Kuo et al., 2002; Stewart et al., 2001).

However, Kobayashi et al. (2013) found that if the cohesion force is considered in the DEM simulation of a powder system, the powder becomes more “cohesive” with reduced particle stiffness. Several studies have been conducted to better understand the link between particle stiffness scaling and cohesion force (Hærvig et al., 2017; He et al., 2021; Thakur et al., 2016; Washino et al., 2024, 2018). Among them, Washino et al. (2018) addressed the issue of reducing particle stiffness for both linear and nonlinear spring-dashpot contact models, with and without attraction forces, providing a generic scaling law based on dimensionless equations of motion. Their work explored the effectiveness of particle stiffness scaling specifically in the context of single particle-wall collisions. Furthermore, Washino et al. (2024) extended this generic form of the scaling law to cover translational, rotational, and multi-body interactions.

2.2.3.3 Coarse Graining Approach

Additionally, the development of coarse graining approach has also shown promise in reducing DEM computational time. Pöschel et al. (2001) proposed a general approach for scaling down experiments to laboratory size, revealing that the dynamics of a particulate system are altered when all particle sizes are scaled up by a certain factor, while material properties remain constant. In contrast, Feng et al. (2009) demonstrated that reducing the number of particles using a coarse-graining technique can enhance computational efficiency. However, they noted that maintaining the size of the original particulate system unchanged can conflict with geometrical similarity, potentially introducing errors in the bulk response of the system. Several coarse graining approaches have been proposed (Feng and Owen, 2014; Lommen et al., 2019; Sakai and Koshizuka, 2009) and this concept of scaling particle sizes has been utilised in several DEM studies (Ciantia et al., 2016; Coetzee, 2019; Lommen et al., 2019; Thakur et al., 2016; Wang et al., 2022). An example of the use of coarse graining method is shown in Figure 2.4. Still, a comprehensive investigation of DEM model parameters, including particle properties and model geometry, is essential before the coarse-graining technique can be effectively utilised. This ensures that the large-grain DEM simulations accurately replicate the dynamic and static properties of the smaller, more realistic particles. Proper calibration of these parameters is necessary to prevent discrepancies in the particulate system behaviour, ensuring that the simplified model preserves the physical integrity of the original, finer-scale simulation.

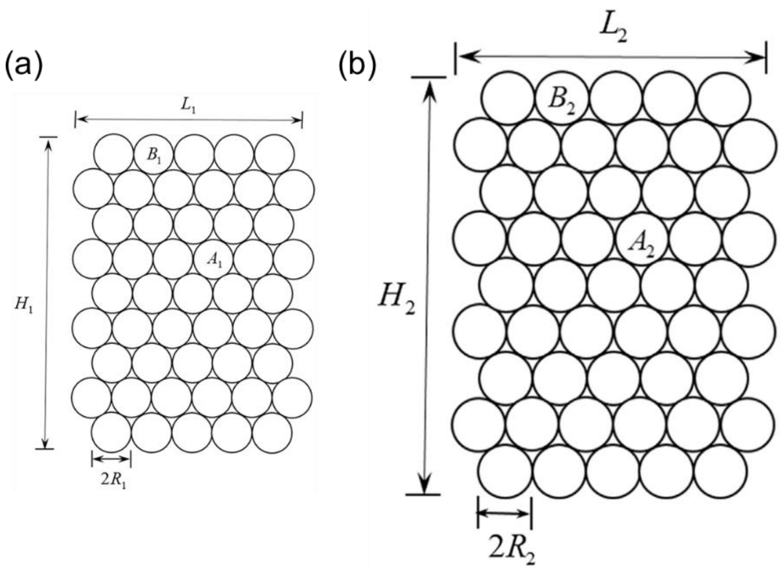

Figure 2.4. Comparison of model before and after coarse graining: (a) before and (b) after. All characteristic lengths are proportional, $L_1/L_2 = H_1/H_2 = R_1/R_2$ (Wang et al., 2022).

2.3 DEM Modelling of Crushable Material

Particle breakage is an essential factor in industries such as food processing (Patwa et al., 2016), power technology (Nan et al., 2017), mining (Lichter et al., 2009; Quist and Evertsson, 2016), and geotechnical materials (Ciantia et al., 2015; Rahimzadeh Oskooei et al., 2021). It alters the size distribution of particles in the particulate system (Bandini and Coop, 2011; Fukumoto, 1992), the packing properties (Bolton et al., 2008), the shear strength (Lobo-Guerrero and Vallejo, 2005), and the microstructure of the granular material (Ma et al., 2014). Since the discrete element method can track the kinematic behaviour of particles under loading, DEM-based numerical modelling techniques have been widely used to better understand the crushing process and its effect on the macroscopic behaviour. In this section, four modelling techniques commonly employed for crushable particles will be briefly introduced, bonded particle model (BPM), particle replacement model (PRM), cohesive interface element (CIE), and bonded cell method (BCM).

2.3.1 Bonded Particle Model

The breakage of an individual particle (e.g., sand particle) into several fragments under mechanical load can be modelled in DEM simulations (Fu et al., 2017; Wang and Arson, 2016; Wu et al., 2022), using the bonded particle model (BPM) developed by Potyondy and Cundall (Potyondy and Cundall, 2004). This model is also widely utilised in many commercial software packages, such as Altair EDEM™ (EDEM, 2021). In BPM, each individual particle is represented as a cluster of independent spherical or irregular shaped fragments bonded together with a finite-sized bond which can resist tension pulling fragments apart. Figure 2.5 presents the forces and moments that act on a single bond between two contacting spherical fragments.

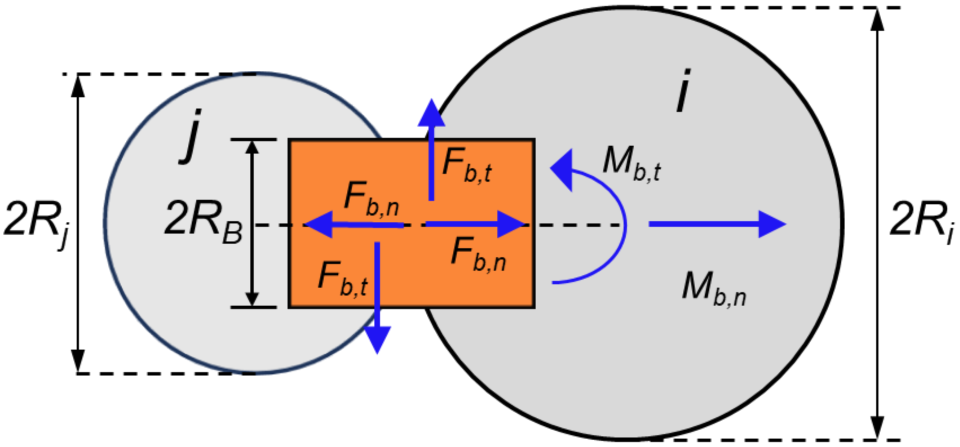

Figure 2.5. Schematic of the bonded particle model: cementing of two spheres by a 'cylindrical' bond and the corresponding mechanical properties.

Each bond is modelled as a set of elastic springs distributed on the circular cross-section at the surface of each of the fragments, transferring the translational and rotational motion that one fragment experiences to the other fragments to which it is bonded. In addition, this bond introduces forces that can resist normal and tangential motions, thus limiting stretching between fragments. After bonding, the forces and moments acting on the bond are adjusted incrementally at every time step which can be written as follows:

$$\Delta F_{b,n} = -v_n k_{b,n} A \Delta t \tag{2.27}$$

$$\Delta F_{b,t} = -v_t k_{b,t} A \Delta t \tag{2.28}$$

$$\Delta M_{b,n} = -\omega_n k_{b,t} J \Delta t \tag{2.29}$$

$$\Delta M_{b,t} = -\omega_t k_{b,n} \frac{J}{2} \Delta t \tag{2.30}$$

where A $(=\pi R_B^2)$ is the area, J $(=\frac{1}{2}\pi R_B^4)$ is the polar moment of inertia, R_B is the radius of bond, respectively. $k_{b,n}$ and $k_{b,t}$ are the normal and shear stiffness of bonds. v_n and v_t are the velocities of the fragments in the normal and tangential direction. ω_n and ω_t are the normal and tangential angular velocities of the fragments. In the above equations, multiplying the time step

Δt with the normal velocities v_n and tangential velocities v_t of the fragments calculates the relative displacement and shear displacement increments. Likewise, the relative rotation and tangential rotation increments can be obtained by multiplying the time step Δt with the angular velocities of the fragments in the normal ω_n and tangential ω_t direction, which can then be used to account for stretching of the bonds in any direction.

In DEM simulations involving bonded particles, the forces and moments acting at the bonds—namely the incremental normal forces $\Delta F_{b,n}$, incremental tangential forces $\Delta F_{b,t}$, incremental normal moments $\Delta M_{b,n}$, and incremental tangential moments $\Delta M_{b,t}$. They play a crucial role in capturing bond dynamics and fracture behavior. These incremental quantities evolve over multiple time steps, allowing for the simulation of bond degradation and eventual breakage.

To determine if the bond strength is exceeded, leading to fracture or separation, the stresses along the bond interface — both normal and tangential — are compared to threshold values. The governing conditions for bond failure can be expressed mathematically as criteria for when the normal and tangential stress components surpass certain critical values. The normal and tangential components are typically defined as follows:

$$\sigma_{\max} < \frac{-F_{b,n}}{A} + \frac{2M_{b,t}}{J} R_B \tag{2.31}$$

$$\tau_{\max} < \frac{-F_{b,t}}{A} + \frac{M_{b,n}}{J} R_B \tag{2.32}$$

where σ_{max} and τ_{max} are the critical normal and tangential stress cut-off values, respectively. When the normal and tangential stresses acting on the bond exceed the critical values, the bond breaks. Another important part of BPM is that the sizes of the fragments that make up an individual particle can be monodisperse (Metzger and Glasser, 2012; Spettl et al., 2015), bimodal (Quist and Evertsson, 2016) or normally distributed (Antonyuk et al., 2006).

2.3.2 Particle Replacement Model

The particle replacement model (PRM), first introduced by Cleary (2001), operates by instantly replacing a particle with a set of progeny fragments when a specified failure criterion is met. These progeny fragments can take various forms, including individual spheres, clumped spheres, or superquadrics. The model has been effectively utilised to represent particle crushing by modelling compression and impact conditions (Barrios et al., 2020; Jiménez-Herrera et al., 2018; Tavares et al., 2021), ballast fragmentation in geotechnical engineering applications (Cil and Buscarnera, 2016; de Bono and McDowell, 2016), and for the simulation of comminution machinery, including various types of crushers (Cleary and Sinnott, 2015; Delaney et al., 2015; Weerasekara et al., 2013; Zeng et al., 2022), as well as high pressure grinding rolls (HPGRs) (Barrios and Tavares, 2016).

In this section, a version of PRM discussed was implemented in Altair EDEM^{TM} by Tavares et al. (2021) using a high-level application programming interface (API). The model employs the Hertz-Mindlin contact model. Under this scheme, if the contact force exerted on a particle exceeds a critical threshold leading to fracture, the parent particle is instantaneously replaced by fragments. This fracturing process continues across the resulting daughter particles until the fragments reach a defined minimum size. Consequently, the multi-stage fracture process ceases once the primary fragments generated during a fracture event are smaller than the prescribed minimum particle size. Figure 2.6 depicts the PRM fracture process as employed in Altair EDEM^{TM}, where the parent particle i_p is removed from the simulation upon fracture and replaced by a collection of progeny particles i_f, referred to as the primary fracture distribution (Saeidi et al., 2016).

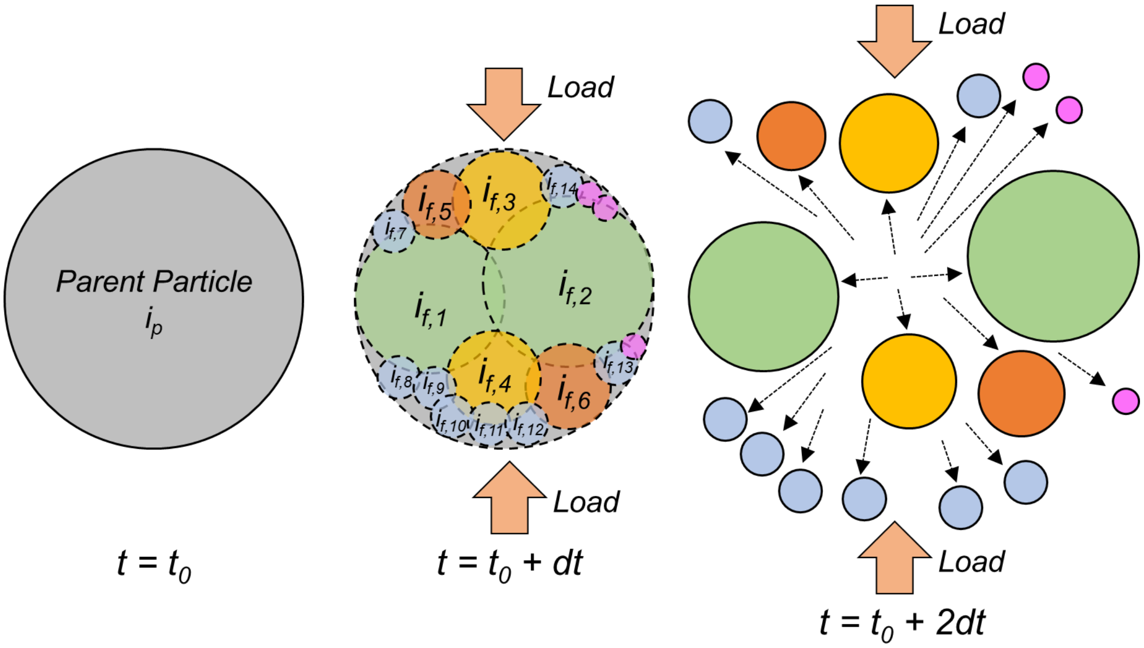

Figure 2.6. Schematic of the particle replacement model.

Upon replacement, these daughter particles are generated, leading to an initial superposition of the particles. To avoid the generation of excessive repulsive forces between fragments due to this overlap, which could destabilise the simulation, a relaxation factor is introduced (Jiménez-Herrera et al., 2018). This constant is applied to the Hertz-Mindlin interaction forces immediately following particle replacement, serving to limit the forces arising from the initial overlap. By doing so, it prevents unrealistically high fragmentation velocities, ensuring the simulation remains computationally feasible.

To effectively simulate the primary breakage function while maintaining computational simplicity and efficiency, it is often essential to determine the primary progeny size distribution. This distribution represents the size range of particles following breakage under a stress level corresponding to the median energy required for fracture. Tavares (2009) proposed a relationship between the applied stress energy and the parameter t_{10}, which corresponds to the proportion passing in 1/10th of the original particle size in a sample:

$$t_{10} = A_m \left[1 - \exp\left(-b^* E_k \right) \right] \tag{2.33}$$

where A_m and b^* are defined as model parameters of the relationship between t_{10} and the impact energy, in which A_m corresponds to the maximum value of t_{10} that can be achieved when the material is fractured under a single stress. E_k is kinetic energy during collision. Then, based on the suggestion from (Tavares, 2007), Equation 2.33 can be rewritten as:

$$t_{10} = A_m \left[1 - \exp\left(-b^* \frac{E_k}{E_{50b}} \right) \right] \tag{2.34}$$

where E_{50b} are defined as the median fracture energy of the crushed particles, respectively. In particular, the two model parameters A_m and b^* have to be fitted to the single-particle breakage data. Note that when particles experience repetitive stresses with insufficient energy to cause fracture in all particles, the E_{50b}, will represent the energy required for the particles that do fracture. This value will be lower than the median fracture energy of the original material, E_{50}.

2.3.3 Cohesive Interface Elements

The versatility and simplicity of cohesive interface elements (CIEs), along with their capacity to model both the initiation and propagation of delamination in a single analysis, have made them an increasingly popular and powerful tool for simulating delamination damage in composite materials. While CIEs is primarily employed within the framework of finite element method (FEM), as shown in Figure 2.7a, it is also highly effective in predicting the failure behaviour of granular materials under a variety of loading conditions. A number of applications of the CIEs have also been found in the literature to study the fracture behaviour and mechanical response of composite materials (Kawashita and Hallett, 2012; Nguyen et al., 2016; Yuan et al., 2014) as well as geotechnical materials (Jiang and Meng, 2018; Ma et al., 2014; Zhang et al., 2024, 2023) under different loading conditions. Among them, Ma et al. (2014) developed a combined finite–discrete element method (FDEM) to simulate the breakage of irregularly shaped particles in granular materials like rockfill using pre-inserted CIEs to represent fracture paths, with results aligning with experimental stress–strain responses and highlighting the role of particle breakage in mechanical behaviour. Zhang et al. (2023) performed the FEM simulations incorporating CIEs to study the fracture behaviour of brittle materials under different contact topologies in Brazilian tests, with simulations confirming that flat-to-flat contact provides the most accurate representation of crack initiation and propagation without compression failure at the ends. Furthermore, Zhang et al. (2024) applied CIEs to sand particle modelling which then investigated the effect of sand on tribological behaviour at wheel-rail interface. Therefore, this section provides a brief overview of the fundamentals of CIEs based on the particle modelling from Zhang et al. (2024, 2023).

By employing CIEs, contact detection and interaction within finite elements is extended beyond modelling the continuum behaviour of particles to effectively capture the formation and propagation of internal cracks. To analyse large deformation models consisting of numerous elements, and to simulate discontinuities within relatively short dynamic response times, computationally efficient finite element simulations are typically conducted using Abaqus/Explicit.

In simulating the fracture process, the energy dissipation within the cohesive zone of CIEs can be represented using cohesive crack models proposed by Barenblatt (1959) and Dugdale (1960), as well as the frictional crack model introduced by Hillerborg et al. (1976). These models assume that the mechanical behaviour within the cohesive zone is governed by material bonding, aggregate interlocking, and surface friction. At the fracture surface, normal traction t_n

and tangential traction (shear force) t_s are present. As the relative displacements, i.e., crack opening displacement $\delta_{n,d}$ and crack sliding displacement $\delta_{s,d}$ in the 2-D case, increase and the traction forces diminish, tensile or strain softening occurs.

Figures 2.7b and 2.7c illustrate typical linear softening curves for $t_n - \delta_{n,d}$ and $t_s - \delta_{s,d}$, respectively, where δ_n^o (δ_s^o) and δ_n^{sep} (δ_s^{sep}) correspond to the displacements at crack initiation and full fracture, respectively. To simulate the pre-crack initiation stage, a linear ascending branch is incorporated into each softening curve, with an unloading path also included. The areas beneath the curves in Figures 2.7b and 2.7c represent the mode I fracture energy (G_n) and twice the computational mode II fracture energy (G_s), both of which are material properties used in simulating damage to geotechnical materials such as rocks and sand particles. The initial tensile stiffness k_n^o and shear stiffness k_s^o must be sufficiently high to accurately model undamaged material. However, excessive stiffness can lead to distorted results, so a trial-and-error approach is often employed to determine appropriate values for k_n^o and k_s^o.

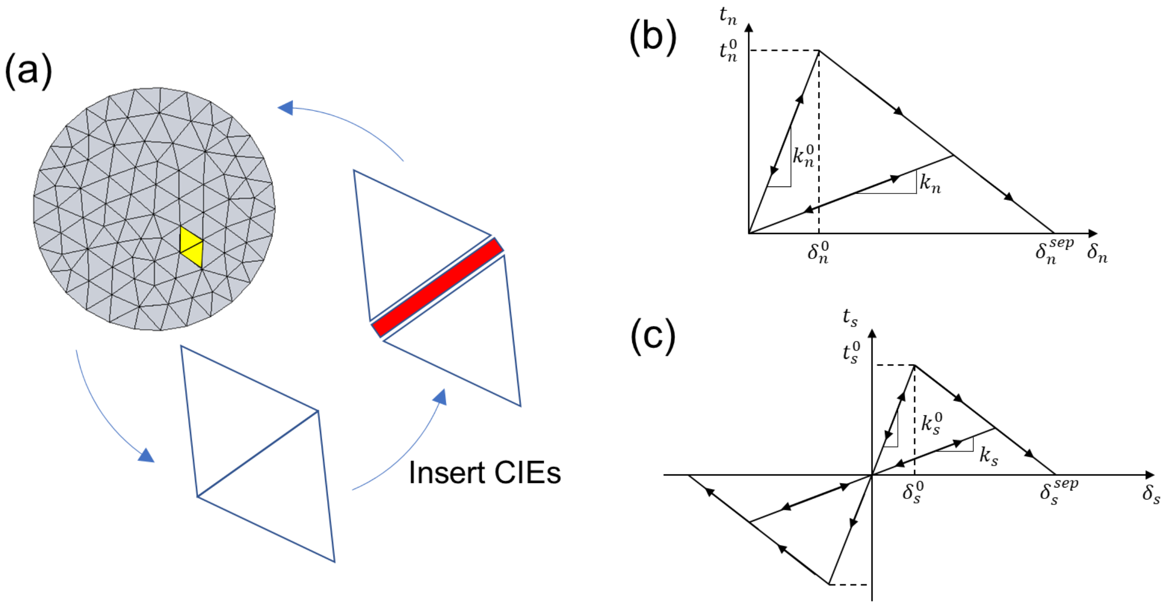

Figure 2.7. (a) Schematic for inserting CIEs between two triangle elements, and linear softening laws for the CIEs in (b) normal direction and (c) tangential direction (edited from Zhang et al. (2023)).

The element COH2D4 in Abaqus/Explicit represents a cohesive element with zero in-plane thickness, designed in accordance with the cohesive crack model. The softening laws depicted in Figure 2.7 are utilised to define the constitutive behaviour of this element. Given that the damage progression within the material is irreversible, the key feature of COH2D4 lies in its ability to simulate this by allowing the stiffness values k_n and k_s, to degrade as the relative displacements $\delta_{n,d}$ and $\delta_{s,d}$ increase during both unloading and reloading phases. A scalar damage variable D_s is employed to quantify the total damage within the material, accounting for all active damage mechanisms. This variable is derived from the effective relative displacement δ_m:

$$D_s = \frac{\delta_m^{sep}\left(\delta_m^{\max} - \delta_m^0\right)}{\delta_m^{\max}\left(\delta_m^{sep} - \delta_m^0\right)} \tag{2.35}$$

Where $\delta_m^{\max}$ refers to the maximum effective displacement achieved during the loading history, while δ_m^0 and δ_m^{sep} represent the effective relative displacements corresponding to δ_n^o (δ_s^o) and δ_n^{sep} (δ_s^{sep}), respectively. The effective relative displacement δ_m, can be defined as a combination of the normal displacement $\delta_{n,d}$ and the tangential displacement $\delta_{s,d}$, capturing both modes of fracture behaviour. Mathematically, δ_m can typically be expressed as:

$$\delta_m = \sqrt{\left\langle \delta_{n,d} \right\rangle^2 + \delta_{s,d}^2} \tag{2.36}$$

where δ_n, denoted by the Macaulay bracket $\left\langle \delta_n \right\rangle^2$ adopts different representations for tension and compression:

$$\left\langle \delta_{n,d} \right\rangle = \begin{cases} \delta_{n,d},\ \delta_{n,d} \geq 0\ \left(tension\right) \\ 0,\ \delta_{n,d} < 0\ \left(compression\right) \end{cases} \tag{2.37}$$

According to Equation 2.35, D_s monotonically evolves from 0 to 1 upon further loading after the onset of damage. Additionally, the tractions are also affected by D_s. Then, k_n, k_s and the traction forces are calculated as:

$$k_n = \left(1 - D_s\right) k_n^0 \tag{2.38}$$

$$k_s = \left(1 - D_s\right) k_s^0 \tag{2.39}$$

$$\left\langle t_n \right\rangle = \begin{cases} \left(1 - D_s\right)\overline{t_n},\ \overline{t_n} \geq 0\ \left(tension\right) \\ \overline{t_n},\ \overline{t_n} < 0\ \left(no\ damge\ to\ compressive\ stiffness\right) \end{cases} \tag{2.40}$$

$$t_s = \left(1 - D_s\right)\overline{t_s} \tag{2.41}$$

where $\overline{t_n}$ and $\overline{t_s}$ are defined as the traction components of the current prediction of elastic traction separation behaviour for damage-free separation. In addition to the damage evolution characterised by D_s, it is necessary to define a damage evolution model to account for the energy dissipated during fracture. Given that mixed-mode fracture (a combination of Mode I and Mode II) is the predominant failure mechanism in brittle materials, as opposed to unimodal fracture, the B-K fracture criterion proposed by Benzeggagh and Kenane (1996) is employed to define the mixed-mode fracture energy:

$$G^c = G_n^c + \left(G_s^c - G_n^c\right)\left\{\frac{G_s}{G_n + G_s}\right\}^{\eta} \tag{2.42}$$

where G^c, G_n^c, G_s^c, and η are defined as the mixed-mode fracture energy, the fracture energy for Mode I, the fracture energy for Mode II, and a semi-empirical index governing the initiation and growth of delamination, respectively. Beyond defining damage evolution, it is also essential to establish a criterion for damage initiation, which marks the onset of stiffness degradation. Rocha (2016) recommends adopting the maximum nominal stress criterion for materials characterised by low tensile strength. In this approach, damage is assumed to initiate when the ratio of maximum nominal traction reaches unity, as expressed in the following formulation:

$$\max\left\{\frac{\langle t_n \rangle}{t_n^0}, \frac{t_s}{t_s^0}\right\} = 1 \tag{2.43}$$

2.3.4 Bonded Cell Method

The bonded cell method (BCM), a variation of the bonded particle model (BPM), constructs particles by aggregating potential fragments (Nguyen et al., 2015). These fragments are bonded by various mechanisms, with each contact point characterised by a specific bond strength. While the bonding of spheres is commonly used to simulate three-dimensional (3-D) fragmentation, it struggles to accurately replicate the diversity of fragment shapes, and the apparent volume of the sphere agglomerates often exceeds that of the real fragments (Cantor et al., 2017). To address these limitations, some researchers have employed polygonal (Kun and Herrmann, 1996; Nguyen et al., 2015) or polyhedral sub-particles or cells (Cantor et al., 2017; Galindo-Torres et al., 2012; Orozco et al., 2019), typically generated using the Voronoi mesh method (Galindo-Torres et al., 2012; Kun and Herrmann, 1996). An example of BCM is shown in Figure 2.8a. Orozco et al. (2019) employed BCM to simulate dynamic particle fracture upon impact, demonstrating that fragmentation efficiency depends on the ratio of consumed fracture energy to impact energy, with maximum efficiency occurring at a specific impact energy level. Additionally, Cantor et al. (2017) utilised BCM to model particle crushing under diametral compression, revealing a power-law relationship between particle strength and intercell shear and tensile strengths, highlighting the role of interlocking effects in strengthening particles even at low tensile strength.

Note that when modelling particles using BCM, which involves extended intercellular contacts, these contacts must be treated differently from those between spherical particles. In earlier research, the cells were connected by linear springs with an associated fracture threshold (D'Addetta et al., 2002; Galindo-Torres et al., 2012). However, representing cell-to-cell contacts using a linear force law, as applied to spherical sub-particles, is an unrealistic approximation. This is because cell-to-cell interactions occur along lines in two-dimensional (2-D) systems or surfaces in 3-D systems, requiring the consideration of at least two or three displacement variables, respectively. Cracks propagate along these extended contacts, similar to intergranular cracking in polycrystalline materials.

The contact between two polyhedral shapes can manifest in three different forms: point contact, line contact, or surface contact, as shown in Figure 2.8b. In BCM, it is usually assumed that rigid cells interact solely through cohesive forces at face-to-face contacts (Cantor et al., 2017; Orozco et al., 2019). The normal interface force threshold $f_{n,t}^{c}$ is dependent on the contact area S. Since the contact plane is represented by three points, the tensile threshold at each contact point is given by $f_{n,t}^{c} = C_n S/3$, where C_n represents the internal cohesion of the material. Similarly, the shear interface force threshold at each contact point on the contact plane is expressed as $f_{s,t}^{c} = C_t S/3$, where C_t denotes the contact shear strength. Both C_n and C_t are independent material strength parameters. Once either of the critical stress thresholds is reached, the bond between the cells irreversibly breaks, transitioning into a frictional contact with a defined coefficient of friction. Importantly, since the cells are rigid, a cohesive face-to-face contact will not break kinematically until all three points representing the interface fail, which occurs when one of the thresholds is reached at each of the three points. The relationship between normal force f_n^c and normal velocity v_n^c at each contact point is (Radjai and Richefeu, 2009):

$$\begin{cases} v_n^c > 0 \;\Rightarrow\; f_n^c = 0 \\ v_n^c = 0 \;\Rightarrow\; f_n^c + C_n S/3 > 0 \end{cases} \tag{2.44}$$

This simply expresses the nature of unilateral contact between two cells at the point of contact in the presence of cohesive force. Similarly, along the tangential direction, the tangential force f_t^c is related to the tangential velocity v_t^c as follows:

$$\begin{cases} v_t^c > 0 \;\Rightarrow\; f_t^c = -C_t S/3 \\ v_t^c = 0 \;\Rightarrow\; -C_t S/3 \le f_t^c \le C_t S/3 \\ v_t^c < 0 \;\Rightarrow\; f_t^c = C_t S/3 \end{cases} \tag{2.45}$$

These "complementary relationships" are represented in Figures 2.8c and 2.8d. The aforementioned relationships must be integrated with the equations of motion to calculate the velocities and forces at all contact points within the system. If Molecular Dynamics (MD) or a traditional DEM approach were used, these relationships would need to be regularised to fit the explicit integration scheme typically employed in those methods. During each time step, "critical" contacts where v_n^c > 0 (separation) or $\left|v_t^c\right|$ > 0 (sliding) will irreversibly break, converting into cohesionless frictional contacts, which are then governed by the following set of relations (Figures 2.8e and 2.8f):

$$\begin{cases} v_n^c > 0 \;\Rightarrow\; f_n^c = 0 \\ v_n^c = 0 \;\Rightarrow\; f_n^c > 0 \end{cases} \tag{2.46}$$

and

$$\begin{cases} v_t^c > 0 \;\Rightarrow\; f_t^c = -\mu f_n^c \\ v_t^c = 0 \;\Rightarrow\; -\mu f_n^c \le f_t^c \le \mu f_n^c \\ v_t^c < 0 \;\Rightarrow\; f_t^c = \mu f_n^c \end{cases} \tag{2.47}$$

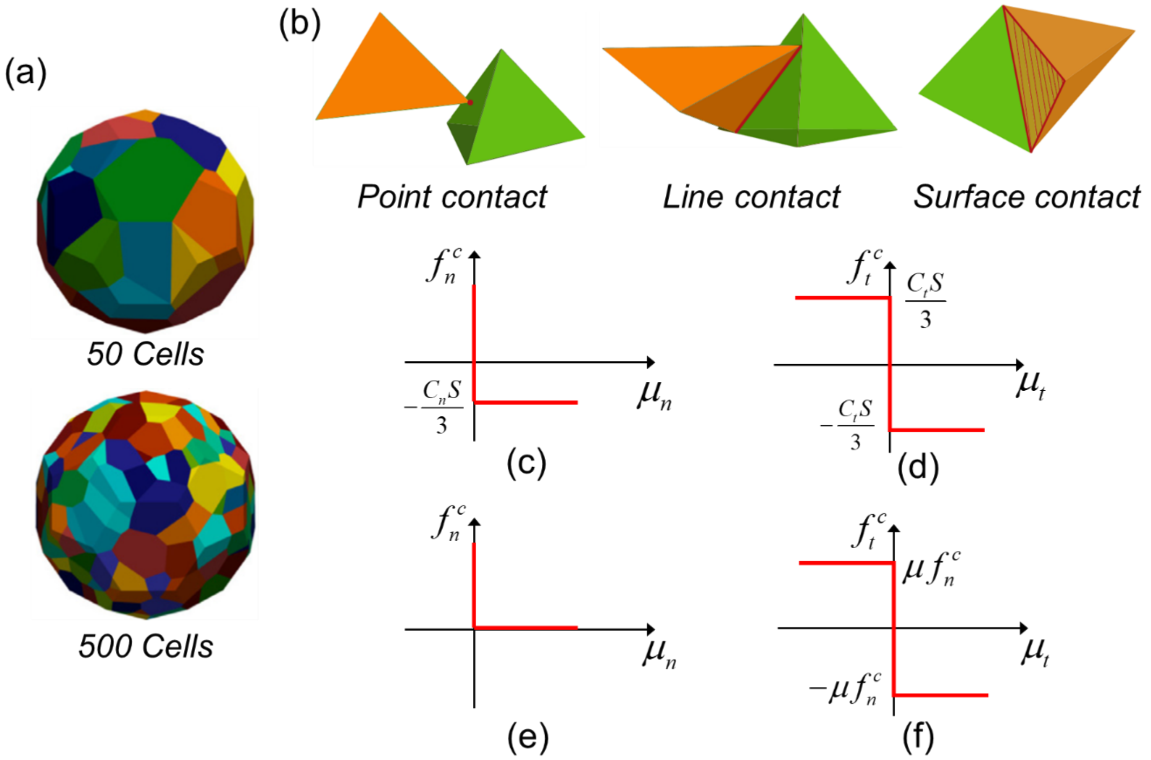

Figure 2.8. (a) Examples of particles generated with different number of cells which are represented by different colour, (b) generic contact types between polyhedral, interface behaviour along (c) normal direction and (d) tangential direction, and frictional contact law defined at (e) normal direction and (f) tangential direction (edited from Orozco et al. (2019)).

Overall, this sub-chapter provides a brief description of BPM, PRM, CIEs and BCM. BPM will be used to model sand particles in this study. PRM, while computationally efficient, oversimplifies the fracture process by instantly replacing particles with smaller fragments, thus lacking the physical realism required for studying detailed crack initiation and propagation in sand grains. CIE, though excellent for capturing crack propagation and delamination in composites, is less suited for large-scale granular systems due to its high computational cost and complexity in modelling particle-scale behaviours. BCM provides more realistic particle shapes through polyhedral sub-particles, but its complexity and computational demands make it challenging for large systems like sand, where multiple particles need to interact and fracture simultaneously. In contrast, BPM can balance between accuracy and computational feasibility for modelling sand. It allows for realistic particle breakage by simulating bond rupture between particles, closely mimicking the crushing behaviour observed in real sand grains. Its flexibility in defining bond strength parameters makes it adaptable to different types of sand, providing a more precise model for understanding the effect of particle breakage on macroscopic properties like shear strength and compaction.

2.4 Mechanical Response of Particulate Systems under Loading

The arrangement of particles, driven by inherent inhomogeneities or externally applied mechanical loads, often results in granular systems exhibiting pronounced anisotropy (Kodicherla et al., 2024). Understanding anisotropy is crucial for assessing the mechanical response of granular materials under various loading conditions, particularly in relation to deformation, strength, and failure mechanisms (Collins and Muhunthan, 2003). This has long been a central focus of research. In the context of geotechnical materials, anisotropy encompasses not only the structural composition of soil, which relates to the spatial arrangement of soil particles, voids, and inter-particle contacts, but also the alterations in these microstructures induced by applied loads (Cambou et al., 2004; Oda, 1972). An example of the evolution of anisotropy due to changes in the mean coordination number (*CN*) and void ratio (*e*) in a particulate system as a result of different directions of externally applied loads is shown in Figure 2.9.

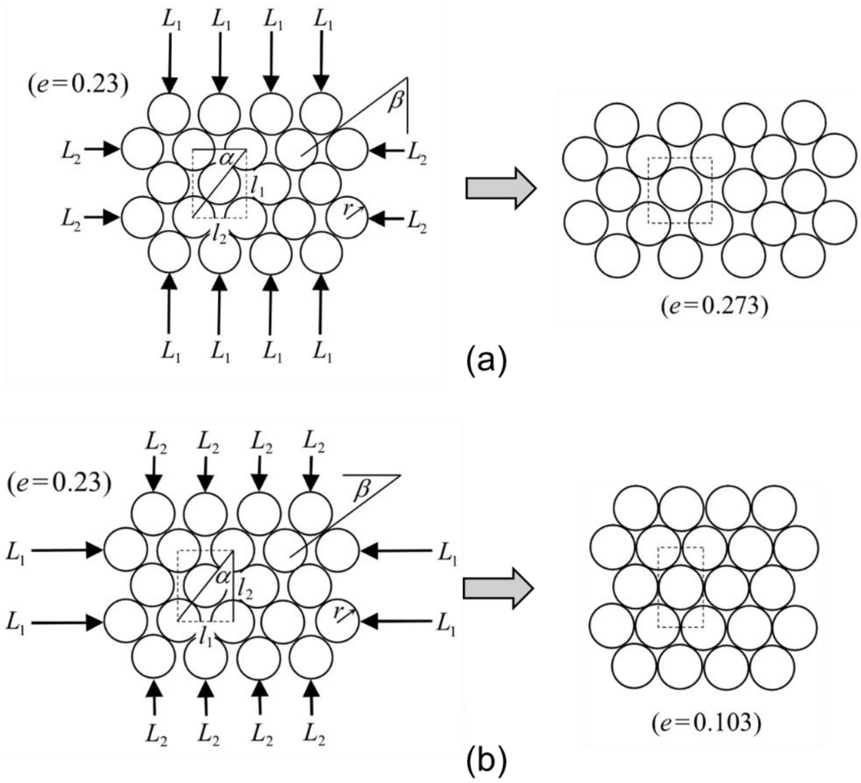

Figure 2.9. Schematic representation of the regular packing of rigid spherical particles showing the effect of loading direction: (a) dilative and (b) contractive (edited from Li and Dafalias (2012)).

Moreover, liquefaction in granular soils, where the effective stress is reduced to zero, can cause severe damage to infrastructure (Seed and Lee, 1966; Ishihara and Koga, 1981). Both experimental and theoretical studies have demonstrated that the fabric anisotropy and its evolution during shear of granular soils have an impact on key aspects of the macroscopic response of sandy soils, including dilatancy, non-coaxiality and shear strength (Collins and Muhunthan, 2003; Li et al., 2023; Li and Dafalias, 2012; Rothenburg and Bathurst, 1989; Yang et al., 2015). Mathematical models often struggle to provide faithful reflections and reasonable explanations for the microstructural changes associated with the macro mechanical response of particulate systems. Experimental approaches face similar challenges, particularly in quantifying induced anisotropy in granular materials under loading conditions and in assessing their impact on the mechanical behaviour of these systems. The Discrete Element Method (DEM) offers a powerful alternative for investigating these issues. DEM enables detailed quantification of the fabrics within particulate systems by analysing the contact normals between particles, as illustrated in Oda's (1982) foundational work. A key advantage of the DEM lies in its capacity to track the evolution of induced anisotropy as the stress state changes over time.

Kuhn (1999) conducted numerical DEM experiments on a large 2-D disk assembly under quasi-static biaxial loading to study microscale deformations. The results showed that deformation was highly nonuniform, with microbands forming spontaneously. These microbands exhibited intense slip and dilation, with energy dissipation concentrated within them. The microbands were dynamic, appearing and disappearing throughout the loading process. This indicates that the particles are constantly realigned under loading, resulting in a continuously changing average coordination number (*CN*) and void ratio (*e*), which is macroscopically reflected in a variation of the volumetric strain of the particulate system. As force chains are central to the development and evolution of anisotropy in granular materials, and force chain buckling limited laterally by weakly networked particles has long been recognised as a fundamental mechanism for key instabilities in dense cohesionless granular assemblies (e.g., shear bands and slip-stick phenomena). Therefore, Tordesillas and Muthuswamy (2009) presented the first structural mechanical model of force chain buckling in granular materials, focusing on how lateral support from weak network particles affects the stability of force chains. The study finds that rolling resistance stabilises force chains, delaying buckling and enhancing the macroscopic strength of the material, with the model showing strong agreement with DEM simulations. Li et al. (2009) established macro–micro relationships in granular mechanics by deriving micro-structural expressions for the macroscopic stress and strain tensors in terms of contact forces and relative displacements. The study also investigated the evolution of fabric tensors by 2-D DEM, highlighting their role in characterizing the internal structure and their correlation with stress-strain behaviour (Figure 2.10), particularly under continuous shearing towards a critical state.

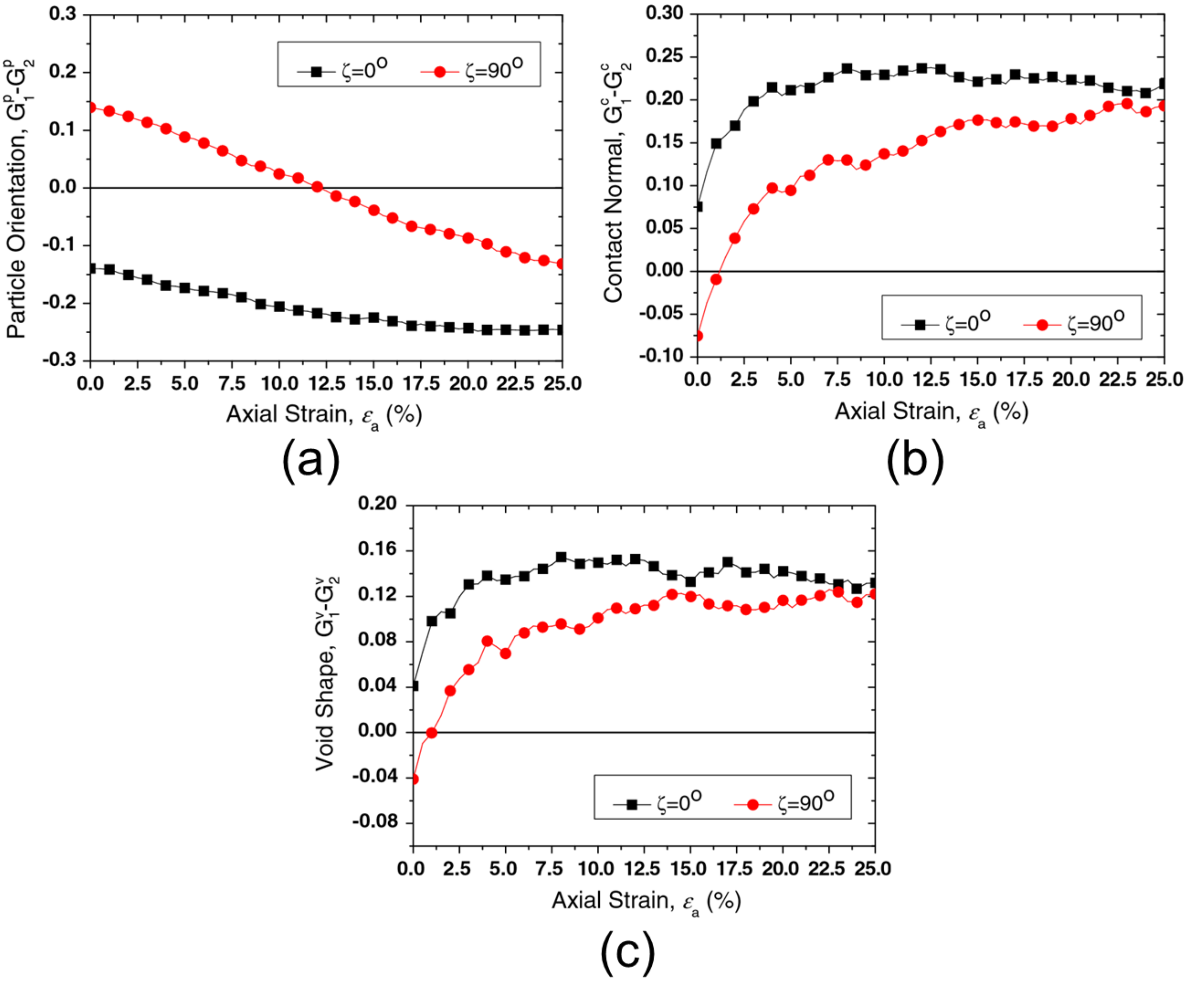

Figure 2.10. (a) Particle orientation anisotropy, (b) contact normal anisotropy, and (c) void space anisotropy (edited from Li et al. (2009)).

To quantify the effect of the evolution of induced anisotropy under complex loading on the strains or stresses in particulate systems, Li and Yu (2010) utilised DEM to study the behaviour of 2-D granular materials under continuous principal stress rotation, revealing that the material exhibited non-coaxial and more contractive behaviour compared to unidirectional shearing. The study found that the ultimate void ratio and anisotropy depend on the stress ratio, not the initial void ratio (Figure 2.11), and that stress rotation leads to a smaller internal structure and void ratio than in biaxial shearing.

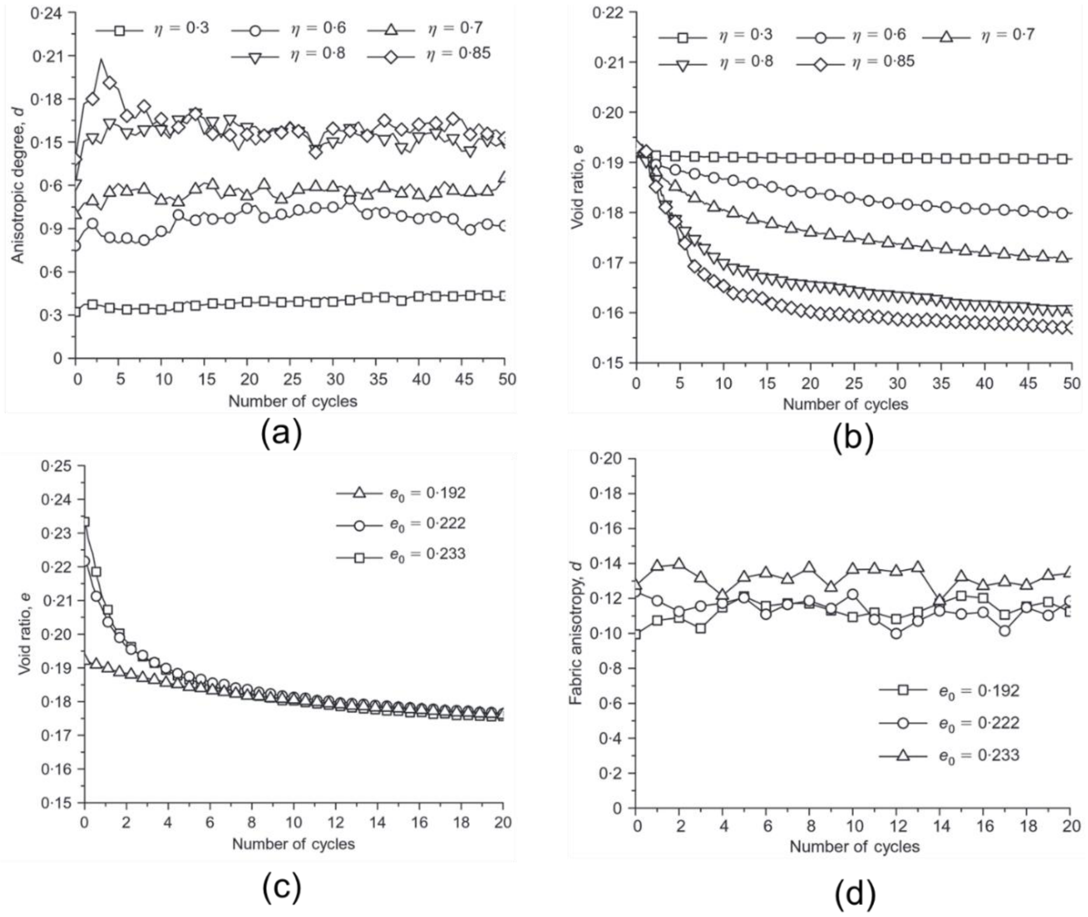

Figure 2.11. (a) Anisotropic degree of the internal structure at different stress ratios, (b) void ratio at different stress ratios, (c) void ratio with different initial void ratios, and (d) anisotropic degree in the internal structure for different initial void ratios (edited from Li and Yu (2010)).

Guo and Zhao (2013) investigated shear-induced anisotropy in granular media, focusing on the evolution of internal structure during drained and undrained shearing through 3-D DEM simulations. The key findings indicated that the dominance of the strong force network in driving anisotropy, the critical role of mechanical anisotropy in shear resistance. The variation of the deviatoric stress with increasing axial strain for a particulate system under undrained shear, and its force chain network distribution in the critical state are shown in Figures 2.12a and 2.12b, respectively.

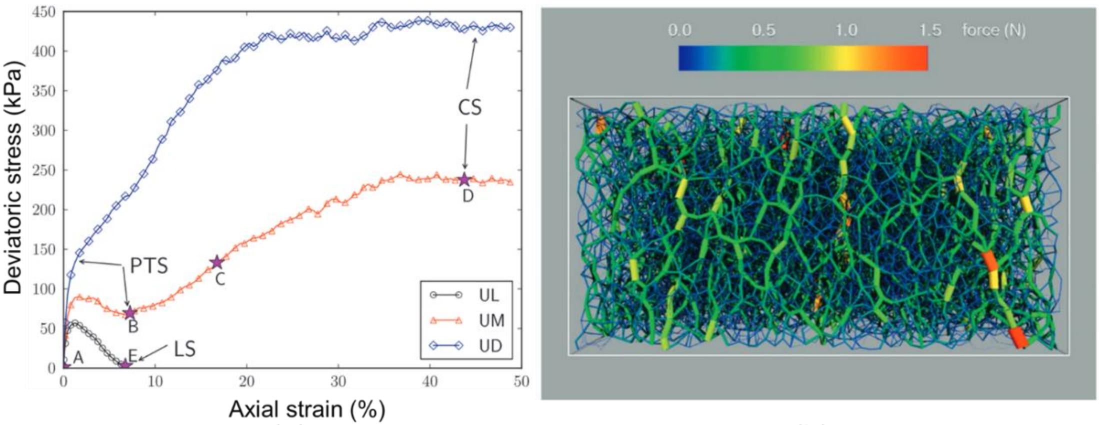

(a) (b)

Figure 2.12. (a) Relationship between axial strain and deviatoric stress when the sample is subjected to undrained shear (PTS: phase transformation state; LS: liquefaction state; CS: critical state; UL: undrained shear on loose sample; UM: undrained shear on medium dense sample; UD: undrained shear on dense sample) and (b) the distribution of the force chain network in the critical state, i.e., the point D (edited from Guo and Zhao (2013b)).

The CN and e in a particulate system affects the particle arrangement during loading conditions, leading to changes in anisotropy, Wang and Wei (2016) introduced a new "centroid distance" fabric index to quantify particle-void distribution, which then applied to granular soils during undrained cyclic loading and post-liquefaction by DEM. The results revealed that anisotropic load-bearing structures and irreversible particle redistribution occurred before and after liquefaction, strongly influencing cyclic mobility and post-liquefaction deformation. An example to illustrate the centroid distance is shown in Figure 2.13.

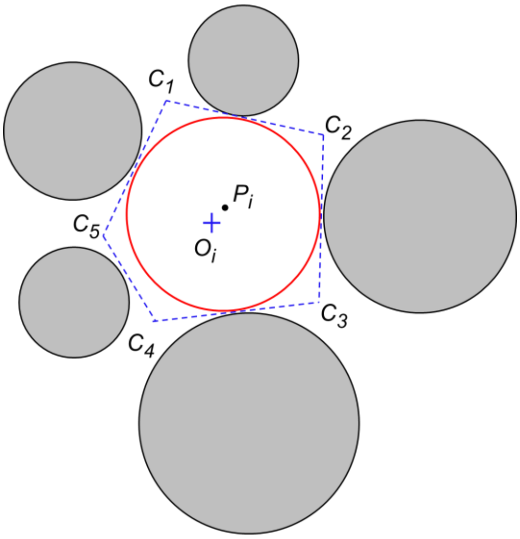

Figure 2.13. Schematic illustration of the centroid distance. The Voronoi cell of particle *i* is a convex polygon whose centre of mass and the centre of mass of the particle are denoted by the vectors O_i and P_i respectively (edited from Wang and Wei (2016)).

Their following study of undrained cyclic shear simulations by DEM found that highly anisotropic samples induced by pre-shear had a lower liquefaction resistance (Wei et al., 2018). Kodicherla et al. (2024) used DEM simulations to investigate the strength and fabric anisotropy of granular materials under true triaxial conditions. Strain hardening and softening behaviours were independent of mean effective stress and intermediate stress ratios. Peak state friction angles, however, depended on the intermediate principal stress parameter value. The simulations showed that clumped particles effectively replicated granular material behaviour. Non-coaxiality was observed, except in specific shear modes.

In addition, The inherent anisotropy, or initial structure, plays a significant role in determining the liquefaction resistance of soil materials (Tatsuoka et al., 1986). Ishibashi and Capar (2003), Sze and Yang (2014), Tatsuoka et al. (1986), and Vaid et al. (1999) pointed out that different sample preparation methods, such as moist tamping (MT), dry deposition (DD), and air pluviation (AP), can result in vary degrees of inherent anisotropy in soil samples. However, due to technical constraints, only a limited number of studies have been found in the literature that have quantified the inherent anisotropy of the prepared samples using microscopic methods (Ni et al., 2021; Yang et al., 2008). Another major advantage of the DEM is the quantification of the inherent anisotropy in a system that initially exhibits an isotropic stress state (Dai et al., 2016; Morimoto et al., 2021; Ni et al., 2024; Otsubo et al., 2023, 2022; Yimsiri and Soga, 2010). Among them, Yimsiri and Soga (2010) used DEM simulations to investigate the impact of initial soil fabric on the shear behaviour of granular materials, showing that fabric anisotropy significantly influences stiffness, strength, and dilatancy, with behaviour varying depending on the direction of shearing. An example of how the degree of initial fabric anisotropy (a_0) affects stress-strain relationship under both drained and undrained behaviour is shown in Figure 2.14. The results align with experimental data and reveal that fabric anisotropy changes rapidly during transitions from compression to dilation and contractive to dilative states, with minimal influence from inter-particle friction angle.

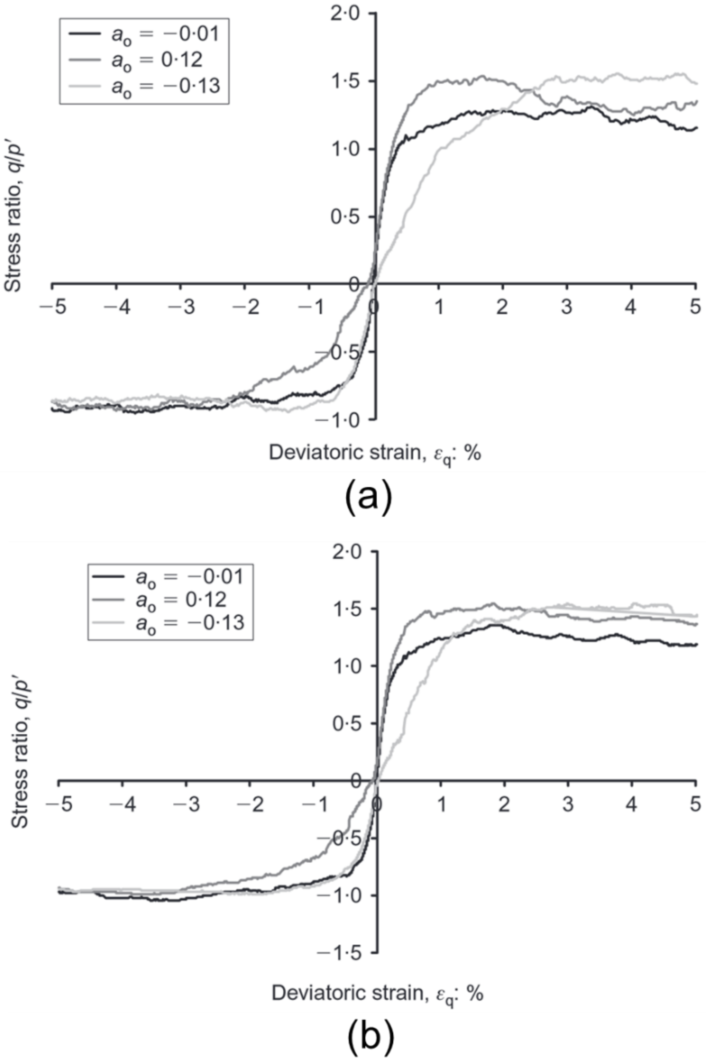

Figure 2.14. Effects of initial soil fabric on: (a) drained behaviour and (b) undrained behaviour using dense specimen with inter-particle friction angle 45° (edited from Yimsiri and Soga (2010)).

Otsubo et al. (2022), building on the work of Yimsiri and Soga (2010), explored the effect of inherent anisotropy on the liquefaction resistance of granular materials by DEM simulations. The findings revealed that anisotropic samples deform more in their weaker directions, leading to lower liquefaction resistance compared to isotropic fabrics. A new index, effective anisotropy ($a \times CN$), was proposed to effectively track anisotropy evolution during both undrained monotonic and cyclic loading.

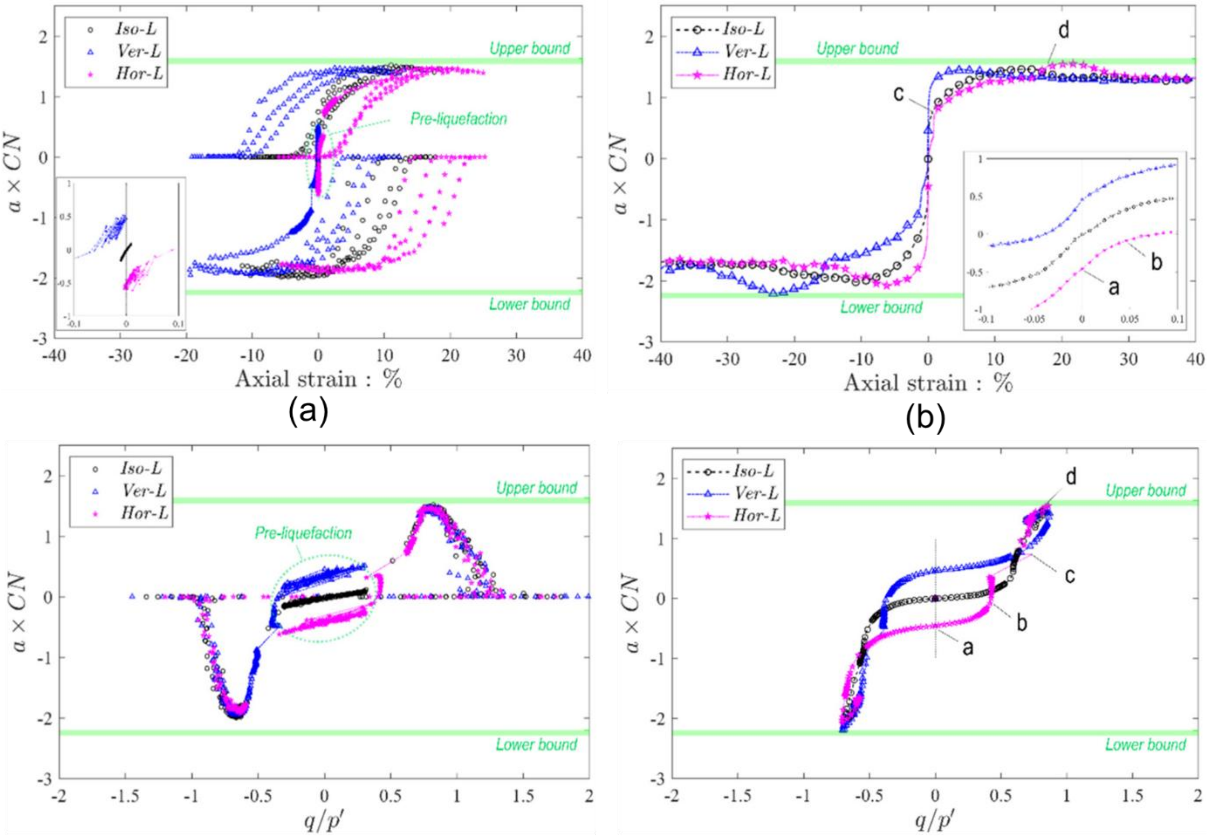

(a)

(b)

(c)

(d)

Figure 2.15. Changes in effective anisotropy (*a*×*CN*) with (a) axial strain under undrained cyclic loading at cyclic stress ratio (CSR) = 0.15, (b) axial strain under undrained monotonic loading, (c) deviator stress ratio under undrained cyclic loading at CSR = 0.15, and (d) deviator stress ratio under undrained monotonic loading. (Otsubo et al., (2022)).

2.5 Electrical Behaviour of Particulate Systems under Loading

Electrical behaviour in granular materials under mechanical loading has been extensively studied (Feki et al., 2012; Machado, 2018; Mohammadi et al., 2020) and is applied across various industries. Applications such as optimizing metal powder compaction through electrical measurements (Eidem et al., 2009), detecting mechanical defects via abnormal electrical resistance (Bourbatache et al., 2013), and identifying train locations using electrical signals from track circuits (Lewis and Masing, 2006) demonstrate the integration of mechanical and electrical responses. Beyond these industrial uses, recent advancements have extended the electro-mechanical behaviour into fields like battery material calendaring (Li et al., 2024), wound healing in human tissue (Yao et al., 2022), eco-friendly device innovation (Liu et al., 2024), and polymer development (Chen et al., 2022; Wang and Liao, 2022). Although numerous experimental studies have advanced our understanding of the interplay between mechanical response and electrical behaviour (Arias-Cuevas et al., 2010a; Creyssels et al., 2017; Falcon et al., 2004; Falcon and Castaing, 2005; Lewis et al., 2014; W. Skipper et al., 2023), these experiments are often time-consuming, costly, and face challenges in capturing particle behavior and electro-mechanical mechanisms at particle-scale. The discrete element method (DEM), recognised for its robust capability to analyse particle dynamics, is widely employed by researchers for simulating the electrical transfer characteristics of particles under loading conditions (Abbaspour et al., 2010; Machado et al., 2019; Schneider et al., 2006). This sub-chapter reviewed DEM studies of the electrical behaviour in particulate systems due to mechanical response and the corresponding electro-mechanical contact models utilised to evaluate the electrical conduction for inter-particles under loads.

Renouf and Fillot (2008) identified a conductivity model for calculating electrical conductance of 2-D particle contacts (Figure 2.16):

$$C_{\alpha} = \frac{C_i C_j}{C_i + C_j + \frac{C_i C_j}{C_m}} \tag{2.48}$$

where C_i and C_j are defined as conductance for particles i and j, respectively. C_m is contact conductance, which can calculate explicitly by using normal contact forces f_n from Hertz model (Hertz, 1882):

$$C_m = \left(\left| f_n \right|\right)^{\frac{1}{3}} \tag{2.49}$$

They used 2-D DEM simulations to investigate the electrical response of particulate systems under mechanical actions.

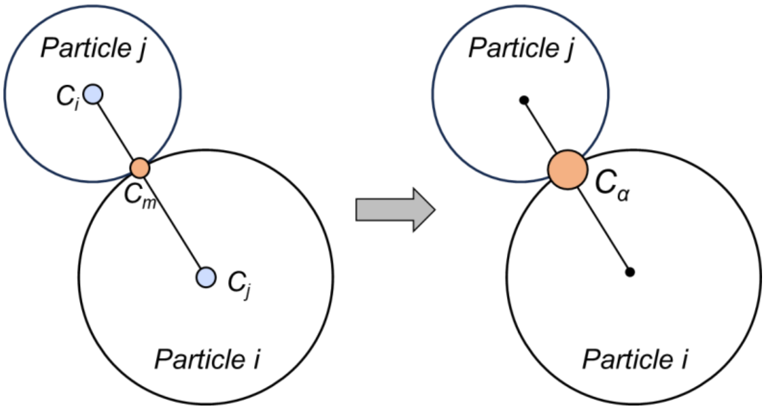

Figure 2.16. Schematic of the components of the total conductance of two contacting particles (edited from Renouf and Fillot (2008)).

This model was later applied by Descartes et al. (2008) in the field of railway engineering to study the impact of the "third-body" layer (e.g., bonded leaf layer) on electrical conduction at wheel-rail interface. Ott et al. (2013) utilised three-dimensional (3-D) DEM simulations to explore the calendaring process of granular electrode structures. Hubert et al. (2017) characterised the contact area between two overlapping particles as a transmission surface S_{ij} facilitating current flow:

$$S_{ij} = \sqrt{S_i S_j} \tag{2.50}$$

where S_i and S_j are defined as the transmission surfaces related to particles i and j. Following this, the value of the electrical resistance generated between two contacting particles i and j is calculated as (Figure 2.17):

$$R_{ij} = \frac{\rho_e l_{ij}}{S_{ij}} \tag{2.51}$$

where ρ_e and l_{ij} are defined as the electrical resistivity of particle material and the length between centres of two particles, and DEM simulations were conducted to study the variation of resistance in a cylindrical rod subjected to a torsion test.

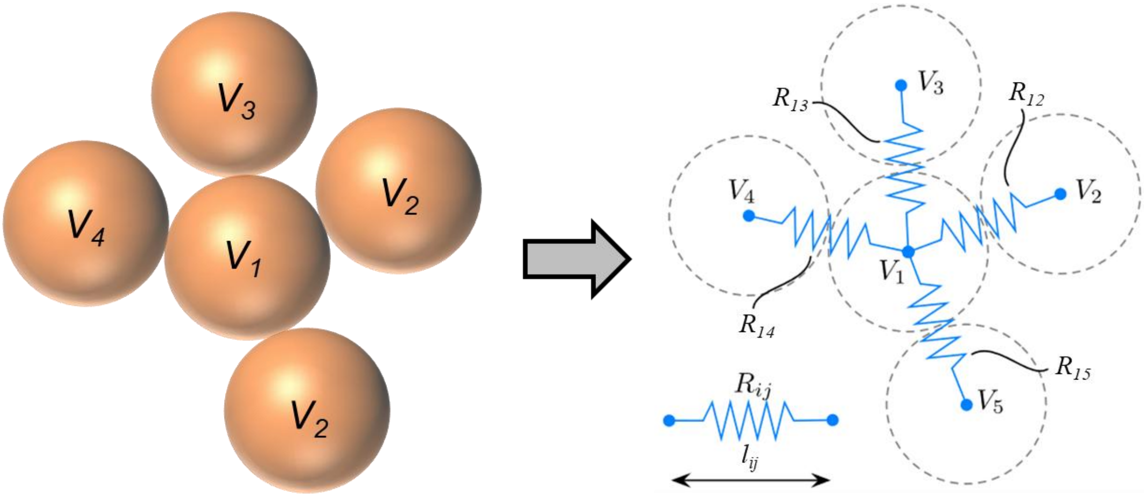

Figure 2.17. Schematic of the circuit consisting of five discrete spherical particles (edited from Hubert et al. (2017)).

Chapteuil et al. (2018) used DEM to model the "third-body" material composed of copper and graphite, and examined the influence of this mixture on the electrical properties of the wheel-rail contact area during train braking. Reynolds et al. (2021) calculated the electrical resistance between two overlapping particles from their centres to their common contact surface (Figure 2.18):

$$\Omega_{ij} = \frac{1}{\pi\sigma_i r_i}\operatorname{arctanh}\left(\frac{r_i^2 - r_j^2 + r_{ij}^2}{2r_i r_{ij}}\right) + \frac{1}{\pi\sigma_j r_j}\operatorname{arctanh}\left(\frac{r_j^2 - r_i^2 + r_{ij}^2}{2r_j r_{ij}}\right) \tag{2.52}$$

where σ_i and σ_j are defined as the electrical conductivities due to particle material for particles i and j, respectively. The electrical behaviour of the burden layer in a ferroalloy furnace system was then evaluated through DEM simulations.

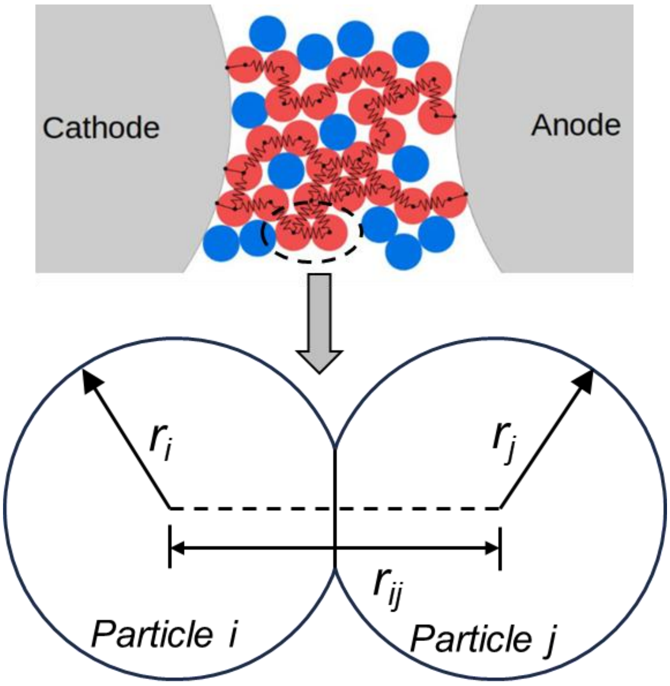

Figure 2.18. Conceptual illustration of the construction of a resistance network in a bed containing conductive (red) and non-conductive (blue) particles along with a schematic of two of these spherical particles in contact (edited from Reynolds et al. (2021)).

The electrical resistance between two overlapping particles involves not only the bulk resistance of each particle but also their contact resistance, and thus requires a comprehensive formulation. From this perspective, Bourbatache et al. (2012) defined the electrical conductance between two extended electrode surfaces S_{ik} and S_{jk} (the contact surfaces at contact points i and j, respectively) located anywhere on the surface of a homogeneous spherical particle k as:

$$C_{ij}^{k} = \frac{\sigma S_{ik} S_{jk}}{2V_p}\left(1-\cos\theta\right) \tag{2.53}$$

where σ, and V_p are defined as the electrical conductivity of material and volume of particle, respectively. θ is the angle formed by points i and j with the centre of the particle, as shown in Figure 2.19a.

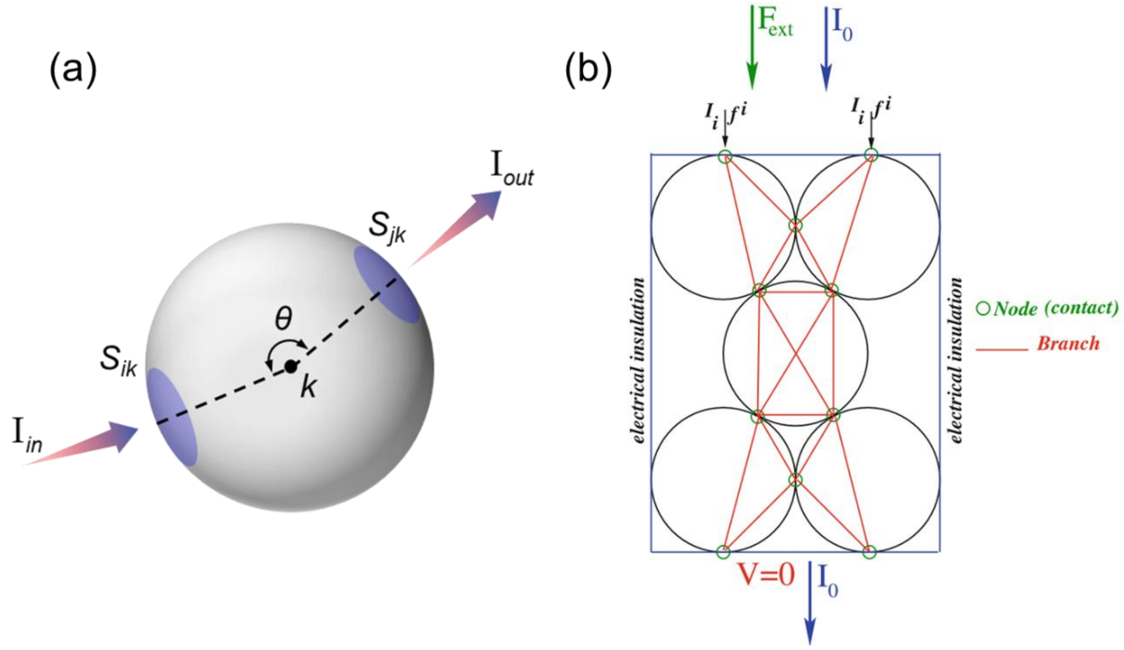

Figure 2.19. (a) Schematic illustration for modelling the electrical conductance between two contact points and (b) particulate system with the corresponding electrical network (edited from Bourbatache et al. (2012)).

In their model, contact points were defined as circuit nodes, leading to multiple potentials and additional current paths within each particle, as shown in Figure 2.19b. Following this, Machado et al. (2015) improved the model for application in ball bearings, using DEM simulations to identify defects based on unusual resistance readings. Sangrós Giménez et al. (2020) presented a numerical method for modelling electrical resistance networks applicable to all-solid-state batteries. The particulate system can be equated to a circuit by identifying the effective conductive paths in the contact network (Figure 2.20). The results showed that DEM simulation results can reproduce experimental data trends and serve as a tool for predicting the conductivity of electrode materials and designing enhanced electrode structures.

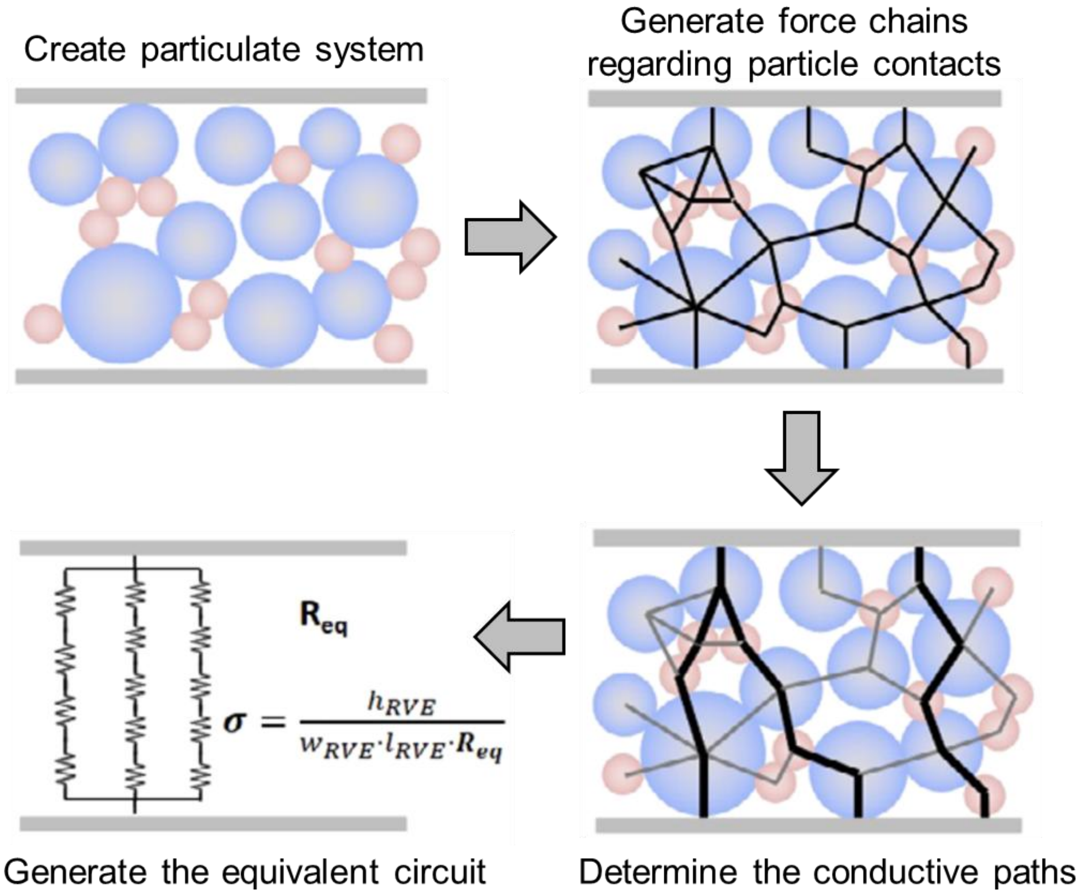

Figure 2.20. Two-dimensional schematic of the numerical procedure for determining the equivalent circuit for simulating the DEM particulate system. (edited from Sangrós Giménez et al. (2020)).

Yim et al. (2023) studied the milling process of ball-milled powder using DEM coupled with experimental observations. The results indicated that the possible path for charge transfer expanded as the coordination number increased, and the electrical resistivity of powders decreased progressively with longer milling times.

As mentioned by Kuhn et al. (2015), the anisotropy can affect the bulk electrical properties of particulate systems, meaning that the internal structure of the material may make it more conductive in certain directions. However, there is very limited research on the effect of anisotropy on the electrical behaviour of particulate systems under load. In this study, the effect of the inherent anisotropy on the mechanical response as well as the electrical behaviour of the particulate system in the small-strain range is investigated, and the evolution of the anisotropy during drained triaxial compression is analysed by DEM simulations, as well as its link with the mechanical and electrical behaviour.

2.6 Practical Application

Given that Chapters 3 and 4 focus on investigating the effect of sand particles on the tribological performance at the wheel-rail interface as well as the electrical behaviour under mechanical loading, this sub-chapter begins with an overview of the wheel-rail contact mechanism and the factors contributing to its low adhesion. It also provides a description of the sanding technique employed to restore adhesion between wheels and rails. Following this, four commonly used tests to assess the impact of sand particles in sanding methods on the frictional behaviour of the wheel-rail interface are discussed, along with the corresponding DEM studies. In addition, the effect of the fragment layer formed by the sand particles crushed under high contact pressure on the electrical conduction at the wheel-rail interface has been reviewed.

2.6.1 Wheel-Rail Adhesion Restoration

It is estimated that the UK railway industry spends approximately £350 million a year to address the issue of low adhesion[1]. This problem induced a significant safety risk to rail operations and can lead to accidents caused by delayed braking, passing signals at danger, or even collisions (Rail Accident Investigation Branch, 2007; Gray, 2018). Additionally, low wheel-rail adhesion can prevent effective train acceleration, resulting in timetable delays and increased operational costs (Fulford, 2004; Gary, 2018).

The contact between the wheels and rails is complicated due to varying wheel and rail geometries, rail curves, railhead conditions, as well as moving vehicles. Figure 2.21a shows three separate regions where contact can occur between the wheel and the rail. Generally, the most common contact between wheels and rails occurs in Region A; also, it is the most desirable contact region because of lower contact stresses and less damage between wheels and rails. When a train turns a corner on the rail, contact usually occurs in Region B. Lastly, if contact between the wheels and the rails occurs in Region C, this can lead to very high contact stresses and severe damage, but it is very unlikely that contact will occur in this area.

Three different contact mechanisms can take place between the wheels and the rails, as

---

[1] In the railway industry "adhesion" or "adhesion coefficient" is defined as the amount of traction present when the wheel-rail contact enters partial slip. In this paper, the terms are used interchangeably.

shown in Figure 2.21b. A pure rolling contact occurs when the points on the wheel and the rail enter and exit the contact together and stick throughout. This contact mechanism usually occurs when the train is "coasting" and does not generate tractive force. When a pure sliding contact is produced between the wheel and the rail, it results in wheel spinning under acceleration and wheel locking under braking, both of which are undesirable as they can damage the wheel and the rail. During the movement through the contact point, the point on the wheel slides before the point on the rail due to elastic deformation of the wheel surface, namely rolling-sliding contact, which is desirable for acceleration or braking as the tractive force generated under this contact mechanism.

In addition, the ratio between the wheel speed under rolling-sliding contact and the wheel speed under pure rolling contact is referred to as the creep rate or slip rate at the wheel-rail interface. Through the maintenance of the creep rate, it is feasible to keep the wheel-rail contact in an ideal condition, i.e. to prevent the wheels and rails from entering full slip and to limit their damage, while maximising the tractive effort.

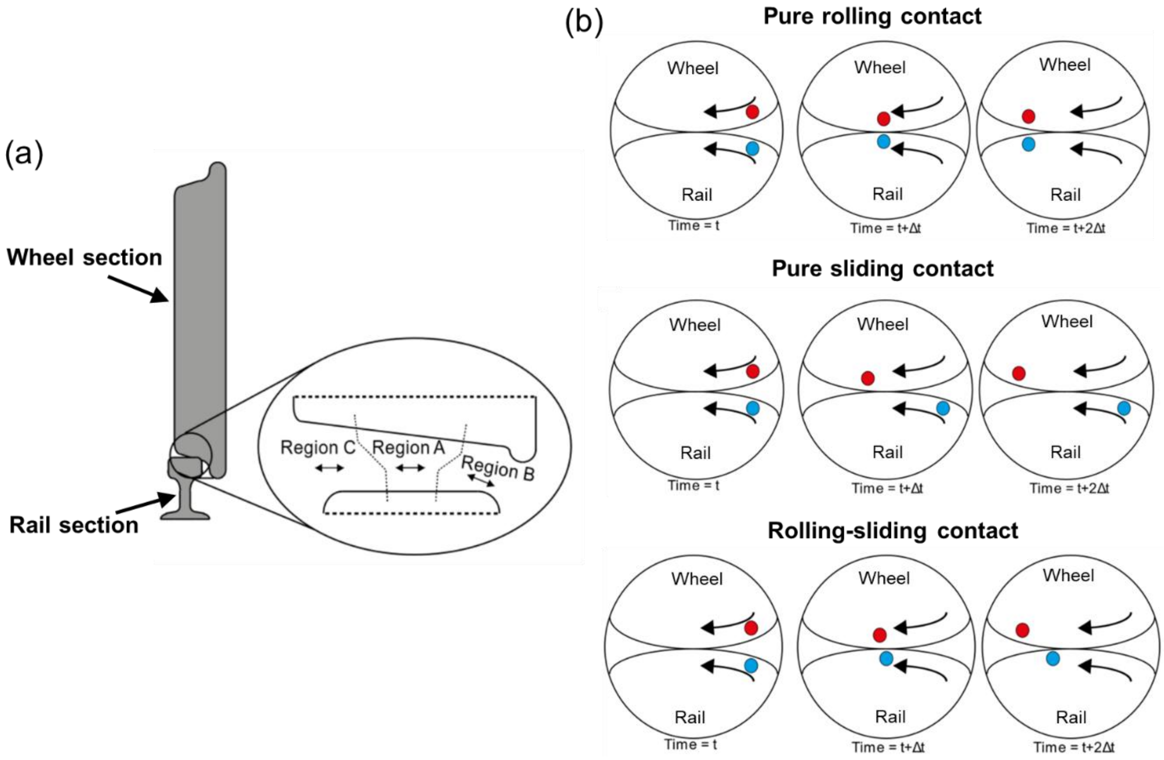

Figure 2.21. Schematics of (a) wheel-rail contact regions and (b) contact mechanisms between wheel and rail (edited from Skipper, 2021).

In Great Britain, the minimum accepted adhesion values at the wheel-rail interface are

0.09 and 0.2 for braking and acceleration, respectively (Fulford, 2004). However, the presence of a third body layer at the wheel-rail interface can induce low adhesion conditions, such as oil (Beagley et al., 1975), water (Beagley and Pritchard, 1975; Buckley-Johnstone et al., 2016), water mixed with iron oxides (Buckley-Johnstone et al., 2019), or leaves tightly bonded to the railhead (Ishizaka et al., 2017), makes it challenging to restore the surface to a clean state. This third body layer acts as a lubricant, reducing the contact friction between the wheels and rails, which in turn decreases the amount of creep that can be sustained. As a result, this may lead to pure slip at the contact surface when the driver expects normal acceleration or braking behaviour, potentially causing wheel flattening or surface damage to the rail.

Sanding as a means of adhesion restoration for wheel-rail contact has been used since the early days of the railway industry (Skipper et al., 2018). Its principle of operation is the deposition of dry sand particles from a compressed air steam in an on-board sand hopper onto the wheel-rail contact surface through a hose (Rail Safety and Standards Board, 2013), as shown in Figure 2.22. The presence of sand changes the characteristics of the wheel-rail contact area, thus restoring adhesion. In addition, sand particles can be mixed into a gel medium and applied directly to the railhead using a pumping system, either from a trackside applicator or a train-mounted one, and these particles are often referred to as friction modifiers (FM) (Fulford, 2004). However, sanding can have unwanted negative effects when it is applied, such as damage caused by sand particles abrading the surface of the wheel and rail when passing through the contact point (Skipper et al., 2018), or the isolation of the wheel and rail due to the contact point being completely covered by insulating sand and the electrical signals not being transmitted properly (Skipper et al., 2020).

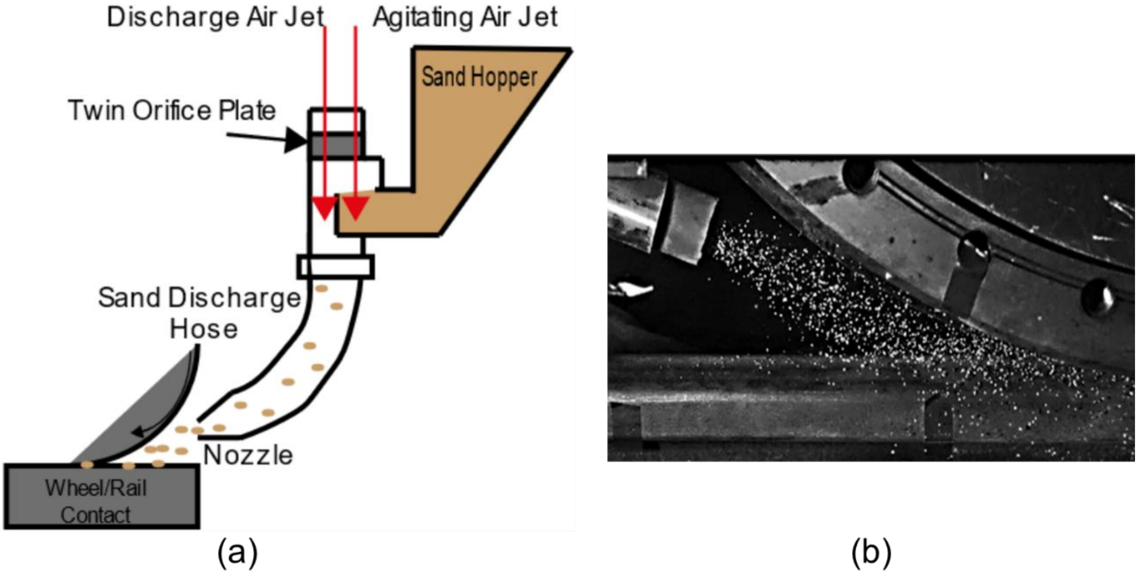

Figure 2.22. (a) Schematics of a typical sander and (b) high-speed photograph during the sanding test process (edited from Lewis et al. (2018) and Skipper et al. (2019)).

Standards for sand particle characteristics that meet sanding equipment guidelines have been established in several countries (Rail Safety and Standards Board, 2018; Société Nationale des Chemins de fer Français, 2004; DB/EBA/VDB/VDV Working Group, 2016; Australian Rail Track Corporation, 2017). These standards provide the benchmarks for selecting sand particles used to restore adhesion between wheels and rails. However, due to the variety and complexity of sand particle characteristics, such as particle shape, size, and mineralogy, it is necessary to investigate how these characteristics affect the tribological behavior of wheel-rail contact.

2.6.2 High Pressure Torsion Rig

The HPT rig has traditionally been utilised to investigate the effect of high plastic strain, where large compressive forces can prevent failure (Edalati and Horita, 2016; Fujioka and Horita, 2009; Wetscher et al., 2005). But the HPT test also allows for the study of the tribological performance of wheel-rail contact as its high contact pressure and stick-slip nature simulate in some aspects the contact between the wheel and rail (Skipper, 2021). Previously, the University of Sheffield developed a platform for the HPT and successfully applied sand to the test to investigate the effect of particles on the frictional characteristics of wheel-rail contact (Evans et al., 2021; Skipper et al., 2019; W. A. Skipper et al., 2023). The principle behind the HPT test is to compress two flat test specimens together to a set normal pressure and generate an annulus contact, and subsequently apply a torque to the bottom (rail) specimen until it has moved through a required sweep length at a low velocity (<1 mm/s). In the initial stage of HPT testing, the interface between the specimens deforms elastically. However, as the test continues, parts of the contact areas begin to deform plastically until full sliding occurs. In addition, the torque that maintained the rotation of the system is measured which can allow to calculate the shear stresses at the interface and enable to evaluate the frictional characteristics when the specimens are rotated from the neutral position. Schematics of the platform and HPT set-up used for testing, as well as an example of typical HPT output, are shown in Figure 2.23, where the labels denote the following components: (1) wheel specimen, (2) rail specimen, (3) sample holders, (4) rotational hydraulic actuators, (5) linear hydraulic actuator, (6) rotary variable differential transducer (RVDT)/load cell, (7) linear variable differential transducer (LVDT)/load cell, (8) controller, (9) crosshead and (10) hydraulic ring main.

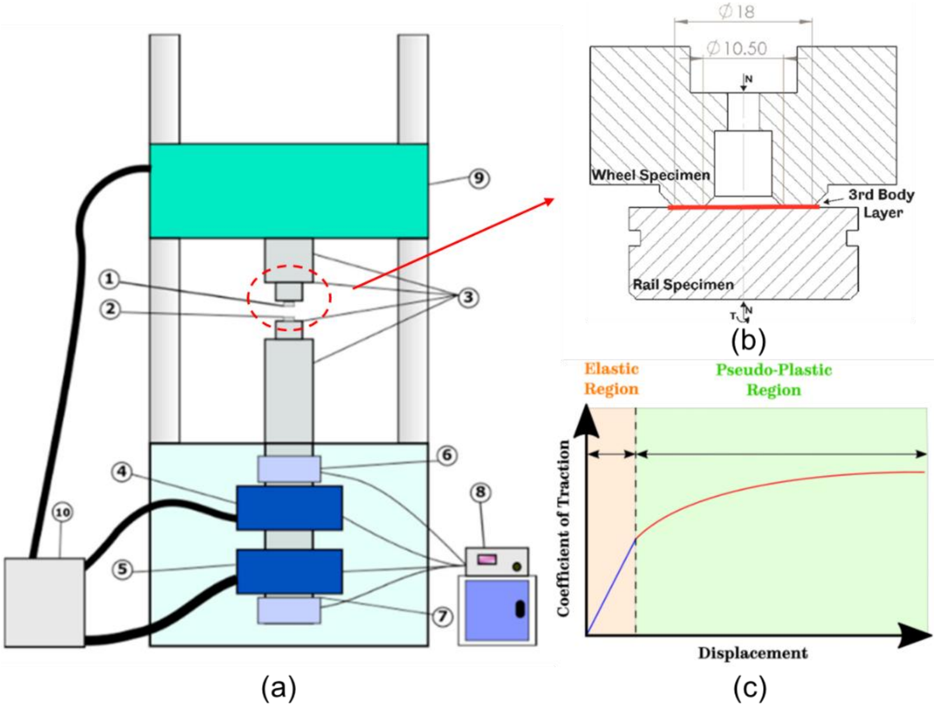

(a) (b) (c)

Figure 2.23. Schematics of (a) HPT rig platform and (b) HPT set-up, as well as (c) a typical example of HPT output (edited from Evans et al. (2021) and Skipper et al. (2023)).

For HPT rig, it allows for the achievement of high contact pressures while maintaining a sufficiently large contact area, preventing particle dominance. It also enables precise control over the amount of sand applied to the contact surface in each cycle, making the test conditions more realistic. As a result, the HPT rig has been gradually introduced as a bench test for the effect of different third body layers (e.g., sand particles) on the frictional characteristics as well as the mechanical behaviour in the wheel-rail contact. Meierhofer (2015) performed a work on the effect of sand particles on the friction characteristics of wheel-rail contact using the HPT rig and developed a new wheel-rail creep force model. However, there is limited scope for this work as only one sand type was considered and there are no realistic application amounts. Recently, Skipper et al. (2019) conducted HPT tests using three types of sand under dry, wet, and leaf contaminated conditions to quantify the impact of particle characteristics on improving adhesion of wheel-rail contact. The HPT results showed that all three types of sand had little effect under dry contact conditions. However, silica sand was effective in improving traction between the wheel and rail in both low adhesion condition, namely wet and leaf contaminated layers, compared to un-sanded scenario. Subsequently, Skipper et al. (2023) performed a series of HPT tests under different contact conditions by using numerous different sources of sand. Then, a comprehensive investigation of how particle characteristics affect the tribological performance of wheel-rail contact was conducted by means of particle characterisation, tribological testing and statistical modelling. They found that the peak CoT increased with particle hardness and circularity under both dry and wet conditions. Under leaf contamination conditions, both particle size and hardness positively affected the peak CoT, with particle size having a more pronounced impact. Buckley-Johnstone (2019) used the HPT rig to explore the effect of small amounts of water and iron oxides mixtures on the wheel-rail interface. The results indicate that the adhesion in wheel-rail interface decreases compared to dry contact but does not produce sustained low adhesion (<0.05).

In addition, the collected HPT data can be utilised to parameterise the extended creep force (ECF) model for full-scale wheel-rail adhesion predictions. Evans et al. (2021) introduced the ECF model to predict the force characteristic at wheel-rail interface, and demonstrated how the ECF model can be parameterised with typical HPT outputs from dry baseline. This was followed by another HPT work by Evans et al. (2023), which was used to investigate the effect of water-based Top-of-Rail Friction Modifiers (TOR FMS) on the frictional characteristics at the wheel-rail interface. The obtained HPT results were used to parameterise the ECF model to include TOR FM characteristics and the model was validated against field test data. Afterwards, Skipper et al. (2024) applied data from a series of HPT tests under dry, wet and leaf contamination conditions to parameterise the ECF model. As a result, full-scale creep curves were predicted for different combinations of adhesion restoring materials and contaminants, which were then validated using published field test data (Meierhofer, 2015; Purcell and Lightoller, 2018; Fischer et al., 2020). The above studies provide some insights into the preliminary progress towards the prediction of full-scale creep curves at the wheel-rail interface in real-world scenarios.

2.6.3 Twin Disc Set-Up

An example of twin disc set-up as shown in Figure 2.24a, which uses two discs (i.e., one disc represents the wheel, and the other is rail) rolling against each other to simulate a wheel running over a rail (Skipper, 2021). However, the geometries of the twin discs differ significantly from real wheels and rails and their dimensions are much smaller compared to the actual wheels and rails, as illustrated in the Figure 2.24b. In addition, the actual contact between the discs is a line contact with a width of 10 mm, which differs from the actual wheel-rail contact. Another limitation of the twin disc set-up is the lack of realistic velocity between the surfaces, typically reaching only around 2 mph. However, the contact pressure between the discs is similar to that of a real wheel-rail interface, with average contact pressures of 900 - 1,500 MPa achievable.

The sanding system has also been applied to the twin disc set-up, thus promoting the widespread application of this test method in the investigation of how sand particles affect tribological performance between wheel and rail (Arias-Cuevas et al., 2010a, 2010b; Lewis et al., 2003, 2016; Lewis and Dwyer-Joyce, 2006). An example of sand particles application set-up is shown in Figure 2.24c. Lewis and Dwyer-Joyce (2006) carried out dynamic tests with and without sand on a twin disc set-up to study the effect of particles on surface wear for wheel and rail. The results showed that the application of sand led to an increase in the wear of the discs by a factor of 2 to 10. But the discs were scaled down, the surface damage on the discs was more severe than in actual wheel-rail contact. Arias-Cuevas and Lewis (2010) found that larger particles generally lead to better adhesion between wheel and rail. The results also showed that when the discharge rate of sand exceed a critical value, the sand at the wheel-rail interfaces forms a solid lubricant resulting in lower adhesion. Following the previous work, Arias-Cuevas et al. (2011) conducted a twin disc test on the effect of particle size on the improvement of wheel-rail adhesion under leaf contaminated conditions. They found that particles of any size removed the leaf layer and improved adhesion but could only provide some indication as the contact mechanism of twin disc is different from the actual situation. Several other studies investigated the effect of sand on wheel-rail adhesion under various contamination layer conditions using twin disc set-up (Kumar et al., 1986; Omasta et al., 2015; Wang et al., 2014, 2011). For oil contaminated contact surfaces, the application of sand restores wheel-rail adhesion when the slip rate is high (Kumar et al., 1986); and due to the high viscosity of the oil, it prevents the sand from entering the wheel-rail contact (Wang et al., 2014). For wet contact, sand particles have a positive adhesion effect, and the effect of sand application rate on recovery of wheel-rail adhesion increases progressively with increasing slip rate and surface velocity (Omasta et al., 2015; Wang et al., 2011). In addition to the use of sand particles, Wang et al. (2014) tested the effect of alumina particles on the adhesion between wheel and rail in the presence of different contamination layers. The results showed that alumina particles proved more effective than sand in restoring adhesion on oiled and wet contact surfaces due to their higher hardness. However, because the alumina particles were smaller than sand, they could not effectively penetrate the leaf layer and thus performed less effectively than sand in those conditions.

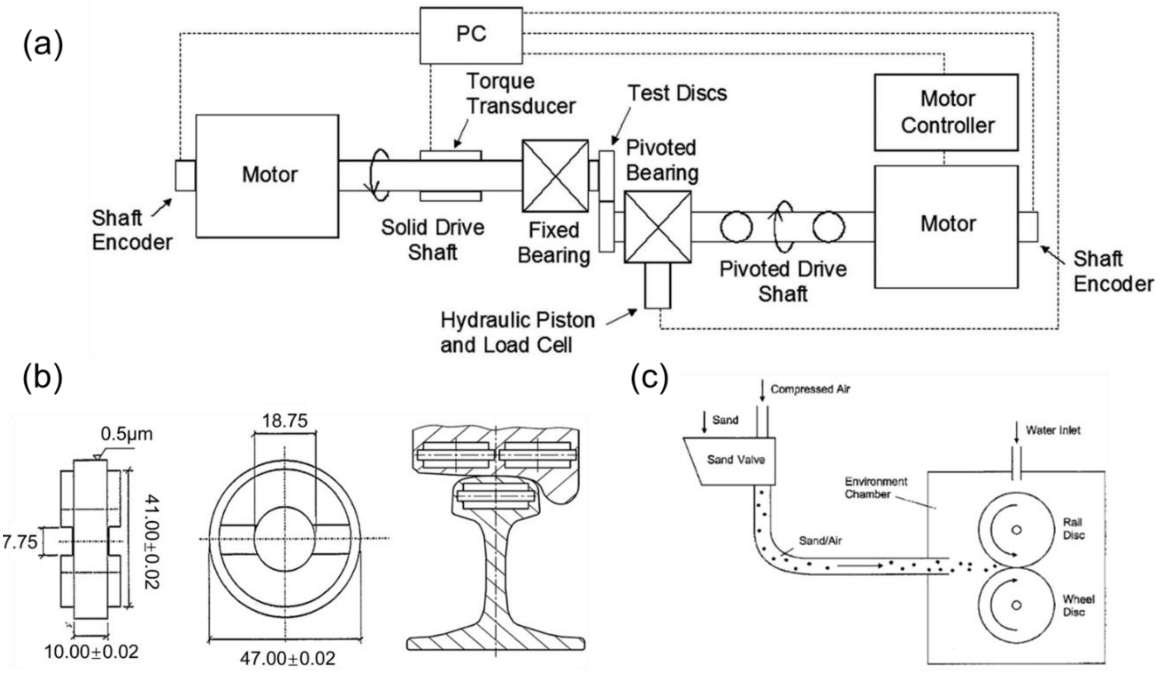

Figure 2.24. Schematics of (a) twin disc set-up, (b) wheel and rail disc geometry and (c) particle application set-up (edited from Arias-Cuevas et al. (2010b) and Lewis et al. (2003)).

2.6.4 Linear Full-Scale Rig

Linear full-scale rigs employ actual wheels and rails, replicating realistic contact pressures (900 – 1,500 MPa) and geometries, which is valuable for studying the application of particles into the wheel-rail contact area (Lewis et al., 2018; Pollicott, 1977). An example of a full-scale rig is shown in Figure 2.25. The wheel is marked as (1), and (3) represents a 1,010 mm length of rail moved by a linear slider bed (4). Sand is introduced into the contact area from the hopper (10) through the hose (12) and nozzle (14). The rest of labels denote the following components: (2) load frame, (5) PTFE strips, (6) horizontal actuator, (7) vertical actuator, (8) creep actuator, (9) chain and pulley assembly, (11) sand value, (13) air compressor, (15) control frame, (16) computer, (17) centrifugal fan, and (18) high speed camera. In addition, the fans can be used in the test to simulate and investigate the effect of prevailing winds and crosswinds. However, this set-up is limited by the truncated rail length used (600 mm for one such rig (Lewis et al., 2018)) and safety concerns, resulting in a lack of realistic wheel velocity.

Some studies investigated the relationship between sand particle size and adhesion of wheel-rail interface in an oiled contact using the full-size rig (Cooper, 1972; Tanvir, 1972). They found a positive correlation between particle size and wheel-rail friction. However, the effect of fine particles on the friction characteristics of wheel-rail contact was very weak, especially when the particle size was smaller than 53 μm. Following the above studies, Zobel (1974) investigated the effect of hardness of different types of sand on the adhesion between wheels and rails under oiled contact conditions by full-scale tests. The results show that harder particles have a positive effect on traction enhancement, but the efficiency of adhesion recovery decreases when the hardness of the particles exceeds that of quartz. Also, it was noticed by Zobel (1974) that the actual amount of sand used to improve adhesion was apparently less than the amount of sand actually discharged from the hose. Addressing the accuracy of the sanding system and the reduction of sand waste, Lewis et al. (2015) focused on the effect of application rate on improving adhesion in a full-scale rig. They found that a small amount of sand can restore low adhesion between the wheel and the rail and that a sand density of 7.5 g/m is sufficient. Lewis et al. (2018) also investigated the effect of sand entrainment on the wheel-rail contact surface by adjusting the hose position and the sand flow rate. The results indicated that the ideal position for the hose is as close as safely possible to the contact point and aligned with the nip. Additionally, reducing the sand flow rate below the 2 kg/min threshold significantly decreases the amount of sand entering the contact.

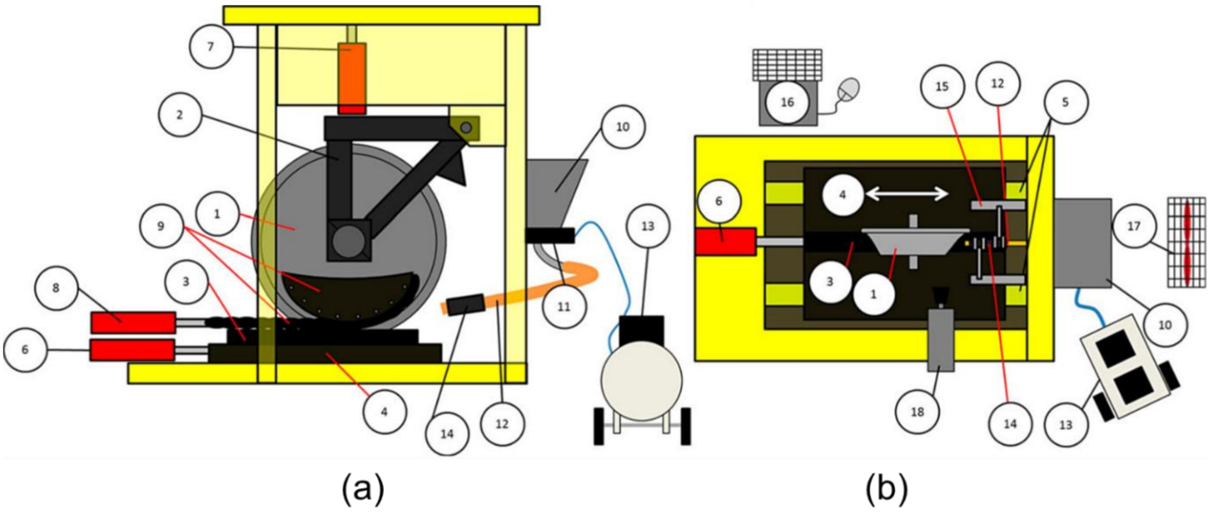

Figure 2.25. Schematic of linear full-scale rig sanding set-up: (a) side view and (b) top view. (edited from Lewis et al. (2018)).

2.6.5 Track Tests

Many on-site track tests have primarily been qualitative due to the challenges of conducting tests on operating railway lines (McEwen & Taylor, 1975; McEwen, 1977; Taylor & Pollicott, 1978). Also, the majority of studies have focused on the qualitative effects of sanding on adhesion improvement for wheel-rail contact (Pollicott, 1977). Most of these quantitative data come from either tribometer trains (Zobel, 1972), which provide actual adhesion values, or from actual train performance metrics, such as journey times, slip detection, and braking distances (Schofield et al., 1995; Marks, 1996; Tunley, 1999). While track tests offer inherent realism, the lack of control over variables can lead to potentially misleading results, necessitating that many conclusions from these tests be taken with caution.

Several studies have reported on tests conducted by British Rail Research using an emergency one-shot sander system to evaluate its effectiveness under critical braking conditions with low adhesion. Schofield et al. (1995) found that stopping distances were halved when the emergency sander was deployed, indicating an increase in adhesion. Marks (1996) also observed improvements based on feedback from drivers. Waring (1966) conducted a more detailed study and discovered that the emergency sander, with a discharge rate of 5 kg/min/rail, increased train retardation from 2% g to 9% g, enabling full braking to be achieved. Recently, a field work undertaken by Rail Safety and Standards Board (RSSB) (2018) validated Waring's findings that higher discharge rates lead to more effective braking. In addition, Arias-Cuevas and Li (2011) performed some field work to examine the influence of particle size on the removal of the leaf layer using an actual sander and real leaves. Their results showed that the use of sand was more effective in removing the leaf layer compared to not using sand. Moreover, they found that particle sizes ranging from 0.3 to 0.6 mm were the most effective in removing the leaf layer. An example of a track test using different sanding materials in dry, leaf contaminated conditions is shown in Figure 2.26.

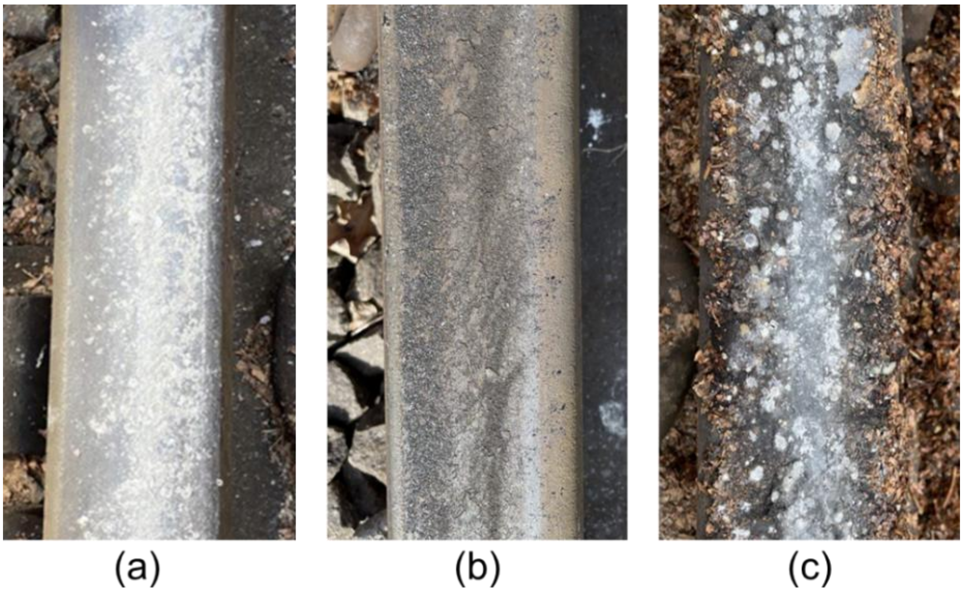

Figure 2.26. Track tests of (a) silica sand particles and (b) alumina particles in dry conditions, as well as (c) silica sand particles in leaf contaminated conditions.

2.6.6 DEM Simulations

The application of sand particles at the wheel-rail interface is a critical practice in the railway industry, restoring wheel-rail adhesion under adverse conditions. However, its tribological impact—specifically how sand particles affect friction properties at wheel-rail interface—has been a subject of increasing interest. Due to the complexity of particle characteristics, experimental methods present challenges in quantitatively analysing a specific signature of a particle. Discrete Element Method (DEM) simulations have emerged as a powerful tool to study these complex interactions, offering insights into particle behaviour under real-world conditions.

Several DEM studies have been conducted to investigate how sand particles affect the tribological behaviour at wheel-rail interface (Gao et al., 2024.; Gautam and Green, 2021; Maramizonouz et al., 2024, 2023a; Suhr et al., 2024a, 2024b).

Maramizonouz et al. (2023a) investigated particle entrainment efficiency in rail-sanding applications by DEM simulations, validating the results against full-scale experimental data. The findings suggest that aiming the sander nozzle closer to the wheel-rail interface (nip) significantly increases both entrainment efficiency and the coefficient of traction, with further investigation needed into particle properties and environmental factors. An example of the geometric layout of the DEM model and particle entrainment for three case studies for the sander is shown in Figure 2.27.

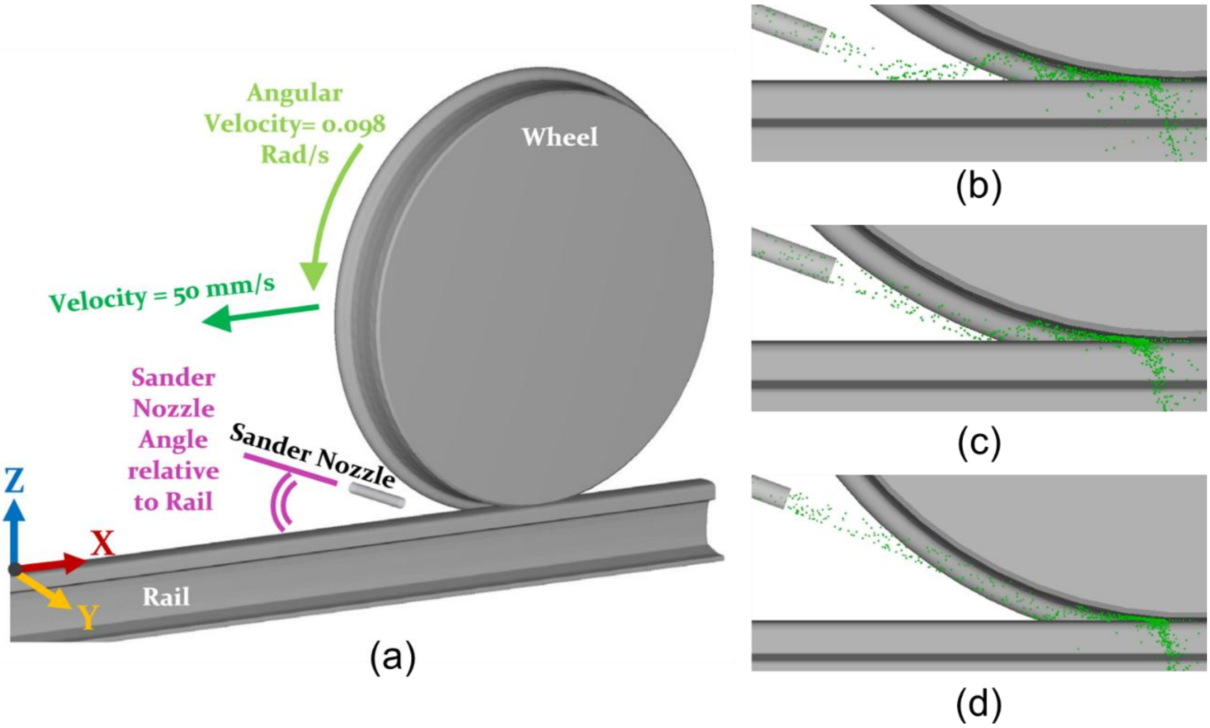

Figure 2.27. (a) Geometric layout of numerical model, and particle entrainment for the sander aimed at (b) the rail with a 20° angle, (c) the nip with a 20° angle, and (d) the wheel with a 20° angle in the DEM simulations (edited from Maramizonouz et al. (2023a)).

In a following study, Maramizonouz et al. (2024) considered important features such as train speed, sand flow rate and utilised CFD-DEM simulations to investigate rail-sanding efficiency. The results revealed that higher train velocities significantly reduce sand particle entrainment, with velocities over 30 m/s leading to near-zero efficiency (Figure 2.28a).

Additionally, optimising sander nozzle geometry, sand flow rate, and particle size can enhance entrainment efficiency, with longer sander lengths and downward cuts performing best (Figures 2.28b and 2.28c).

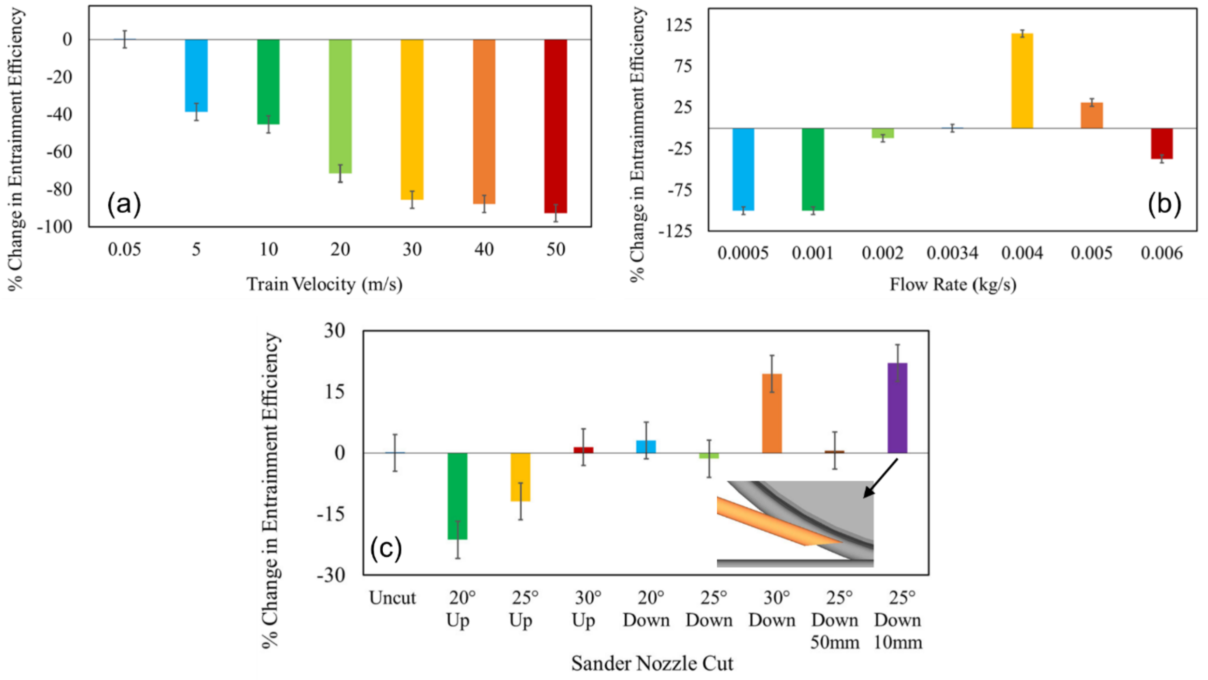

Figure 2.28. Percentage change in the entrainment efficiency of the rail-sanding for (a) different train velocity, (b) different sand flow rate, and (c) different sander nozzle configurations and placements (edited from Maramizonouz et al. (2024)).

Suhr et al. (2024a) represented the first step in developing a DEM model to simulate the sanding process in wheel-rail contacts, focusing on the adhesion-increasing mechanisms during sand particles crushing under high contact pressures. The DEM model successfully replicated experimental observations of fragment spread and cluster formation for different sand types and contact conditions. In addition, regarding sand particles can be indented into the rail under high pressure causing surface damage, Suhr et al. (2024b) incorporated a surface indentation model to DEM model of wheel-rail sanding. The model, validated through sand grain crushing tests, successfully reduced particle overlap and provided insights into the differences in cluster formation and indentation behaviour, marking a key step towards a comprehensive DEM model for rail sanding.

2.6.7 Electrical Isolation of Wheel-Rail Interface

The sanding process is widely recognised as a common method for restoring low adhesion conditions of wheel-rail contact area (Fulford, 2004). However, the presence of sand particles can lead to electrical isolation between the wheels and rails, particularly when a contamination layer (e.g., leaves) adheres to the railhead surface, potentially interfering with the proper functioning of rail circuits. Figure 2.29 illustrates a schematic diagram of a simple track circuit used in UK railways. Typically, the track is divided into blocks, each forming a “track circuit” for train detection. Within these sections, a transmitter at one end sends an electrical signal to a detector at the other end. When a train is present, it shorts the track circuit, enabling train detection. However, if the wheel-rail interface is insulated by a third body layer, there is a risk of train detection failure, which can lead to severe safety issues, such as near collisions at level crossings (Rail Accident Investigation Branch, 2019). It is reported from RSSB (2015) that 97% of electrical isolation between wheels and rails is due to railhead contamination, while only 3% is caused by sand application. However, these findings relate to the current representative sand application, i.e., 7.5 g/m (RSSB, 2018). Addressing low adhesion issues more effectively may require the application of larger quantities of sand, which could exacerbate electrical isolation between wheels and rails and increase the risk of train detection failures.

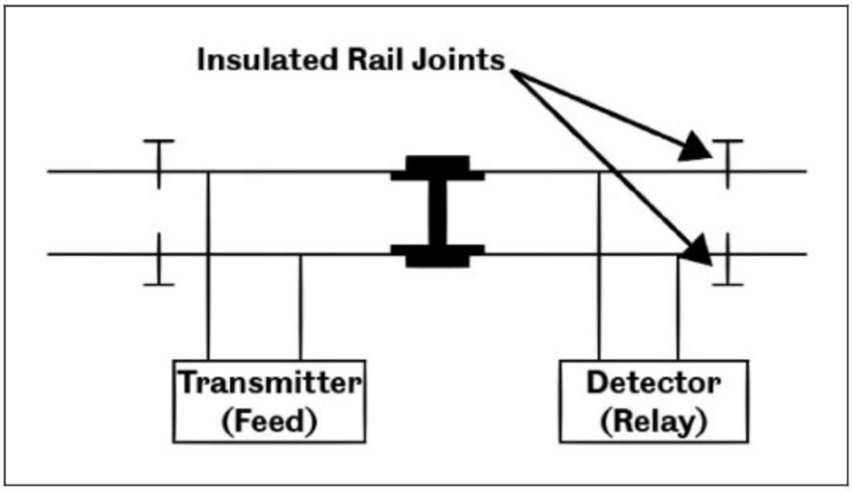

Figure 2.29. Schematic of the track circuit (Skipper et al., 2020).

Despite its importance, little research has been conducted on the effect of particles on wheel-rail electrical isolation and how particles might be redesigned to mitigate this issue. To date, two twin disc studies have been conducted (Arias-Cuevas et al., 2010a; Lewis et al., 2003), but their scope has been limited. These studies often involve contact conditions and dimensions that are not representative of real-world scenarios and are further constrained by the need to recycle contact surfaces. In addition, Chapteuil et al. (2018) used DEM to numerically model the presence of copper/graphite mixture at the wheel-rail interface. Their model was “a simplified version of reality” which intended to be qualitative rather than quantitative. Their results demonstrated that an optimal copper/graphite ratio could achieve a balance between electrical and tribological properties. Recently, Skipper et al. (2023) have conducted the HPT tests to investigate the impact of newly developed conductive sand particles, as well as the commonly used silica sand particles in the UK railways, on the electrical resistance at the wheel-rail contact area. These tests aim to provide insights into how different types of sand particles affect electrical isolation and suggest potential improvements for particle design to ensure effective adhesion without compromising electrical conductivity.

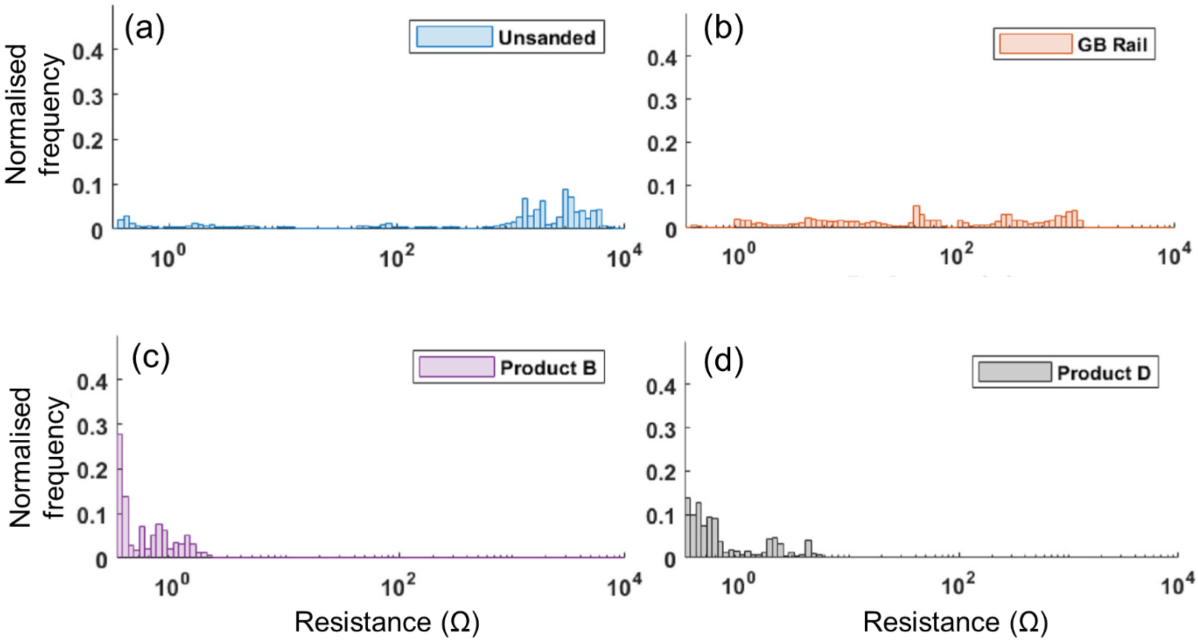

Figure 2.30. Histogram plots of time the HPT system spent at a given electrical resistance in leaf contaminated conditions (a) without sand, and with representative amount (i.e., 7.5g/m) of (b) silica sand, (c) conductive material Product B, and (d) conductive material Product D (edited from Skipper et al. (2023)).

2.7 Summary

This chapter reviewed previous DEM studies on modelling techniques for crushable particles, alongside the mechanical and electrical behaviour of particulate systems under load. The fundamental principles of DEM, the theoretical foundation of contact models for smooth surfaces, and the scaling laws employed to enhance the computational efficiency of DEM were discussed. Furthermore, sanding techniques used to improve adhesion at the wheel–rail interface were reviewed, including testing methods for evaluating the impact of sand particles on the tribological behaviour between the wheel and the rail, as well as the relevant DEM studies.

This study discussed four methods for modelling crushable particles—BPM, PRM, CIE, and BCM—and models sand particles using BPM. BPM offers a good balance between accuracy and computational efficiency by simulating bond fractures to replicate realistic sand grain crushing. Its flexibility in defining bond strength makes it adaptable to various sand types, providing a more accurate representation of particle breakage effects on macroscopic properties like shear strength and compaction.

According to the DEM literature, it is noted that the inherent anisotropy due to sample preparation and the induced anisotropy during loading can cause variations in particle alignment and contact. This alteration can result in the more conductive paths in certain contact directions thus leading to changes in the bulk electrical properties of the particulate system. However, the effect of anisotropy on the electrical behaviour of particulate systems under load was rarely discussed in the literature.

The DEM literature of sanding review found knowledge gaps associated with the lack of how particle characteristics, such as particle size, particle shape, and fragment size distribution (FSD), affect their tribological behaviour in wheel-rail interface. Additionally, there is limited research on the impact of sand particles on the electrical behaviour at the wheel-rail interface, specifically the electrical conduction characteristics of the wheel-rail interface when physical separation between the rails occurs due to the excessive use of sand, and the corresponding solutions to promote electrical transfer.

Chapter 3 Effect of Sand Characteristics in the Wheel-Rail Interface

3.1 Introduction

The study of the mechanical and tribological behaviour of granular materials at particle-structure and particle-particle interfaces is crucial across various engineering disciplines, such as pharmaceuticals, geotechnical engineering, the railway industry, and construction (Huang et al., 2014; Lewis and Dwyer-Joyce, 2006; O'Sullivan, 2011.; Sandeep et al., 2021; Wang et al., 2023; Wu et al., 2005). An example is the wheel-rail contact in railway engineering. Sanding has been utilised since the early days of railway engineering to restore wheel-rail adhesion. Despite its importance, there is still limited understanding of how the properties of sand particles, such as size, shape, and hardness, influence the tribological performance and mechanical behaviour at the wheel-rail interface. This knowledge gap presents significant challenges in optimising the use of granular materials to enhance performance and safety in railway engineering.

To investigate the effects of sand particle characteristics on the tribological behaviour between the wheel and rail, extensive experimental studies, such as HPT (Buckley-Johnstone et al., 2019; Evans et al., 2021; Skipper et al., 2023, 2019), twin-disc (Arias-Cuevas et al., 2011, 2010c; Huang et al., 2016; Wang et al., 2014), linear full-scale (Lewis et al., 2018), and track tests (Arias-Cuevas and Li, 2011) have been conducted. The above studies offer valuable insights into how sand particle characteristics affect wheel-rail traction enhancement. Due to the complexity of sand particle characteristics, targeting particular feature at the particle-scale in experiments is challenging. DEM (Cundall and Strack, 1979), which can analyse the particle kinematics at the particle-scale, has been utilised to investigate the effect of particle characteristics on the tribological performance at wheel-rail interface. Several DEM studies have been conduct to examine the influence of train speed, sand flow rate, and the geometry and positioning of sanders on the effectiveness of particle entrainment (Maramizonouz et al., 2024, 2023a), as well as the effect of sand particle crushing under high contact pressure on the mechanisms responsible for restoring adhesion (Suhr et al., 2024a, 2024b). However, further DEM research is required to explore how particle characteristics, such as size, shape, and FSD, affect the tribological behaviour between the wheel and rail.

In comparison to other experimental approaches, the HPT is regarded as capable of precisely regulating the amount of sand at the wheel-rail interface, thereby replicating real-world conditions more accurately, as discussed in Chapter 2. In this chapter, a DEM model of HPT is developed[2] to investigate the effects of different sand particle characteristics on the tribological behaviour at wheel-rail interface. At the macroscopic level, the tribological performance between wheel and rail is quantified by estimating the CoT; while at the particle-scale, the sand particle characteristics as well as the effect of fragments generated after sand fragmentation are examined on the tribological characteristics of the wheel-rail contact. This contributes to the current understanding of how the particles affect the tribological performance and mechanical behaviour of wheel-rail contact.

3.2 Methodology

3.2.1 Modelling of HPT Set-Up

A realistic simulation model of the HPT set-up is shown in Figure 3.1, where the geometry of the DEM model and the dimensions of the wheel-rail contact area are based on the HPT set-up used in the experiments by Evans et al. (2021). The EDEM™ software package (version 7.1.0) developed by Altair (2021) is employed in this study, while its in-built Hertz-Mindlin (no slip) contact model based on Hertz contact theory (Hertz, 1882) and Mindlin-Deresiewicz's work (Mindlin, 1949; Mindlin and Deresiewicz, 1953) is utilised to calculate the normal and tangential forces in wheel-rail contact area. The damping component of the forces in both normal and tangential directions, as well as the damping coefficient, are linked to the coefficient of restitution (Tsuji et al., 1992). Additionally, the tangential friction force follows Coulomb's law of friction (Cundall and Strack, 1979), and rolling friction is represented by a directional constant torque model that is independent of the contact (Sakaguchi et al., 2012).

---

[2] Zhang, C., Nadimi, S., Maramizonouz, S., Milledge, D. and Lewis, R., 2024. A discrete element model of high-pressure torsion test to assess the effect of particle characteristics in the interface. ASME Journal of Tribology, 146, pp.081501-1.

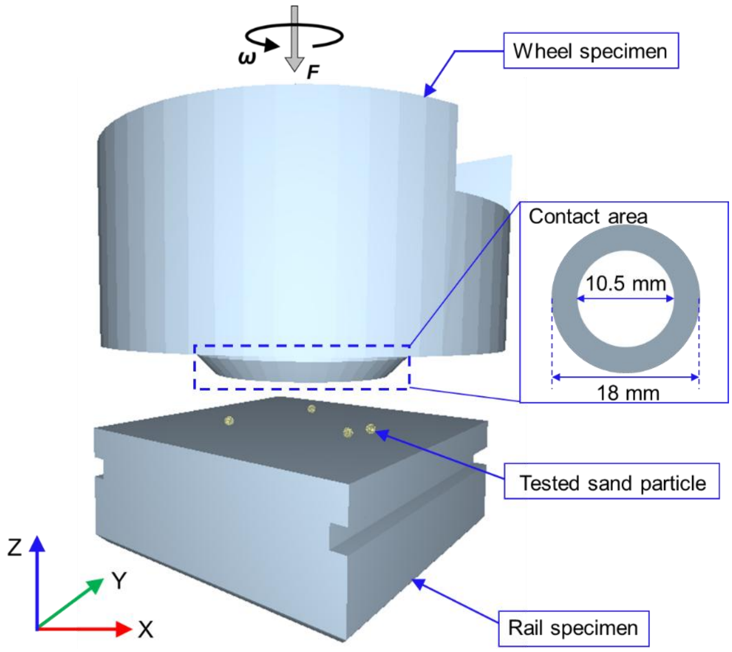

Figure 3.1. DEM model of the HPT setup and its geometrical parameters of the contact area between the wheel and rail specimens.

Firstly, the contact between the wheel and rail specimens under unsanded conditions is simulated by applying a constant vertical velocity of 0.05 m/s to the wheel specimen, bringing it into contact with the rail specimen and achieving the required contact pressure of 10 MPa. Once contact is established, the rail specimen rotates at a constant angular velocity of 1 deg/s. This rotation continues until the sweep length reaches 0.4 mm, marking the end of the simulation. In addition, to investigate the effects of sand particle characteristics on the tribological performance at the dry wheel-rail interface, 0.025 g of material (approximately 4 silica sand particles) is applied to the wheel-rail contact area. This amount corresponds to a sand concentration of 0.15 kg/m^2 at a rail speed of 10 mph, calculated by dividing the critical sand density of 7.5 g/m, as allowed by British Railways, by the estimated rail head width of 50 mm (Edalati et al., 2011; Lewis et al., 2003; Lewis and Masing, 2006; RSSB, 2013).

3.2.2 Scaling of Simulation Parameters

According to Equation 2.3 in Chapter 2, the mass, size, and stiffness of the particle influence the computational time. In the HPT simulation, for the sand particle crushed by the wheel specimen, increasing the fragment density while keeping the fragment size and stiffness constant will result in an increased fragment mass and a larger critical time step. Similarly, increasing the fragment size or decreasing the shear stiffness of the fragments will speed up the computation time. However, given the mass, size, and stiffness of actual sand fragments, a 20% Rayleigh time step in this simulation would be too small, resulting in a prohibitively high computational cost (Cundall and Strack, 1979; O'Sullivan, 2011). Therefore, the actual Young's modulus E (70 GPa) and density ρ (2,650 kg/m^3) of the sand are appropriately adjusted according to the scaling criteria proposed in the literature (Behjani et al., 2017; Hærvig et al., 2017; Washino et al., 2018) and Equation 2.3 allowing for an increase in the time step from 10^{-8} s to 10^{-7} s.

Moreover, to test the validity of the results after scaling the parameters, HPT simulations are performed on a Dell i5-core laptop for both actual and scaled sand to compare the effects of scaling on the numerical data of wheel-rail traction presented in Figure 3.2 and computational time. Due to the dynamic similarity characteristics of the two models (actual and scaled), the contact pressure for the HPT simulations is scaled from 1,000 MPa to 10 MPa according to the dimensionless analysis method (Wang et al., 2022).

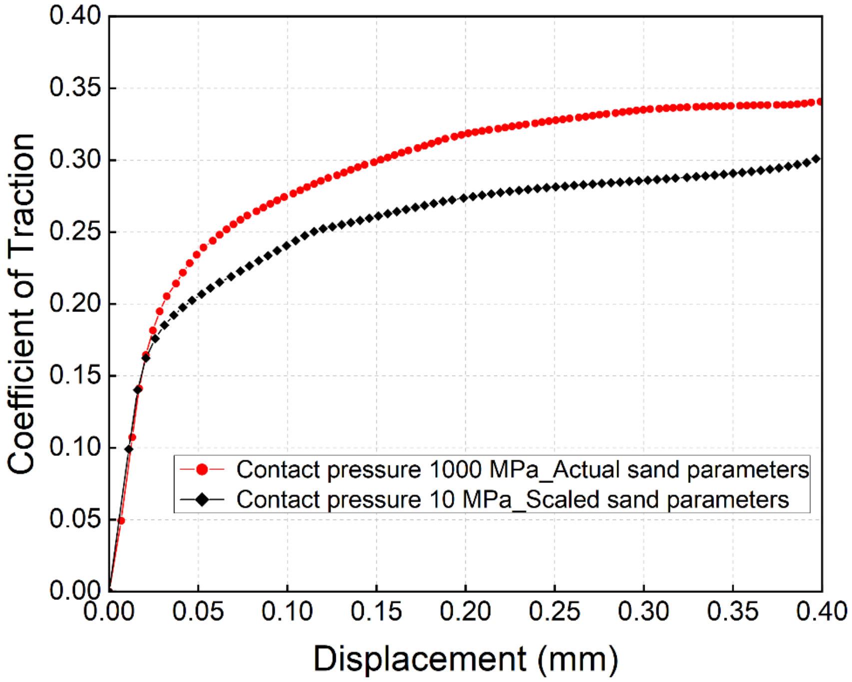

Figure 3.2. Comparison of the coefficient of traction obtained from DEM modelling of the HPT set-up for the two cases using actual (red) and scaled (black) sand parameters.

As shown in Figure 3.2, the relationship between the CoT and the displacement in both cases exhibits a similar trend, with CoT values decreasing by only 0.04 when the scaled parameters are utilised. Additionally, the efficient HPT prediction model developed in this study does not require High Performance Computing (HPC), as the average computation time for one simulation with scaled parameters is about 5 hours, whereas simulation using actual parameters takes more than a week.

Therefore, the adjusted parameters used in the HPT simulations are listed in Table 3.1, where the materials used for wheel specimen, rail specimen, and sand particle are R8T steel, R260 steel, and silica sand. The material properties are taken from literature (Skipper et al., 2019; Skipper, 2021; Skipper et al., 2021; Szczotok et al., 2018); while the interaction parameters used in the simulations are taken from literature (Skipper, 2021; Skipper et al., 2021).

Table 3.1 Material parameters used in the HPT simulations.

<table>
<tr><th>Material Parameter</th><th>Unit</th><th>Value</th></tr>
<tr><td>Silica Sand</td><td></td><td></td></tr>
<tr><td>Poisson’s ratio (υ_m)</td><td>–</td><td>0.3</td></tr>
<tr><td>Scaled Density (ρ)</td><td>kg/m^3</td><td>2.65×10^4</td></tr>
<tr><td>Scaled Young’s modulus (E)</td><td>GPa</td><td>0.7</td></tr>
<tr><td>Wheel</td><td></td><td></td></tr>
<tr><td>Poisson’s ratio (υ_m)</td><td>–</td><td>0.28</td></tr>
<tr><td>Density (ρ)</td><td>kg/m^3</td><td>7,850</td></tr>
<tr><td>Young’s modulus (E)</td><td>GPa</td><td>229.45</td></tr>
<tr><td>Rail</td><td></td><td></td></tr>
<tr><td>Poisson’s ratio (υ_m)</td><td>–</td><td>0.3</td></tr>
<tr><td>Density (ρ)</td><td>kg/m^3</td><td>7,850</td></tr>
<tr><td>Young’s modulus (E)</td><td>GPa</td><td>210</td></tr>
<tr><td>Interaction Parameters</td><td colspan="2">Value</td></tr>
<tr><td>Coefficient of restitution (e_p)</td><td colspan="2">0.8</td></tr>
<tr><td>Coefficient of static friction (μ_s)</td><td colspan="2">0.5</td></tr>
<tr><td>Coefficient of rolling friction (μ_r)</td><td colspan="2">0.01</td></tr>
</table>

3.2.3 Sand Particle Modelling

The breakage of a single sand particle into several fragments under mechanical loading can be reproduced in DEM simulations (Fu et al., 2017; Wang and Arson, 2016; Wu et al., 2022). The BPM developed by Potyondy and Cundall (2004) is employed to model an individual sand particle in this study. In the HPT simulation, it is assumed that the fragments produced by the crushed sand particles indent the metal surface, but fully recover from the deformation as they follow elastic contact behaviour. Surface damage resulting from particles indented into the wheel and the rail specimens is not considered here as it falls outside the scope of this study. Figure 3.3 illustrates a modelled sand particle, with the red parts representing the bonds between the fragments. The forces and moments acting on the bond are adjusted incrementally at each time step during the compaction of the particles by the wheel specimen. When the applied stresses in the normal and tangential directions exceed a predetermined value, the bond breaks, simulating the breaking behavior of a sand particle at each time step. Considering the brittle characteristics of silica sand particles and their corresponding particle breakage modelling (Metzger and Glasser, 2012; Schilde et al., 2014), the benchmark bond properties for the HPT simulation are identified (Normal stiffness (k_n): 1×10^{10} N/m^3, stiffness ratio (k_n/k_t): 1.0, critical normal strength (σ_{max}): 1×10^8 Pa, strength ratio (σ_{max}/τ_{max}): 1.0, and bonded disk scale (λ): 1.25). A parametric study of the bond properties is conducted (as mentioned above in Table 3.1) to investigate their effects on the frictional characteristics at the wheel-rail interface; as well as the effect of size and the number of sand particles on the wheel-rail adhesion are also investigated, as listed in Table 3.2.

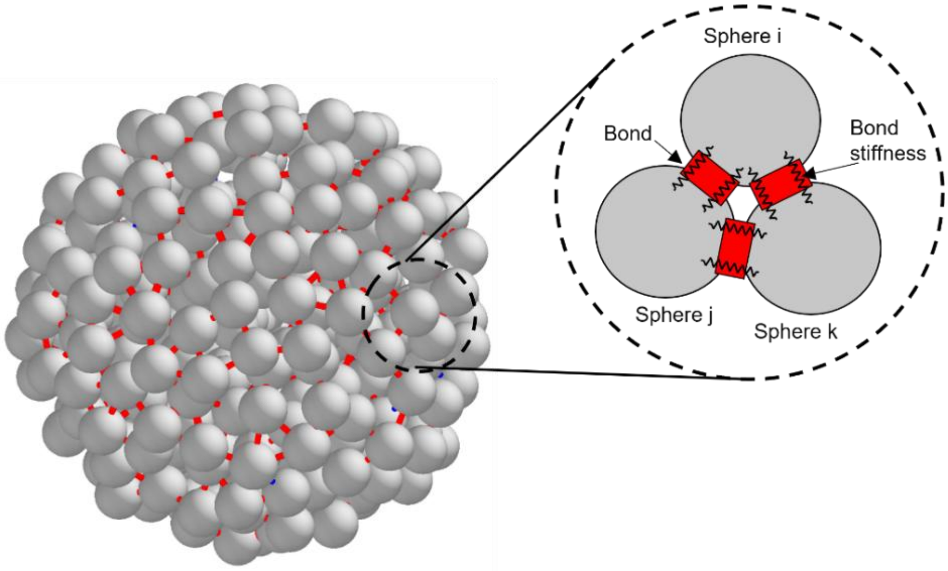

Figure 3.3. Schematic of a sand particle represented as a cluster of spherical fragments bonded together using the bonded particle model.

Table 3.2 Particle properties used as input parameters in each simulation scenario.

Case No.	Bond strength [Pa]	Bond stiffness [N/m^3]	Particle diameter [mm]	Number of particles
a.1	1×10^{7}	1×10^{10}	1.0	4
a.2	5×10^{7}	1×10^{10}	1.0	4
a.3	1×10^{8}	1×10^{10}	1.0	4
a.4	5×10^{8}	1×10^{10}	1.0	4
a.5	1×10^{9}	1×10^{10}	1.0	4
a.6	5×10^{9}	1×10^{10}	1.0	4
a.7	1×10^{10}	1×10^{10}	1.0	4
b.1	1×10^{8}	1×10^{9}	1.0	4
b.2	1×10^{8}	2.5×10^{9}	1.0	4
b.3	1×10^{8}	5×10^{9}	1.0	4
b.4	1×10^{8}	1×10^{10}	1.0	4
b.5	1×10^{8}	2.5×10^{10}	1.0	4
b.6	1×10^{8}	5×10^{10}	1.0	4
b.7	1×10^{8}	1×10^{11}	1.0	4
c.1	1×10^{8}	1×10^{10}	0.83	4
c.2	1×10^{8}	1×10^{10}	1.0	4
c.3	1×10^{8}	1×10^{10}	1.5	4
c.4	1×10^{8}	1×10^{10}	2.0	4
d.1	1×10^{8}	1×10^{10}	1.0	4
d.2	1×10^{8}	1×10^{10}	1.0	8
d.3	1×10^{8}	1×10^{10}	1.0	16

In addition, to determine the size of the fragments, a sample of the crushed sand collected from the railhead has been analysed using laser diffraction (Figure 3.4). Given that the size of spherical fragments produced by sand particle fragmentation significantly impacts the computational time of the DEM simulation (Cundall and Strack, 1979; O’Sullivan, 2011), a fragment diameter of 100 μm (<D_{90}) has been selected to ensure the simulation can be completed within a reasonable timeframe.

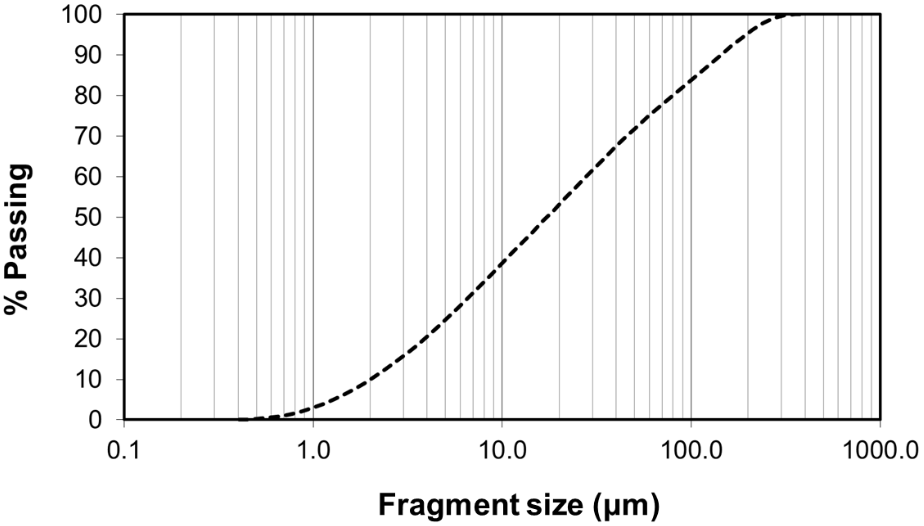

Figure 3.4. Size distribution curve of the crushed sand obtained using laser diffraction ("% Passing" on the y-axis represents the percentage of fragments in the sample that have a size smaller than or equal to a particular fragment size on the x-axis).

3.2.4 Calculation of Effective Radius of Friction

In the HPT test, although creep stresses are uniform across the contact area (Figure 3.1), the contribution of these stresses to the support torque is greater at higher radii. Thus, using the midpoint radius to calculate creep stress from the measured torque is not correct (Evans et al., 2021). To determine the creep stress in the contact area, the "effective radius of friction (ERF)", a concept commonly used in clutch design, is used as the point at which creep stress is calculated (Budynas et al., 2015). The outer and inner radius of the HPT contact area yield an ERF of 7.29 mm. However, in the HPT simulation, the ERF can be more accurately estimated by considering the distance of each individual fragment to the centre of the annular contact area. The ERF, accounting for all fragments, can be computed in each simulation by defining the average effective radius of friction (ERF_{avg}):

$$ERF_{avg} = \frac{\sum_{i} \sqrt{\left|\left(x_i - x_o\right)\right|^2 + \left|\left(z_i - z_o\right)\right|^2}}{N} \tag{3.1}$$

where x_i and z_i are the coordinates of each fragment on the X-Z plane, x_o and z_o are the coordinates of the centre of the annular contact area on the X-Z plane, and N is total number of fragments present in the contact area.

After the ERF_{avg} is calculated, the CoT at the wheel-rail interface can be estimated (Buckley-Johnstone et al., 2019):

$$CoT = \frac{F_S}{F_N} = \frac{T_m / ERF_{avg}}{F_N} \tag{3.2}$$

where F_N and F_S are the normal load and shear force, respectively. T_m is the torque measured by the HPT apparatus.

3.3 Effects of Bond Properties on the Coefficient of Traction

The effects of bond properties between fragments of sand particle on the CoT at the wheel-rail interface is discussed in this sub-chapter, where the simulation scenarios used are presented in Table 3.2. Figure 3.5 shows how varying bond strength affects the CoT at wheel-rail contact area, while bond stiffness remains constant. Altering the bond strength between particle fragments from 1×10^7 Pa to 1×10^{10} Pa has a negligible effect on the CoT. The number of fragments in the contact area was determined using an annular bin, matching the wheel-rail contact dimensions. The total fragments remained relatively stable across varies bond strengths.

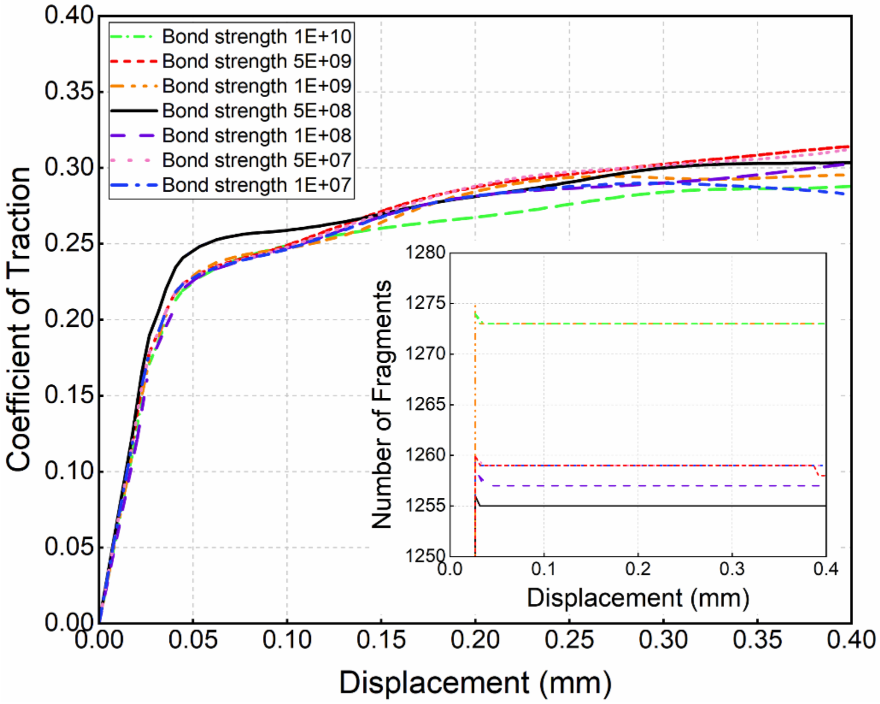

Figure 3.5. Comparison of the coefficient of traction obtained from DEM modelling of the HPT set-up using different values of bond strength (The insert graph shows the number of fragments remaining on the contact area for each value of the bond strength).

To investigate how bond strength affects the breakage behaviour of sand particles during the HPT test, case study a.7 (see Table 3.2) is selected, with a particle diameter of 1.0 mm, and bond strength and stiffness of 1×10^{10} Pa and 1×10^{10} N/m^3, respectively. Figure 3.6a-1 shows that in the first stage, when the wheel specimen initially contacts the sand particle before a normal load is applied, the particle retains its shape and remains in a steady state. In the second stage (Figure 3.6a-2), applying a normal load causes the particle to deform under compressive forces, with a sudden increase in compressive forces at the centre of the particle and tensile failure at the edges. During the third stage of compaction (Figure 3.6a-3), the particle fragments detach completely and come into direct contact with the wheel and rail specimens, with the vertical load remaining constant until the end of simulation.

Figure 3.6b presents the changes in the angular velocity of fragments from the beginning to the end of the torsion phase. Fragments in the central area exhibit greater angular velocity than those in the surrounding area, though the difference is not significantly large. The sand fragment layer remains stable under vertical and torsional loads from the wheel and rail, as normal and tangential stresses rarely exceed the critical strength of the bonds. This stability prevents fragment detachment, leading to negligible differences among cases 4, 5, and 6 in Figure 3.6b.

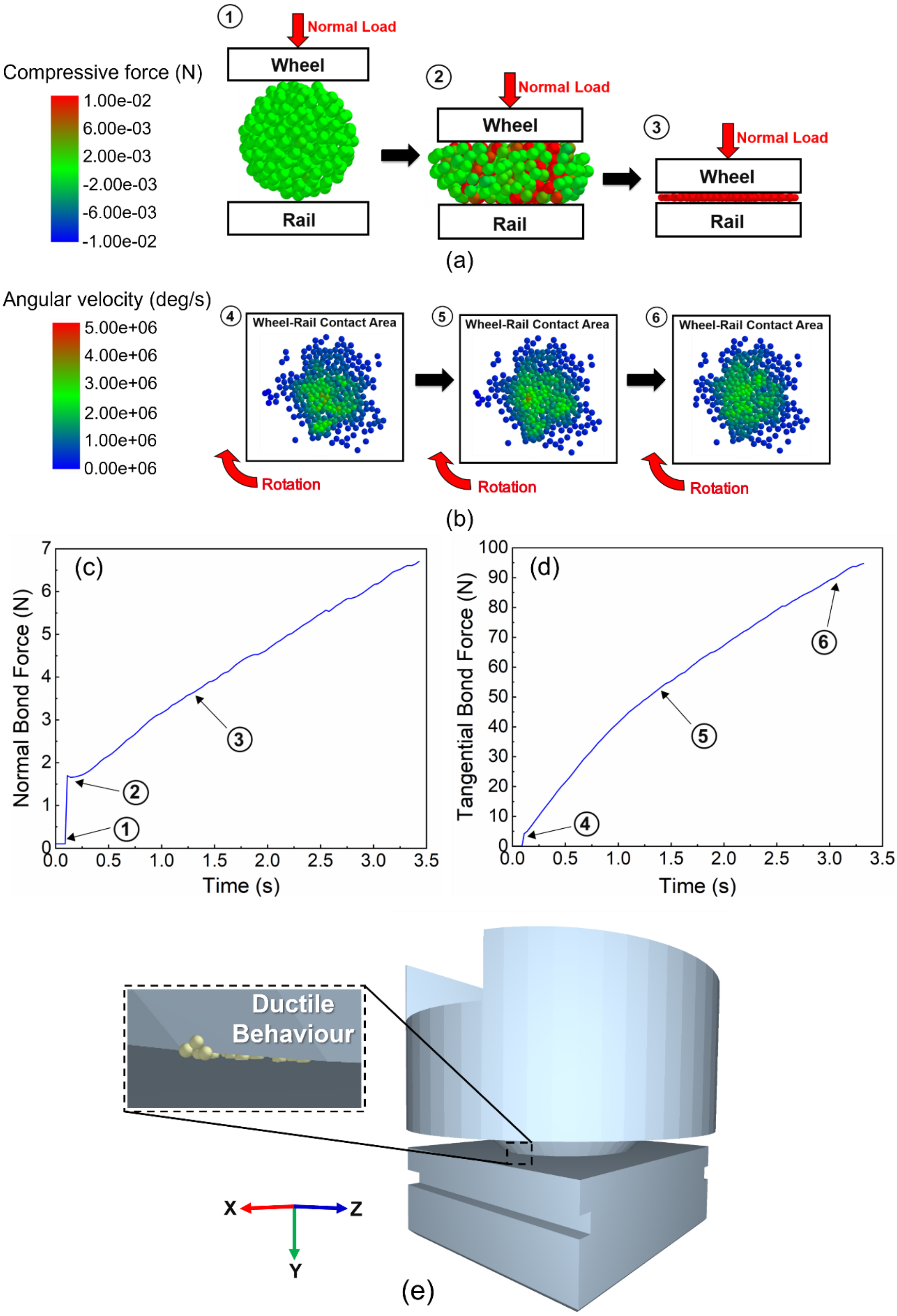

Figure 3.6. The breaking behaviour of the sand particle and the evolution of the bond force in the normal and tangential directions for particle with a 1.0 mm diameter, and a bond strength and stiffness of 1×10^{10} [Pa] and 1×10^{10} [N/m^3], respectively, during the DEM modelling: (a) Changes in the compression force of fragments during compaction (side view), (b) Changes in the angular velocity of the fragments during torsion (top view), (c) Normal bond force, (d) Tangential bond force, and (e) the particle showing ductile behaviour when breaking.

Figure 3.6c illustrates that bond force in the normal direction increases sharply during the second stage of compaction, while Figure 3.6d shows no abrupt increase in tangential bond force. The bond force in both normal and tangential directions increase gradually but neither exceed the corresponding critical bond strength. However, high bond strengths may cause inappropriate breakage behaviour in sand particles, as shown in Figure 3.6e, where a small fraction of agglomerates accumulates at the edge of the wheel-rail intersection region at a bond strength of 1×10^{10} Pa, and the sand particles exhibit breakage behaviour of ductile material rather than the expected brittle material.

Figure 3.7 presents the effect of different bond stiffness values on the CoT while keeping the bond strength constant. As the bond stiffness varies between 1×10^{9} and 1×10^{11} N/m^{3}, its effect on the CoT is more pronounced compared to the bond strength. Additionally, for bond stiffness values which below 5×10^{10} N/m^{3}, the change in bond stiffness has a minimal effect on the number of fragments generated at the wheel-rail contact area due to particle breakage. However, when the bond stiffness values exceed 5×10^{10} N/m^{3}, the number of fragments generated in the contact area gradually decreases during torsion, with the rate of decline becoming more pronounced at higher bond stiffness values (i.e., 1×10^{11} N/m^{3}).

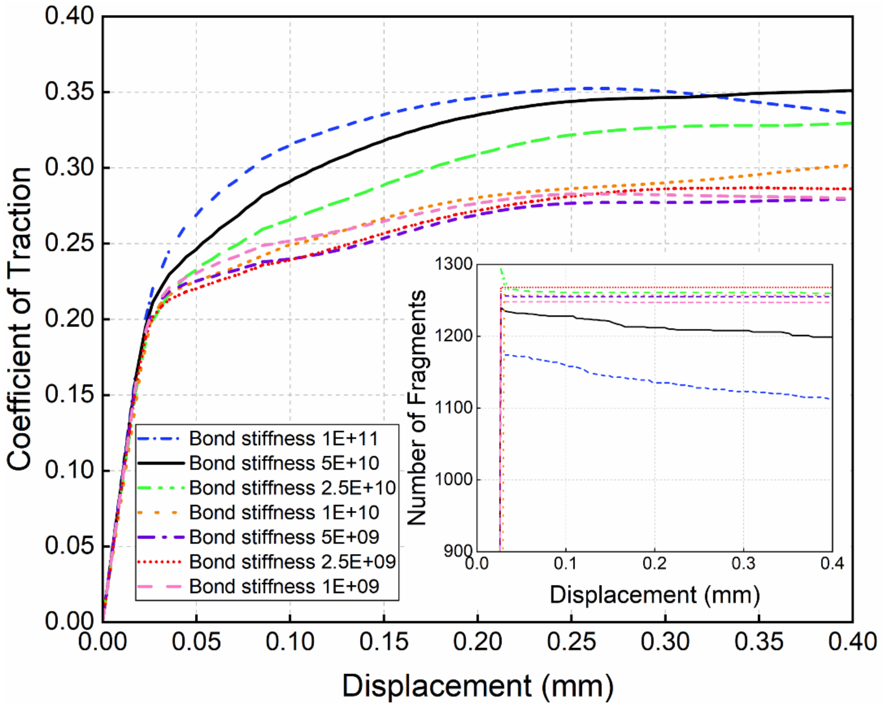

Figure 3.7. Comparison of the coefficient of traction obtained from DEM modelling of the HPT set-up using different values of bond stiffness (The insert graph shows the number of fragments remaining on the contact area for each value of the bond stiffness).

To investigate the effect of bond stiffness on the breakage behaviour of sand particles during the HPT test, case study b.7 (refer to Table 3.2) is chosen. This case study involves a particle diameter of 1.0 mm, with bond strength and stiffness set at 1×10^8 Pa and 1×10^{11} N/m^3, respectively. When a normal load is applied to the wheel specimen (Figure 3.8a-1), the force transfers to the particles, resulting in a sudden increase in compressive force on most of the particle fragments as they extend outward from the centre of the particle (Figure 3.8a-2). In the third stage (Figure 3.8a-3), the particle is completely crushed and subjected to a continuous normal load until the end of the test.

As shown in Figure 3.8b, there is a significant increase in the angular velocity of the fragments at the beginning of the twist, with the overall angular velocity being greatest in the central region of the fragment layer. At this stage, the normal and tangential stresses acting on the bond increase dramatically and exceed the critical strength of the bonds, leading to fragment detachment. Subsequently, the angular velocity of the fragments decreases and stabilises from the middle stage of torsion to the end of the simulation.

In Figure. 3.8c, the normal bond strength increases sharply to about 28 N during the second stage of compaction, exceeding the critical normal bond strength (approximately 67 N) after entering the third stage. In Figure 3.8d, the tangential bond force increases abruptly at the start of the twist, and then exceeds the critical tangential bond strength (around 385 N) at around 0.75 s into the test. With high bond stiffness, the forces generated to resist bond stretching can easily exceed the critical bond strength, resulting in bond breakage and a gradual reduction in the force exerted on the bond.

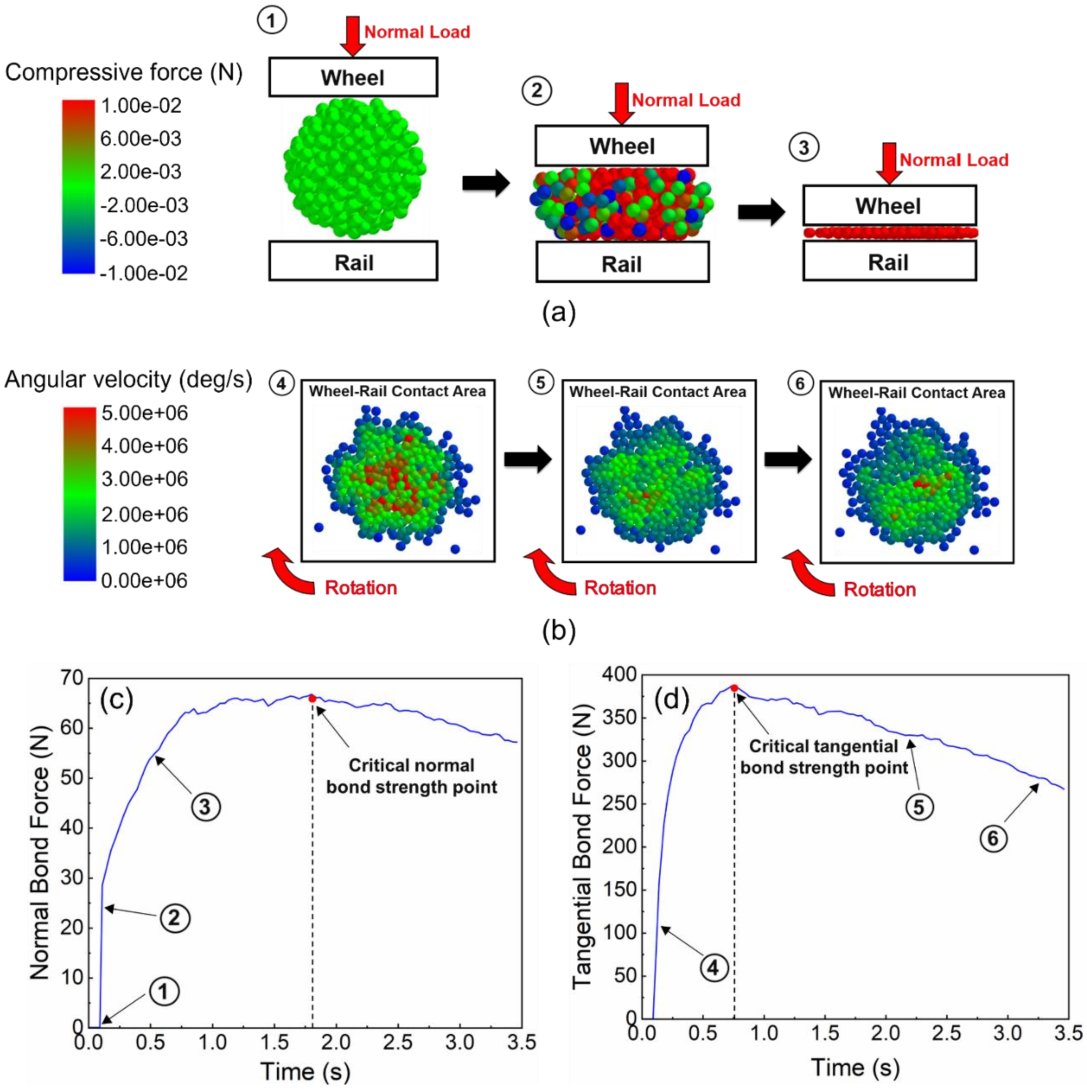

Figure 3.8. The breaking behaviour of the sand particle and the evolution of the bond force in the normal and tangential directions for particle with a 1.0 mm diameter, and a bond strength and stiffness of 1×10^8 [Pa] and 1×10^{11} [N/m^3], respectively, during the DEM modelling: (a) Changes in the compression force of fragments during compaction (side view), (b) Changes in the angular velocity of the fragments during torsion (top view), (c) Normal bond force, and (d) Tangential bond force.

3.4 Effects of Particle Size on the Coefficient of Traction under Torsional Loading

In this sub-chapter, the effects of sand particle size on traction at wheel-rail contact area is discussed, and the detailed parameters for particle with different size are listed in Table 3.3. Figure 3.9 shows that the CoT decreases as particle size increases. During the HPT simulations, the wheel specimen gradually approaches the rail specimen and compacts the particles. The sand particles with smaller size are completely broken under this load. This causes the fragments to detach fully from the parent particles and come into direct contact with the wheel and rail specimens. However, when the particle diameter is increased to 2 mm, the particles do not completely break under the load. Instead, the fragments cluster together and form layers at the wheel-rail contact area.

Table 3.3 Number of fragments and bonds and average effective radius for each particle size.

Particle diameter [mm]	Number of fragments	Number of bonds	Fragments diameter [mm]	Average effective radius of friction in HPT [mm]
0.83	210	486	0.1	7.52
1.0	326	739	0.1	7.40
1.5	1,000	2,892	0.1	7.24
2.0	2,840	6,855	0.1	7.32

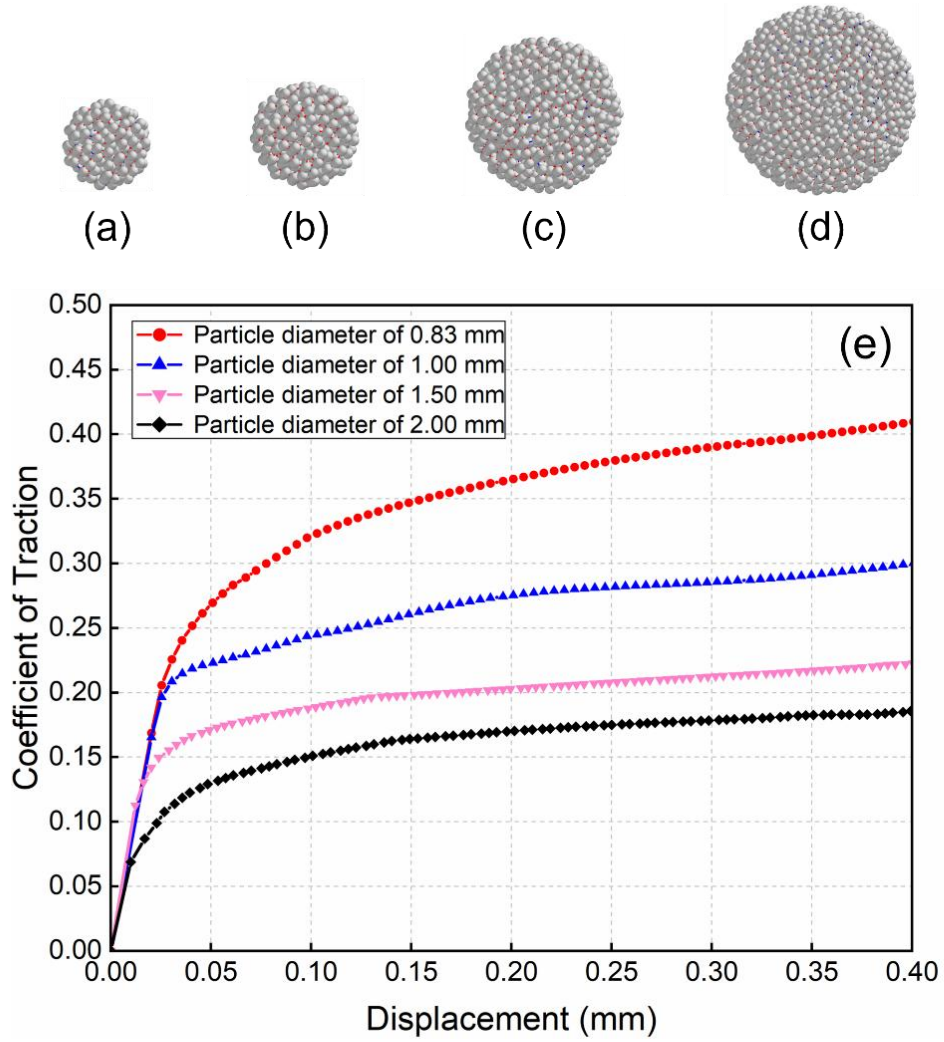

Figure 3.9. Sand particles of different size with a diameter of: (a) 0.83mm, (b) 1.0mm, (c) 1.5mm, and (d) 2.0mm used in the DEM models and (e) comparison of the coefficient of traction obtained from DEM modelling of the HPT set-up using different particle sizes.

Figure 3.10 provides a closer view of the force transfer mechanism. When a normal load is continuously applied to smaller particles (Figure 3.10a), the fragments completely detach from the parent particle, forming a single layer that indents into both the wheel and rail surfaces. This results in the creation of a reaction force that transmits the torsional force more effectively (Skipper et al., 2023). In contrast, as shown in Figures 3.10b to 10d, for larger particle diameters of 1 mm, 1.5 mm, and 2 mm, the fragments break away during compaction, but numerous overlapping fragments are observed at the wheel-rail interface. This indicates that some fragments cluster together, forming weak shear bands and resulting in lower traction forces.

Additionally, Figure 3.10e shows that for particle diameters smaller than 2 mm, the number of fragments in the contact area remains constant during the test. However, for particles with a diameter of 2 mm, the number of fragments increases as the sweep length increases. This is due to the expansion of the fragment layer as the wheel and rail specimens twist against each other, allowing more fragments to come into direct contact with the wheel and rail surfaces.

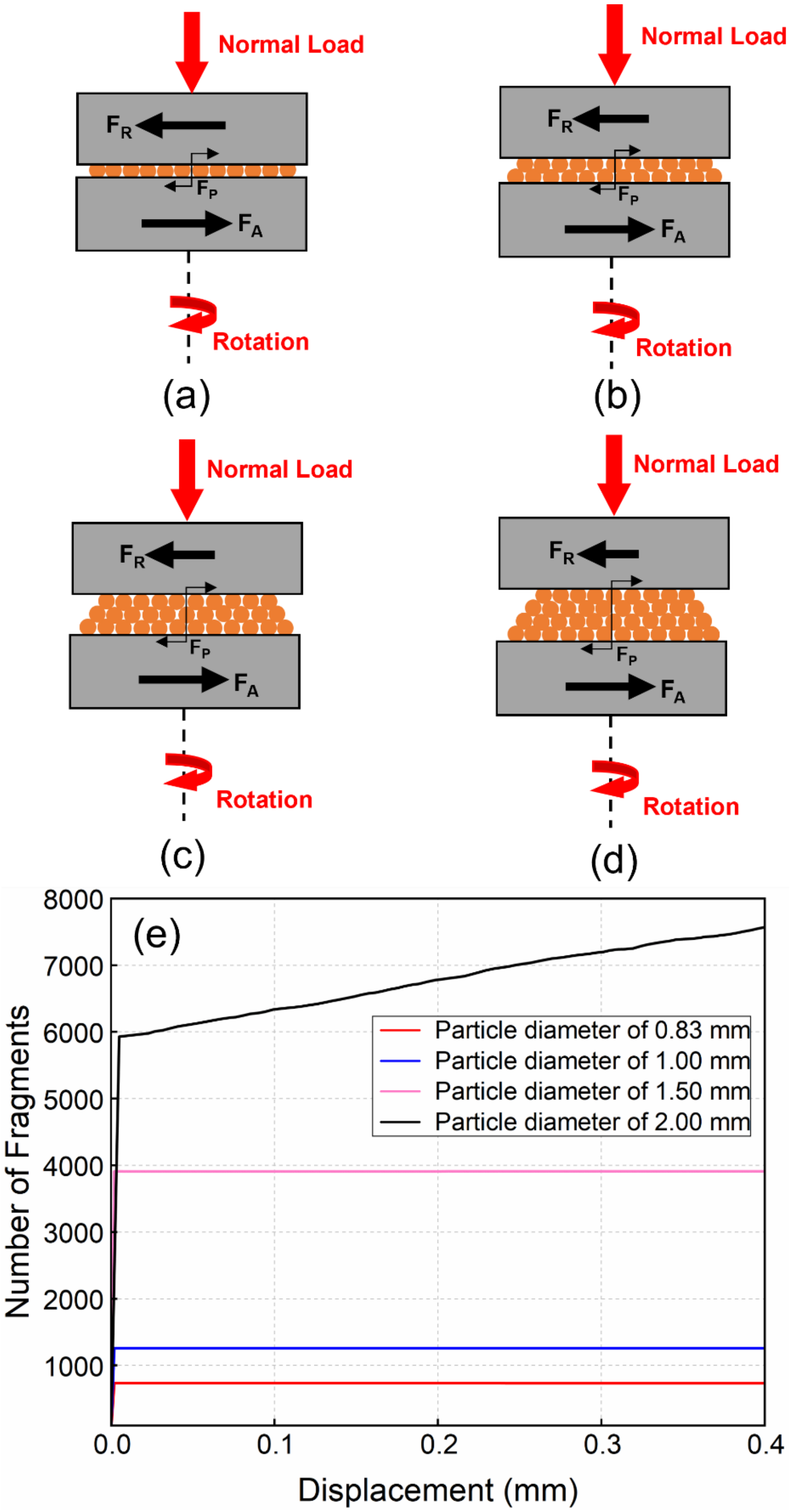

Figure 3.10. Particle breakage in the contact area, the variation in the number of fragments depending on the particle size, and the possibility of the formation of fragment clusters and weak shear bands during the DEM simulation for particles with a diameter of: (a) 0.83mm, (b) 1.0mm, (c) 1.5mm, and (d) 2.0mm, and (e) comparison of the number of fragments produced during the DEM modelling of the HPT set-up for the above four particle sizes.

Figure 3.11 compares the peak CoT values for different particle sizes obtained from the simulations to the experimental results for both dry and leaf-contaminated conditions provided by Skipper et al. (2023). The peak CoT of the DEM simulations is determined as the maximum value reached at the end of the simulation. It is important to note that the HPT test focuses exclusively on the friction effect as the crushed particles move through the contact. It does not account for particle trapping in the actual wheel-rail nip, where particles indent the rail and are subsequently crushed by friction forces. The simulation results indicate that as particle size increases, the peak CoT values decrease. In contrast, the experimental observations do not show a clear relationship between particle size and peak CoT under both dry and leaf-contaminated conditions. In the DEM simulations, particles are positioned identically to those in the experiments, and material heterogeneity effects are absent. The peak CoT values from the DEM simulations are closer to those observed in the leaf-contaminated condition in the experiments. This similarity may be due to the exclusion of metal-to-metal contact in the DEM simulations (Zhang et al., 2024a).

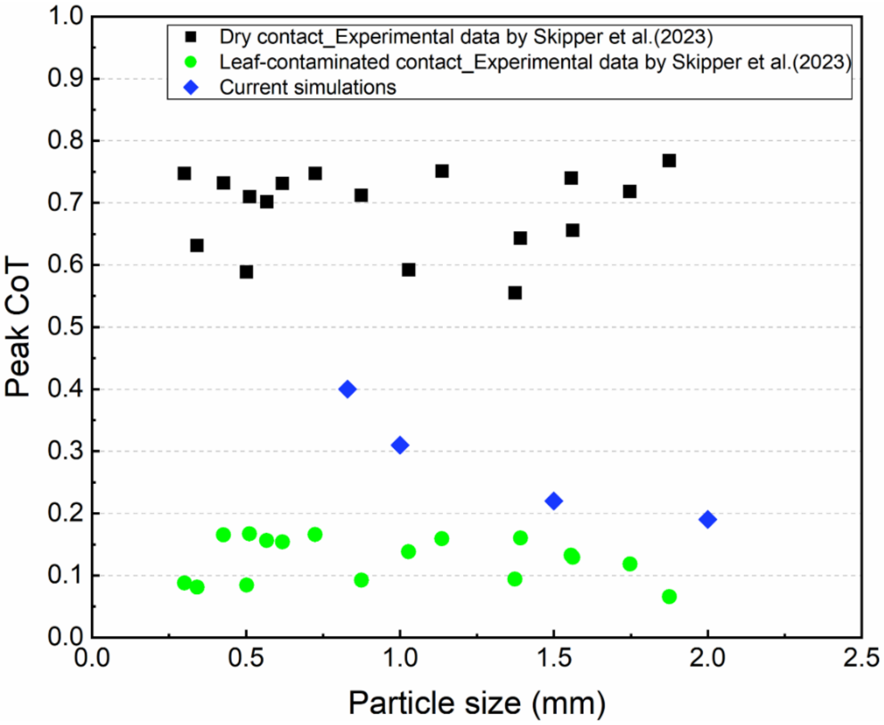

Figure 3.11. Comparison of the peak coefficient of traction obtained from DEM modelling of the HPT set-up (blue diamond) using different particle sizes to the experimental results for dry (black square) and leaf-contaminated (green circle) contact condition by Skipper et al. (2023).

In Figure 3.12, the branch vectors, defined as lines connecting the centroids of each pair of particle fragments, are shown for the four different particle sizes and are coloured based on their contact normal forces. For the smallest sand particle, with a diameter of 0.83 mm (Figure 3.12a), the branch vectors do not overlap. However, as the size of the sand particles increases, the number of overlapping branch vectors in the central region of the particles increases sharply (Figures 3.12b to 3.12d). This indicates that the particles are rolling and sliding on top of each other in the central region during torsion.

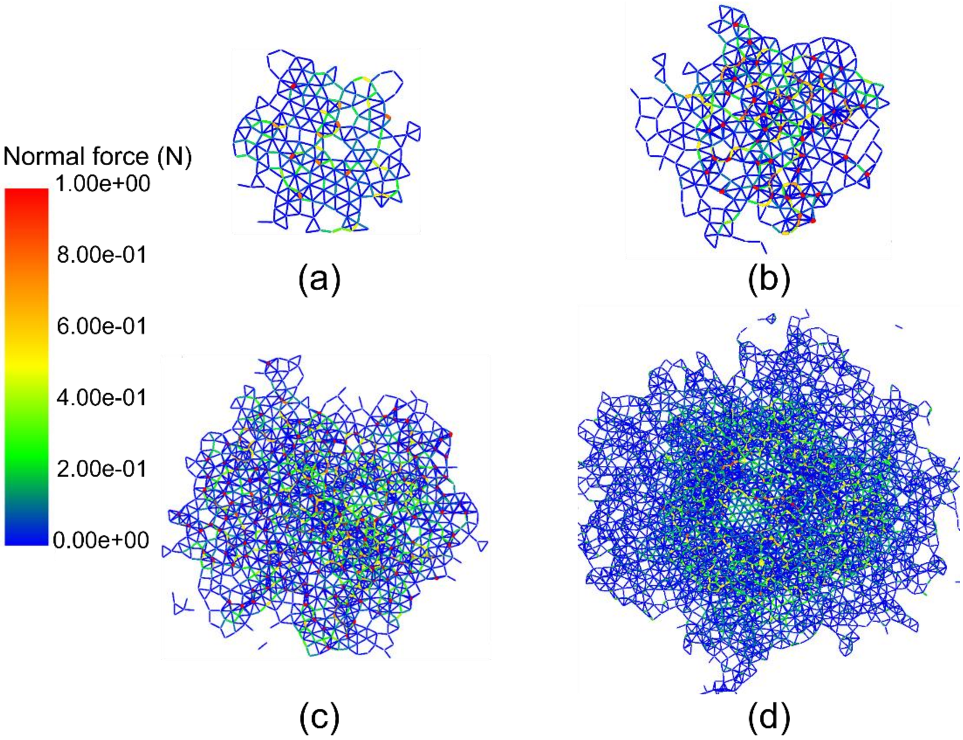

Figure 3.12. The contact force network formed during crushing of a particle with a diameter of: (a) 0.83mm, (b) 1.0mm, (c) 1.5mm, and (d) 2.0mm obtained from the DEM models.

3.5 Effects of Number of Particles on the Coefficient of Traction

The effects of the number of sand particles on frictional characteristics at wheel-rail contact area is investigated in this sub-chapter, the fragment and ERF_{avg} for each HPT simulation scenario can be found in Table 3.4. Figure 3.13 shows that when 4 sand particles are present in the wheel-rail contact area, the CoT can increase up to 0.3. However, increasing the number of sand particles to 8 or 16 decreases the CoT to 0.21 and 0.15, respectively. This reduction is due to two factors. First, increasing the number of particles increases the contact area between the fragments and the wheel/rail specimens. Second, with a higher number of particles, the fragments can distribute more evenly over the wheel-rail contact area, providing lubrication, which is consistent with the effects of particle size.

Table 3.4 Fragments and average effective radius for three different scenarios.

Number of particles	**Number of Fragments**	**Fragments diameter [mm]**	**Average effective radius of friction in HPT [mm]**
4	1,304	0.1	7.40
8	2,608	0.1	7.11
16	5,216	0.1	7.08

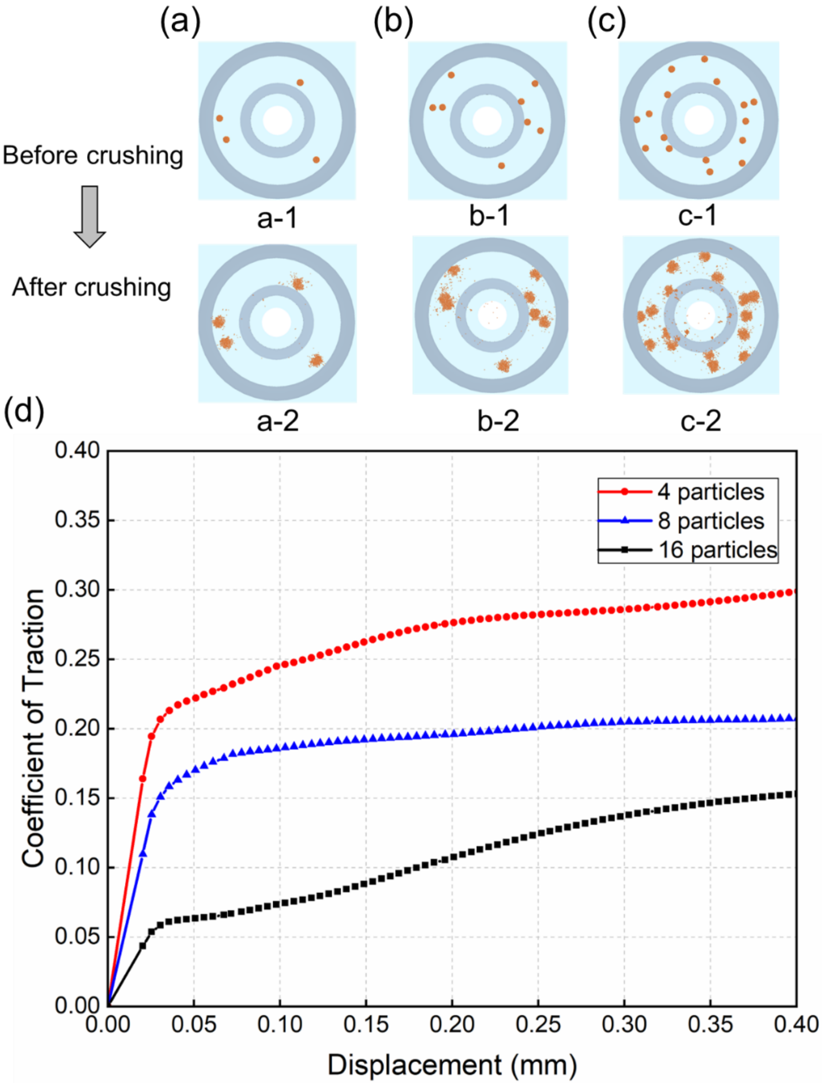

Figure 3.13. The particle distribution used in simulations for different number of particles present at the wheel-rail contact area (1) before and (2) after crushing shown from the top view for: (a) 4 particles, (b) 8 particles, and (c) 16 particles and (d) comparison of the coefficient of traction obtained from DEM modelling of the HPT set-up using different number of particles at the contact area.

3.6 Controlling Particle Size Distribution of Fragments for Modelling the Breakage of Arbitrary-Shaped Sand Particles

The previous sub-chapters discussed the effects of bonding properties between spherical fragments, particle size, and the number of particles applied to the wheel-rail contact area on tribological behaviour between the wheel and the rail. However, when modelling a sand particle, mono-sized spherical fragments were employed. In order to simulate a more realistic fragmentation of sand particle at the interface under high contact pressures, it is essential to incorporate the size distribution of the fragments post-fragmentation into the model. In this sub-chapter, a study is conducted to investigate how the fragment size distribution (FSD) data created by crushed sand particles affects wheel-rail adhesion. An in-house python code developed by Nadimi's research group is utilised to model sand particles, incorporating fragments with the corresponding size distribution. The performance and reliability of the code are evaluated by modelling two different types of sand particles and comparing the predicted fragment size distribution with experimental data. Subsequently, the sand particles modelled by the code are applied to the HPT simulations.

3.6.1 Motivation and Significance

Granular materials are commonly encountered and utilised in a variety of engineering fields such as pharmaceutical engineering (Tamadondar and Rasmuson, 2020), chemical engineering (Nan et al., 2017), agriculture (Pasha et al., 2016), civil engineering (Suhr and Six, 2020; Wang et al., 2007) and mining engineering (Cho et al., 2007). These particles can break into smaller fragments during high stress compression or shearing events, and the particle size distribution (PSD) of the fragments plays a crucial role in the behaviour of the entire particulate system, such as force transmission (O'Sullivan, 2011). DEM is a technique typically employed in academic research and industries to study granular materials and their behaviour during the breakage process. Since the contact models and contact detection algorithms in DEM are mainly developed for rigid spherical particles, modelling the breakage of arbitrarily shaped particles can present two main challenges. First is to represent the shape of non-spherical particles, and second is how to reproduce the particle breakage process in the DEM model along with realistic FSD data.

For arbitrarily shaped non-spherical particles, the common practice in academic and industrial research is to model the actual particles as clumps of overlapping spheres or clusters of non-overlapping spheres (Orefice and Khinast, 2020). This approach allows for the inclusion of more detailed particle morphology characteristics, such as local roundness, roughness or concavities. Regarding the modelling of non-spherical particles, commercial DEM software, such as PFC3D (Itasca) and EDEM^{TM} offer specialised methods developed in-house; some open-source codes are also currently available to implement the corresponding requirements, such as Bradshaw & O'Sullivan (2004), Haeri (2017), and Angelidakis et al. (2021).

In addition, some studies are successfully using the BPM to simulate the crushing response of grains and assemblies of silica sand (Cheng et al., 2003; McDowell and Harireche, 2002; Metzger and Glasser, 2013, 2012; Zhang et al., 2024). However, only clumps and/or clusters consisting of monodisperse spherical fragments arranged in regular lattices are considered in these applications. To incorporate the post-fracture behaviour meaningfully into the model, it is necessary to construct clumps and/or clusters from polydisperse fragments with sizes that match a realistic post-fracture FSD. Therefore, this sub-chapter employs an in-house code named Voro-Pack based on Python programming language dominated by a technique for generating polydisperse spherical stacks to reproduce arbitrarily shaped particles with realistic FSD. This code relies solely on computational geometry, utilising a simple but effective Vorono relaxation algorithm to subdivide and populate arbitrary regions with polydisperse spherical fragments in a controlled FSD.

3.6.2 Description of the Voro-Pack code

The algorithm used to generate polydisperse agglomerates relies on two related key ideas: Laguerre-Voronoi diagrams and Voronoi relaxation.

The traditional Voronoi diagram partition Euclidean space into polygonal cells, each centred around a generator point, as shown in Figure 3.14a. Laguerre-Voronoi diagram, as shown in Figure 3.14b, is a weighted variant of the traditional Voronoi diagram, where each generator point p_i is assigned a weight w_i. In Laguerre-Voronoi diagram, given a set of generator points $\{p_1, p_2, \dots, p_n\}$ in $\mathbb{R}^d$ and corresponding weights $\{w_1, w_2, \dots, w_n\}$, the power distance from a point x to a generator point p_i with weight w_i can be defined as:

$$\prod\left(p_i,x\right)=\left\|x-p_i\right\|^2-w_i^2 \tag{3.3}$$

where $\left\|x-p_i\right\|$ denotes the Euclidean distance between x and p_i. This power distance determines the boundaries of the Laguerre cells, which are infuenced by both the spatial position of the generator points and their respective weights. The laguerre cell $L(p_i)$ for a generator point p_i is then:

$$L\left(p_i\right)=\left\{x\in\mathbb{R}^d\,\middle|\,D_L\left(p_i,x\right)\le D_L\left(p_j,x\right)\,for\ all\ j\ne i\right\} \tag{3.4}$$

Geometrically, these weights can be visualised as the square of a radius around each generator point. Therefore, the cells in a Laguerre-Voronoi diagram represent the set of points closest to a generator circle (or sphere in higher dimensions) compared to any other.

The difference between traditional Voronoi and Laguerre-Voronoi diagrams is illustrated in Figure 3.14. Both methods generate convex polygonal cells, but the weighting in Laguerre-Voronoi diagrams provides control over the relative sizes of the cells. This allows for more flexibility in modelling situations where influence varies between generators. It can be observed that a smaller circle is completely contained within a larger circle, and overlapping generator circles may cause some cells to have zero area, resulting in the cells of the smaller generator not being present. This demonstrates that Laguerre-Voronoi diagrams have the ability to model layered or nested influences, and that their flexibility allows the creation of spatial partitions that are more representative of real-world scenarios where influence and dominance are not uniformly distributed (Chaidee and Sugihara, 2020; Lautensack, 2008).

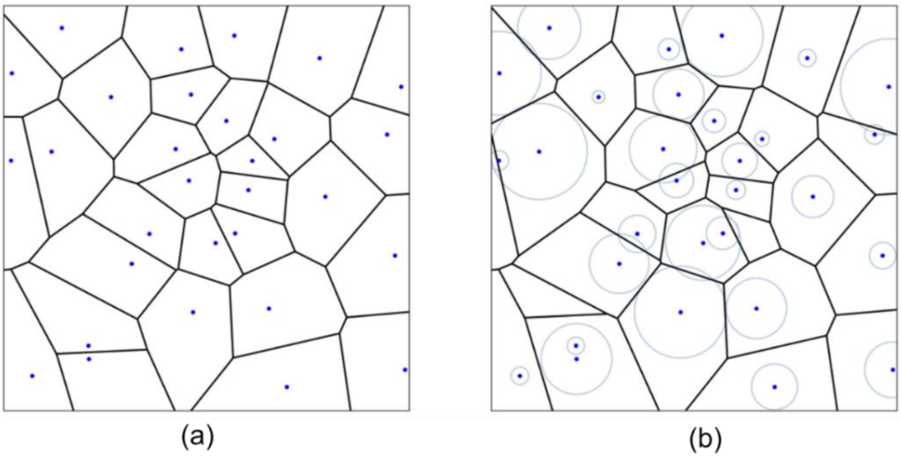

Figure 3.14. Examples of (a) traditional Voronoi diagram constructed from 24 generator points and (b) Laguerre-Voronoi diagram of the same generator points with randomly assigned cell weights.

To achieve a more uniform and well-distributed set of Voronoi cells, Voronoi relaxation is introduced. The aim of this concept is to improve the quality of a Voronoi diagram or mesh by iteratively adjusting the positions of the generator points. Moreover, Lloyd's algorithm (Lloyd, 1982), is the most commonly used technique to achieve Voronoi relaxation. The algorithm is used to approximate the "Centroidal Voronoi Diagrams (CVD)", which is a special subset of the Voronoi diagram characterised by the fact that each generator point is located at the centroid of its respective cell. When applying Lloyd's algorithm to Voronoi diagrams, it follows a relatively straightforward iterative process. The steps include starting with an initial Voronoi diagram, calculating the centroid of each Voronoi cell, moving each generator point to the centroid of its corresponding cell, and then reconstructing the Voronoi diagram. These steps are repeated until the generator points converge to a stable configuration, resulting in an approximation of a CVD. The convergence of the system can be monitored using an energy function, which is proportional to the displacement of the generator points between iterations. This approach ensures that the generator points gradually move towards the centroids of their cells, optimising the spatial partitioning. The energy function γ that describe convergence is expressed as follows:

$$\gamma = \frac{\sum \Delta vc_i}{n} \tag{3.5}$$

where Δvc_i is the distance between the centroid and the generator point of the ith Voronoi cell and n is the number of cells.

An example of Voronoi relaxation using Lloyd's algorithm is illustrated in Figure 3.15a. This figure takes Figure 3.14a as an initial stage and demonstrates a Voronoi diagram with a set of evenly spaced, uniformly sized and well-shaped points generated by the Lloyd's algorithm after 50 iterations have been performed. As the algorithm iterates, the system converges towards a CVD. The convergence process is depicted in Figure 3.15b. Initially, the energy function is relatively high, indicating significant displacements of the generator points. Over successive iterations, the energy function decreases, reflecting a gradual convergence. This reduction in energy corresponds to smaller displacements of the generator points, leading to an increasingly accurate approximation of the CVD. The visualisation of this process highlights how Lloyd's algorithm effectively optimizes the spatial distribution of points, resulting in a well-relaxed Voronoi diagram.

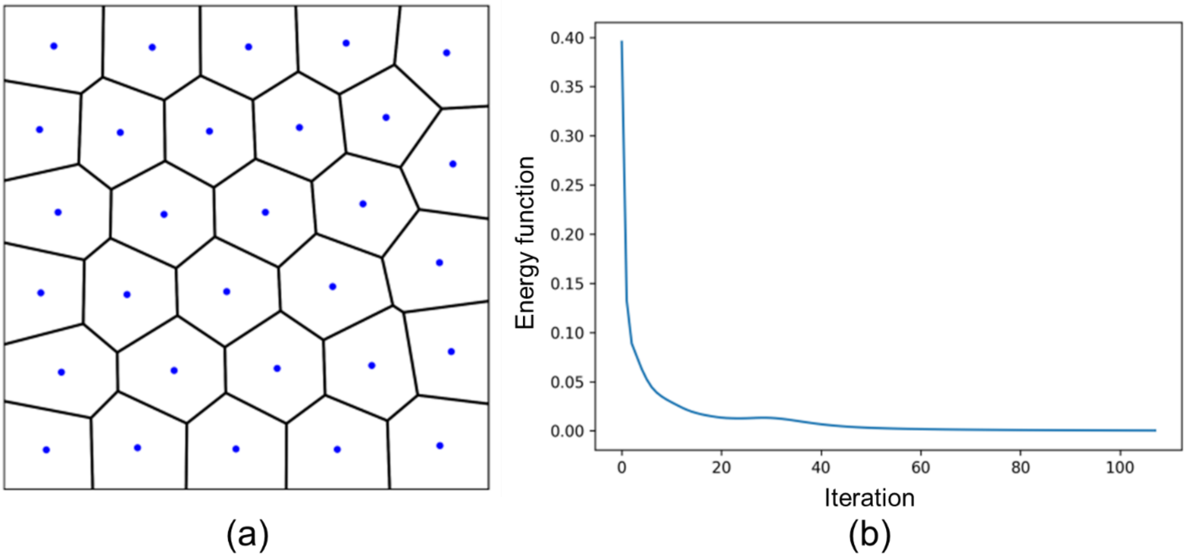

Figure 3.15. (a) Voronoi diagram after completing 50 iterations and (b) Curve of the of the energy function γ during the Lloyds algorithm.

The code utilised in this study extends the concept of Voronoi relaxation to Laguerre-Voronoi diagrams, offering a straightforward algorithm for generating polydisperse agglomerates. This approach allows for the modelling of geotechnical materials such as soil, sand, and rock by incorporating the exterior geometry (*.stl) and PSD data of the corresponding fragments (*.csv). The output files, which represent agglomerates using the centroids and radii of the polydisperse, are compatible with several leading commercial and open-source DEM codes, including EDEM^{TM}, PFC3D, YADE, and LAMMPS. This compatibility ensures that the generated agglomerates can be easily integrated into various simulation environments, facilitating their use in a wide range of applications.

Taking the irregular geometry shown in Figure 3.16 as an example, this algorithm generates polydisperse agglomerates through the following steps:

(1) Generate a cumulative frequency PSD curve from the input binned PSD data.

(2) Randomly scatter particle centres within the axis-aligned bounding box of the external shell of the agglomerate to be generated, as shown in Figure 3.16a. Assign radii to these particles sampled from the desired PSD. Ensure that the total area or volume of the placed particles matches the maximum packing density of the region. This initial distribution will

likely be irregular and contain many overlapping particles.

(3) Construct the Laguerre diagram for the initial arrangement using periodic boundary conditions to prevent unwanted boundary effects. Due to significant overlaps, it is necessary to initially reduce the weightings. Gradually increase the cell weights to avoid particle "swallowing." Stop iterating once the particles reach their full size and the energy tolerance criterion is met, as shown in Figure 3.16b.

(4) Apply convex optimization to locate the Chebyshev centre and determine the largest inscribed particle within each cell (Figure 3.16c).

(5) Trim any excess particles that extend beyond the exterior surface of the agglomerate, as shown in Figure 3.16d.

By following these steps, the algorithm effectively generates polydisperse agglomerates that are compatible with the external geometry and PSD data of fragments. This method ensures that the generated particles fit well within the target agglomerate shape and adhere to the desired size distribution of fragments.

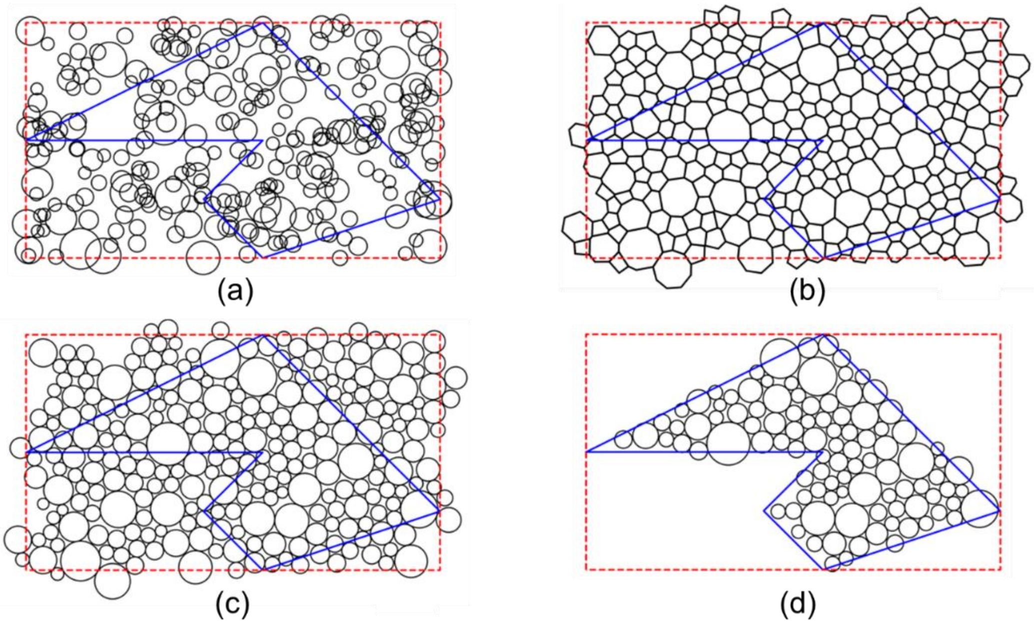

Figure 3.16. Graphical illustration of the algorithm steps to generate polydisperse agglomerates for an irregular geometry.

3.6.3 Case studies

In this section, silica sand from Leighton Buzzard and from central European quarries were selected and then these natural irregular sand particles were imaged using X-ray micro-

Computed Tomography (µCT). To generate the 3-D geometry of the particles, the µCT images were reconstructed into greyscale cross-sectional slices, with a voxel edge length/image resolution of 8.81 µm, producing a 3D image of approximately 7,444 × 7,444 × 7,117 voxels. After that, a total of 100 sand samples from Leighton Buzzard and central European quarries were modelled using the Voro-Pack code. The size distribution of fragments of sand particles was obtained by laser diffraction and the idea is to fit the FSD into an irregular shape of sand sample. Moreover, the coefficient of determination (R^2) (Wright, 1921) and root mean square error (RMSE) (Chicco et al., 2021) are utilised in order to quantify in a straightforward way the difference between the FSD data predicted by the code in the sand particle modelling and the actual test data. The R^2 can be interpreted as the proportion of variation in the dependent variable that can be predicted from the independent variable, which can be expressed as following:

$$R^2 = 1 - \frac{\sum_{i=1}^{m} \left(X_i - Y_i \right)^2}{\sum_{i=1}^{m} \left(\overline{Y}_i - Y_i \right)^2} \tag{3.6}$$

where X_i is the predicted ith value, Y_i is the actual $_i$th value, $\overline{Y}$ is the mean of the actual values, and m is the number of elements for actual values in the data set.

In contrast, the RMSE measures the average difference between the predicted and actual values of the model, providing an estimate of the ability of model to predict the accuracy of target value:

$$RMSE = \sqrt{\frac{1}{m} \sum_{i=1}^{m} \left(X_i - Y_i \right)^2} \tag{3.7}$$

In order to calculate the R2 and RMSE of the sand samples from the two different sources, the fragment sizes obtained from the code are taken as the predicted values while the size of the fragments from laser diffraction are taken as the actual values. As shown in Figure 3.17a, for the first source of sand particles, it reveals a high degree of alignment between the actual and predicted data. Also, the high R^2 values indicate that the code effectively reproduces most of the FSD data from laser diffraction when modelling sand particles. Additionally, for some sand samples, the proximity of the predicted data to the actual data results in low RMSE values, indicating that the average error between the predicted FSD by code and the actual data is small. However, when there is a significant deviation between the actual data and the predicted data, the RMSE value is high, reflecting a large error in the prediction of code for that interval.

For the second source of sand particles (Figure 3.17b), most samples also exhibit high R^2 values and low RMSE values, suggesting that the predicted FSD data by code closely matches the actual data for this type of sand as well. Overall, Figure 3.17 provides a visual representation of the code performance in predicting FSD data, with many scenarios showing excellent predictive accuracy. Metrics such as the combination of R^2 and RMSE confirm the robustness and reliability of code in capturing potential patterns in the data. Additional comparisons for the rest of sand samples can be found in Appendix A.

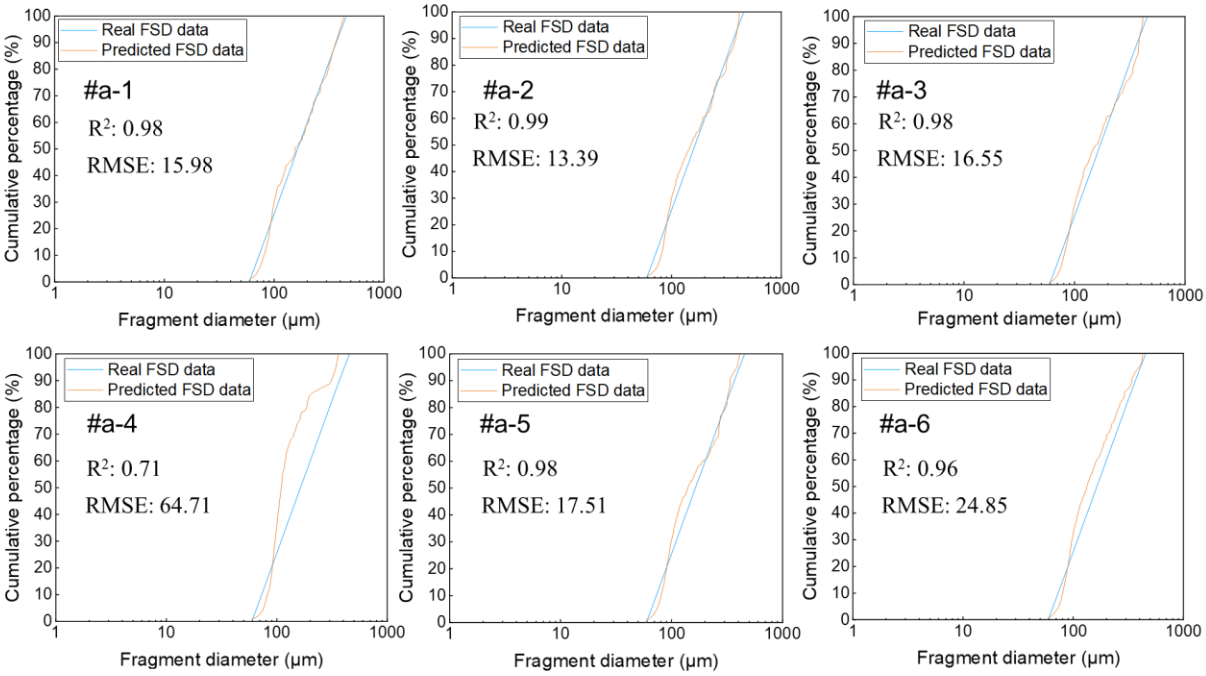

(a)

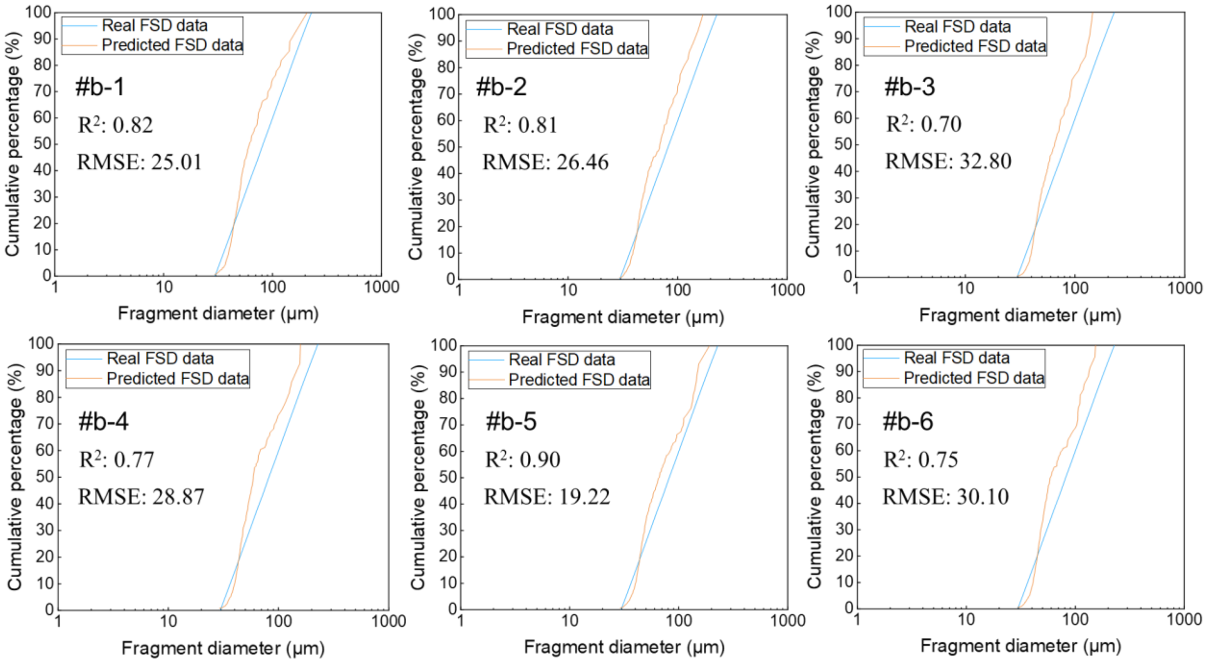

(b)

Figure 3.17. Comparison of code-predicted fragment size distribution data with laser diffraction data: (a) sand samples from the first source and (b) sand samples from the second source.

Figure 3.18 illustrates a comparison of µCT scans (Maramizonouz et al., 2023b) and code modelling for 6 sand samples from each source. It can be observed that the geometries and sizes of the agglomerates obtained from code modelling match well with the corresponding realistic sand particles.

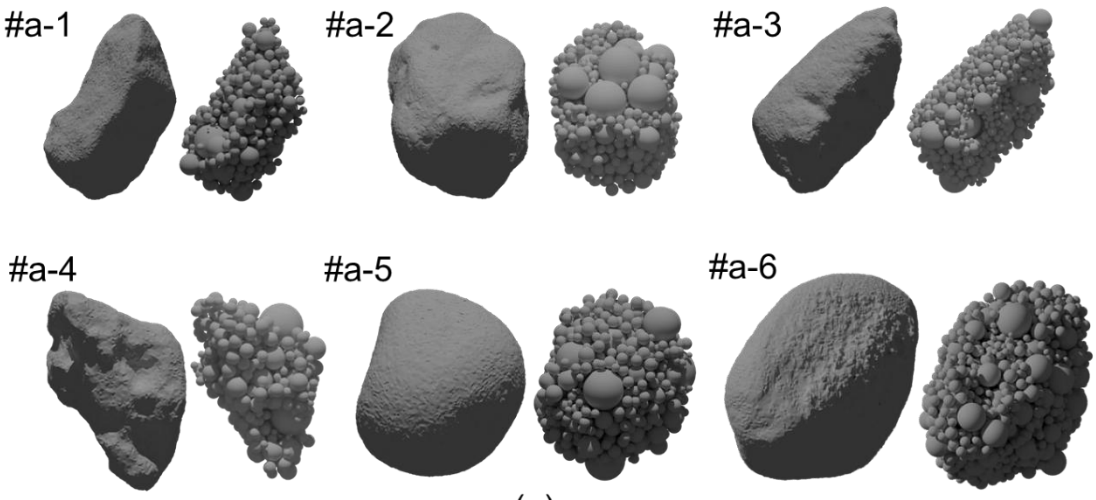

(a)

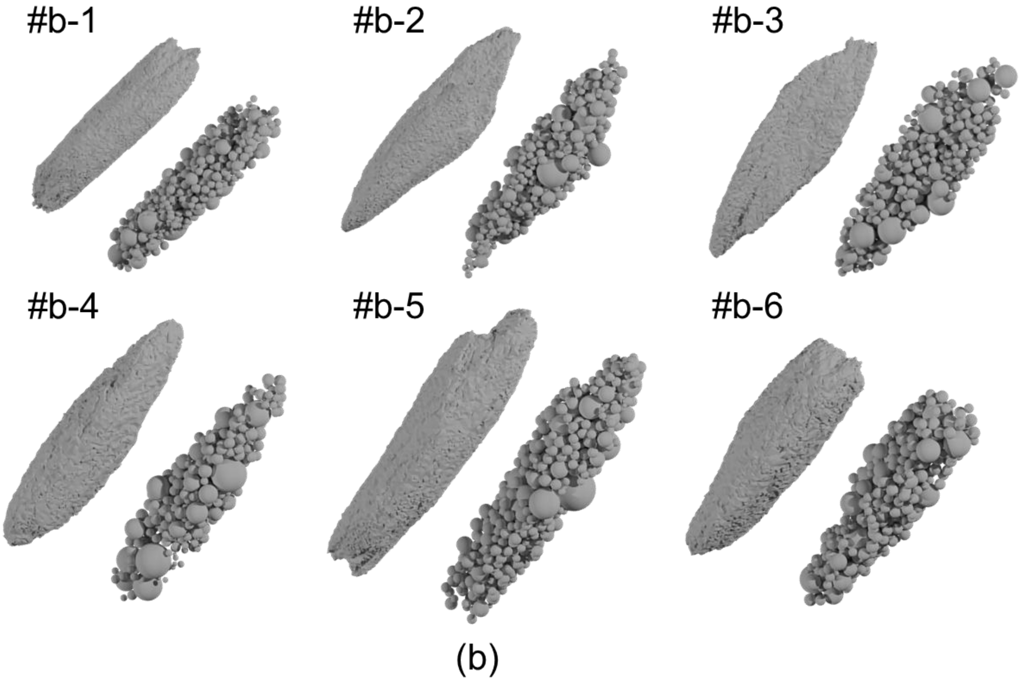

Figure 3.18. Comparison of the geometry between the real sand particles and the ones modelled by the code: (a) sand samples from the first source and (b) sand samples from the second source.

3.6.4 Effects of Fragment Size Distribution on the Coefficient of Traction

The code is then employed to model sand particles in HPT simulations to examine how the size distribution of fragments affects wheel-rail adhesion. To reasonably reflect the size distribution of fragments after particle breakage, the D30-D70 range is selected from Figure 3.4. Additionally, to avoid the expensive computational costs associated with very small spherical fragments, the size of the fragments is enlarged by a scale factor of 10. Another type of sand particle is composed of fragments with a monotonic distribution of sizes, as described in case c.2 in Table 3.1. In the HPT simulation, 4 sand particles are applied in the wheel-rail contact area, with each particle having a diameter of 1 mm.

Figure 3.19 shows that when the fragments in the sand particles are of a uniform size, the CoT at the wheel-rail interface is 0.3. However, after incorporating the FSD into the sand particles, the CoT in the wheel-rail contact area increases to 0.37. This indicates that incorporating the FSD can significantly affect the force transmission between the wheels and rails compared to using monotonically sized fragments, thus it is necessary to consider the size distribution of the fragments within the sand particles in future numerical studies.

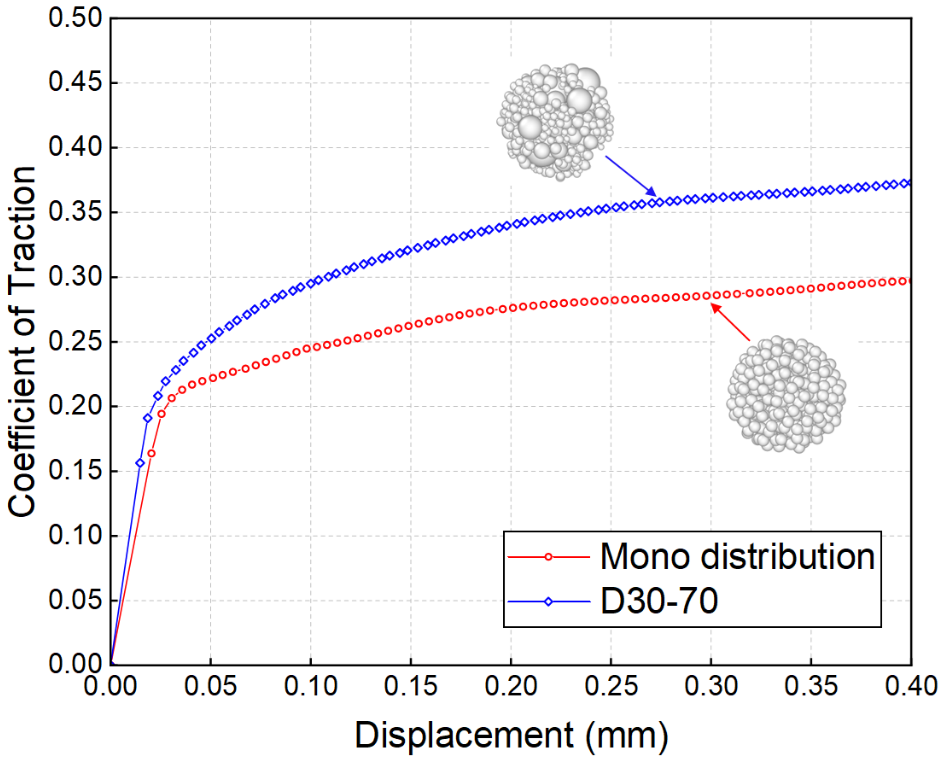

Figure 3.19. Comparison of the coefficient of traction at wheel-rail contact area between the sand particles with uniform size of fragments and those with D30-D70 of fragments.

3.7 Effects of Particle Shape on the Coefficient of Traction

In this sub-chapter, three typical shapes of particles, namely compact, elongated, and flat, are used to study the effect of particle shape on wheel-rail adhesion, as shown in Figure 3.20. For each shape of sand particles, the particle size is 1 mm, and the FSD is consistent with that of spherical particles (D30-D70). In each HPT simulation, four sand particles of identical shape are placed in the wheel-rail interface to obtain the CoT. Figure 3.20d shows the CoT at the wheel-rail interface for each shape of sand particles. It can be seen that the wheel-rail friction is more sensitive to flat and elongated particles, with a CoT of 0.39, which is higher than that for compact particles (CoT of 0.35). However, the difference between their CoT and that caused by spherical particles (CoT of 0.37) is not significant. This suggests that there is no obvious link between particle shape and wheel-rail adhesion, aligning with Skipper's (2021) experimental findings.

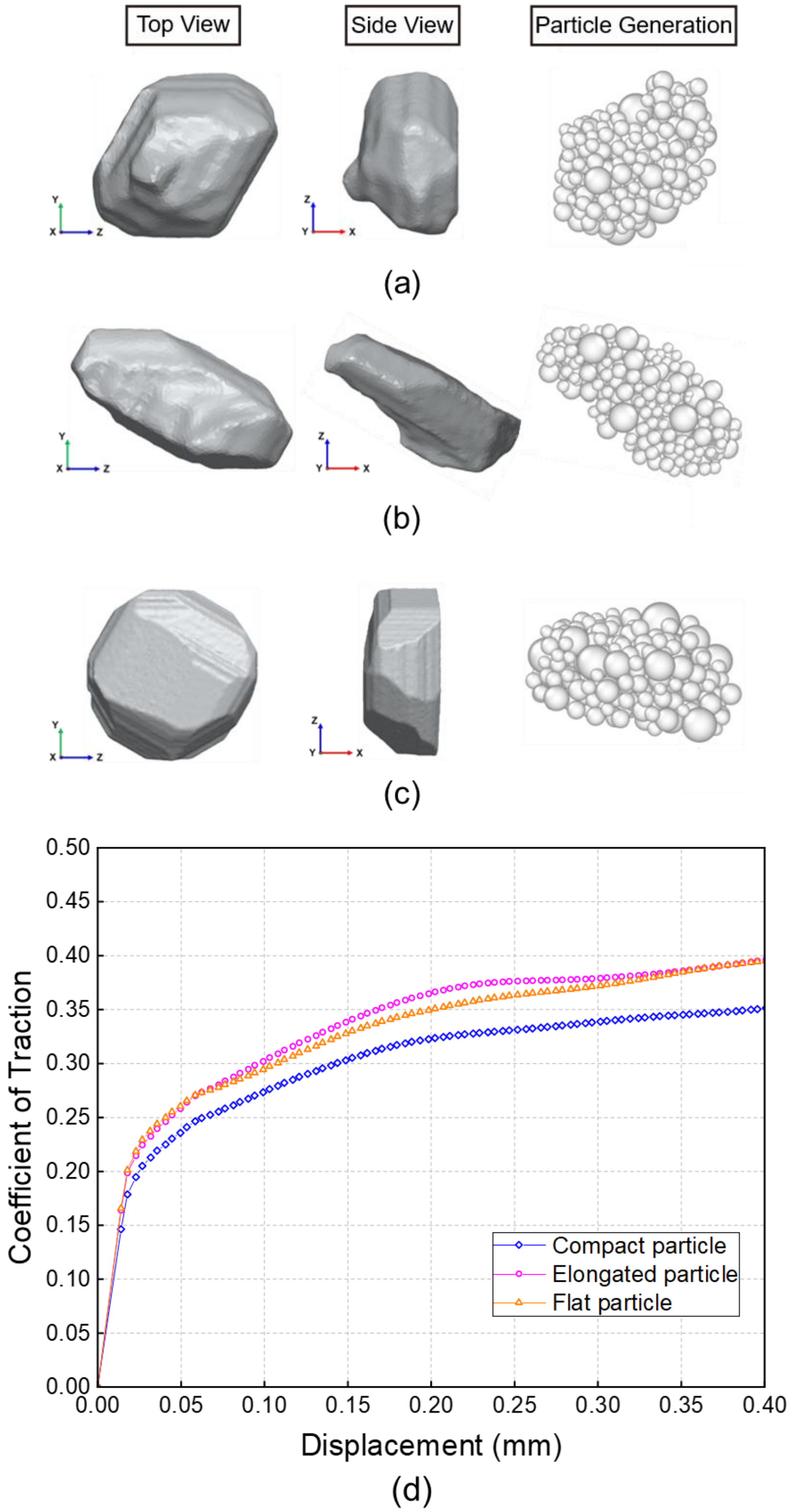

Figure 3.20. Comparison of the coefficient of traction when applied different shapes of sand particles at wheel-rail contact area: (a) compact particle, (b) elongated particle, (c) flat particle, and (d) coefficient of traction at wheel-rail contact area.

3.8 Conclusions

This chapter reported how the particulate materials affect the tribological behaviour at the interface. Taking wheel-rail contact as an example, the effects of particle characteristics on the frictional performance between the wheel and the rail under dry conditions in the sanding operation was discussed by simulating the HPT tests using DEM. The effects of metal-to-metal contact between the wheel and the rail specimens, the properties of the bonds between particle fragments after breakage (i.e., bond stiffness and strength), the size and the number of the sand particles present at the contact area, the size distribution of fragments that make up sand particle, and the particle shape on the frictional behaviour of wheel-rail contact was quantified by the traction coefficient at wheel-rail interface.

It was demonstrated that the properties of the bonds between particle fragments significantly affect the frictional behaviour of the wheel-rail contact. Compared to bond strength, bond stiffness has a stronger effect on the coefficient of traction. Additionally, the bond properties greatly influence the breakage behaviour of sand particles. When bond strength exceeds a certain limit during compaction, sand particles exhibit ductile behaviour rather than the expected brittle fracture.

Increasing the size of sand particles was shown to decrease the coefficient of traction. As particle size increases, the number of fragments and the bonds between them also increase dramatically. This prevents the complete detachment of fragments from the parent particles during compaction, leading to the formation of particle fragment clusters. A high number of fragments in the contact area creates weak shear bands, causing a lubrication effect.

Furthermore, it was necessary to consider the size distribution of the fragments within the sand particles in subsequent numerical studies, as this has a significant effect on wheel-rail traction. However, no obvious link was found between particle shape and wheel-rail adhesion.

Chapter 4 Electro-Mechanical Behaviour of Conductive and Non-Conductive Sands at the Wheel-Rail Interface

4.1 Introduction

Several experimental studies have enhanced our understanding of the interactions between mechanical behaviour and electrical response in particulate systems (Arias-Cuevas et al., 2010a; Creyssels et al., 2017; Falcon et al., 2004; Falcon and Castaing, 2005; Lewis et al., 2014; Skipper et al., 2023). However, such experiments are often time-consuming, costly, and suffer from safety issues, while also facing challenges in capturing the motion and electrical properties of individual particle. The DEM, known for its robust capability to analyse particle dynamics, has been widely employed to simulate the electrical transfer properties of particles under mechanical forces (Abbaspour et al., 2010; Bourbatache et al., 2012; Chapteuil et al., 2018; Descartes et al., 2008; Machado, 2015; Ott et al., 2013; Renouf and Fillot, 2008; Sangrós Giménez et al., 2020; Schneider et al., 2006; Yim et al., 2023). Despite the modelling approaches proposed in the literature for electro-mechanical behaviour in particulate systems, current methods for formulating the electrical resistance between particles still require further development. An electro-mechanical contact model is presented here[3], which is applicable to both particle-to-particle and particle-to-wall contacts. The model considers the particle resistance due to its material and the contact resistance in the overlap region. It has been verified and validated against previously published analytical and experimental data. In addition, the model has been applied to HPT tests to investigate the changes in electrical properties when conductive and non-conductive sand particles are separately acted on the wheel-rail interface. Furthermore, the effects of a mixture of conductive and non-conductive particles on the electrical resistance at the wheel-rail interface is examined. These insights help to understand the complex interaction mechanisms between mechanical behaviour and electrical response within the particulate system.

---

[3] Zhang, C., Maramizonouz, S., Milledge, D. and Nadimi, S., 2024. An electro-mechanical contact model for particulate systems. Powder Technology, 440, p.119759.

4.2 Development of Electrical Transfer Model

In a particulate system, when two particles are pressed together by an external force or a particle comes into contact with a structure, a conductive path is established at the contact region, facilitating the free flow of electrons (Mikrajuddin et al., 1999). To evaluate the electrical response characteristics of a particulate system, it is essential to determine the electrical resistance along this conduction path. In this study, both particle-to-particle and particle-to-structure conduction are considered. Using the nodal analysis method (Ho et al., 1975; Wing, 1972) and circuit analysis principles (Birkholz et al., 2019), each particle and the boundary structure interacting with the particulate system can be treated as a node, which then allows the resistance along the conductive paths to be modelled accordingly.

4.2.1 Particle-to-Particle Electrical Conduction

For two contacting particles i and j, the overall electrical resistance is composed of three components: the particle resistance from the centre of particle i to the overlapping surface (R_i); the contact resistance of the two particles in the contact zone ($R_{c,ij}$); and the particle resistance from the centre of particle j to the overlapping surface (R_j), as depicted in Figure 4.1. Therefore, the electrical resistance R_{ij} between particle i and particle j can be expressed as follows:

$$R_{ij} = R_i + R_{c,ij} + R_j \tag{4.1}$$

In addition, the size of the contact zone between two particles strongly affects their contact resistance, which can be represented by the Holm resistance model as (Holm, 1967; Mikrajuddin et al., 1999):

$$R_{c,ij} = \frac{\rho_i + \rho_j}{4r_c} \tag{4.2}$$

where ρ_i and ρ_j are defined as the electrical resistivity of particles i and j, respectively, while r_c is the radius of the contact area. According to the classical Hertz theory, when two elastic spherical particles are in contact, the contact radius r_c can be written as (Hertz, 1882; Thornton, 2015):

$$r_c = \left(\frac{3 f_n r^*}{4E^*} \right)^{\frac{1}{3}} \tag{4.3}$$

where f_n, E^* and r^* are defined as the normal component of contact force, the equivalent Young's modulus and the effective radius. Substituting Equation 4.3 into Equation 4.2, the contact resistance between two particles can be rewritten as:

$$R_{c,ij} = \frac{1}{4}\left(\rho_i + \rho_j\right)\left(\frac{3 f_n r^*}{4E^*}\right)^{-\frac{1}{3}} = \frac{1}{2}\left(\rho_i + \rho_j\right)\sqrt[3]{\frac{E^*}{6 f_n r^*}} \tag{4.4}$$

For two particles i and j contact with each other, each of them has its own particle resistance, that is from the centre of the particle to the contact plane, which can be written as:

$$R_i = \int_0^{r_i - \delta_i} \rho_i \frac{dz}{\pi\left(r_i^2 - z^2\right)} \tag{4.5}$$

$$R_j = \int_0^{r_j - \delta_j} \rho_j \frac{dz}{\pi\left(r_j^2 - z^2\right)} \tag{4.6}$$

where r_i and δ_i are the radius and deformations of particle i, while r_j and δ_j are defined as the radius and deformations of particle j. To determine the amount of elastic deformation for each particle in the contact zone, the geometric characteristics of the two particles in contact (as shown in Figure 4.1) are considered, thus δ_i and δ_j can be calculated as:

$$\delta_i = r_i - D = r_i - \frac{r_i^2 - r_j^2 + L_{ij}^2}{2L_{ij}} \tag{4.7}$$

$$\delta_j = r_j - L_{ij} + D = r_j - L_{ij} + \frac{r_i^2 - r_j^2 + L_{ij}^2}{2L_{ij}} \tag{4.8}$$

where D is the distance from the centre of particle i to the contact plane, and L_{ij} is the distance between the centres of two overlapping particles. By substituting Equations 4.7 and 4.8 into Equations 4.5 and 4.6, respectively, the particle resistance of the corresponding half-sphere of particle i and particle j under elastic deformation for can be derived as:

$$R_i = \int_0^{\frac{r_i^2 - r_j^2 + L_{ij}^2}{2L_{ij}}} \rho_i \frac{dz}{\pi\left(r_i^2 - z^2\right)} = \frac{\rho_i}{2\pi r_i} \ln\left(\frac{r_i^2 - r_j^2 + L_{ij}^2 + 2r_i L_{ij}}{r_j^2 - r_i^2 - L_{ij}^2 + 2r_i L_{ij}}\right) \tag{4.9}$$

$$R_j = \int_0^{\frac{r_j^2 - r_i^2 + L_{ij}^2}{2L_{ij}}} \rho_j \frac{dz}{\pi\left(r_j^2 - z^2\right)} = \frac{\rho_j}{2\pi r_j} \ln\left(\frac{r_j^2 - r_i^2 + L_{ij}^2 + 2r_j L_{ij}}{r_i^2 - r_j^2 - L_{ij}^2 + 2r_j L_{ij}}\right) \tag{4.10}$$

After that, by substituting Equations 4.4, 4.9 and 4.10 into Equation 4.1, the electrical resistance between the centre of particle *i* and the centre of particle *j* when these two particles are overlapping can be written as:

$$R_{ij} = \frac{\rho_i}{2\pi r_i}\ln\left(\frac{r_i^2 - r_j^2 + L_{ij}^2 + 2r_iL_{ij}}{r_j^2 - r_i^2 - L_{ij}^2 + 2r_iL_{ij}}\right) + \frac{1}{2}\left(\rho_i + \rho_j\right)\sqrt[3]{\frac{E^*}{6f_nr^*}} + \frac{\rho_j}{2\pi r_j}\ln\left(\frac{r_j^2 - r_i^2 + L_{ij}^2 + 2r_jL_{ij}}{r_i^2 - r_j^2 - L_{ij}^2 + 2r_jL_{ij}}\right) \quad (4.11)$$

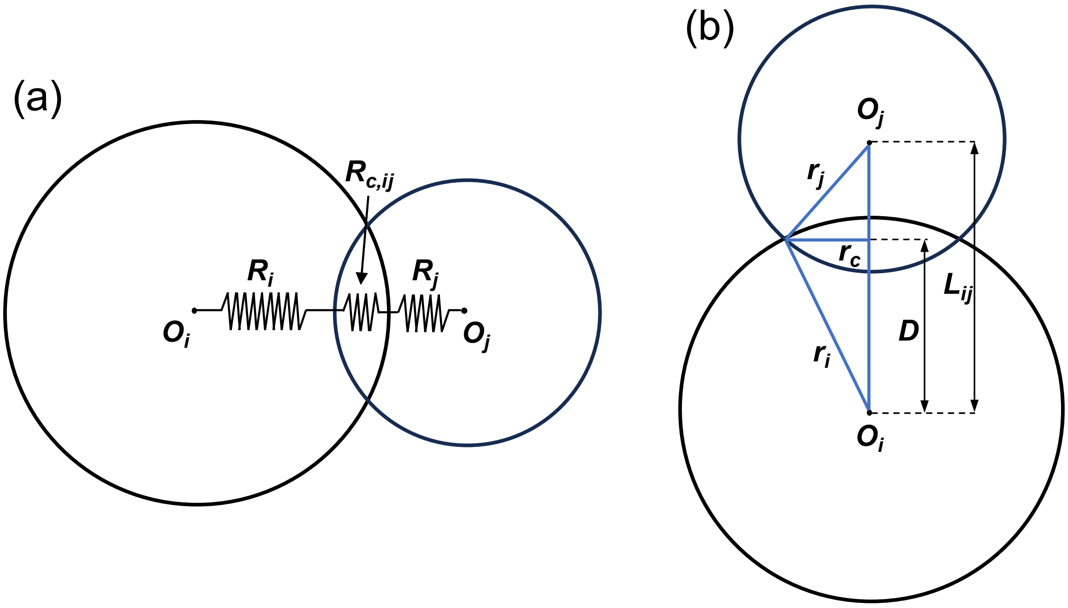

Figure 4.1. Schematic of particle-to-particle contact: (a) components of electrical resistance in two particles overlapping, (b) geometry of two particles generating an overlap.

4.2.2 Particle-to-Structure Electrical Conduction

During the application of mechanical loads to the particulate system, some particles come into contact with the boundary structures, creating channels in the overlap region that facilitate the free passage of electrons, leading to electrical transfer between the particles and the structures. In this study, the structure (i.e., wall) is assumed to have a uniform and constant electric potential. When a particle contacts the wall, electrons flow from the wall to the particle through the contact region. Therefore, the electrical resistance R_{iw} resulting from the contact between the particle and the wall should take into account the contact resistance $R_{c,iw}$, as well as the resistance of the particle itself (R_i) from the centre of particle *i* to the contact surface of the wall, as illustrated in Figure 4.2, which can be expressed as:

$$R_{iw} = R_i + R_{c,iw} \quad (4.12)$$

The elastic deformation of the particle *i* subjected to mechanical loading by a wall is δ, and the distance from the centre of the particle to the contact plane is $S = r_i - \delta$. This can be then used to calculate the electrical resistance of particle *i* itself and written as follows:

$$R_i = \int_0^S \rho_i \frac{dz}{\pi\left(r_i^2 - z^2\right)} = \frac{\rho_i}{2\pi r_i}\ln\left(\frac{2r_i - \delta}{\delta}\right) \tag{4.13}$$

At the overlapping area of the particle and the wall, the contact radius of the overlapping circular surface is determined by Hertz contact theory (Hertz, 1882; Thornton, 2015). The Holm resistance model (Holm, 1967; Mikrajuddin et al., 1999) can then be employed to obtain the contact resistance:

$$R_{c,iw} = \frac{1}{4}\left(\rho_i + \rho_w\right)\left(\frac{3 f_n r^*}{4E^*}\right)^{-\frac{1}{3}} = \frac{1}{2}\left(\rho_i + \rho_w\right)\sqrt[3]{\frac{E^*}{6 f_n r_i}} \tag{4.14}$$

where ρ_w is the electrical resistivity of the wall. By substituting the Equations 4.13 and 4.14 into Equation 4.12, the electrical resistance between particle and wall can be written as:

$$R_{iw} = \frac{\rho_i}{2\pi r_i}\ln\left(\frac{2r_i}{\delta} - 1\right) + \frac{1}{2}\left(\rho_i + \rho_w\right)\sqrt[3]{\frac{E^*}{6 f_n r_i}} \tag{4.15}$$

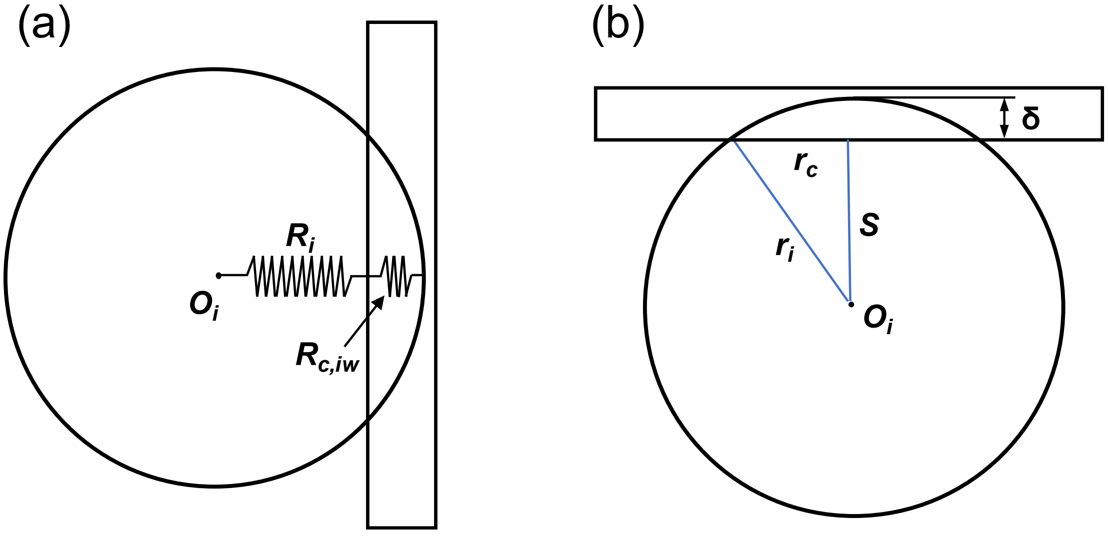

Figure 4.2. Schematic of particle-to-wall contact: (a) components of electrical resistance when a wall and a particle are overlapping, (b) geometrical characteristics of a particle and a wall in their contact region.

4.3 Electro-Mechanical Coupling and Assumptions

In addition to the mechanical loadings that affect the bulk electrical properties of the particulate system, the intrinsic electrical properties of the particles (e.g., electrical resistivity), the size and number of particles, the roughness and contamination film on the particle surface, as well as the temperature variations in the particulate system can influence the conductivity properties (Bourbatache et al., 2012). In this study, to examine the link between mechanical behaviour and electrical response, it is assumed that the temperature of the particulate system is constant, the surfaces of the particles are smooth, and the effect of contamination film is negligible.

Figure 4.3a shows an example of a simple particulate system, where the particles are packed into a rectangular container. The top plate *ad* and bottom plate *bc* are electrically conductive, while the sides *ab* and *dc* are electrically insulated. The entire system is connected to a direct current (DC) source, and a normal load is imposed on *ad*. Once *ad* comes into contact with the particles, current I_0 flows from *ad* into the particles and across the particulate system to *bc*. By referring to the network model of thermal conduction (Feng et al., 2008; Rojek et al., 2022) and the principles of circuit analysis (Birkholz et al., 2019) as well as the nodal analysis method (Ho et al., 1975; Wing, 1972), a particulate system can be likened to a circuit with multiple resistors. In this analogy, each particle is regarded as a node, and the path between the centres of two adjacent particles is treated as a branch with an associated resistance R_{ij}. Furthermore, the two conductive boundaries, *ad* and *bc*, can be viewed as reference points or terminals, labelled as node 0 and node 1, respectively. The conductive path created by the particles in contact with the wall is then treated as a branch with a corresponding resistance R_{iw}. As illustrated in Figure 4.3a, the relationship between the electrical properties of the particulate system can be expressed as follows:

$$\underbrace{\begin{pmatrix} G_{00} & G_{10} & G_{i0} & \cdots & G_{n0} \\ G_{01} & G_{11} & G_{i1} & \cdots & G_{n1} \\ G_{0i} & G_{1i} & G_{ii} & \cdots & G_{ni} \\ \vdots & \vdots & \vdots & \ddots & \vdots \\ G_{0n} & G_{1n} & G_{in} & \cdots & G_{nn} \end{pmatrix}}_{\mathbf{G}} \underbrace{\begin{pmatrix} V_{top} \\ V_{bottom} \\ V_i \\ \vdots \\ V_n \end{pmatrix}}_{\vec{V}} = \underbrace{\begin{pmatrix} -I_0 \\ I_0 \\ 0 \\ \vdots \\ 0 \end{pmatrix}}_{\vec{I}} \tag{4.16}$$

where $\mathbf{G}$, $\vec{V}$ and $\vec{I}$ are defined as the conductivity matrix, the vector of electric potential and current, respectively.

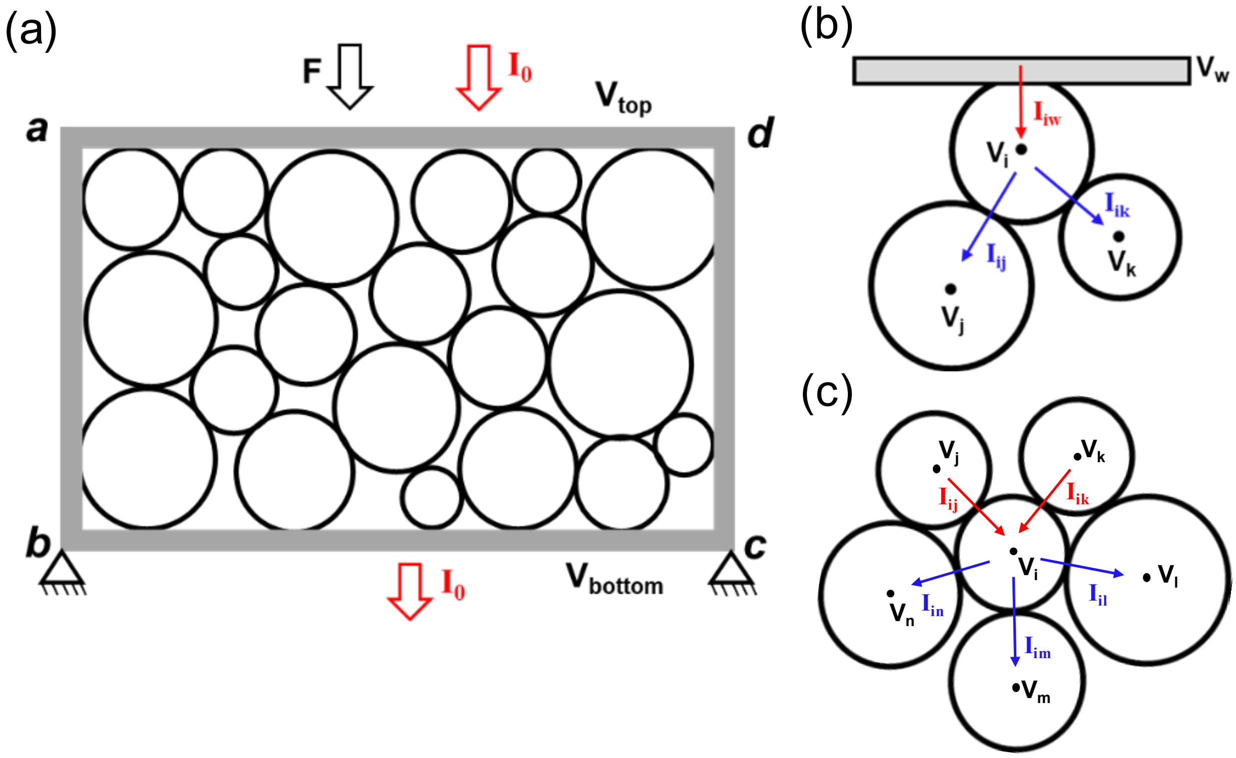

Figure 4.3. (a) schematic of a setup for characterising the electrical transfer properties of a particulate system under mechanical loading, (b) schematic of the electrical conduction when particle *i* is in contact with neighbouring particles and the wall (The red arrows indicate the current entering the particle and the blue arrows indicate the current exiting the particle), (c) schematic of a granular assembly showing the electrical conduction of particle *i* in contact with neighbouring particles.

Each particle in contact with the top plate *ad* creates a circuit branch, causing current to flow through the particle system along each branch. Based on the characteristics of parallel circuits, the sum of each branch currents I_{iw} is equal to the total current I_0 entering or leaving the boundary $\partial\Omega$, as expressed below:

$$\sum_{i}^{N_w} I_{iw} = I_0 \quad i \subset \partial\Omega \tag{4.17}$$

where N_w is the number of particles in contact with the wall. In Figure 4.3b, the branch current flows continuously from particle *i* to particle *j* and *k*, after entering particle *i* from top plate *ad*. Following Ohm’s law, Kirchhoff’s current law, and the relationship between mechanical loading and current (Bourbatache et al., 2012), the above circuit properties can be expressed as follows:

$$I_{iw} = \frac{F_n}{F_{ext}} I_0 \tag{4.18}$$

$$\sum_{j}^{N_{nei}} I_{ij} + I_{iw} = \sum_{j}^{N_{nei}} \frac{\left(V_i - V_j\right)}{R_{ij}} + \frac{\left(V_w - V_i\right)}{R_{iw}} = \sum_{j}^{N_{nei}} C_{ij}\left(V_i - V_j\right) + C_{iw}\left(V_w - V_i\right) = 0 \qquad (4.19)$$

where N_{nei} is the number of particles adjacent to particle i, V_W, V_i, and V_j are the electric potentials of top plate *ad*, particle i and particle j, respectively. R_{ij} is the electrical resistance between particle i and particle j, which is the inverse of the conductance C_{ij}. R_{iw} and C_{iw} are the electrical resistance and conductance, respectively, between the top plate *ad* and particle i.

Figure 4.3c shows a simple granular assembly in which particle i is in contact with surrounding particles. Taking particle i and particle j as an example, a linear relationship between current I_{ij} and the potential drop of these two particles can be established using Ohm's law, where the inter-particle electrical conductance C_{ij} serves as a proportionality constant. According to Kirchhoff's current law, the sum of the currents entering and leaving particle i should be zero, which can be expressed as follows:

$$\sum_{j}^{N_{nei}} I_{ij} = \sum_{j}^{N_{nei}} \frac{\left(V_i - V_j\right)}{R_{ij}} = \sum_{j}^{N_{nei}} C_{ij}\left(V_i - V_j\right) = 0 \qquad (4.20)$$

When the conductive properties are formulated for a particulate system, the mechanical loads acting on the system can be coupled with the corresponding electrical response. The procedure for electro-mechanical coupling in the particulate system is illustrated in Figure 4.4 and involves the following steps:

(1) Generate and initialise the particulate system.

(2) Determine the positions and velocities for each particle.

(3) Calculate the contact radius at the contact plane via Equation 4.3 and update the geometry transformations of particles during mechanical loadings.

(4) Compute the electrical resistance for both particle-to-particle and particle-to-wall contacts via Equations 4.11 and 4.15 based on the contact information.

(5) Evaluate the local electrical conduction properties using Equations 4.19 and 4.20.

(6) Predict the global electrical network of the entire particulate system via Equation 4.16.

(7) Update the electric potential of each particle within the assembly and store the data for this time step.

(8) Return to step (2) to repeat the entire electro-mechanical DEM simulation for the next timestep until the end time is reached.

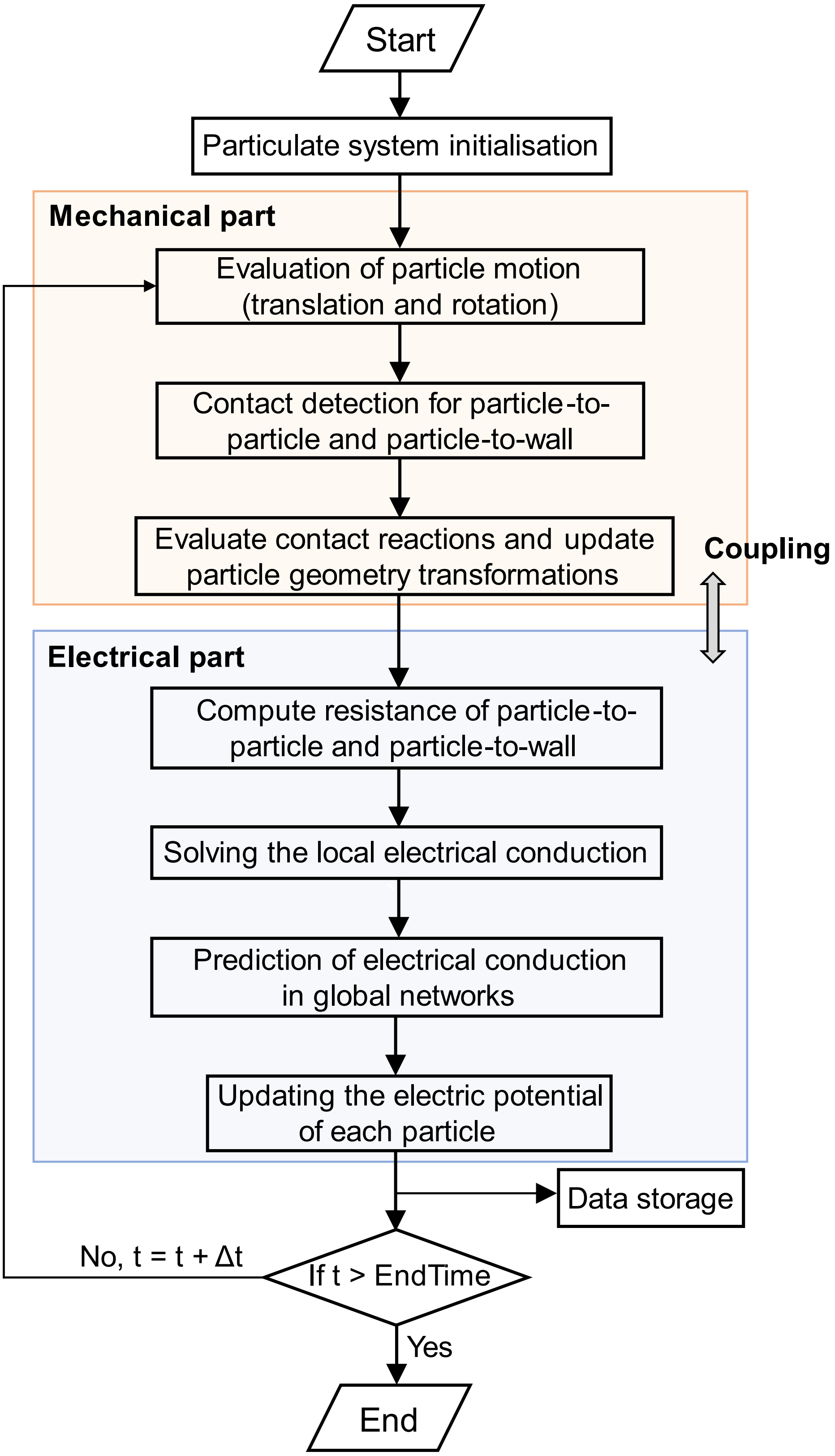

Figure 4.4. Flowchart of the solution in the DEM framework for the electro-mechanical coupled model.

4.4 Validation of the Numerical Model

The above numerical scheme is implemented in the DEM commercial software package EDEM^{TM} developed by Altair (2022) through the application programming interface (API) using C++ programming language. Single-particle compression, particle-particle contact, chains of particles, and particle bed tests are simulated and compared against published analytical solutions and experimental data to validate the implementation. Additionally, to balance the stability of the numerical calculations with the computational cost and to achieve a reasonable simulated phenomena within an acceptable computation time, a 20% of Rayleigh's timestep (Li et al., 2005; Washino et al., 2016) is utilised for all the simulations.

4.4.1 Comparison with the Analytical Solutions

A single-particle compression test and a particle-particle contact test are reported in this section. The parameters used in the simulations are listed in Table 1, which are taken from (Yim and Paik, 1998).

Table 4.1 Adopted parameters of the materials in the DEM simulation.

Parameters	**Unit**	**Value**
Nickel ball		
Poisson's ratio	–	0.312
Particle density	kg/m^3	8,908
Young's modulus	GPa	199.5
Particle diameter	mm	1.0
Electrical resistivity	Ω m	8.0×10^{-8}
Copper pad		
Poisson's ratio	–	0.343
Density	kg/m^3	8,960
Young's modulus	GPa	129.8
Electrical resistivity	Ω m	1.8×10^{-8}

4.4.1.1 Single-particle compression test

To evaluate the solution proposed in this study for calculating the electrical resistance of the particle-to-wall system, the overall electrical resistance R_{wiw} of the particle in contact with two walls is derived based on Equation 4.15:

$$R_{wiw} = \frac{\rho_i}{\pi r_i} \ln\left(\frac{2r_i}{\delta} - 1\right) + \left(\rho_i + \rho_w\right)\sqrt[3]{\frac{E^*}{6 f_n r_i}} \tag{4.21}$$

A single-particle compression test is modelled using copper pads and a nickel ball to investigate the variation of system resistance under different mechanical loading conditions. The simulation results are compared with the analytical solutions from Yim and Paik (1998). Figure 4.5 shows that the numerical results almost perfectly match with the analytical results. The electrical resistance of the particle-to-wall contact system decreases with increasing mechanical force. Notably, the electrical resistance of the system experiences a significant decrease as the applied mechanical force increases from 0 N to 10 N. When a very low mechanical force is applied to the system, a slight overlap generates between particle and wall, thus restricting the flow of electrons and leading to excessively high electrical resistance. As the mechanical force begins to increase from a very small value, the contact area between the particle and the wall expands, allowing more electrons to transfer through this region, which leads to a sharp decrease in resistance. However, as the mechanical force continues to rise to a certain level, the change in contact area becomes less pronounced. Consequently, the resistance of the system does not change significantly, even when the mechanical force reaches very high levels.

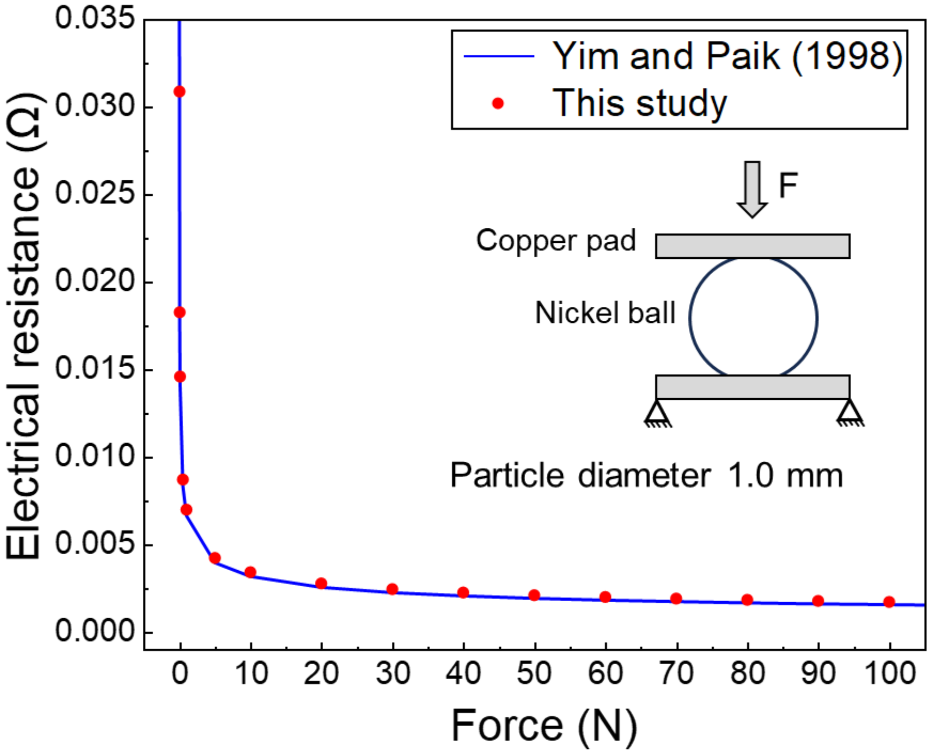

Figure 4.5. Evolution of electrical resistance for particle-to-wall contact under different mechanical forces (red dots are simulation results, blue line is analytical results, and the inset figure is a schematic diagram of a single-particle compression setup).

4.4.1.2 Particle-particle contact test

Figure 4.6 shows that the comparison of the numerical results for a particle-particle contact system under different mechanical forces with the two published analytical solutions (Birkholz et al., 2019; Ott et al., 2013). The numerical results are in excellent agreement with the analytical solutions provided by Birkholz et al. (2019) and Ott et al. (2013). A similar phenomenon to the single-particle compression test is observed: the electrical resistance of the particle-to-particle system decreases sharply as the mechanical force increases from 0 N ~ 10 N. Beyond this point, further increases in mechanical force have a minimal effect on the resistance of the particle-to-particle system.

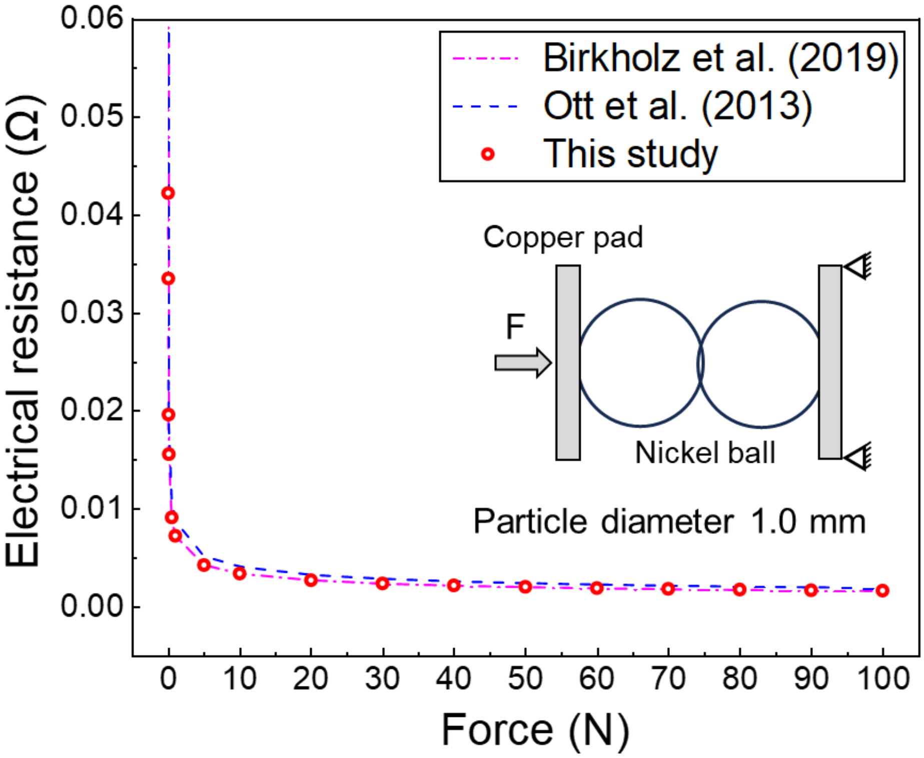

Figure 4.6. Evolution of electrical resistance for particle-to-particle contact under different mechanical forces (red dots are simulation results, blue and pink dash lines are analytical results, and the inset figure is a schematic diagram of a particle-particle contact setup).

4.4.2 Comparison with the Experimental Results

A one-dimensional (1-D) chain of stainless-steel particles is simulated to investigate the effect of contact sequences between the particles on the overall electrical conduction (Creyssels et al., 2017; Falcon et al., 2004; Falcon and Castaing, 2005). Also, a three-dimensional (3-D) spherical steel particle bed test (Bourbatache et al., 2012) is modelled to examine the effects of particle material, the nature of the contacts, and the structural characteristics of the entire granular network on the electrical conduction of the particulate system.

4.4.2.1 Chain of stainless-steel particles

Figure 4.7 illustrates the schematic of the experimental setup. In this setup, a chain of N (N_{max} = 50) identical stainless-steel particles is assembled in series and placed inside a cylindrical container made of polyvinylchloride (PVC) material. A DC current is supplied to the particle-chain system while a piston, applying a static force ranging from 1 to 500 N, exerts pressure on the chain. As the particles come into contact with each other, a series circuit is formed, allowing the calculation of the electrical resistance for the particle-chain system.

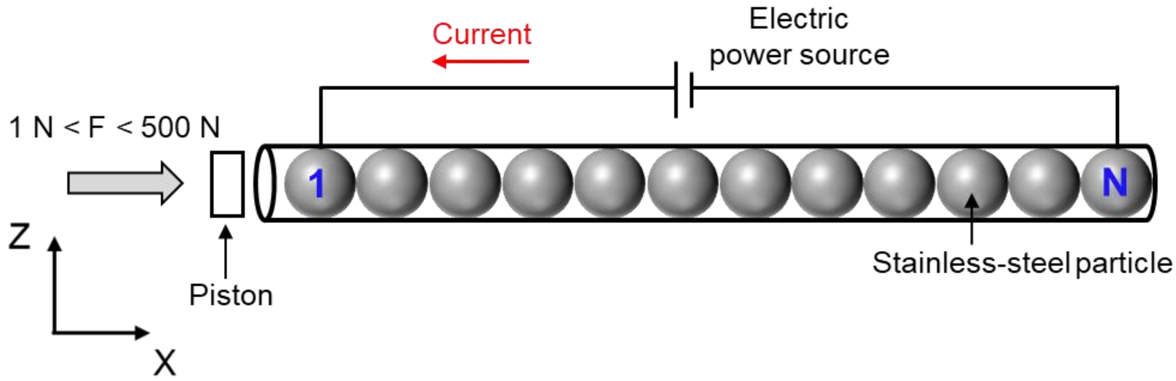

Figure 4.7. Schematic of the experimental setup for a chain of stainless-steel particles.

Three different DC current intensities are applied to the chain of stainless-steel particles to study how its electrical conduction varies under the influence of mechanical forces. The material parameters used in the simulation are listed in Table 4.2, which are taken from Falcon et al. (2004).

Table 4.2 Model parameters used for 1-D stainless-steel bead chain test.

Parameters	**Unit**	**Value**
Number of particles	–	41
Particle diameter	mm	8
Poisson's ratio	–	0.27
Particle density	kg/m^3	7,750
Young's modulus	Pa	1.95×10^{11}
Electrical resistivity	μΩ cm	72
Imposed current intensity	A	0.01, 0.001, 0.0001

Figure 4.8 illustrates an example of the electric potential distribution in a chain of stainless steel particles subjected to a static force of 100 N and a current of 0.0001 A. It can be observed that the particle chain exhibits a potential drop from the left side to the right side. Specifically, electrons flow through the particle chain from the anode (left side) to the cathode (right side). During the compression process, the particles undergo slight deformation under the static force, increasing the contact area between the particles. This deformation can have a significant effect on the contact resistance in the overlapping region of the particles.

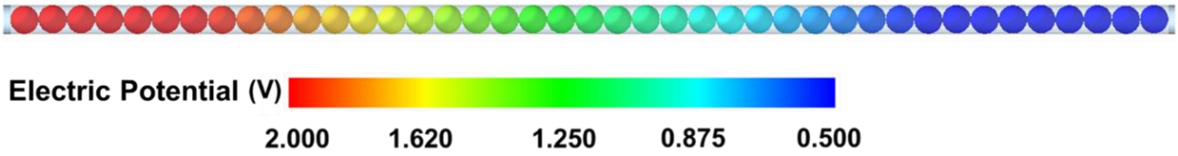

Figure 4.8. The electric potential distribution of the stainless-steel particle chain in the DEM simulation with static force of 100 N and current of 0.0001 A.

Figure 4.9 compares the experimental data and DEM results for the chain of stainless steel particles under different static forces for three specified current intensities. The electrical resistance of the particle-chain system gradually decreases as the static force increases. At the initial stage of static force application, the DEM results underestimate the electrical resistance of the particle-chain system. This discrepancy occurs because the small static force is insufficient to break the oxide layers on the surfaces of the particles, hindering electron penetration and the formation of a conductive channel. Consequently, the resistance of the oxide layer is included in the measured experimental data. A closer match with the experimental results is achieved when the static force exceeds 100 N, aligning with previous theoretical interpretations (Falcon et al., 2004; Falcon and Castaing, 2005; Jakšić et al., 2017).

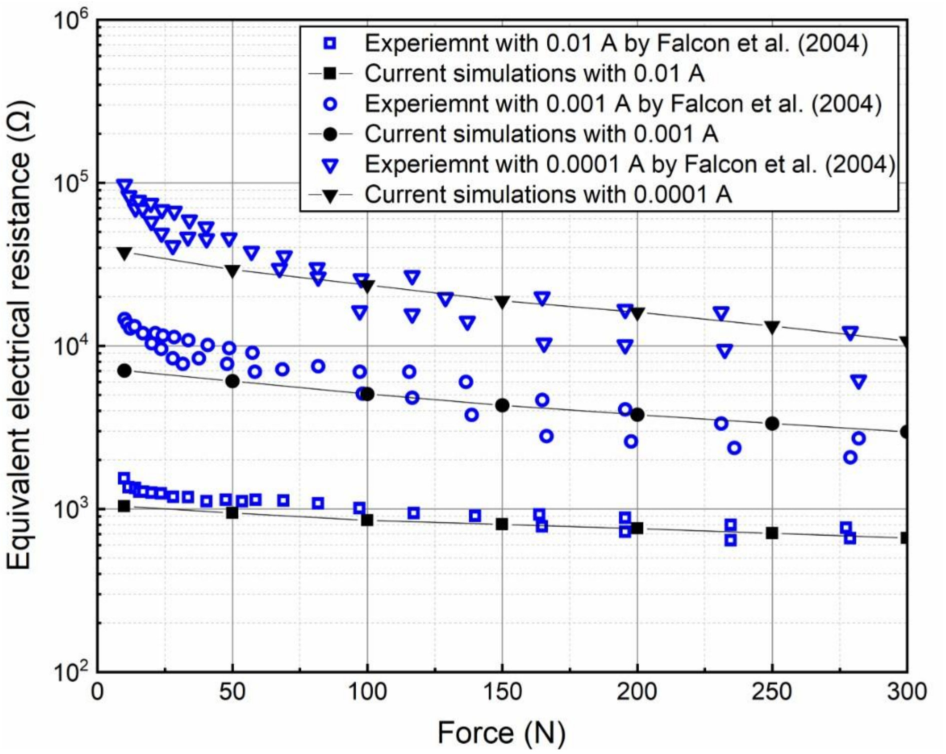

Figure 4.9. Comparison between numerical predictions and experimental data for equivalent electrical resistance of stainless-steel particle-chain system under various mechanical forces.

4.4.2.2 *Particle bed test*

Figure 4.10 shows a schematic diagram of a compaction experiment on a particle bed, where steel particles are placed in a cylindrical container with a diameter of 50 mm. To simplify the simulation, the top and bottom plates are assumed to be made of the same material as the particles, while the cylinder wall is electrically insulated. The anode and cathode of the power supply are connected to the top and bottom plates of the cylindrical container, respectively.

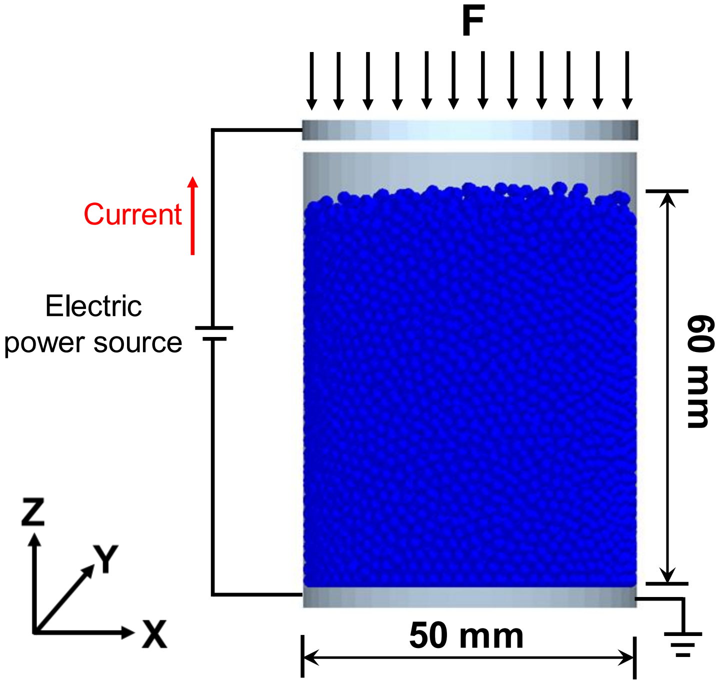

Figure 4.10. Schematic of a compaction experiment on the particle bed subjected to an imposed DC current.

A current of 0.01 A is applied as a boundary condition to the top and bottom plates, with a voltage of 0 volts applied to the bottom plate. This setup specifies that the current flows from the top plate to the bottom plate. At the beginning of the numerical experiment, a compressive load is applied to the top plate. When the top plate comes into contact with the steel particles, a DC current with a specific value enters the particle bed from the top plate and is then transferred to the bottom plate. Once the system stabilises, the electric potential drop between the top and bottom sides of the granular system is obtained, allowing the calculation of the electrical resistance of the particle bed. The properties of the steel particles and the simulation parameters are listed in Table 4.3, based on data from Bourbatache et al. (2012).

Table 4.3 Material properties and numerical parameters for the steel particle bed test.

Parameters	**Unit**	**Value**
Particle diameter	mm	2
Poisson's ratio	–	0.3
Particle density	kg/m^3	7,850
Young's modulus	Pa	2×10^{11}
Electrical resistivity	Ω m	1.71×10^{-8}
Imposed current	A	0.01

Figure 4.11 shows the evolution of electrical conduction for a spherical steel particle bed under simultaneous application of an electric current and a compressive load. Figure 4.11a shows the electric potential distribution, which stabilises at 0.5 s of loading time. Due to the applied boundary conditions, the top platen is at high electric potential, while the bottom platen is grounded (0 V), resulting in a potential gradient driving the current through the granular system. The colour scale in Figure 4.11a represents the electric potential, with red indicating higher potential and blue indicating lower potential. Figure 4.11b displays the current distribution, which follows the force chains within the particulate system. The colour of the lines represents the current intensity, where red lines correspond to stronger force chains carrying higher current, while blue lines indicate weaker force chains with lower current flow. This behaviour is consistent with previous DEM studies (Bourbatache et al., 2012; Hubert et al., 2017), demonstrating the strong correlation between mechanical force transmission and electrical conduction in particulate systems.

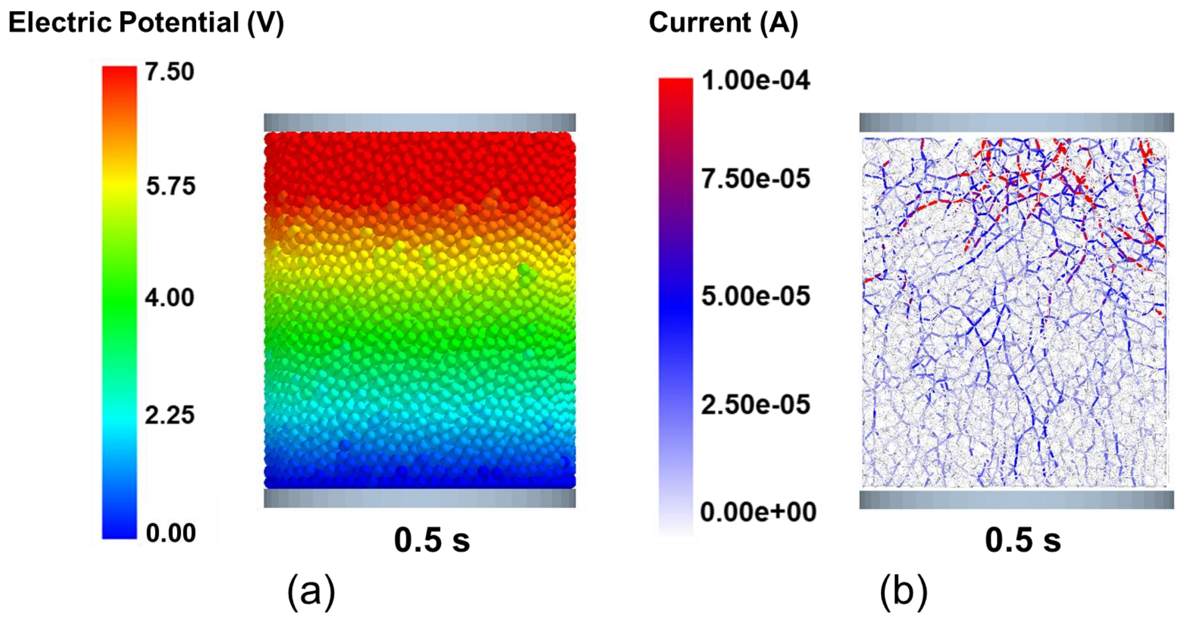

Figure 4.11. Snapshots of the evolution of the electrical conduction for a steel particle bed when it is subjected to a mechanical force of 100 N and a current of 0.01 A: (a) the electric potential distribution of particle bed and (b) the current intensity distribution of particle bed.

Figure 4.12 compares the 3-D numerical predictions and experimental data for particle beds with different numbers of layers; previous 2-D DEM simulation results are also included for comparison (Bourbatache et al., 2012). It is important to note that the steel particles used in the experiments are slightly oxidised, leading to significantly higher measured electrical resistance values than numerical results at lower mechanical loads (i.e., for forces <50 N in Figure 4.12). As the mechanical load increases and reaches a level where the oxidised layer can be crushed and the surface of the particles is exposed, the 3-D numerical predictions align well with the experimental results.

In Figure 4.12a, a compressive load and DC current are applied to a 3-layer particle bed. Both the 2-D and 3-D models predict decreasing resistance as the mechanical force increases, showing minor differences in the form of the relationship, yet both reasonably align with the experimental data. However, as the number of particle bed layers increases, the difference between the 2-D and 3-D numerical results becomes more pronounced (Figures 4.12b and 4.12c). The 2-D simulation, lacking a third dimension, fails to capture the complexity of particle interactions within the granular system. This limitation constrains the ability of model to accurately represent the electrical conduction of the particulate network, resulting in an apparent and increasing divergence of the 2-D calculations from the experimental results.

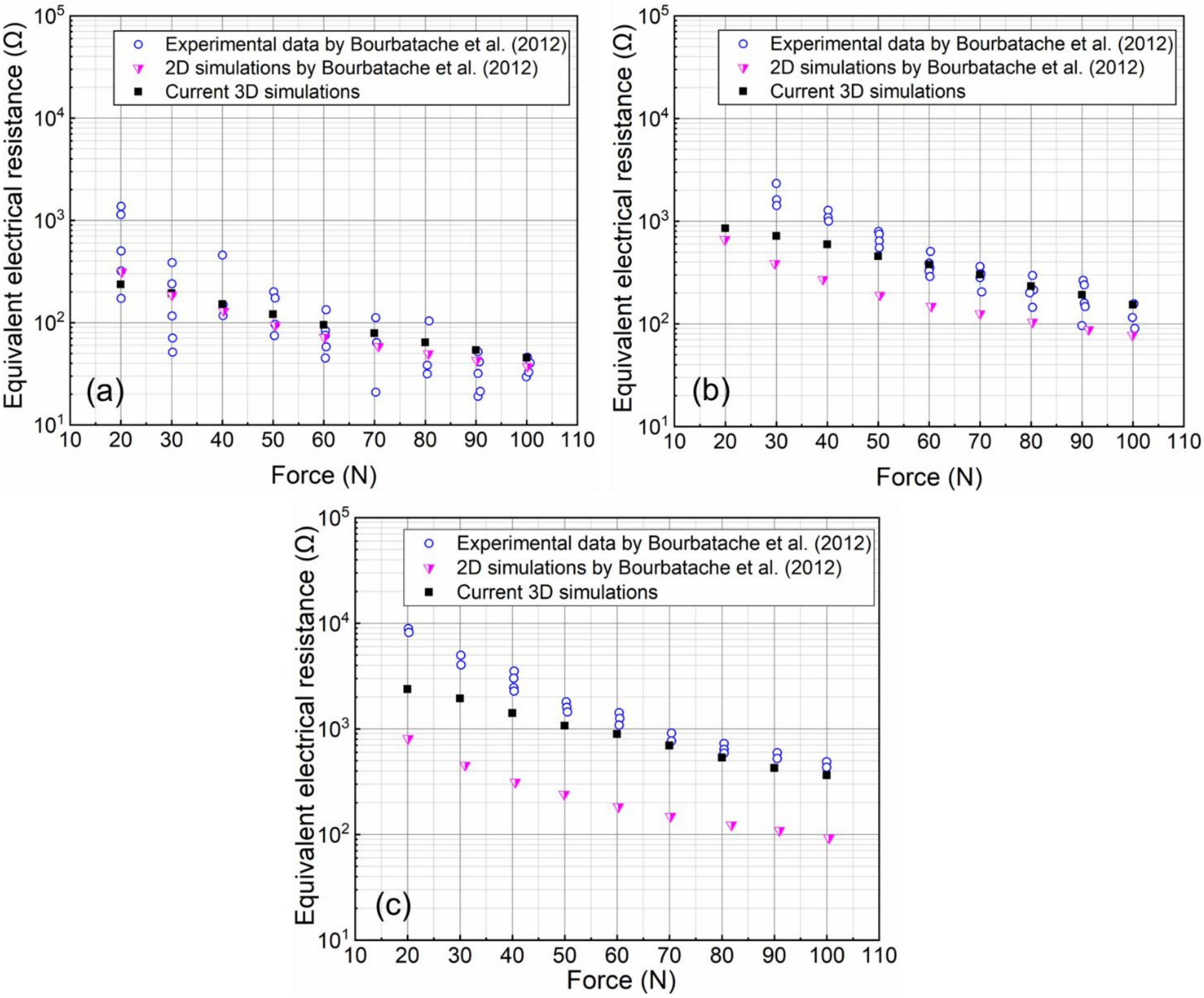

Figure 4.12. Variation of electrical resistance under different mechanical forces in comparison with experimental data and 2-D simulation results: (a) 3-layer particle bed, (b) 5-layer particle bed, and (c) 10-layer particle bed.

4.5 Application: High Pressure Torsion Test

4.5.1 Model Setup

Figure 4.13 shows an example of the actual HPT setup model with an excessive amount of silica sand particles applied to the wheel-rail contact area. To introduce the sand particles into the wheel-rail interface, a geometry bin shaped like a cylindrical shell with an inner diameter of 10.5 mm, an outer diameter of 18 mm, and a height of 2 mm is created. In this case study, the amount of each type of particle is managed by maintaining a consistent volume fraction while ensuring no direct physical contact occurs between the wheel and rail specimens during test.

Subsequently, a 0.5 V_{DC} power supply is connected to the HPT rig while applying a vertical load to the wheel specimen, as illustrated in Figure 4.13. The value of 0.5 V_{DC} represents the worst-performing low-voltage DC track circuit in UK rail operations, with 79% of wrong side track circuit failures occurring on DC circuits between 2012 and 2022 (Skipper et al., 2023). Additionally, a contact pressure of 600 MPa needs to be applied in the wheel-rail contact area to simulate a light vehicle with an axle load of approximately 80 kN (Zhou et al., 2019). This is because a light vehicle is less capable of breaking down the contamination layer between the wheel and the rail, leading to weak conductive performance at the wheel-rail interface. For dynamic similarity purpose between the HPT model and the actual scenario, it is worth noting that the dimensionless analysis method is utilised thereby scaling down the contact pressure from 600 MPa to 6 MPa (Wang et al., 2022). As the wheel specimen moves closer to the rail specimen, it crushes the sand particles into fragment layers. Then, the electric current is transmitted from the wheel specimen to the rail specimen via the fragment layers, creating a closed circuit. When the particles are completely crushed and the wheel specimen is no longer displaced, a uniform angular velocity 1deg/s is applied to the rail specimen. Voltage and current data collected during the rotation can be used to calculate the electrical resistance of the HPT test.

Two newly developed sand-like commercial conductive particles (i.e., coated alumina particles, referred to as Product B and Product D for confidentiality) with electrical resistivity ranging from 1.66×10^{-8} Ω·m to 4.31×10^{-5} Ω·m and silica sand particle are employed in the HPT test. The characteristics of these three types of particle are reported in Skipper et al. (2023). As discussed in Chapter 3, the effect of particle shape on the frictional properties between the wheel and rail is not pronounced. Therefore, all particles in this study are considered spherical. Crushed samples collected from the railhead are analysed using laser diffraction to generate size distribution data of the fragments. This data, applicable to the HPT simulations, is processed using an in-house Python code described in Chapter 3. In addition, the BPM method (Potyondy and Cundall, 2004) is utilised to make up three types of particles, as illustrated in Figure 4.14. Each particle is represented as a cluster of independent spherical fragments bonded together with finite-sized bonds. The translational and rotational motions of each fragment are communicated to other bonded fragments through these bonds under the compression of the wheel specimen. As the wheel specimen continues to compress the particles, the normal and tangential stresses acting on the bonds will exceed their specified critical strength values, leading to bond fracture and particle breakage. Since carbon steel is the primary component of the rails and wheels, the electrical resistivity of the wheel and rail specimens is considered to be the same as that of carbon steel for simplicity in simulation. The numerical parameters used for three types of particles are listed in Table. 4, based on the data from Skipper et al. (2021, 2023) and Knoll (1996).

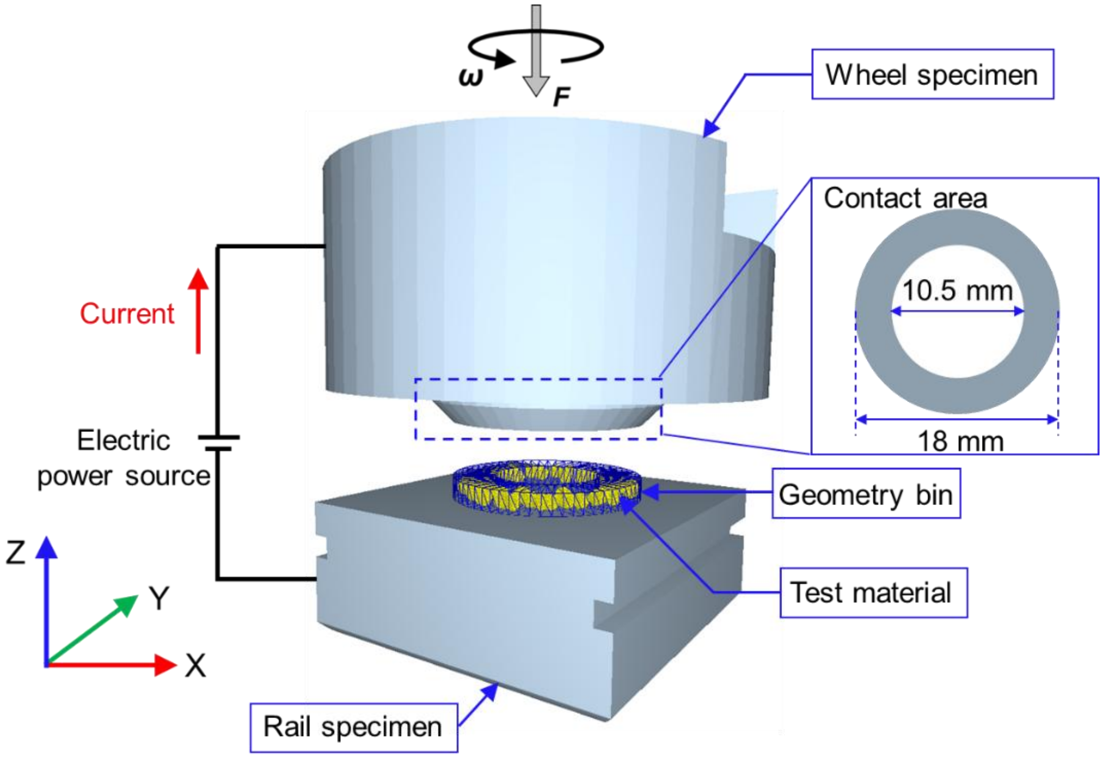

Figure 4.13. The HPT setup connected to a DC circuit and the geometrical parameters of its contact area between wheel and rail specimen.

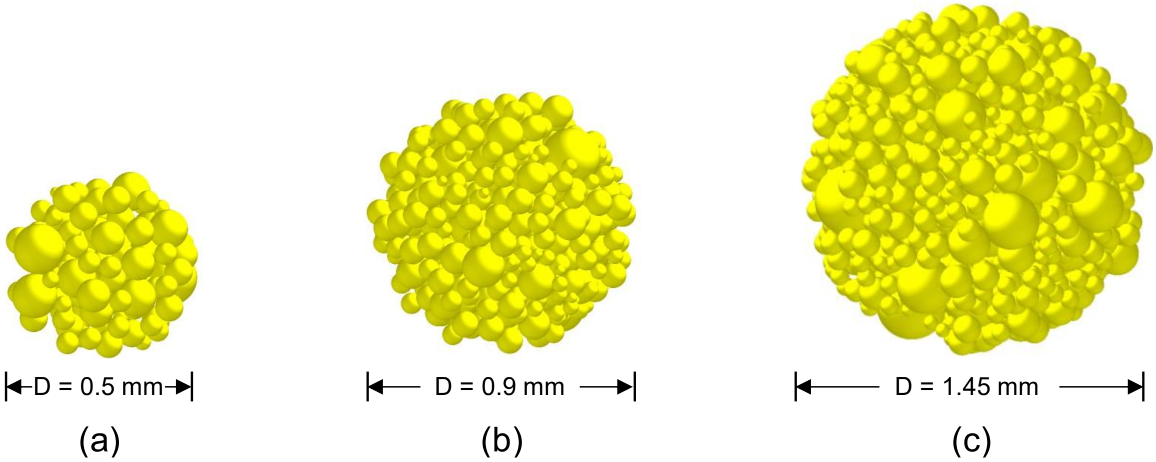

Figure 4.14. Particle modelling of three different crushable particles: (a) Product B with particle size 0.5 mm, (b) Product D with particle size 0.9 mm, and (c) Silica sand with particle size 1.45 mm.

Table 4.4 Properties of three types of particles used in the HPT simulations.

Parameters	**Unit**	**Value**
Product B		
Particle diameter (d_p)	mm	0.5
Number of particles (N_p)	–	1,051
Fragment diameter (d_f)	mm	0.06 ~ 0.2
Number of fragments (N_f)	–	154,497
Poisson ratio (υ_m)	–	0.3
Density (ρ)	kg/m^3	3.81×10^4
Young's modulus (E)	Pa	7×10^8
Electrical resistivity (ρ_e)	Ω·m	4.31×10^{-5}
Product D		
Particle diameter (d_p)	mm	0.9
Number of particles (N_p)	–	180
Fragment diameter (d_f)	mm	0.06 ~ 0.3
Number of fragments (N_f)	–	82,440
Poisson ratio (υ)	–	0.3
Density (ρ)	kg/m^3	3.75×10^4
Young's modulus (E)	Pa	7×10^8
Electrical resistivity (ρ_e)	Ω·m	4.31×10^{-5}
Silica sand		
Particle diameter (d_p)	mm	1.45
Number of particles (N_p)	–	43
Fragment diameter (d_f)	mm	0.06 ~ 0.38
Number of fragments (N_f)	–	55,384
Poisson ratio (υ)	–	0.3
Density (ρ)	kg/m^3	2.65×10^4
Young's modulus (E)	Pa	7×10^8
Electrical resistivity (ρ_e)	Ω·m	5.56×10^6

4.5.2 *HPT Simulation Results*

Figure 4.15 shows the electrical conduction of the fragment layers formed by the breakage of the three different types of particles at the end of the HPT simulation. The electric potential of the fragment layers of each type of particles decreases from top to bottom. The electric current is transferred through the overlapping surfaces between the fragments, with the amount of current being transmitted proportional to the contact area. In addition, an analogy can be drawn between the current paths and the force chains within the particulate system, which aligns with the findings of Bourbatache et al. (2012) and Machado et al. (2015).

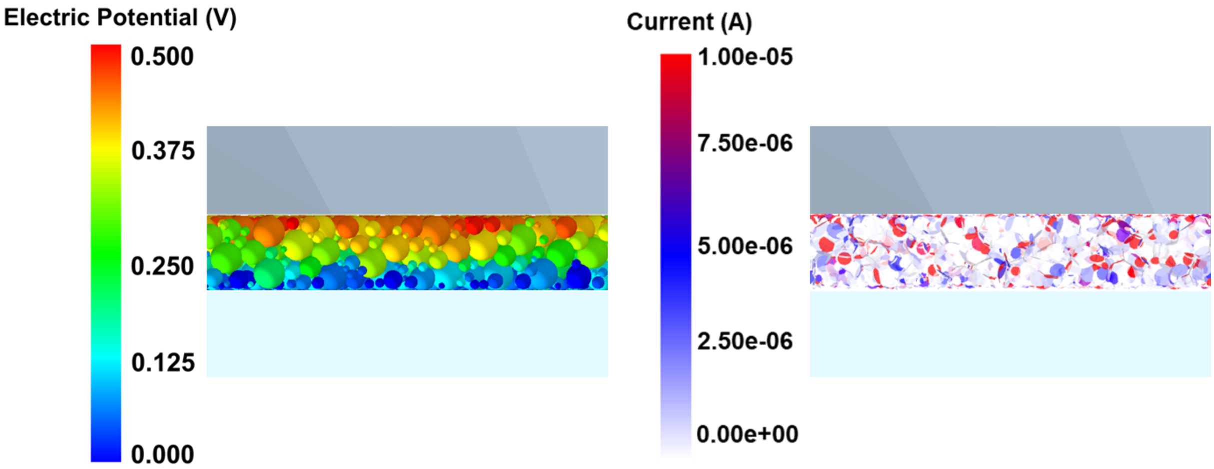

(a)

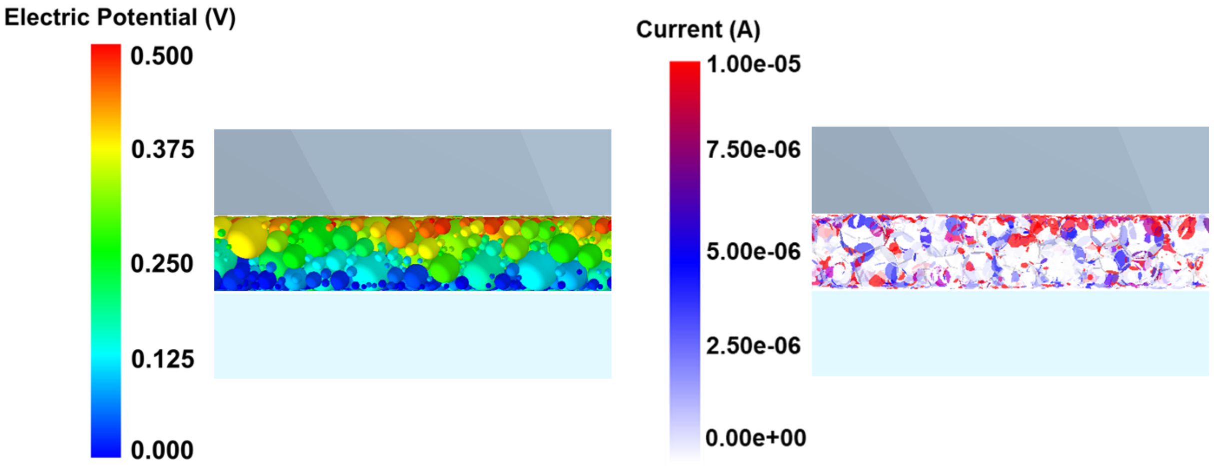

(b)

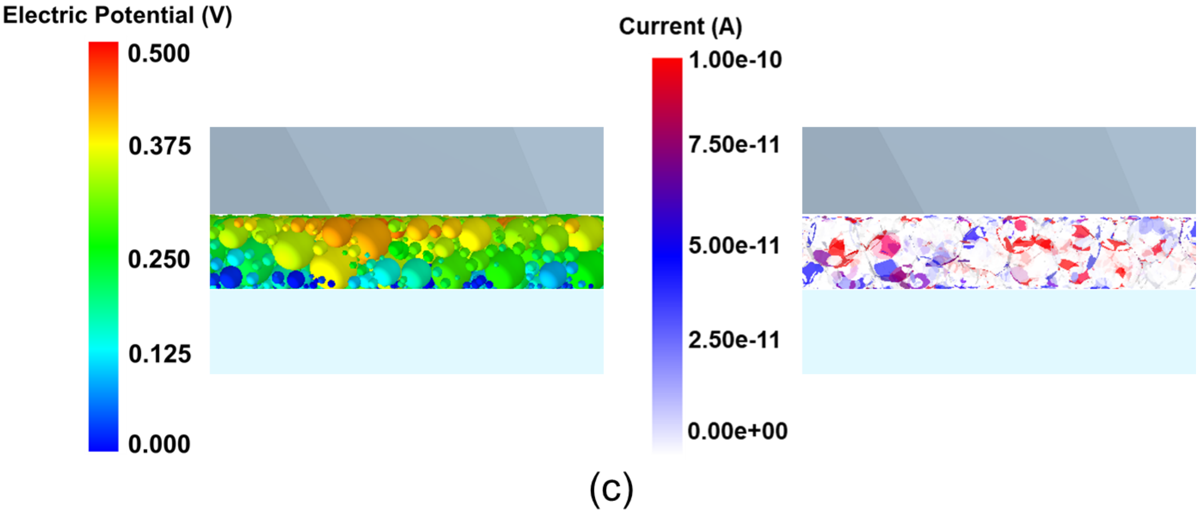

Figure 4.15. Snapshots of the electric potential distribution and current intensity distribution across the fragment layers formed by the crushing of the three different types of particles: (a) Product B, (b) Product D, and (c) Silica sand.

Figures 4.16a and 4.16b demonstrate that the high electrical conductivity of Products B and D ensures that the electrical resistance between the wheel and rail specimens remains low (<10 Ω), even when excessive amounts of these conductive particles are used in the HPT test. In contrast, an excess of silica sand particles results in significant electrical resistance. The fragment layers produced by the sand prevent direct metal-to-metal contact between the wheel and rail specimens, and since silica sand particles have very weak conductivity, the current intensity remains extremely low, as shown in Figure 4.16c.

At the start of the HPT simulation, the system is an open circuit, resulting in infinite electrical resistance because the wheel specimen is not in contact with the particles. At t = 0.005 s, the electrical resistance drops to a finite, measurable value, as the conduction paths are generated by the crushed particles between the wheel and rail specimens, allowing current flow. As the rail specimen begins to rotate, the electrical resistance of the HPT system fluctuates significantly. During this phase, the fragments transition from static (being crushed) to dynamic (rotating), altering the contact conditions and local alignment between fragments. This change leads to fluctuations in the contact forces and, consequently, the current. By approximately 0.02 s, the HPT system is fully sliding, the contact state between fragments stabilises, and the resistance value gradually smooths out.

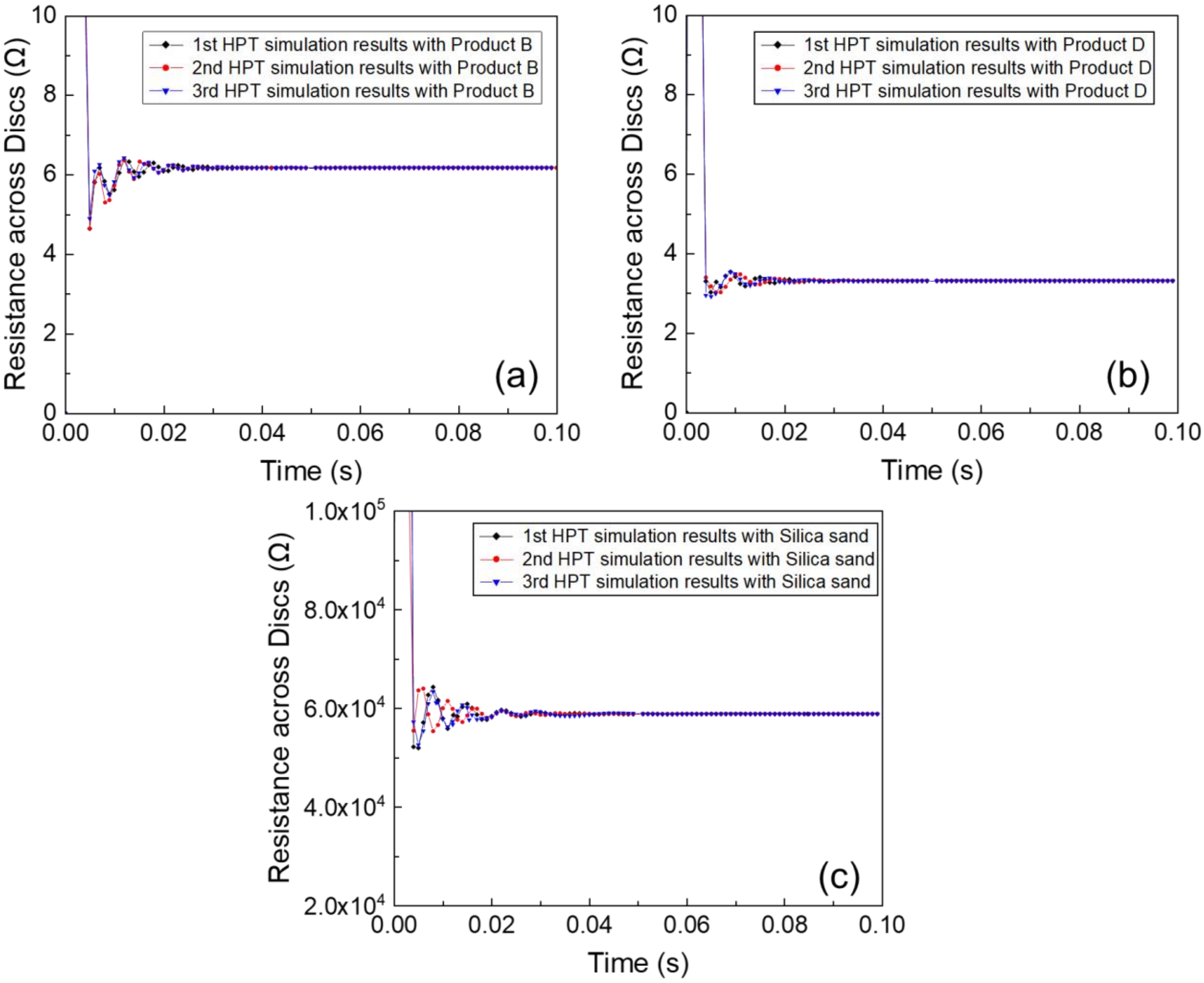

Figure 4.16. Numerical results of electrical resistance for the HPT system with over-application of different types of particles: (a) Product B, (b) Product D, and (c) Silica sand.

Figure 4.17 compares the experimental data with the HPT numerical results for three types of particles when applied excessively to the wheel-rail contact region. The numerical predictions for each type of particles fall within the range of the experimental data reported by (Skipper et al., 2023). In all HPT tests, over-application of particles at the wheel-rail interface is used to prevent direct physical contact between the wheel and rail specimens. However, this also results in material heterogeneity in each test repetition, making the experimental results inherently stochastic. Moreover, in Figure 4.17c, the electrical resistance data (1 ~ 100 Ω) for certain tests appear significantly lower than the numerical results. This discrepancy may be due to the silica sand particles fragmenting and being expelled from the wheel-rail interface under compressive force. Alternatively, the fragments might be displaced during rotation, leading to direct metal-to-metal contact between the wheel and rail specimens.

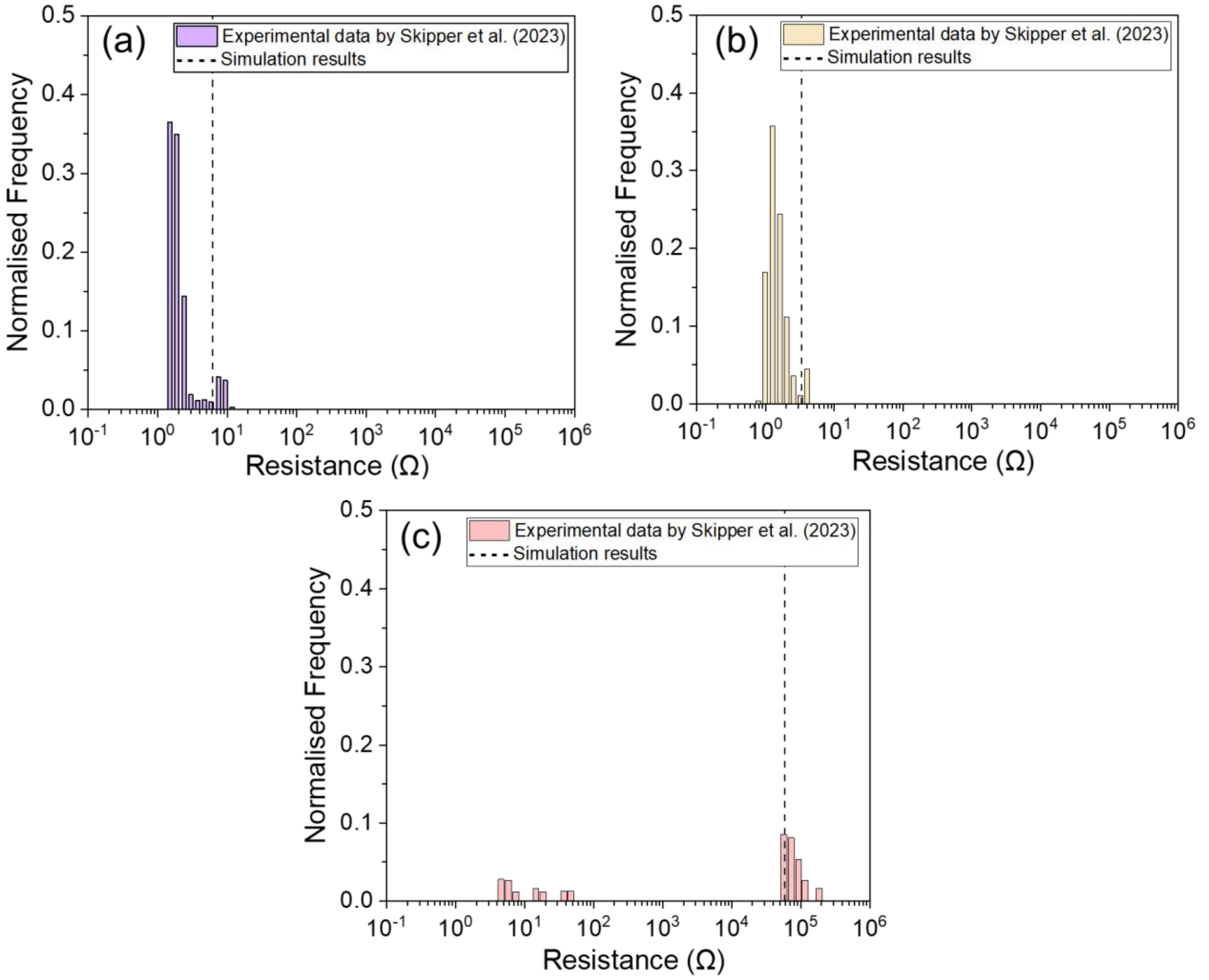

Figure 4.17. Comparison between numerical predictions and the HPT experimental outputs: (a) Product B, (b) Product D, and (c) Silica sand.

Products B and D are selected to evaluate the impact of fragments generated after particle crushing on electrical transfer at the wheel-rail specimen interface on a microscopic scale. Figure 4.18a illustrates the number of fragments that are electrically active (i.e., those through which electric current passes) for both Product B and Product D at the wheel-rail interface. The majority of electrically active fragments fall within the smaller size range. However, this does not imply that smaller fragments are inherently more electrically active or that they contribute more significantly to electrical transfer within the particulate system compared to larger fragments. To address this, an electroactivity index is proposed in this study for evaluating the contribution of each fragment sieve cut on the bulk electrical conduction behaviour. This index helps to quantify how different fragment sizes influence the bulk electrical conductivity of the particulate system, ensuring a more comprehensive understanding of their roles.

$$Electroactivity\ Index = \frac{Number\ \ of\ electroactive\ fragments\ at\ each\ size}{Total\ \ number\ of\ fragments\ at\ each\ size} \tag{4.22}$$

Figure 4.18b illustrates the degree of electrical activity for each fragment size, as evaluated by the electroactivity index. Generally, the degree of electroactivity increases with fragment size. This suggests that many smaller fragments do not make effective contact with the wheel-rail specimen or with other fragments, limiting their role in forming conductive paths within the particulate system. In contrast, larger fragments are more often involved in the force-chain network, facilitating easier current flow through them. This observation aligns with the understanding that current paths in particulate systems follow the force-chain network (Bourbatache et al., 2012; Machado et al., 2015). Furthermore, the absence of current flow through some non-contacting small fragments results in a zero electric potential for these fragments, as seen in Figure 4.15.

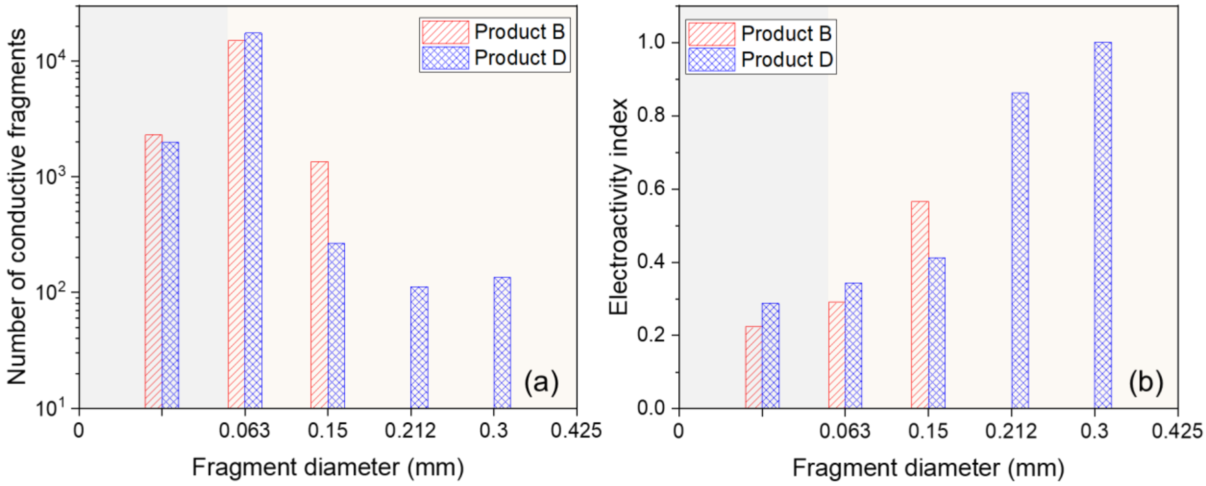

Figure 4.18 (a) The number of electroactive fragments and (b) the degree of electrical activity of the fragments at each corresponding size for two types of conductive particles in the HPT test (The X-axis values represent the test sieve aperture size following BS1377-2:1990. The light orange area indicates that fragments retained by the specified sieve size, whereas the light grey area shows fragments that pass through the smallest sieve size).

4.6 Experimental and Numerical Investigation of the Mixing of Conductive and Non-conductive Particles at an Interface

The following sub-chapter explore the effects of mixing conductive and non-conductive particles on the electrical response characteristics at the interface under mechanical forces, through both experimental and numerical simulations. Experimentally, a mixture of conductive and non-conductive particles is applied to the contact region between two metallic objects, followed by compression tests. During these tests, changes in electrical resistance under compressive force are monitored in real time. Additionally, the phase composition of the particles is analysed using Powder X-ray Diffraction (XRD), and the microstructure of the fragment layer formed after crushing of the particle mixture is observed with SEM. In the numerical simulations, the HPT test is modelled to investigate changes in electrical resistance of the particle mixture at the wheel-rail interface. The electrical resistivity of the conductive particles is parameterised to evaluate the effect of particles with varying conductivity on the electrical transfer behaviour at the interface when mixed with a constant number of non-conductive particles. This comprehensive study allows for a detailed analysis of how different particle compositions influence the overall interfacial electrical conduction properties under mechanical loading.

4.6.1 Previous work

In railway engineering, electrical isolation between wheels and rails, leading to potential safety issues, can be caused by contaminants on the railhead surface or the excessive use of sanding materials. Research efforts to redesign particles with the aim of overcoming electrical isolation at the wheel-rail interface have been limited (Skipper et al., 2020). Two twin disc tests have been carried out by Arias-Cuevas et al. (2010a) and Lewis et al. (2003). However, the contact conditions and dimensions of the twin discs do not reflect the real-world scenario and are further limited by the need to recycle the contact surfaces. Additionally, Chapteuil et al. (2018) investigated how the mixture of highly conductive copper and self-lubricating properties of graphite works at the wheel-rail interface through DEM. The results demonstrated that the optimal mixture ratio in the wheel-rail contact region could balance electrical and tribological properties, but their model is a ‘simplified version of reality’ intended to be qualitative rather than quantitative. Recently, Skipper et al. (2023) and the author, based on the HPT rig, explored the effects of several newly developed conductive particles on both adhesion recovery and electrical resistance at the wheel-rail interface, from both experimental and numerical simulations, respectively. Their findings indicate that while conductive particles can greatly enhance electrical conduction properties, the associated costs could pose a significant constraint.

To minimise the costs, the usage of commercial conductive particles can be reduced by mixing them with the standard rail-sand. The effects of mixing electrically conductive and non-conductive particles on the electrical conduction of the wheel-rail interface and the required ratios to specifically regulate the electrical behaviour at the interface has not been thoroughly understood. Therefore, it is crucial to investigate the electro-mechanical properties of mixed conductive and non-conductive particles at the wheel-rail interface, which can contribute to ongoing efforts to enhance railway safety and performance by providing a cost-effective approach to managing electrical isolation challenges.

4.6.2 Experimental Investigation

4.6.2.1 Testing Setup

Figure 4.19a shows a compression test system for measuring the electrical resistance at the interface between piston and base specimens. The piston and the base specimens are both fabricated from O1 tool steel, which is hardened and tempered to 58 – 60 Rockwell C grade hardness, with high resistance to abrasion and toughness to ensure the test can be completed under high pressure conditions. The piston specimen is a cylinder with a diameter of 35 mm and a height of 50 mm, while the dimensions of the base specimen are 50 mm×50 mm×40 mm. In addition, a circuit is developed to measure the electrical resistance between the piston and the base specimens when they are in contact, as shown in Figure 4.19b. To prepare the circuit mentioned above, the piston and base specimens are sanded using 400-grit silicon carbide abrasive paper to ensure that the surfaces are smooth. Then, an electronic glue is used to adhere the wires to the surfaces of the specimens and keep good electrical contact between them, and the wires are fixed by using hot-melt adhesive. A TENMA 72-7732A Digital Multimeter is used, which applies a constant current and then measures the electrical resistance value between the interface of the piston and the base specimen using the instrument's voltmeter. The test materials are spread evenly on the base specimen and the piston specimen is placed on the top of the materials. The spherical platen is positioned directly above the piston specimen to prevent non-parallel situation in the system caused by uneven loading. Moreover, a lubricant layer is applied to the surface of spherical platen, as shown in Figure 4.19c. This arrangement ensures that current flows only through the closed circuit between the piston and the base specimens.

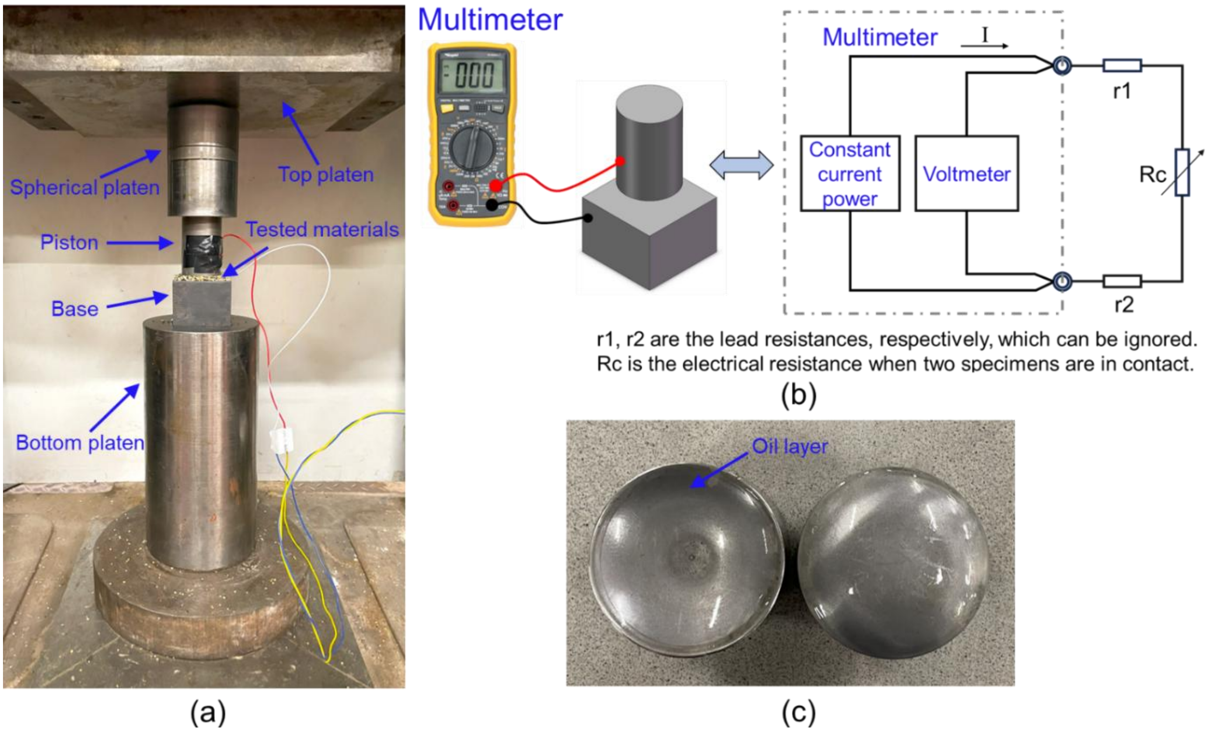

r1, r2 are the lead resistances, respectively, which can be ignored.
Rc is the electrical resistance when two specimens are in contact.

Figure 4.19. (a) 1-D compression test system for measuring electrical resistance at the interface between piston and base specimen, (b) schematic of a simple circuit used in the compression test, and (c) spherical platen with lubrication coating.

4.6.2.2 Particle Characteristics

The results of particle characterisation and HPT testing by Skipper et al. (2023) indicated that Product D would be of particular interest for further investigation. Therefore, silica sand and Product D are selected for compression tests, as shown in Figures 4.20a and 4.20b, respectively. The particle size distribution (PSD) of silica sand and Product D are characterised through sieve analysis following BS1377-2:1990, and their PSD is presented in Figure 4.20c. It can be seen that PSD of these two materials range from 0.6 mm to 2 mm.

XRD of product D and silica sand particles is performed by a Bruker D2 Phaser with LynxEye detector using Cu Kα radiation. For phase identification of finely ground samples, the diffraction parameters including divergence slit, 2θ range, step size and setp-1 are set to 1.0 mm, 10-100°, 0.033° and 0.5 s, respectively. The phase compositions of Product D and silica sand particles are determined and their XRD results are shown in Figure 4.21. The highest diffraction peak of Product D particles, located at $2\theta = 53°$, is identified as the Al_2O_3 phase (reference code 96-100-0033) (Maramizonouz et al., 2023b). For silica sand particles, the principal peak appears at $2\theta = 27°$, corresponding to the SiO_2 (quartz) phase (reference code 96-153-2513)

(Maramizonouz et al., 2023b). To ensure the reliability of these XRD results, they are corroborated with SEM and Energy-Dispersive X-ray (EDX) analyses provided by the School of Engineering at Newcastle University, United Kingdom.

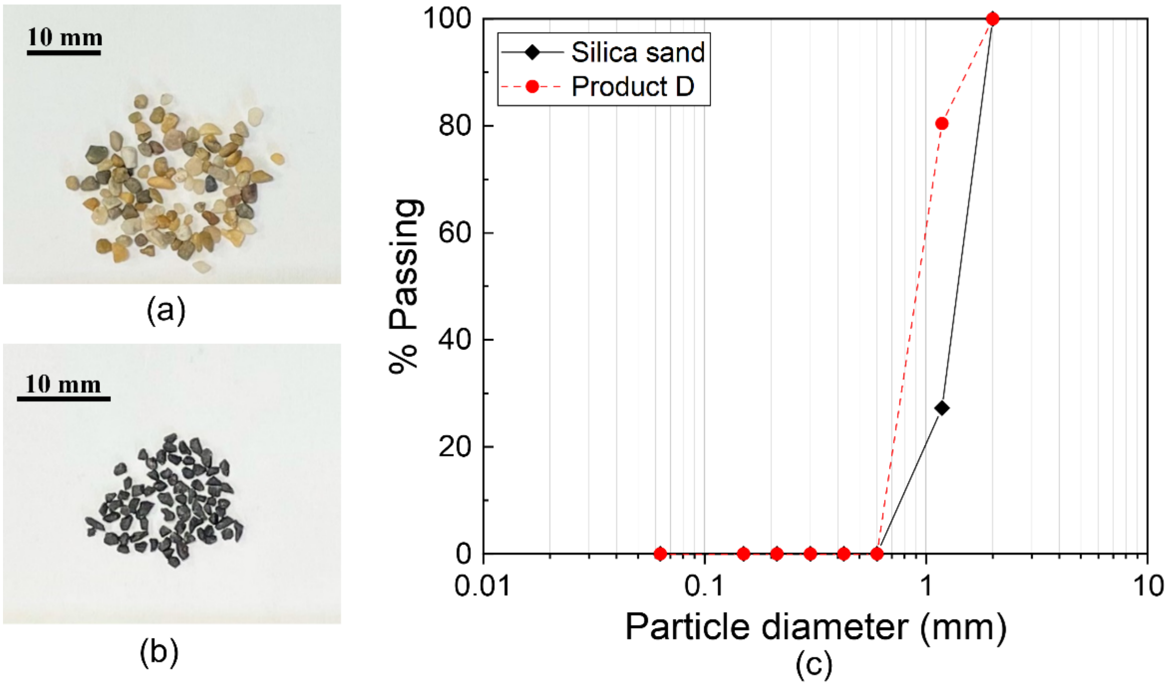

Figure 4.20. (a) Photo of silica sand particles used in the test, (b) photo of Product D particles used in the test, (c) particle size distribution of two tested materials obtained by sieve analysis.

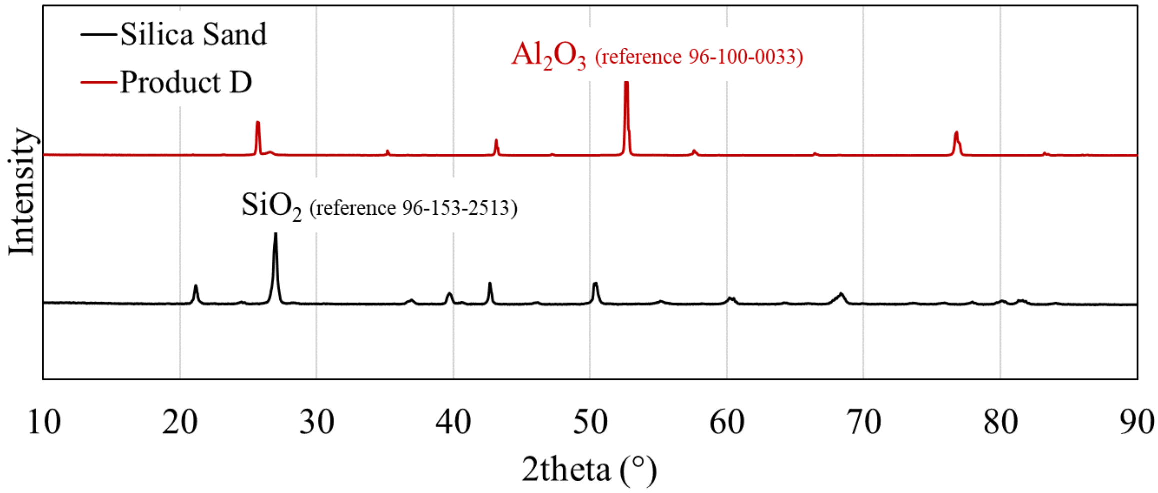

Figure 4.21. XRD spectrum of the Product D and silica sand particles.

4.6.2.3 *Experimental Scenarios*

To investigate the effect of silica sand, Product D, and their mixture on the interfacial electrical resistance between the piston and the base specimen, the experimental scenarios employed in this study are listed in Table 4.5. Following the practice of Skipper et al. (Skipper et al., 2023), each test uses a total mass of 10 g of particles to ensure continuous physical separation between the piston and the base specimen. A loading force is applied, increasing at a rate of 20 kN, with the corresponding electrical resistance recorded throughout the process. When the loading force reaches 577 kN, resulting in a contact pressure of 600 MPa between the piston and the base specimen (Zhou et al., 2019), the force is maintained for 10 s, and the electrical resistance values are measured and noted.

Table 4.5 Proportion of Product D and silica sand particles in each test scenario

Test No.	**Silica sand (g)**	**Product D (g)**
1	10	0
2	9.5	0.5
3	9	1
4	8	2
5	7	3
6	5	5
7	0	10

The silicon carbide abrasive paper is used to sand piston and base specimens before each test to ensure a smooth surface finish. Figures 4.22a and 4.22b display examples of the surfaces of the piston and the base specimens before and after each test. These examples include contact area covered by silica sand, a mixture of silica sand and Product D, and Product D.

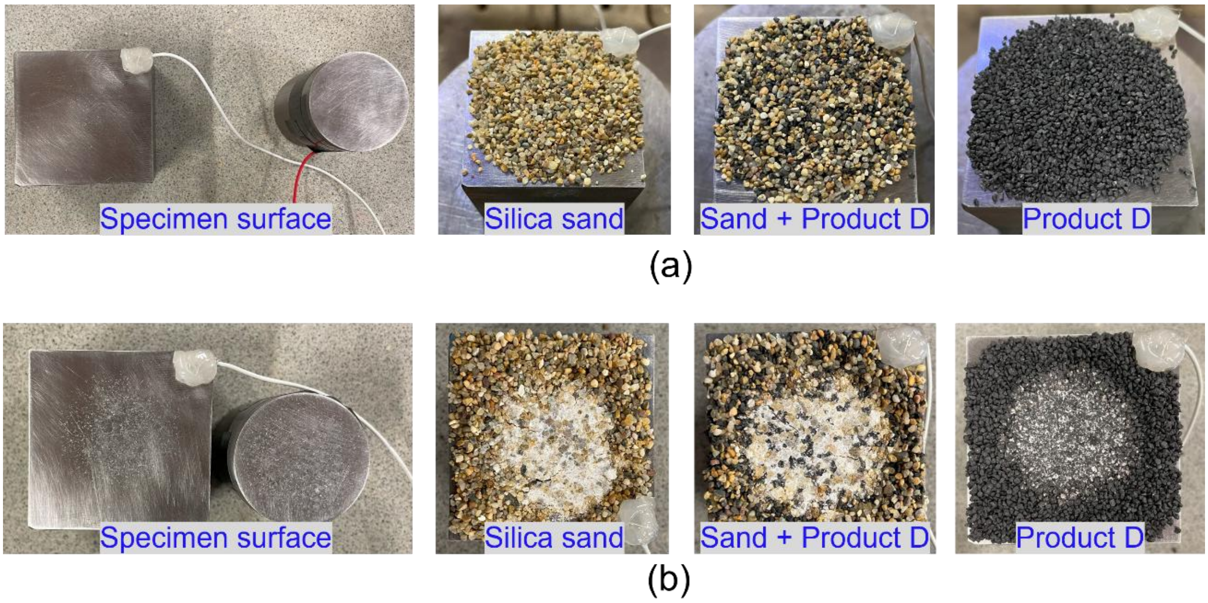

Figure 4.22. Photos of the surfaces of the piston and the base specimens, accompanied by silica sand particles, a mixture of silica sand and Product D particles, and Product D particles: (a) before test, (b) after test.

4.6.2.4 Effect of Conductive Particle Content on Interfacial Electrical Resistance

Figure 4.23 shows the evolution of the electrical resistance at the interface between the piston and the base specimen under mechanical loading conditions for various mixing ratios of Product D and silica sand particles. The data clearly indicate that when the test material is composed entirely of sand particles, mechanical loading has a minimal effect on interfacial electrical resistance. However, for all mixing scenarios, a significant decrease in interfacial electrical resistance is observed with increasing mechanical loading. Previous studies suggest that current flows between two metals along conductive micro-channels in the oxide film and that an increase in loading causes the oxide film to be crushed, increasing the number of conductive micro-channels proportionally to the contact area (Bourbatache et al., 2012; Creyssels et al., 2017). This implies that the fragment layer behaves similarly to the oxide film, allowing current to transfer along conductive micro-channels. For 100% silica sand particles, the increased load enhances the contact area between the particles and the specimens, but the intrinsic electrical properties of the sand impede current transmission within the fragment layer. Conversely, when a certain proportion of Product D particles is mixed in, the increased load enhances their contact area with the piston and the base, thereby creating more conductive micro-channels for current to pass through in the fragment layer.

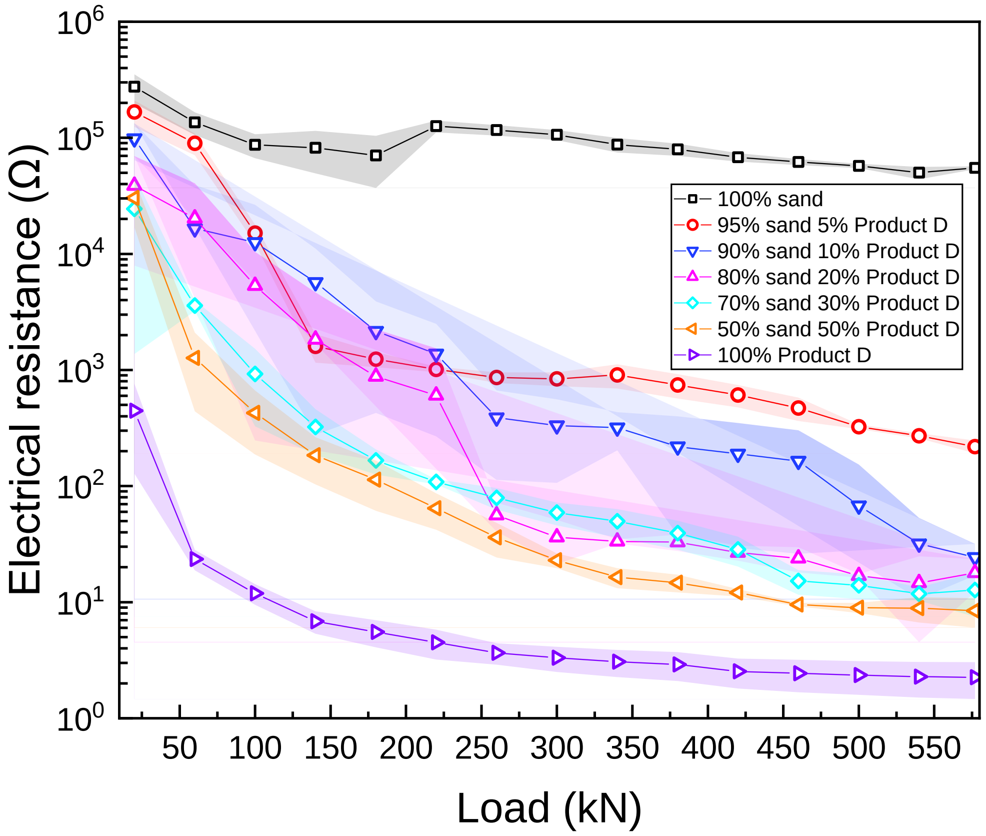

Figure. 4.23. Variation of electrical resistance at the interface between piston and base specimen with increasing mechanical loads for different mixing ratios of Product D and silica sand particles.

Figure 4.24 illustrates the relationship between the content of Product D particles and the interfacial electrical resistance at a load of 577 kN, corresponding to a contact pressure of 600 MPa at the interface. The data reveal a significant decrease in the final electrical resistance at the interface as the proportion of Product D particles increases. Notably, the interfacial electrical resistance drops sharply from approximately 55 kΩ to around 220 Ω when the content of conductive particles is increased from 0% to 5%. This sharp decline indicates that Product D particles effectively enhance the conduction performance of the fragment layer and establish good electrical contacts with the specimens. This observation aligns with previous studies that qualitatively analysed conductive micro-channels in oxide films formed by metal particle contacts (Falcon et al., 2004; Falcon and Castaing, 2005). Additionally, as the percentage of Product D particles continues to increase, the final electrical resistance at the interface decreases progressively. However, the reduction in electrical resistance when the percentage of Product D particles increases from 10% to 100% is less pronounced compared to the initial drop from

0% to 10%. This is because the initial addition of conductive particles rapidly forms conductive paths, drastically improving conductivity of fragment layer. Beyond this point, further increases yield diminishing returns, as most available pathways are already established.

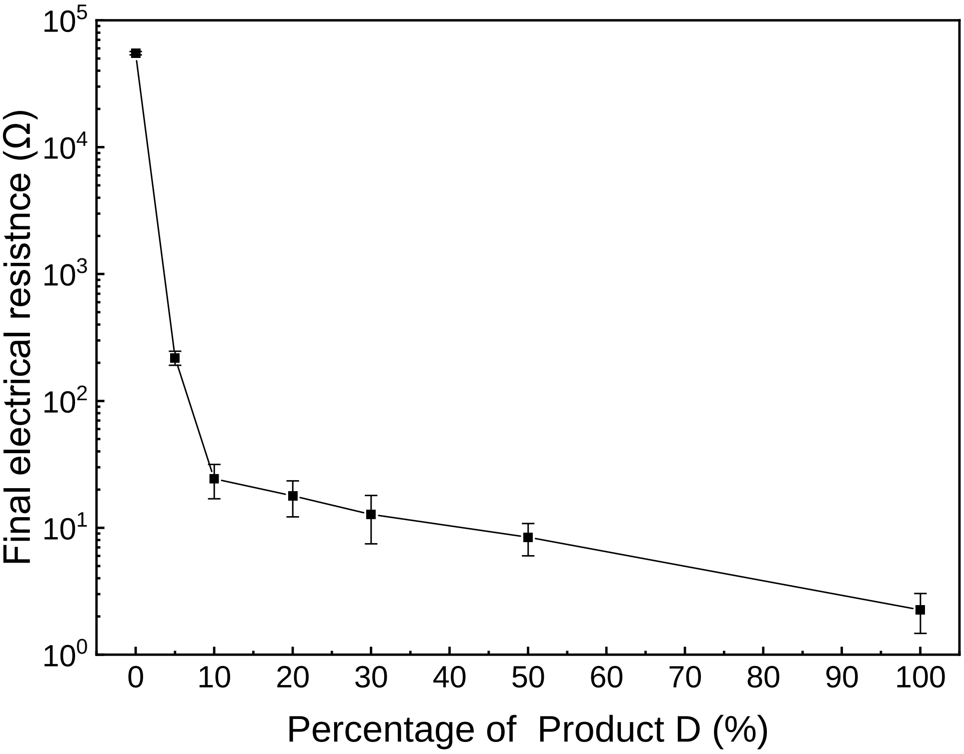

Figure 4.24. Final electrical resistance at the interface of the piston and base specimen as a function of the percentage of Product D particles at a constant mechanical load (The final resistance value is determined once the contact pressure at the metal-to-metal interface reaches 600 MPa, while maintaining a constant load. This value represents the stabilised electrical resistance of the interface under high-pressure conditions).

4.6.2.5 Microstructural Observation of the Fragment Layer

The fragment layer formed by the fragmentation of different particles between the piston and the base specimen is collected, with some examples shown in Figures 4.25a, 4.25b, and 4.25c. The microstructure of these fragment layers is then observed using JSM-IT510 Scanning Electron Microscopy, as presented in Figure 4.25d.

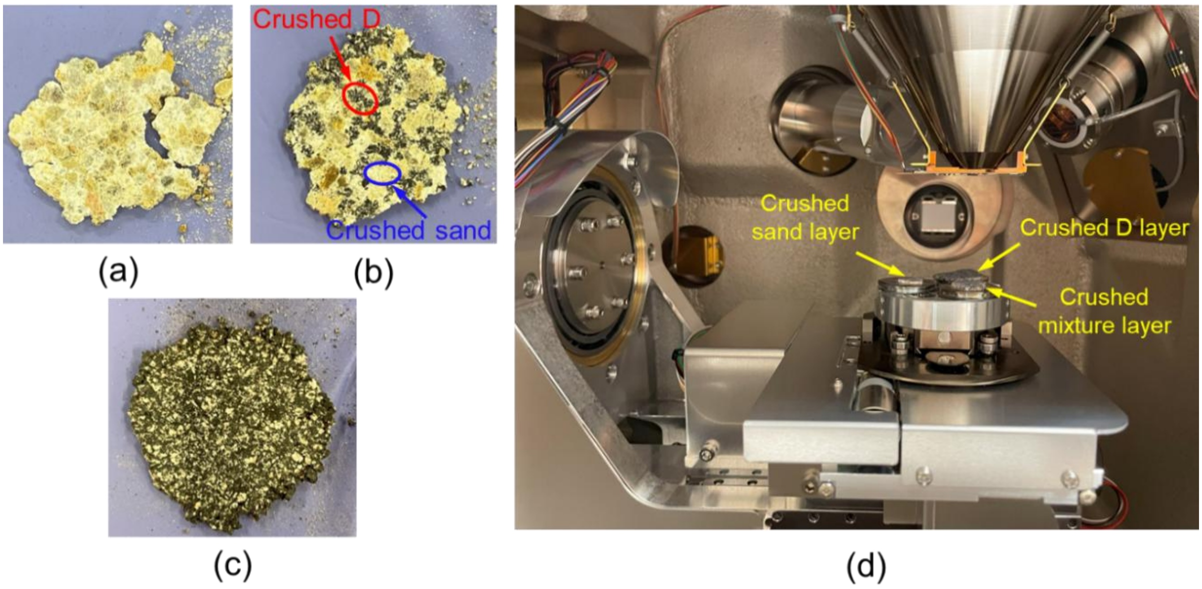

Figure 4.25. Photos of (a) fragment layer of crushed silica sand particles, (b) fragment layer of crushed mixed particles, (c) fragment layer of crushed Product D particles and (d) SEM analysis.

The SEM images depict in Figure 4.26 that reveal the morphological characteristics and layered structuring of different composite particles. It can be observed that the thickness of each fragment layer is around 1 mm. Figures. 4.26a and 4.26b clearly illustrate the compact nature of the fragment layer after crushing Product D particles. The texture of the fragment layer is relatively homogeneous with the presence of larger angular fragments. Additionally, the overall brightness of the fragment layer is uniform, and together with the XRD results from Figure 4.21, it indicates that the fragments are mainly embedded in Al_2O_3 crystals, which can effectively dissipate the electrons and prevent the accumulation of charges. Figure 4.26c shows the fragment layer after crushing from a mixture of Product D and silica sand particles, with the interface between the two particles clearly visible. The contrast between the bright and dark areas in the image is remarkable, suggesting that SiO_2 may be concentrated in the bright area, allowing charging in this region and leading to an accumulation of charge. It is also notable that Al_2O_3 crystals are interspersed in the matrix, showing that mechanical interlocking may exist between these particles and that conductive micro-channels are established in the fragment layer. Figure 4.26d displays the fragment layer of silica sand particles with a more uniform texture and composition. Since SiO_2 is interspersed in the matrix as the main component, the accumulation of charge is very evident throughout the region, resulting in a high brightness in the image. This also illustrates the difficulty in creating effective conductive micro-channels in the fragmented layer of silica sand particles, resulting in impeded transfer of current through the medium.

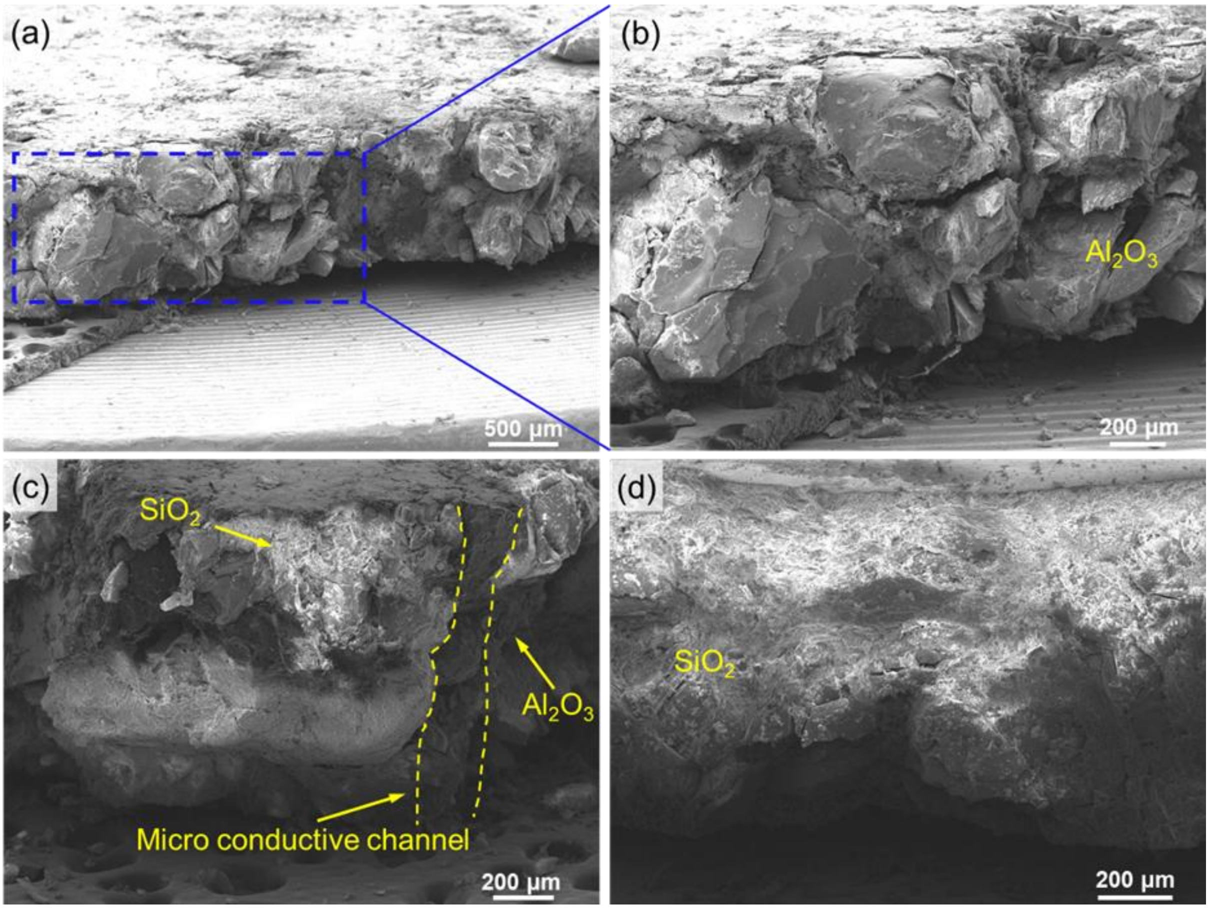

Figure 4.26. SEM images of the side of the fragment layer: (a) and (b) Product D particles, (c) mixture of Product D and silica sand particles, and (d) silica sand particles.

4.6.3 Numerical Investigation

4.6.3.1 Updated HPT Model

In this section, the effects of mixing Product B and D with silica sand particles, respectively, on the electrical conduction properties at the wheel-rail interface of HPT system is investigated through numerical simulations. Also, this study compares the impact of the size of the conductive particles on the electrical resistance of the HPT system. Figure 4.27 presents an example of an HPT model with Product B and silica sand particles mixed at the contact area between the wheel and rail specimen. The simulation parameters used for the HPT model are detailed in Table 4.4. In addition, a median electrical resistivity value of 1×10^{-6} Ω·m for the conductive particles is chosen for the simulation. This value serves as a benchmark which can be used in later section to study the effect of resistivity changes on the electrical conduction properties of the particulate system.

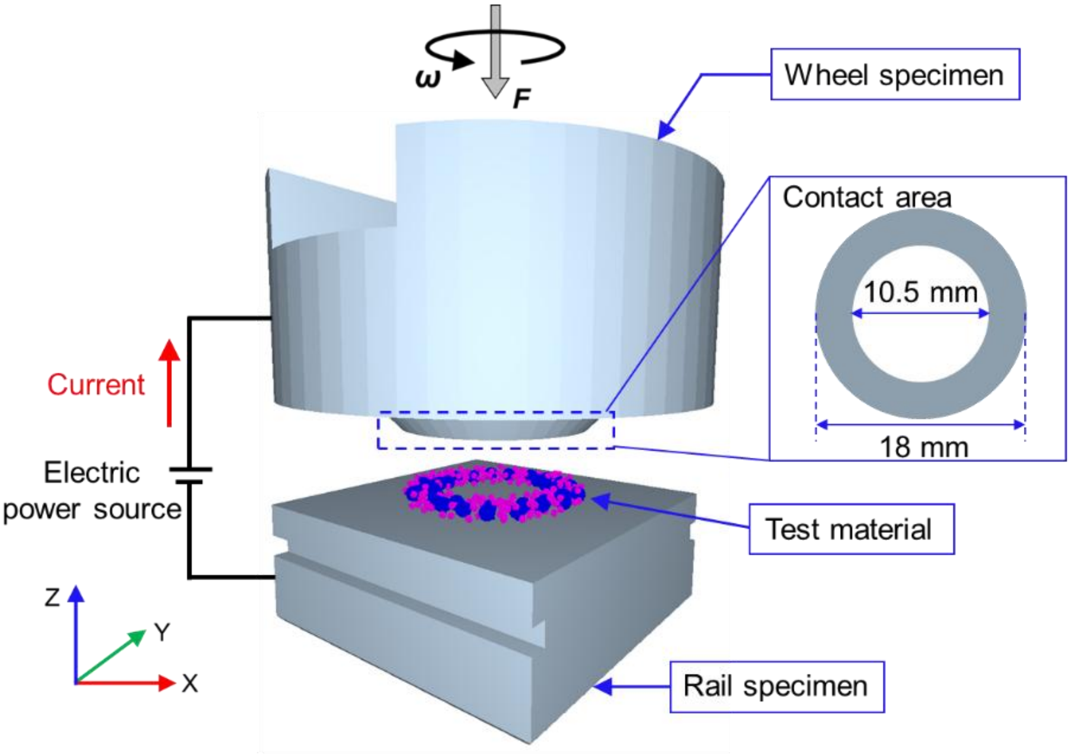

Figure 4.27. The real HPT model connected to a DC circuit with a mixture of Product B and silica sand particles applied at the wheel-rail interface (pink cluster particles represent Product B, while blue ones represent silica sand).

In a particulate system composed of conductive and non-conductive particles, it is crucial to categorize the types of particle-to-particle and particle-to-wall contacts under loads. Consequently, the C++ script of electro-mechanical contact model used in sub-chapter 4.5 is updated to accommodate these classifications. For particle-to-particle contacts, three categories are identified: (i) two conductive particles, (ii) one conductive and one non-conductive particle, and (iii) two non-conductive particles. For particle-to-wall contacts, the classifications include (i) conductive particle-wall contact and (ii) non-conductive particle-wall contact. The electrical resistivity properties of the particles are used to determine their conductivity, guiding the appropriate computational scheme. Figure 4.28 presents the pseudo-code of the complete computational workflow for calculating the electrical resistance of both particle-to-particle and particle-to-wall contacts.

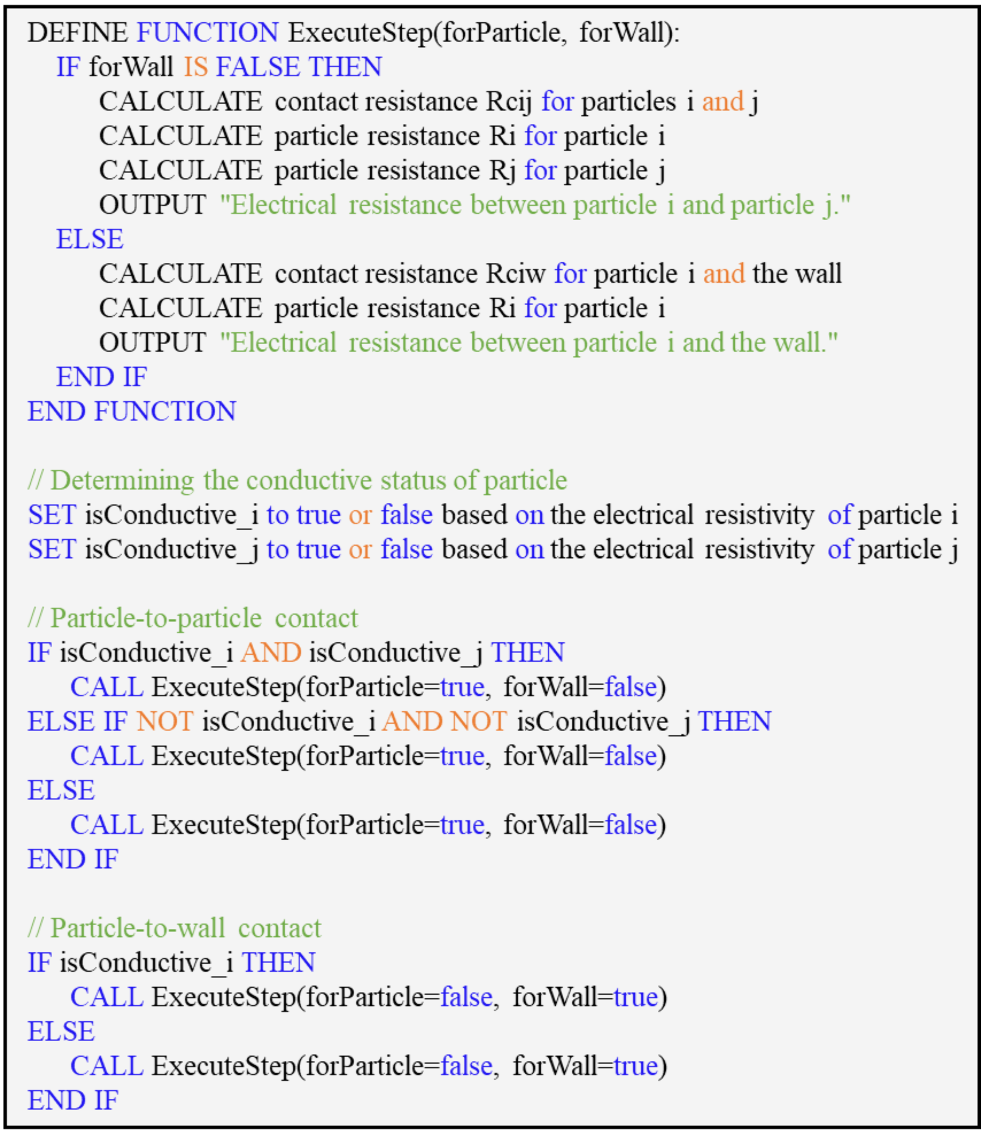

```
DEFINE FUNCTION ExecuteStep(forParticle, forWall):
   IF forWall IS FALSE THEN
      CALCULATE contact resistance Rcij for particles i and j
      CALCULATE particle resistance Ri for particle i
      CALCULATE particle resistance Rj for particle j
      OUTPUT "Electrical resistance between particle i and particle j."
   ELSE
      CALCULATE contact resistance Rciw for particle i and the wall
      CALCULATE particle resistance Ri for particle i
      OUTPUT "Electrical resistance between particle i and the wall."
   END IF
END FUNCTION

// Determining the conductive status of particle
SET isConductive_i to true or false based on the electrical resistivity of particle i
SET isConductive_j to true or false based on the electrical resistivity of particle j

// Particle-to-particle contact
IF isConductive_i AND isConductive_j THEN
    CALL ExecuteStep(forParticle=true, forWall=false)
ELSE IF NOT isConductive_i AND NOT isConductive_j THEN
    CALL ExecuteStep(forParticle=true, forWall=false)
ELSE
    CALL ExecuteStep(forParticle=true, forWall=false)
END IF

// Particle-to-wall contact
IF isConductive_i THEN
    CALL ExecuteStep(forParticle=false, forWall=true)
ELSE
    CALL ExecuteStep(forParticle=false, forWall=true)
END IF
```

Figure 4.28. A pseudo-code for calculating the electrical resistance of a mixture of conductive and non-conductive particles corresponding to the HPT modelling.

4.6.3.2 Mixing Scenarios in Simulations

Following the modelling approach detailed in Sub-Chapter 4.5, a geometric bin in the shape of a cylindrical shell is created at the interface between the wheel and rail specimens to place a mixture of conductive and non-conductive particles. The volume fraction of the mixture is kept consistent in each simulation to regulate the number of conductive and non-conductive particles, ensuring no direct contact between the wheel and rail specimens. The simulated mixtures of Product B with silica sand and Product D with silica sand are depicted in Figures 4.29a and 4.29b, respectively. Table 4.6 lists the number, volume, and mass ratios of conductive and non-conductive particles used in each simulation.

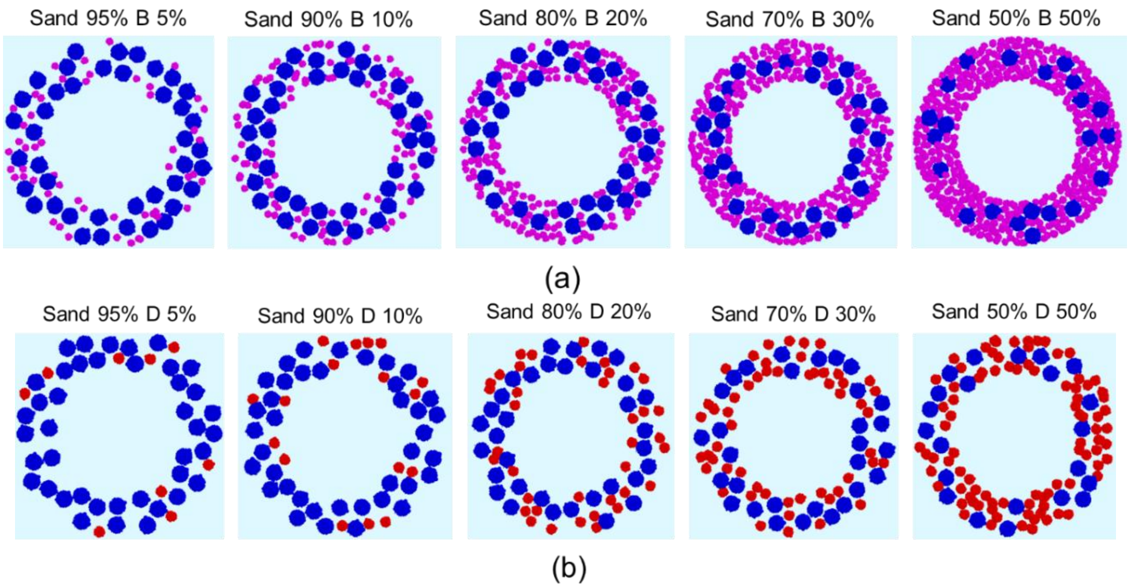

Figure 4.29. Simulation scenarios with various mixing ratios of conductive and non-conductive particles: (a) silica sand and Product B, (b) silica sand and Product D (The blue, pink, and red cluster particles represent silica sand, Product B, and Product D, respectively).

Table 4.6 Mixing scenarios of conductive and non-conductive particles in the HPT simulation.

Case No.	**Conductive particle**			**Non-conductive particle**		
	Product B			Silica sand		
	Number of particles	Volume ratio (%)	Mass ratio (%)	Number of particles	Volume ratio (%)	Mass ratio (%)
a1	52	5	7	41	95	93
a2	105	10	13.7	39	90	86.3
a3	210	20	26.7	34	80	73.3
a4	315	30	38.2	30	70	61.8
a5	524	50	58.4	22	50	41.6
	Product D			Silica sand		
	Number of particles	Volume ratio (%)	Mass ratio (%)	Number of particles	Volume ratio (%)	Mass ratio (%)
b1	9	5	6.9	41	95	93.1
b2	17	10	12.9	39	90	87.1
b3	38	20	27.4	34	80	72.6
b4	55	30	38.3	30	70	61.7
b5	88	50	57.5	22	50	42.5

4.6.3.3 *Simulation Results*

Figures. 4.30a and 4.30b show the electric potential distribution of the fragment layer in the wheel-rail contact region for Product B and silica sand particles as well as for Product D and silica sand particles in each mixing scheme, respectively. Due to the imposed boundary conditions (i.e., voltage), the figures clearly indicate that the electrical potential of the fragment layer in each mixing scheme decreases sequentially from top to bottom. As the number of conductive particles increases, the interlocking between the crushed conductive and sand particles induced by mechanical loading makes the fragmented layer more uniform and denser. In addition, the fragments from conductive particles are interspersed in the matrix, and thus the potential distribution on the upper surface of the fragmentation layer gradually becomes more even as the conductive particles increase.

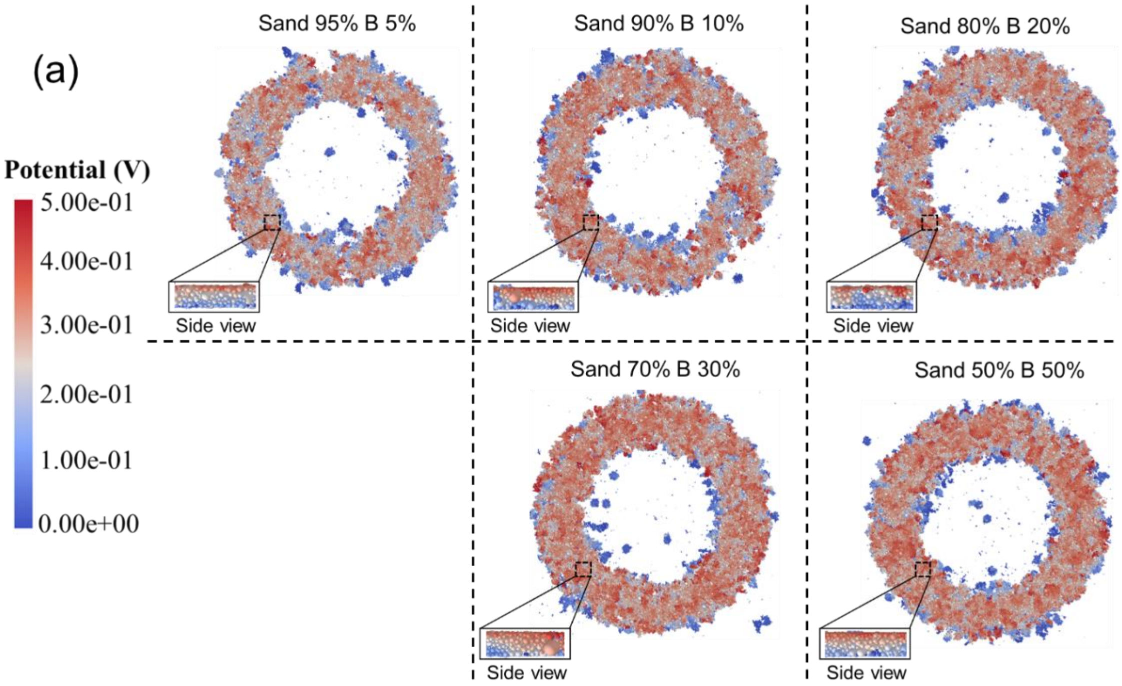

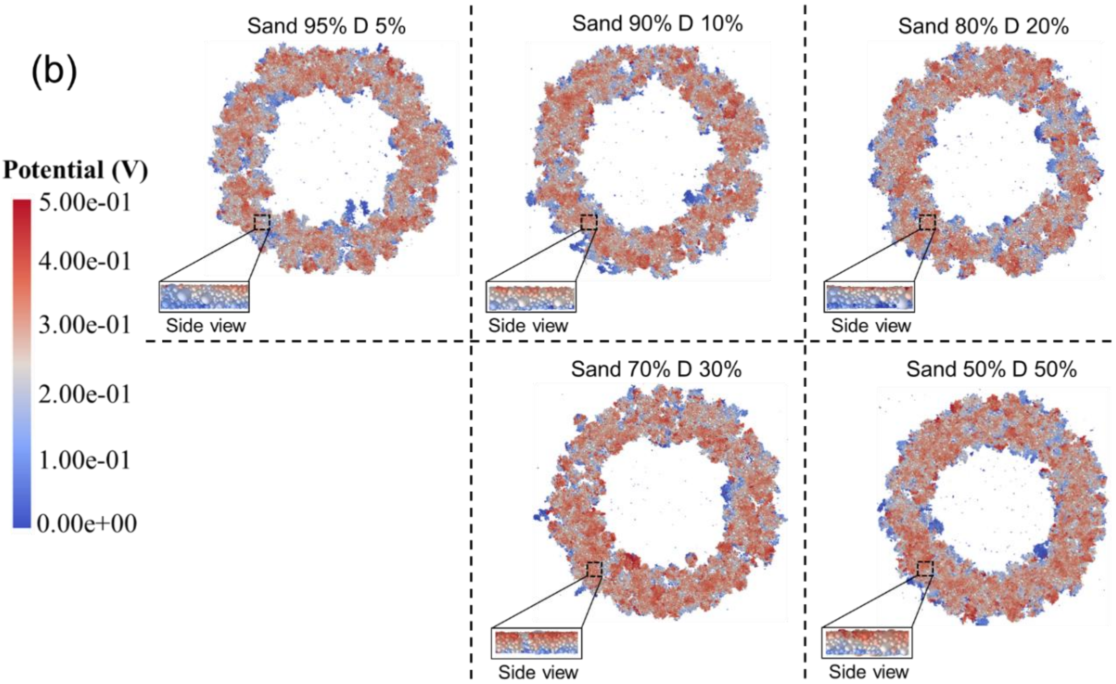

Figure 4.30. Snapshots of the electric potential distribution in the fragment layer for each mixing scenario of conductive and non-conductive particles: (a) silica sand and Product B, (b) silica sand and Product D.

Figure 4.31 is current intensity distribution in the fragment layer after a mixture of conductive and non-conductive particles is crushed in each mixing scheme. In Figure 4.31a, a significant increase in current intensity can be observed in a growing part of the fragmentation layer as the number of Product B particles increases. As the crushed Product B particles are inserted in the fragment layer, resulting in the construction of conductive micro-channels to facilitate the current transfer, which is similar to Figure 4.26c. Also, as the fragment layer becomes more uniform and denser, the interaction between the fragments is stronger, leading to an improvement in the magnitude of the electric current transmitted across the fragments (from side view). The trend of the current intensity distribution in the fragment layer for a mixture of Product D and silica sand particles is shown in Figure 4.31b, which is in general consistent with Figure 4.31a.

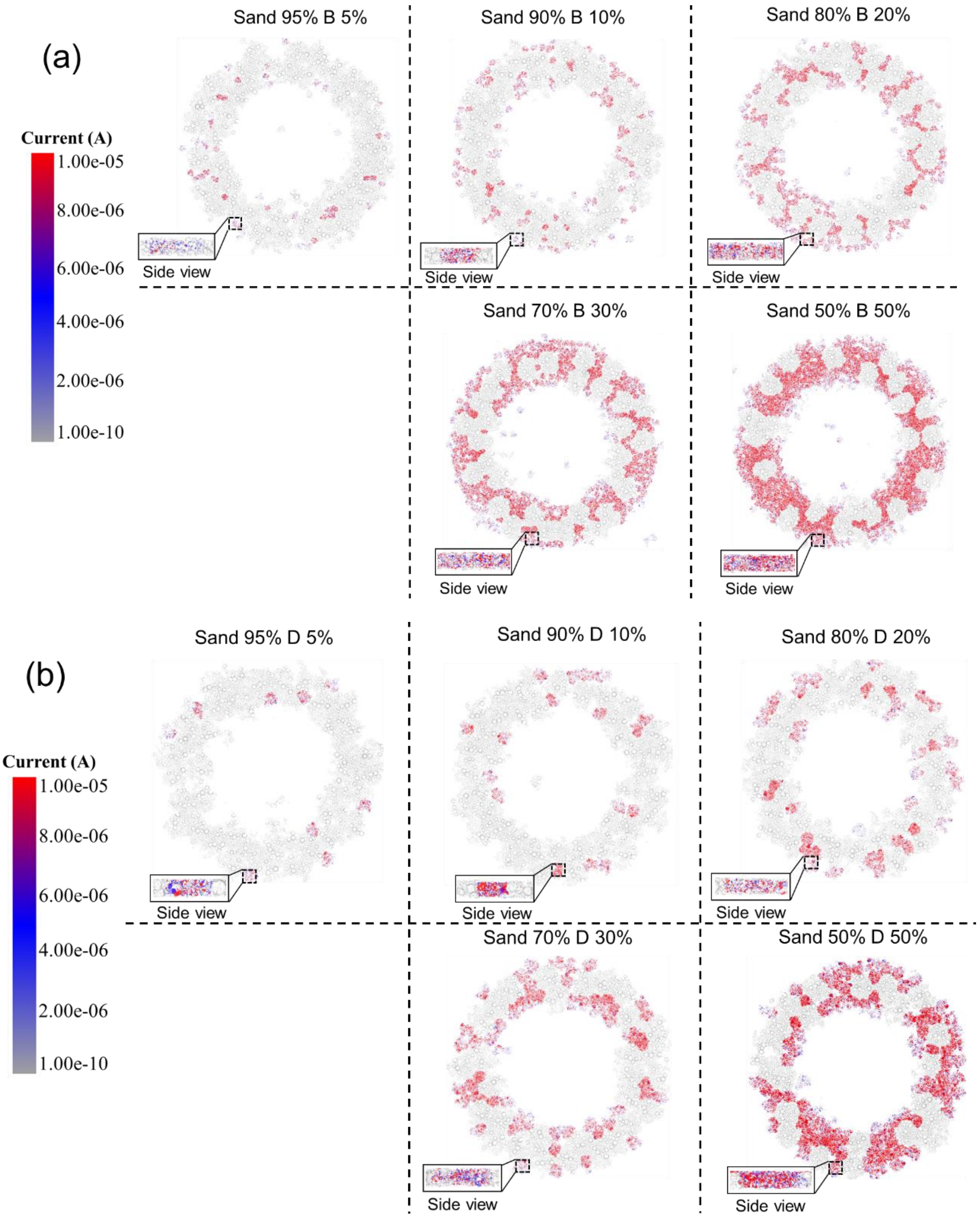

Figure 4.31. Snapshots of the current intensity distribution in the fragment layer for each mixing scenario of conductive and non-conductive particles: (a) mixing of silica sand and Product B, (b) mixing of silica sand and Product D.

Figures. 4.32a and 4.32b show the variation of electrical resistance for HPT system when using different mixing ratios for Product B and silica sand particles as well as for Product D and silica sand particles under a constant mechanical loading, respectively. Before the wheel specimen comes into contact with the particles, the entire HPT system is in open circuit, leading to an infinite electrical resistance value. Due to the mechanical action of the wheel specimen, the particles are gradually crushed and the contact area with the wheel as well as the rail specimen increases. During this process, the fragments are detached from particles and realigned by the mechanical behaviour, and the conductive micro-channels for current transfer from wheel to rail specimen are built. At t = 0.005s, the electrical resistance of HPT system decreases to a measurable value. At the initial stage of the rotation of the rail specimen, the HPT resistance value appears to fluctuate. Afterwards, the HPT system slides completely at around 0.02 s and the resistance value remains stable. For 100% silica sand particles scheme, the high electrical resistivity of the sand particles prevents the efficient current transmission through the fragment layer, thus leading to a resistance of 58 kΩ in HPT system. However, the resistance of HPT system drops dramatically when the proportion of conductive particle (Product B or D) in the test material is increased to 5%. As the percentage of conductive particles continues to increase to 30%, the HPT system resistance decreases to an acceptable value (<10 Ω) (Skipper et al., 2023).

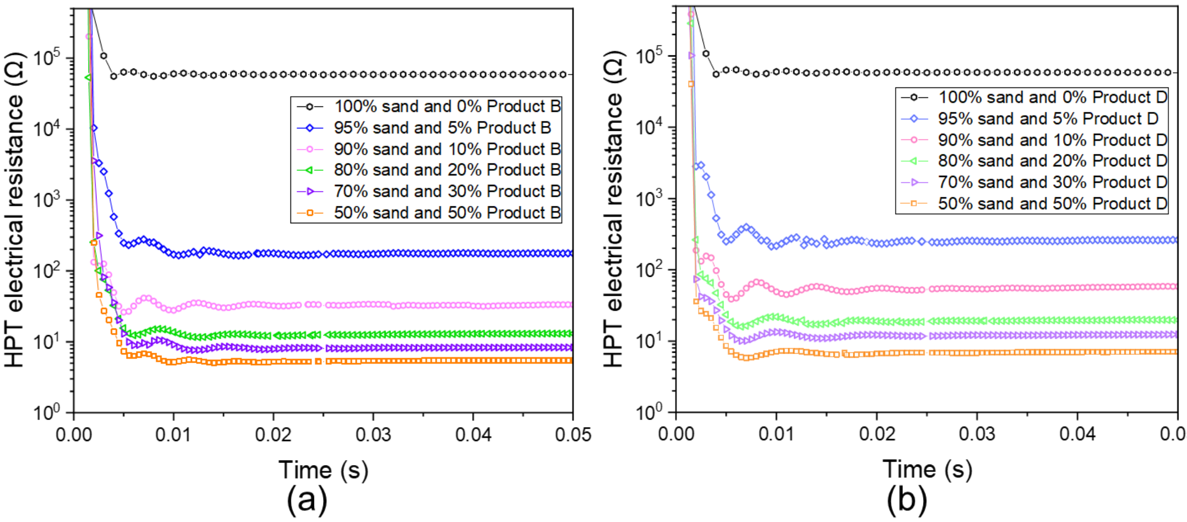

Figure 4.32. The electrical resistance of the HPT system for each mixing scenario of conductive and non-conductive particles at constant mechanical load: (a) silica sand and Product B, (b) silica sand and Product D.

Figure 4.33 compares the effect of Product B and D particles at each mixing ratio on the HPT resistance in the final stage of the simulation. An effective reduction in the electrical resistance of HPT system can be achieved by mixing either Product B or Product D particles in the silica sand particles. Moreover, it can be observed that Product B can reduce the electrical resistance of HPT system to some extent better than Product D when using the same percentage of conductive particles. This is because the particle size of Product B is smaller compared to Product D. When the same volume of test material is used in the simulation, more Product B particles are mixed in, thus building more conductive micro-channels, as shown in Figures 4.31a and 4.31b.

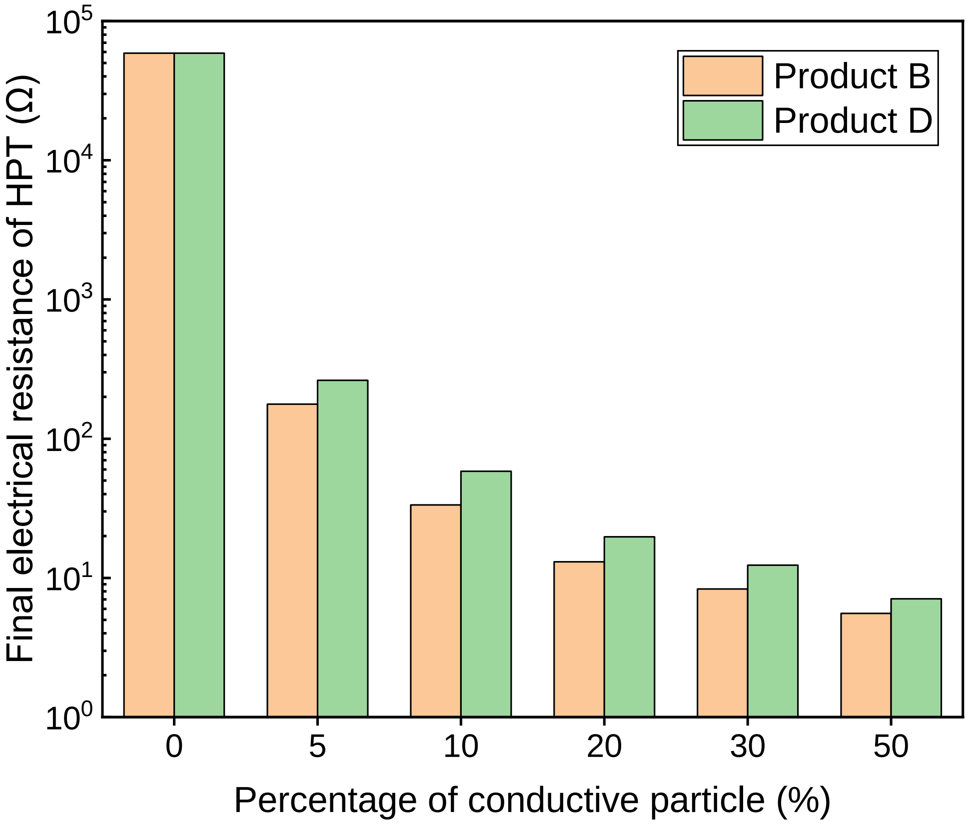

Figure 4.33. Comparison of the effect of Products B and D on the final electrical resistance of the HPT system at each mixing scenario.

4.6.3.4 Effect of Electrical Resistivity of Conductive Particle on HPT Electrical Resistance

The electrical resistivities of the conductive particles Product D range from 4.31×10^{-5} to 1.66×10^{-8} Ω·m according to Skipper et al. (2021). To investigate how electrical resistivity of conductive particles affect the electrical resistance at the wheel-rail interface of HPT, the resistivity of Product D is altered accordingly, and the resistivity value 1×10^{-6} Ω·m as a benchmark. The different electrical resistivities of Product D particle used in the HPT model are listed in Table 4.7.

Table 4.7 Resistivity values of Product D and sand particles used in the HPT simulation.

Case No.	**Unit**	**Product D**	**Silica sand**
1	$\Omega\cdot$m	4.31×10^{-5}	5.56×10^{6}
2		5×10^{-6}	
3		1×10^{-6}	
4		1×10^{-7}	
5		1.66×10^{-8}	

Figure 4.34 clearly demonstrates that the electrical resistance is significantly influenced by both the proportion of Product D and its electrical resistivity. When the resistivity of Product D is held constant, the electrical resistance of the HPT system decreases as the proportion of conductive particles increases, which aligns with the above analysis. Additionally, the resistivity of Product D particles is correlated with the overall electrical resistance of the HPT system. For the same mixing ratio, Product D particles with lower resistivity effectively reduce the HPT electrical resistance. Under dry contact conditions, the primary mechanism for current transfer is the formation of conductive micro-channels in the fragment layer through contact paths (Yang et al., 2020). Lower resistivity in Product D particles means there are fewer collisions between electrons and atoms in the material, resulting in less resistance to current flow through the conductive micro-channels in the fragment layer (Housecroft and Sharpe, 2008).

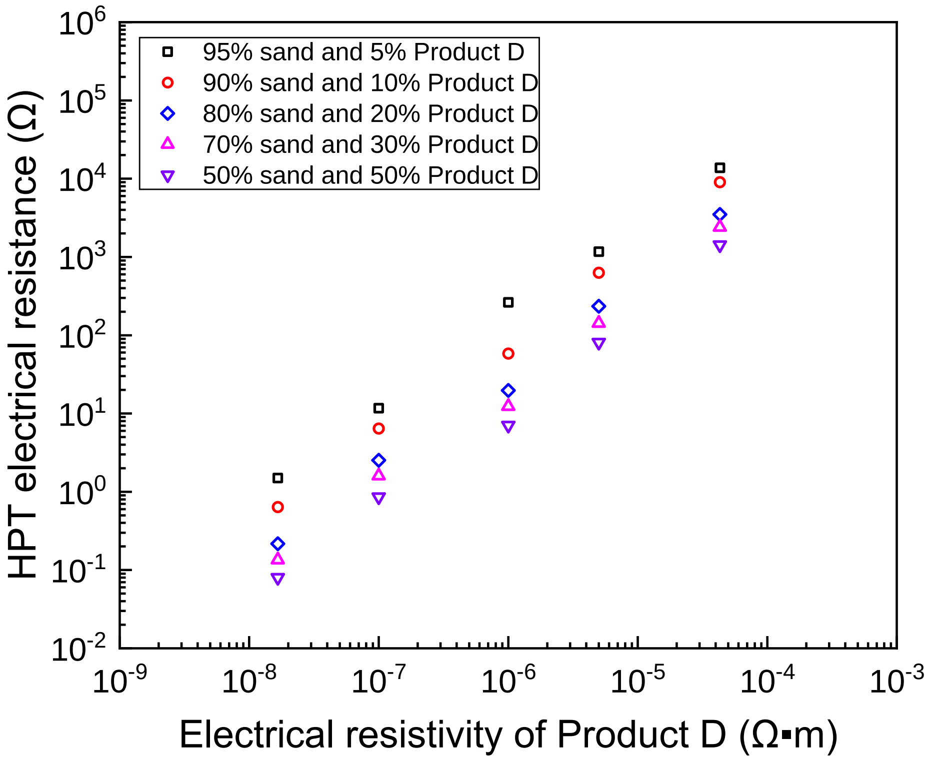

Figure 4.34. Comparison of the effect of Product D with different resistivities on the electrical resistance of the HPT system.

The above investigations have demonstrated that incorporating a small amount of a conductive material with low electrical resistivity into silica sand can significantly reduce the electrical resistance at the wheel-rail interface of the HPT system. Effective electrical conduction between the wheel and rail specimens is typically achieved when the HPT electrical resistance is below 10 Ω (Skipper et al., 2023). As illustrated in Figure 4.35, the resistivity of the conductive material and its proportion in the mixture play a critical role in determining the resistance of the HPT system. The figure clearly shows that selecting the appropriate resistivity and proportion of conductive material can reduce the HPT resistance below a critical threshold. Specifically, if the resistivity of the conductive material is less than 1 x 10^{-7} Ω·m, only about 5% of the conductive material needs to be mixed with silica sand to achieve good electrical contact. Conversely, if the resistivity of the conductive material is higher, a larger proportion of the material is required—potentially up to 100% in some cases with high electrical resistivity values—to ensure effective electrical conduction in the HPT system.

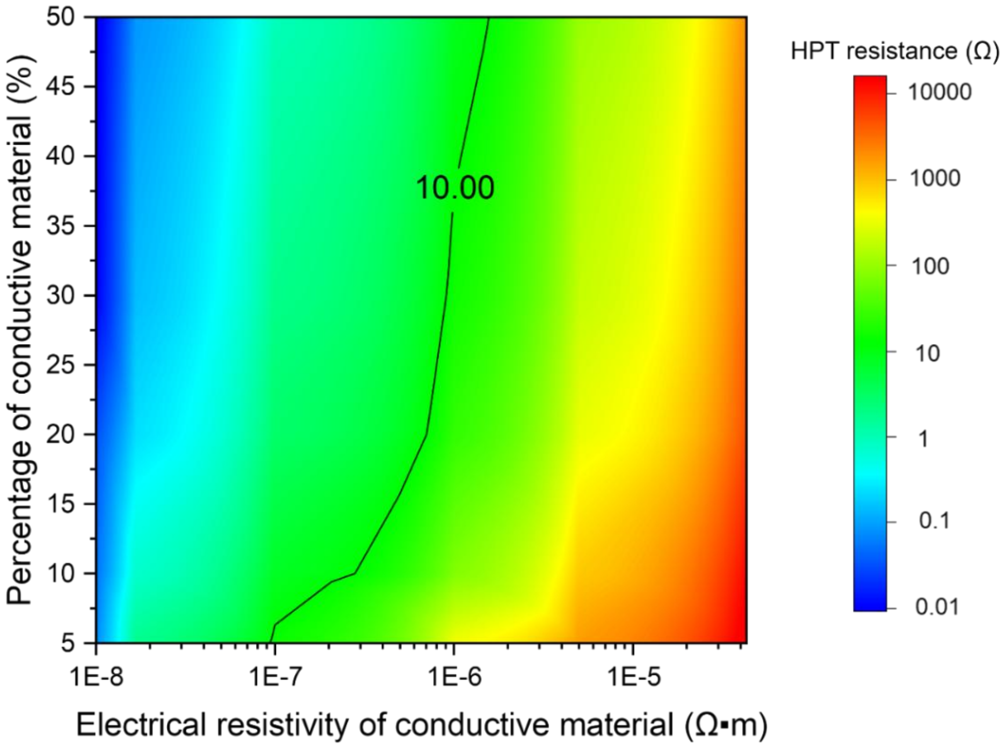

Figure 4.35. Heatmap of electrical resistivity of conductive material versus its percentage for the electrical resistance estimation of the HPT system (The demarcation line indicates the threshold value of 10 Ω for the electrical resistance of HPT system which from Skipper et al. (2023)).

4.7 Discussion

4.7.1 Features of Electro-Mechanical Contact Model

The electro-mechanical contact model proposed in this chapter for evaluating electrical resistance in particle-to-particle and particle-to-wall interactions incorporates both the contact resistance of the overlapping regions between solids and particle resistance from inherent material. This enhancement allows the model to be applied to particulate systems with varying particle size distributions, as well as a mixture of conductive and non-conductive particles.

The numerical results from the validation section exhibit a trend in the electrical resistance of metal particle systems that is consistent with elastic Hertz theory (i.e., $R \sim F^{-1/3}$) under mechanical loading conditions. This suggests that contact resistance plays a dominant role when this electro-mechanical contact model is applied to the metal particle system. The current model does not account for the effect of contamination layers on particle surfaces, leading to discrepancies between numerical predictions and experimental data at lower static forces. Future model development should address how contamination layers obstruct metal-to-metal conductive paths on a microscopic scale to better understand their role as barriers to electrical transmission. Additionally, the real contact area between particles may be larger than the nominal contact area due to the surface roughness of actual particles (Zhai et al., 2016). More advanced models are needed to accurately track current transfer at the contact interfaces between rough particles.

The present numerical framework is based on the Hertz-Mindlin model, making it suitable for modelling the electrical conduction behaviour of particulate systems under dry contact conditions. However, real-world scenarios are more complex. When this electro-mechanical model is applied to real railway projects, for example, requires considering various contact conditions at the wheel-rail interface, such as wet (Buckley-Johnstone et al., 2020) or leaf contaminated (Arias-Cuevas and Li, 2011) conditions. Future work should refine the model to better align with experimental and field data. Moreover, while this model primarily focuses on elastic particle-to-particle and particle-to-wall contacts, it is applicable to DEM simulations of many fundamental particulate systems. Nevertheless, further improvements are needed, particularly for scenarios involving elasto-plastic deformation, such as wheel-rail contact (Evans et al., 2021). Despite these limitations, the proposed model offers a new approach for analysing the electrical response of particulate systems under mechanical loadings and its potential applications are broad.

4.7.2 Effect of the Particulate Systems on the Current Transfer Mechanism at An Interface

This section discusses the current transfer mechanisms at the wheel-rail interface across four distinct scenarios: the absence of particles, the presence of only one type of non-conductive particles, a mixture of conductive and non-conductive particles, and the presence of only one type of conductive particles. Using the wheel-rail contact as an illustrative example, a case where the wheel and rail are in direct contact, and no particulate system interferes with the interface (as depicted in Figure 4.36a). In this scenario, the current transfer mechanism is primarily facilitated by the high electrical conductivity of carbon steel, the material from which both the wheel and rail are typically constructed. At the microscopic level, current flows through the asperities—tiny contact points—where the two metallic surfaces physically meet (Brodnik Zugelj and Kalin, 2020; Liu et al., 2021). This direct electron flow between the wheel and rail significantly lowers electrical contact resistance at the interface, promoting efficient current transfer. On the other side, the substantial mechanical forces exerted by the weight of the train enhance this electrical conduction properties at the interface. The mechanical forces increase the real contact area by deforming the asperities and breaking through any thin insulating layers that may form on the surface, such as oxides or contaminants. This deformation ensures that a stable and effective contact area is maintained, which is crucial for a reliable electrical connection. Moreover, in the absence of any isolating (oxide or contaminants) films, the electrical contact resistance at the wheel-rail interface is predominantly determined due to current constriction (Persson, 2022). This type of resistance arises from the limited number of real contact points, where the current is forced to pass through narrow paths, leading to localised increases in electrical resistance. However, due to the materials involved and the mechanical forces at play, this electrical contact resistance is minimised, ensuring that the interface remains conductive.

When an excess of non-conductive particles (e.g. silica sand particles) is used at the wheel-rail contact area, how the current transfer at the interface is shown in Figure 4.36b. Under normal load, silica sand particles at the wheel-rail interface are crushed, forming a fragment layer often referred to as a friction film (Grandin and Wiklund, 2018). This layer transforms the direct metal-to-metal contact between the wheels and rails into an indirect contact (Liu et al., 2021). As the sand particles crushed, the contact area between the resulting fragments increases under mechanical loading. However, due to the insulating nature of sand particles, which is primarily composed of SiO_2, the formation of this fragment layer produces a long insulating path for electron flow from the wheel to the rail. While this insulating layer does not completely prevent current transmission across the interface, it significantly hinders electron movement, thereby increasing the overall electrical contact resistance.

As depicted in Figure 4.36c, when a mixture of conductive and non-conductive particles, such as Product D and silica sand, is applied to the wheel-rail contact are, the mechanical action causes the mixture to crush and compact into a friction film. Although this fragment layer induces an indirect contact between the wheel and rail, the conductive fragments of Product D become distributed throughout the layer. Under continued mechanical loading, the contact area between these conductive fragments progressively increases, facilitating the formation of conductive micro-channels. These channels enable the transfer of electrons from the wheel to the rail, thereby allowing for partial electrical conductivity through the otherwise insulating friction film, and thus significantly reducing the electrical contact resistance at the interface. When all the particles present at the wheel-rail interface are conductive, their fragmentation results in the formation of a fragment layer that not only contributes to the repair of surface defects and interfacial microcracks on the wheel and rail but also facilitates electron transfer. In this scenario, the conductive fragment layer enables continuous and efficient electron flow from the wheel to the rail, ensuring effective electrical conductivity across the entire interface, as shown in Figure 4.36d.

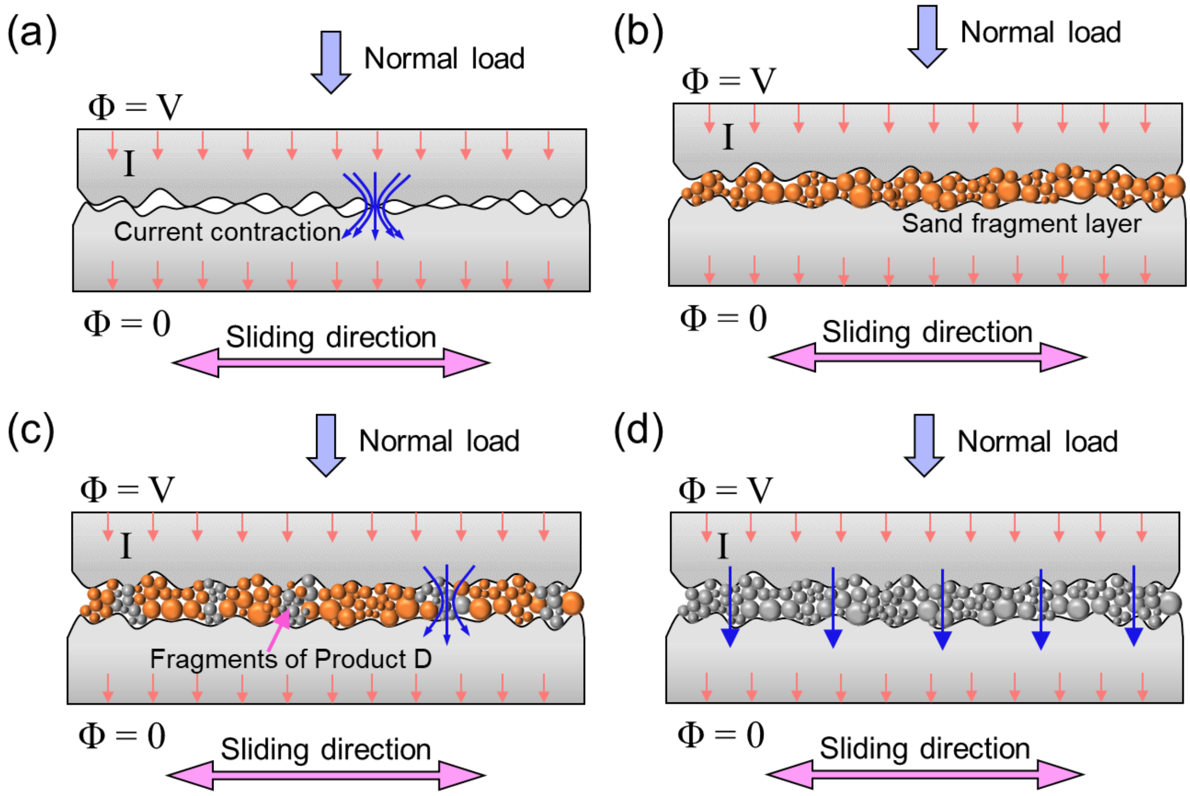

Figure 4.36. Schematic of the effect of the particulate systems on the current transfer mechanism at the interface between two metal objects: (a) no particles, (b) sand particles after crushing, (c) a mixture of Product D and sand particles after crushing, and (d) Product D particles after crushing (Orange and grey spheres represent sand fragments and Product D fragments, respectively).

When two metal surfaces are in contact, the asperities at the interface undergo shearing, leading to the formation of wear particles under the influence of normal loads and shear forces during parallel sliding (Liu et al., 2024, 2021; Wang et al., 2024). However, in this study, the application of conductive, non-conductive, or mixed particles resulted in their fragmentation, forming a fragment layer at the interface. This fragment layer acted as a lubricant, contributing to a stable wear phase between the contacting metal surfaces. Notably, the fragment layer plays a more significant role in governing the electrical conduction properties at the interface than the wear particles themselves. Furthermore, when a representative quantity of particles, i.e., 7.5 g/m, is applied to the metal interface — specifically within the wheel-rail contact area — the resulting current at the interface can reach levels of 5 A or higher (Skipper et al., 2023). Under these conditions, the current tends to concentrate in the asperities of the metal surfaces, where the electrical contact resistance generates significant Joule heating (Liu et al., 2021; Meng et al., 2024; Wang et al., 2024). This localised heating leads to a substantial temperature rise at these points, which may affect the electrical conduction properties of the interface. Consequently, it may need to consider the dynamic thermal equilibrium of the contact materials, an aspect that will be explored in greater detail in future work.

4.8 Conclusions

This chapter presented an electro-mechanical contact model to investigate the electrical response of a particulate system under mechanical loading conditions. The model was validated using analytical solutions for particle-to-particle and particle-to-wall contacts, and experimental data from a stainless steel particle chain and a particle bed test. The proposed model was applied in an example to study the effect of three different materials, each acting individually at the wheel-rail interface, on the electrical response of the system using HPT tests. Additionally, the effect of a mixture of conductive and non-conductive particles on the electrical conduction properties of the wheel-rail interface under mechanical loading was analysed through a combination of laboratory tests and numerical simulations. The influence of the electrical resistivity of conductive particles on interfacial resistance was also investigated.

For both particle-particle and particle-wall conduction, the electrical resistance decreases significantly as mechanical force begins to increase. With further increases in mechanical force, the decline in electrical resistance approaches a constant value. Alterations in the contact surfaces for both particle-to-particle and particle-to-wall contacts can directly impact the electrical resistance of the system.

In a metallic particle system, contact resistance is a far more significant factor than the intrinsic electrical resistance of the particles. This is supported by numerical calculations, which exhibit a trend similar to that predicted by elastic Hertz theory as the mechanical force increases.

Using the HPT test as an application example, the numerical calculations of electrical resistance fall within the range of experimental results. Two commercial conductive materials, Product B and Product D, demonstrate a substantial improvement in electrical conduction between the wheel and rail specimens compared to silica sand. Additionally, the electroactivity index indicates that larger-sized fragments play a more significant role in bulk electrical conduction.

When the percentage of Product D particles gradually increases, the electrical resistance at the interface between the piston and the base specimens decreases significantly with the increasing load. In addition, when the load is maintained at 577 kN, the resistance at the interface decreases as the ratio of Product D in the mixture increases. In particular, the interfacial resistance drops sharply from about 55 kΩ to 220 Ω when the percentage of Product D is raised to 5%.

The main phase of Product D and silica sand is the Al_2O_3 phase and the SiO_2 phase, respectively. For Product D particles, their fragments are interspersed in the fragmentation layer during compression and conductive micro-channels are established. The charging effect in the fragment layer diminishes as the Product D content increases, which means the accumulation of charge due to SiO_2 in the sand particles is gradually reduced.

When the same amount of Product B or Product D is mixed with sand particles, the smaller-sized Product B particles can participate more effectively. Their fragmentation allows for better penetration into the fragment layer, enhancing the formation of conductive micro-channels. Consequently, smaller-sized conductive particles may be more advantageous in reducing the interfacial resistance of wheel-rail interface in HPT system.

The electrical resistivity of the conductive material and its proportion in the mixture significantly impact the electrical resistance at the wheel-rail interface of the HPT system. If a low-resistivity conductive material is mixed with silica sand, only a small number of conductive particles is needed to reduce the electrical resistance of the HPT system to less than 10 Ω. Conversely, if the resistivity of the conductive material is higher, a significantly larger number of conductive particles is required to achieve the same reduction in electrical resistance.

Chapter 5 Effect of inherent anisotropy on electro-mechanical behaviour of particulate systems

5.1 Introduction

The inherent anisotropy of granular soils, defined as the initial structural arrangement of particles and pores, significantly influences the mechanical behaviour of these materials, such as liquefaction phenomenon, a state in which the effective stresses within the soil approaches zero (Seed and Lee, 1966; Tatsuoka et al., 1986). Numerous experimental studies have been conducted to explore the mechanical response of samples with varying degrees of inherent anisotropy, prepared under different loading conditions such as drained/undrained monotonic and undrained cyclic triaxial testing (Ishibashi and Capar, 2003; Ni et al., 2021; Sze and Yang, 2014; Tatsuoka et al., 1986). However, challenges persist in accurately quantifying inherent anisotropy and understanding its effect on mechanical response. Complementary to these experimental approaches, some studies have employed DEM to analyse the evolution of anisotropic degree as the stress state changes, focusing on the quantification of inherent anisotropy and induced anisotropy under different loading conditions (Morimoto et al., 2021; Otsubo et al., 2022; Wang and Wei, 2016; Wei et al., 2018; Wei and Wang, 2017).

On the other hand, the electrical properties of geomaterials have been utilised to monitor the evolution of their mechanical characteristics for decades (Niu et al., 2017; Seladji et al., 2010). For example, the bulk conductivity of sandy materials can serve as an indicator of compaction and shear behaviour within granular systems (Koch et al., 2012). Additionally, the electrical properties of granular materials offer potential applications for non-invasive monitoring of geotechnical phenomena such as slope stability, fault activity, and landslides (Mahardika et al., 2012; Niu et al., 2017). A range of experiments, particularly triaxial tests, have been conducted to analyse the evolution of stress-strain behaviour in samples, informed by electrical property data (Glover et al., 2000, 1996; Zhao et al., 2023). Among these studies, Glover et al. (2000) examined the relationship between bulk conductivity and the mechanical behaviour of saturated sandstones during triaxial tests. Their findings demonstrated that electrical measurements are particularly effective at detecting cracks formation and propagation, especially before rock failure. Recently, Zhao et al. (2023) conducted a series of triaxial shear tests to investigate the link between bulk resistivity and the mechanical damage evolution of soil-rock mixtures. Their results showed that electrical resistivity can effectively characterise the damage process of the soil-rock mixtures. In addition, some studies have investigated the relationship between mechanical response and electrical behaviour in granular systems under compressive conditions using DEM (Niu et al., 2017; Zhang et al., 2024). To the current knowledge of author, only a very limited number of studies have explored the effect of anisotropy on the electrical properties of granular materials in triaxial compression using DEM. Niu et al. (2017) investigated the relationship between bulk conductivity anisotropy and fabric anisotropy during triaxial shearing through DEM simulations. Their findings revealed a strong linear correlation between bulk conductivity and fabric anisotropy factors. Yet, inherent anisotropies can distinctly affect the electrical behaviour of particulate systems under loading conditions, but further studies in this area remain limited.

Drawing on the research by Otsubo et al. (2022), this study employs DEM to model samples with approximately identical void ratios and average coordination numbers, yet differing inherent anisotropies. The study investigates how inherent anisotropy influences the mechanical response and electrical behaviour of particulate system under drained monotonic compression for each sample. Moreover, this study proposes an alternative index that effectively evaluates the evolution of induced anisotropy and the mean contact area between particles, considering the combined effects of macroscopic mechanical response and electrical behaviour.

5.2 Sample Preparation and Test Method

To investigate how the inherent anisotropy of a particulate system affects its mechanical and electrical behaviour, this study follows the modelling approach described by Otsubo et al. (2022) for triaxial compression tests. Afterwards, the electro-mechanical contact model presented in Chapter 4 is applied to these three samples and the mechanical and electrical data are collected during drained monotonic loading.

5.2.1 Material Properties

In this study, the spherical particles were utilised to explore the fundamental impact of inherent anisotropy on the mechanical and electrical behaviour in the particulate system, while also eliminating the complexities associated with particle shape. The particle size distribution (PSD) ranges from 1.2 mm to 2.2 mm, with a median particle size (D_{50}) of 1.89 mm and a coefficient of uniformity (C_u) of 1.37, indicative of a uniformly graded sand. The material characteristics of these spherical particles align closely with typical silica sand properties, which can be found in Table 5.1. To model the interaction between particles, a simplified Hertz-Mindlin contact model was employed in the particulate system, allowing contact stiffness to be automatically adjusted based on the material properties and the load applied between two particles, as detailed by Morimoto et al. (2021). In order to conduct these DEM simulations, a modified version of LAMMPS (Large-scale Atomic/Molecular Massively Parallel Simulator) (Plimpton, 1995) was utilised. A time step of 4×10^{-7} s was used to execute simulations, ensuring compliance with the critical time step for the specified material, as suggested by Otsubo et al. (2017).

Table 5.1 Material parameters utilised in the DEM simulations.

Parameters	**Unit**	**Value**
Poisson's ratio (υ_m)	–	0.23
Specific gravity (G_s)	–	2.7
Young's modulus (E)	GPa	71.6
Shear modulus (G)	GPa	29.1
Electrical resistivity (ρ_e)	Ω m	5.56×10^6

5.2.2 Preparation Steps for Iso, Ver, and Hor Samples

The preparation method of the three samples used for the triaxial compression test followed the steps shown in Figure 5.1. Firstly, a random distribution of 30,000 spherical particles was generated within a cuboidal volume, ensuring that no particles were in contact. Periodic boundary conditions were applied in all three principal directions to maintain uniformity. Subsequently, three different initial compression protocols were employed to prepare the *Iso*, *Ver*, and *Hor* samples, respectively, all conducted under gravity-free conditions. The preparation steps for three samples were as follows:

- *Iso sample*: Isotropic compression was uniformly applied along the *x*, *y*, and *z* axes to achieve an isotropic effective stress, where $\sigma_x' = \sigma_y' = \sigma_z'$ = 100 kPa, corresponding to an initial isotropic effective stress p_0' = 100 kPa.

- *Ver sample*: Uniaxial compression was applied vertically along the *z*-axis to reach a stress of σ_z' = 1 kPa, while the incremental axial strains in the horizontal *x* and *y* directions were constrained, ensuring $\Delta\varepsilon_x = \Delta\varepsilon_y$ = 0, i.e., the horizontal strain during sample preparation $\Delta\varepsilon_h$ = 0.
- *Hor sample*: Horizontal compression was applied along the *x* and *y* axes to achieve a stress of $\sigma_x' = \sigma_y'$ = 1 kPa, with the vertical strain along the *z*-axis kept fixed at zero, i.e., $\Delta\varepsilon_z$ = 0, ensuring that the vertical strain ($\Delta\varepsilon_v$) = 0 during sample preparation.

Thirdly, the *Ver* and *Hor* samples underwent additional compression until the stress state in all principal directions reached $\sigma_x' = \sigma_y' = \sigma_z'$ = 100 kPa (i.e., p_0' = 100 kPa). During the sample preparation phase, a maximum strain rate of 0.2 s^{-1} was employed, gradually decreasing as the target stress level was approached, in accordance with the methodology outlined by Otsubo (2016). Throughout the above process, an inter-particle friction coefficient (μ_{pre}) of approximately 0.15 was used as suggested by Otsubo et al. (2022). This process produced three loose samples, i.e., *Iso_L*, *Hor_L*, and *Ver_L*. In addition, the initial void ratios (e_0 = 0.643 – 0.645) and the initial mean coordination number (i.e., the number of contact points per particle, CN_0 = 4.68 – 4.69) for three samples were very similar using this preparation method, with the corresponding expressions as follows:

$$e = \frac{V_v}{V_p} \tag{5.1}$$

$$CN = \frac{2N_c}{N_p} \tag{5.2}$$

where V_v and V_p are defined as the volume of voids and particles, respectively; while N_c and N_p are the numbers of the contacts and the particles within the particulate system, respectively. Figure 5.2 shows an example of an *Iso_L* sample at p_0' = 100 kPa, where the colour of each particle indicates its diameter.

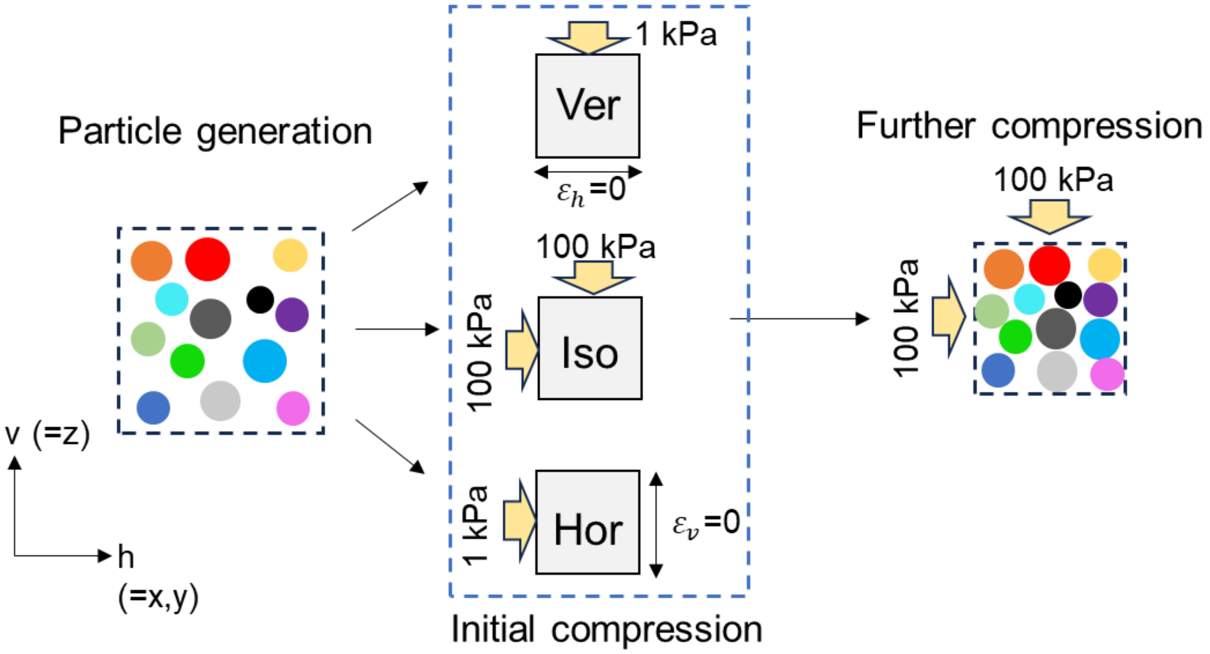

Figure 5.1. The steps used in this study to prepare the three samples.

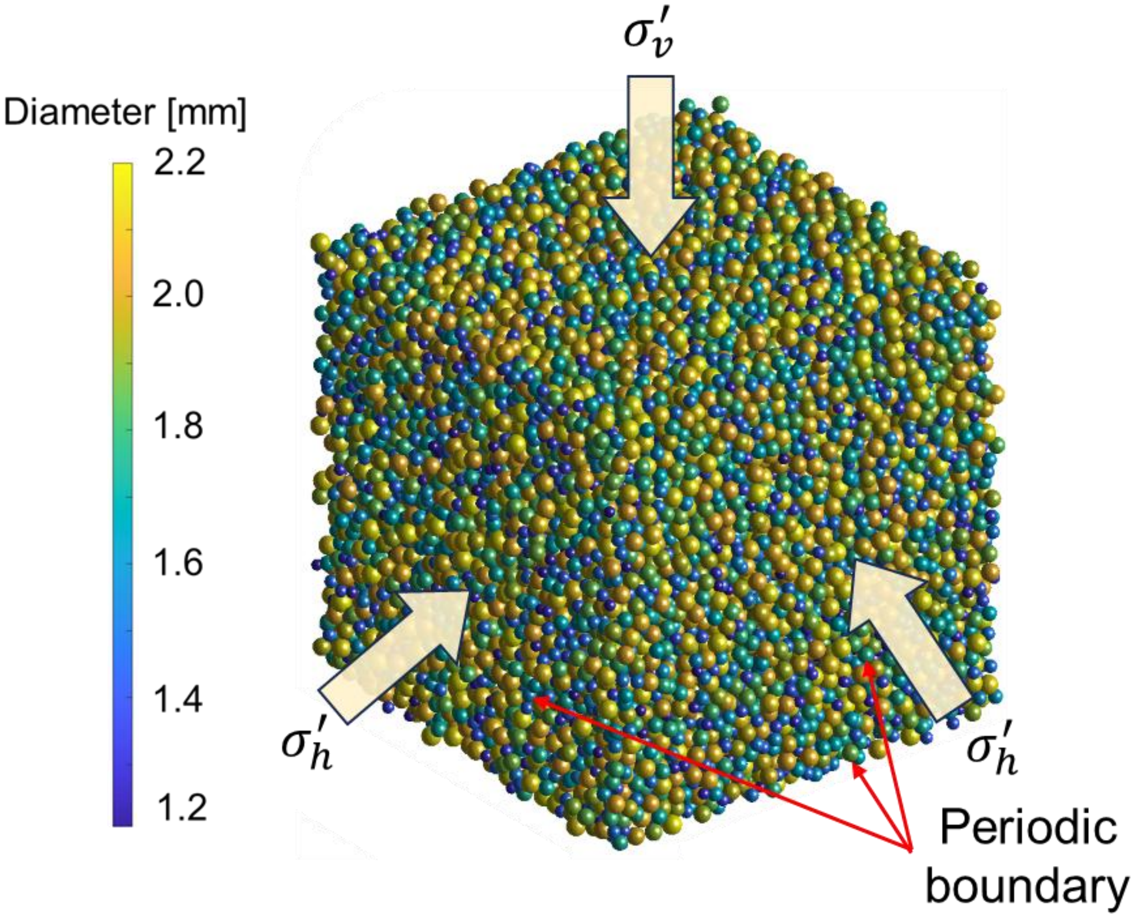

Figure 5.2. Representative DEM sample (*Iso-L*) at p_0' = 100 kPa with periodic boundaries (colour bar shows the range of particle diameter within the sample).

5.2.3 Quantifying Inherent Anisotropy for Samples

To describe the differences in packing properties of three samples, *Iso_L*, *Hor_L*, and *Ver_L*, the second-order fabric tensor Φ_{ij} was quantified according to the contact normal orientations (Satake, 1982; Yimsiri and Soga, 2010) as:

$$\Phi_{ij} = \frac{1}{N_c} \sum_{Nc} n_i n_j \tag{5.3}$$

where N_c represents the total number of contact points, and n_i and n_j denote the contact normals in the *i*- and *j*-directions, respectively ($i, j = x, y, z$). In addition, the principal components of the fabric tensor (Φ_{xx}, Φ_{yy}, and Φ_{zz}) can be used to quantify the vertical and horizontal components, which can be expressed as follows:

$$\Phi_v = \Phi_{zz} \tag{5.4}$$

$$\Phi_h = \frac{\left(\Phi_{xx} + \Phi_{yy}\right)}{2} \tag{5.5}$$

$$\Phi_v + 2\Phi_h = 1 \tag{5.6}$$

where Φ_v and Φ_h are defined as vertical and horizontal component of fabric tensor, respectively. In accordance with the method presented by Yimsiri and Soga (2010), the anisotropic degree (a) is employed to quantify a fabric tensor as a single scalar assuming the cross-anisotropic condition:

$$\Phi_{ij} = \begin{pmatrix} \frac{3a-5}{5(a-3)} & 0 & 0 \\ 0 & \frac{3a-5}{5(a-3)} & 0 \\ 0 & 0 & \frac{-(5+a)}{5(a-3)} \end{pmatrix} \tag{5.7}$$

The value of anisotropic degree for the three samples utilised in this study are calculated using Φ_{zz}, under the assumption that Φ_{xx} and Φ_{yy} are equal, as follows:

$$a = \frac{5\left(3\Phi_v - 1\right)}{5\Phi_v + 1} \tag{5.8}$$

Figure 5.3 illustrates the orientations of the contact normal vectors for the three samples, along with their corresponding initial anisotropic degree (a_0). In the *Iso_L* sample, the contact orientations are uniformly distributed in all directions, indicating a minimal degree of anisotropy. A positive value of a (>0) indicates a higher concentration of contacts in the vertical direction, as observed in the *Ver_L* sample, whereas a negative value of a (<0) indicates more contacts in the horizontal plane, as seen in the *Hor_L* sample. When compared to previous studies, the anisotropy levels of the samples in this study align closely with those reported in the literature. For instance, Yimsiri and Soga (2010) demonstrated that their prepared loose samples exhibited a_0 values of -0.04, 0.01, and 0.06, respectively, where samples with positive a_0 value are referring to experimental preparation methods such as dry deposition (DD) or air pluviation (AP). Also, Otsubo et al. (2022) prepared a sample with the a_0 value of 0.083 by the AP method using the same material as in this study. By comparing these values with the a_0 derived from the DEM models utilised in this study, it is evident that the inherent anisotropy of the *Hor-L* and *Ver-L* samples falls within a comparable and reasonable range, despite differences in preparation methods. The findings of Sze and Yang (2014) suggest that the moist tamping (MT) method, a sample preparation technique where sand is mixed with a small amount of water to ensure uniform moisture distribution before being compacted in layers, creates a more isotropic fabric. This aligns with the observation that the *Iso_L* sample in the current study exhibit minimal anisotropy. In addition, regarding the *Hor_L* sample, despite its inherent anisotropy, this study can still provide important context of the results and valuable insights into some elaborate experiments that systematically control soil fabrics (e.g., Oda, 1972; Oda et al., 2001). This comparison demonstrates the reliability and validity of the methodology of the current study and that it is consistent with and complementary to established research in the field.

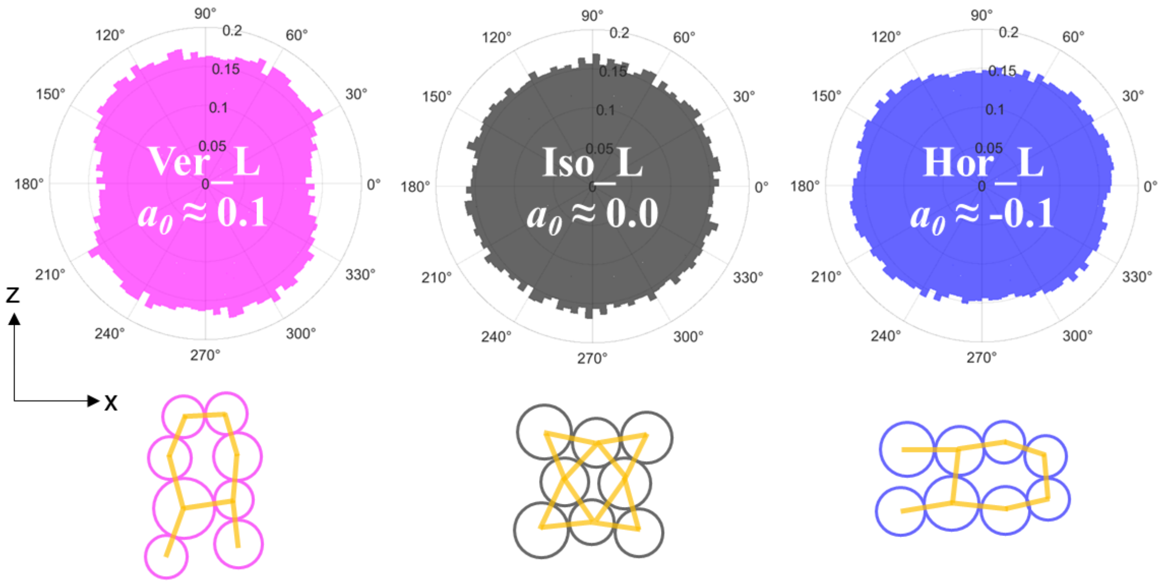

A larger a (>0) means more contact in vertical direction

a ≈ 0
Isotropic

A smaller a (<0) means more contact in horizontal direction

Figure 5.3. Orientation of contact normal vectors and schematic representation of the degree of anisotropy (a) for the *Ver-L*, *Iso-L*, and *Hor-L* samples.

5.2.4 Circuit Setup and Assumptions for Samples

To examine the electrical behaviour within the particulate system during the triaxial compression test, the electro-mechanical contact model presented in Chapter 4 is employed. Given that the DEM model incorporates periodic boundary conditions rather than rigid walls, this study focuses solely on electrical conduction through particle-to-particle contacts, excluding any electrical transfer involving particle-to-wall contacts. In addition, due to the symmetrical nature of the DEM model used in triaxial testing, it is assumed that the upper and lower boundaries are electrically conductive, while the sides of the model are treated as electrically insulated, as discussed by Moraru et al. (2011). As illustrated in Figure 5.4, a constant potential of 0.5 volts is applied to the upper boundary, with the lower boundary grounded (set to zero electric potential), effectively establishing an electrical circuit within the DEM model. In this configuration, DC current will flow from the particles at the upper boundary, through the particle system, and ultimately reach the particles at the grounded lower boundary. Moreover, while the choice of a 0.5-volt potential is originally intended to simulate the performance of low voltage DC track circuits, particularly those performing poorly in UK railway operations (Skipper et al., 2023), this value serves as a practical reference point for exploring the interplay between mechanical and electrical behaviours in granular materials. By employing this voltage level, this study not only aims to reflect specific conditions relevant to railway operations, also provides a controlled environment to investigate how inherent anisotropy affects the electrical response of the particulate system during mechanical loading. This approach enables a broader understanding of the principles governing electrical conduction in stressed granular materials, thereby bridging the gap between geotechnical applications and the study of electrical properties in particulate systems.

The particulate system can be likened to a circuit comprising multiple resistors, drawing on the heat transfer network model (Feng et al., 2008; Rojek et al., 2022), the principles of circuit analysis (Birkholz et al., 2019), and the nodal analysis method (Ho et al., 1975; Wing, 1972). In this analogy, each particle is considered as a node, and the path between the centres of two adjacent particles is viewed as a conductive path with an associated circuit resistance. This resistance includes both the resistance of the material constituting the particles and the contact resistance formed at the overlap region between the two particles. Additionally, the assumptions were made that the DEM simulations were conducted at room temperature and that the particle surfaces were smooth and free from contaminant layers, thereby removing the influence of these complicating factors on the simulation results.

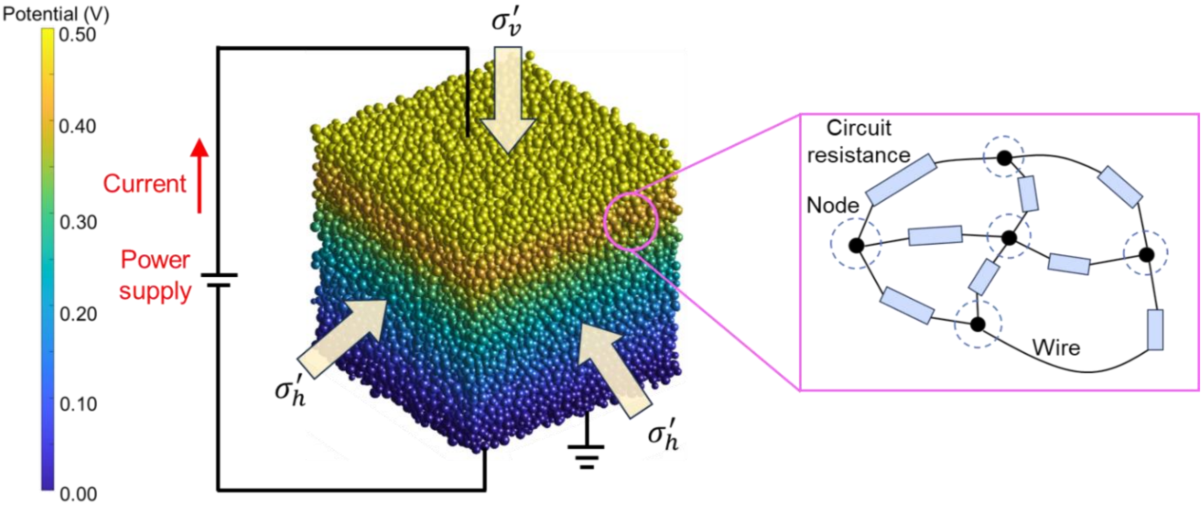

Figure 5.4. Electric potential distribution of *Iso-L* sample at the initial stage with a schematic representation of local circuit branches between particles (colour bar shows the electric potential value of particles).

5.2.5 Drained Monotonic Loading

Drained monotonic loading (triaxial compression) was applied vertically to the three samples while maintaining a constant lateral effective stress. The strain-controlled loading was implemented by displacing the boundaries at a rate of 0.0002 m/s, resulting in an approximate strain rate of 0.0039 [s^{-1}]. This strain rate ensures compliance with the quasi-static flow condition for the material properties under a confining pressure of p_0' = 100 kPa (Lopera Perez et al., 2016). A local damping coefficient of 0.2, as utilised by Morimoto et al. (2021), was applied during loading. The inter-particle friction coefficient (μ_{pre}) was increased to 0.4 (μ_{load}) for all simulations during the loading phase. The deviator stress ratio (*DSR*) during loading is defined as the ratio of the deviator stress (*q*) to the mean effective stress (*p'*), and can be expressed as follows:

$$DSR = \frac{q}{p'} = \frac{\sigma_v' - \sigma_h'}{\left[\sigma_v' + 2\sigma_h'\right]/3} \tag{5.9}$$

where σ_v' and σ_h' are defined as principal stresses in the vertical and horizontal directions, respectively. In this study, $q > 0$ is consider for compression conditions. During drained monotonic loading, the volumetric strain (ε_{vol}) was calculated from the change in sample bulk volume, where $\varepsilon_{vol} > 0$ for dilation and $\varepsilon_{vol} < 0$ for contraction. Table 5.2 summarises the properties of the three samples, *Iso_L*, *Ver_L*, and *Hor_L*, at the initial compression stage (i.e., p_0' = 100 kPa).

Table 5.2 Properties of *Iso_L*, *Ver_L*, and *Hor_L* samples at the initial compression stage

Sample	e_0	CN_0	Φ_{v0}	Φ_{h0}	$\Phi_{v0} - \Phi_{h0}$	Φ_{v0}/Φ_{h0}	a_0
Iso_L	0.644	4.69	0.333	0.333	0.000	0.999	-0.002
Ver_L	0.643	4.68	0.351	0.324	0.027	1.083	0.097
Hor_L	0.645	4.69	0.316	0.342	-0.026	0.926	-0.098

5.3 Mechanical Responses in Drained Monotonic Loading

In this sub-chapter, the macro-mechanical responses of three samples during drained monotonic loading (triaxial compression) was investigated. After that, the evolution of the packing properties of the particulate system, such as void ratio (*e*), mean coordination number (*CN*), and mean contact area (*A*) between particles, was analysed along with drained monotonic loading. Finally, the change in distribution of contact forces within the particulate system during drained monotonic loading was visualised.

5.3.1 Macroscopic Response of Three Samples

Monotonic compression up to an axial strain (ε_a) of 45% was applied to each of the three samples: *Iso_L*, *Ver_L*, and *Hor_L*. Figures 5.5a and 5.5b illustrate the overall variation in the DSR (i.e., *q*/*p'*) for each sample, highlighting the changes occurring within the small-strain range at the initial loading phase. The *Ver_L* sample (a_0 = 0.097) exhibits a rapid increase in *q*/*p'* during compression, indicating a strong initial response. In contrast, the *Hor_L* sample with a negative value of a_0 (−0.098) demonstrates the slowest rate of increase in *q*/*p'*, reflecting a more gradual compressive response. The *Iso_L* sample (a_0 = − 0.002) shows an intermediate response between the two extremes. While their peak *q*/*p'* values differ significantly, the residual *q*/*p'* values of all three samples converge and appear nearly identical under sustained mechanical loading. In addition, Figures 5.5c and 5.5d illustrate the changes in volumetric strain (ε_{vol}) for the three samples during monotonic loading, where negative values (<0) indicate contraction and positive values (>0) indicate dilation. The *Ver_L* sample exhibits more pronounced dilative behaviour during compression. In contrast, the *Hor_L* sample initially shows a tendency to contract, with a transition from contraction to dilation occurring only after the axial strain exceeds approximately 13%. This behaviour is likely due to the rearrangement of particles under mechanical loading, which reduces the void ratio and initially promotes contraction. The observed overall responses in both deviator stress ratio and volumetric strain during drained monotonic compression are consistent with the characterisations provided by Yimsiri and Soga (2010).

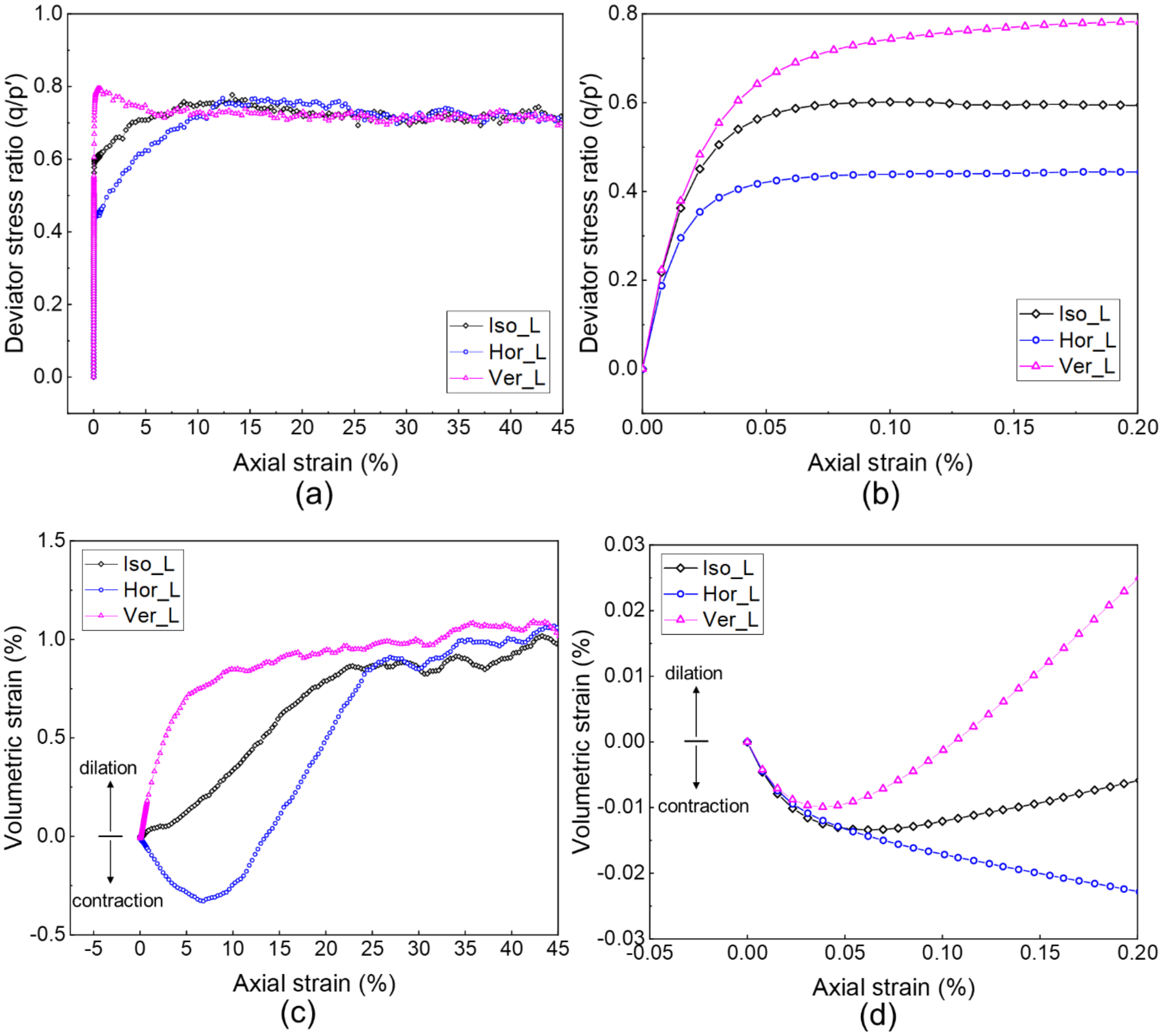

Figure 5.5 Drained monotonic responses of three samples: (a) and (b) deviator stress ratio (*q*/*p'*), (c) and (d) volumetric strain (ε_{vol}) against axial strain. ((a) and (c) are overall response, while (b) and (d) are response at small-strain range).

5.3.2 *Microstructural Responses of Three Samples during Monotonic Compression*

The macroscopic mechanical responses of three samples during monotonic compression was discussed in the previous section. In this section, the *Iso_L*, *Ver_L*, and *Hor_L* samples are utilised to investigate their contact-scale microstructural responses during monotonic loading, with an emphasis on the evolution of packing properties, i.e., *CN*, *e*, and *A*. The results are presented in Figure 5.6. As be seen from Figures 5.6a and 5.6b, the *CN* values of the *Hor_L* sample drop quickly at the small-strain range, while the *CN* values of the *Ver_L* sample show the smallest decrease at the initial monotonic compression. These initial changes (Figure 5.6b) are closely related to the changes in deviator stress ratio (Figure 5.5b), i.e., the lower the *CN* value, the smaller the *q*/*p'* value for a given axial strain.

Figures 5.6c and 5.6d depict the evolution of the void ratio (*e*) for the three samples during monotonic compression. At the beginning of monotonic loading, the *e* of the *Hor_L* sample decreases significantly, indicating compaction. This is consistent with the contraction observed in the volumetric strain in Figures 5.5c and 5.5d. The decrease in void ratio indicates that the particles are rearranging and coming closer together, thus reducing the voids between the particles. This initial contraction phase can be attributed to the inherent anisotropy of the *Hor_L* sample, where the particles are initially more horizontally aligned and must be realigned to accommodate vertical loading. As the axial strain increases to approximately 7%, the void ratio of the *Hor_L* sample begins to increase slightly. Once the axial strain reaches around 13%, the void ratio starts to increase sharply, signifying a transition from the contraction phase to the dilation phase. This transition coincides with the point where the sample begins to exhibit dilative behaviour, as shown in Figure 5.5c. In contrast, the void ratio of the *Ver_L* sample increases throughout the monotonic compression process, especially during the 0% to 5% axial strain range. This indicates a consistent dilative response without a notable contraction phase. The void ratio of the *Iso_L* sample does not display a pronounced increasing or decreasing trend in the initial stage of loading; instead, it increases gradually with the axial strain until reaching a relatively stable state. Overall, the *Ver_L* sample, with its more vertically aligned contacts, underwent less particle rearrangement and maintained a more compact structure. Meanwhile, the *Hor_L* sample, with its primarily horizontal alignment, allowed for a greater degree of particle rearrangement and void reduction before ultimately transitioning to a dilative state.

Figures 5.6e and 5.6f illustrate the evolution of the mean contact area (*A*) for the three samples during monotonic loading, a critical parameter for understanding the force transmission capabilities within the particulate system. At the initial stage of loading, all three samples exhibit an increase in the mean contact area. This increase is most pronounced in the *Ver_L* sample, reflecting a rapid establishment of stronger contacts as particles align and adjust to the applied vertical stress. The substantial increase in contact area for the *Ver_L* sample suggests that the greater contact forces developing between particles. For the *Hor_L* sample, the increase in mean contact area is relatively significant within the small-strain range but diminishes as axial strain continues to rise. This reduction in the rate of increase may be attributed to the loss of stable contacts due to particle rearrangement during the transition from contraction to dilation. As the axial strain increases further, reaching approximately 15%, the value of A for the *Hor_L* sample becomes similar to those of the other two samples. The increase in the mean contact area for the *Iso_L* sample is intermediate between the other two, reflecting a more moderate response. Throughout the monotonic loading process, the *Ver_L* sample maintains a relatively high mean contact area, indicating its ability to sustain contact forces more effectively under vertical loading conditions. The evolution of the mean contact area is directly linked to the mechanical behaviour observed at the macroscopic level. For the *Ver_L* sample, the consistently high mean contact area supports the higher deviator stress ratio observed in Figure 5.5a, as stronger contacts facilitate more efficient load transfer. In contrast, the *Hor_L* sample, which shows the smallest increase in mean contact area, corresponds with lower deviator stress ratio and a shift to a dilative state, as shown in Figure 5.5a and 5.5c, respectively.

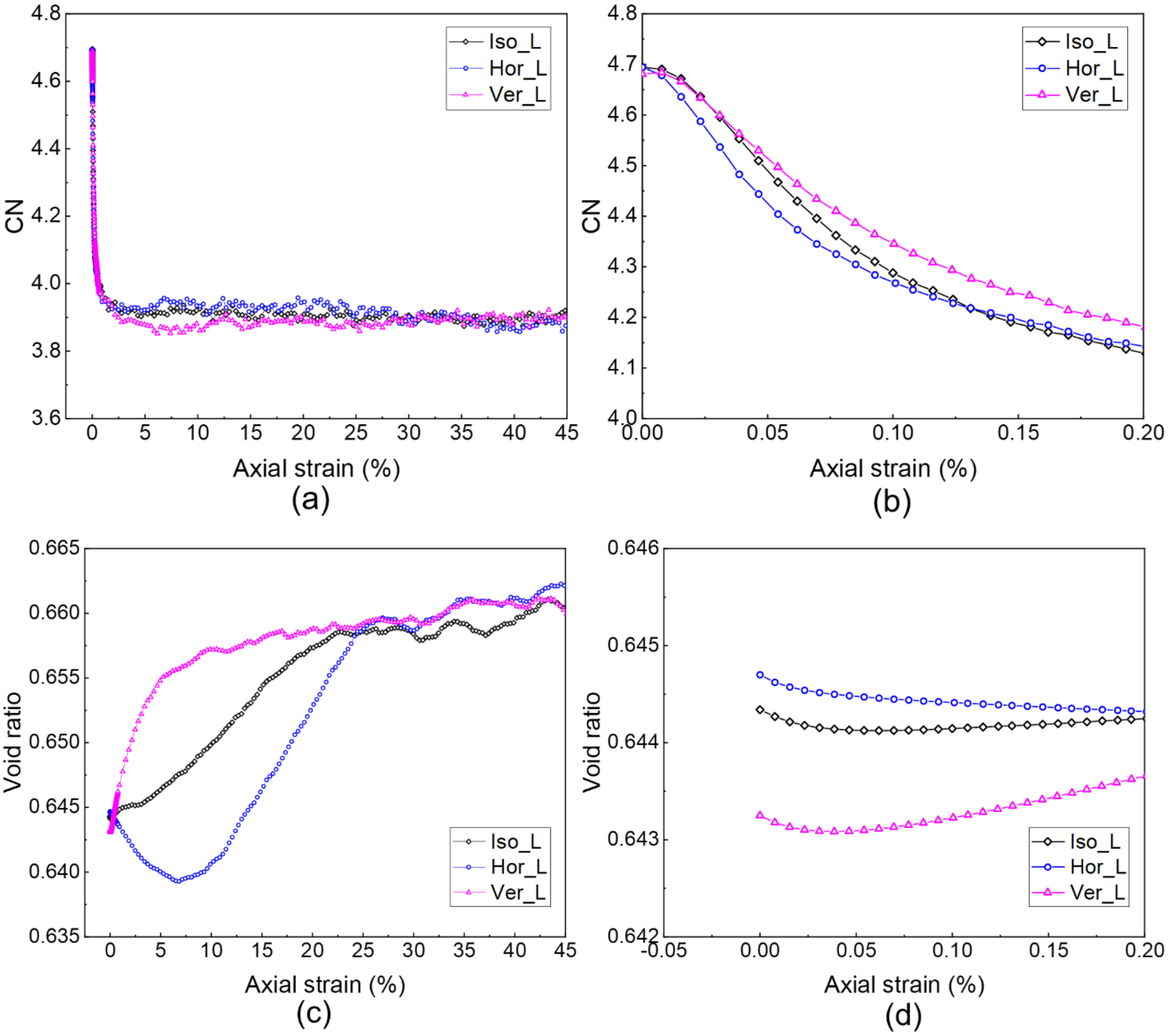

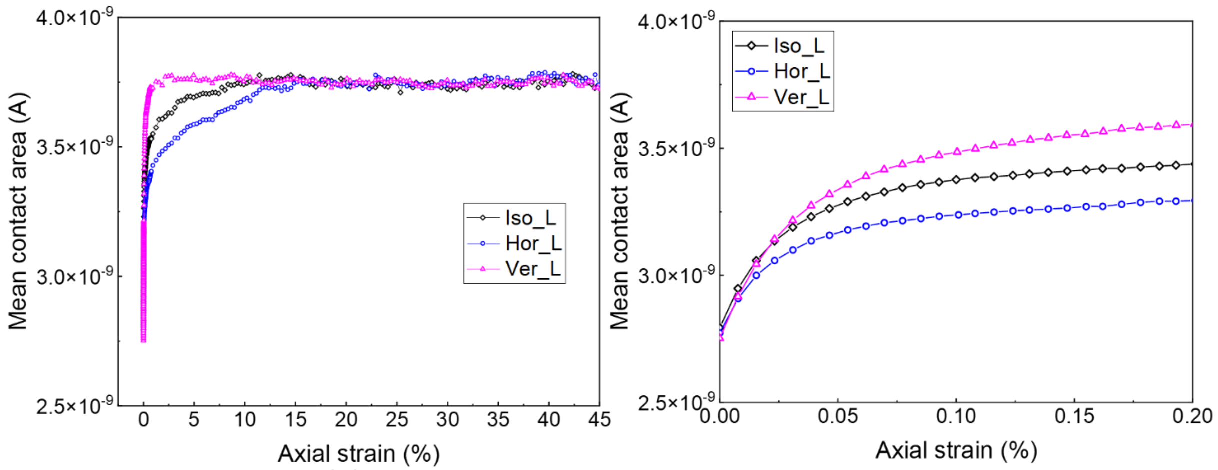

(e) (f)

Figure 5.6 Responses of the packing properties of three samples during drained monotonic compression: (a) and (b) mean coordination number (*CN*), (c) and (d) void ratio (*e*), and (e) and (f) mean contact area (*A*) against axial strain. ((a), (c), and (e) are overall response, while (b), (d), and (f) are response at small-strain range).

5.3.3 Change in Distribution of Contact Forces

The macro-mechanical responses and the evolution of the microstructure during drained monotonic loading for *Iso_L*, *Ver_L*, and *Hor_L* samples have been analysed in the above sections. It can be found that the mechanical behaviour of *Hor_L* sample is more sensitive to the monotonic compression process compared to the other two samples, particularly within the phase of axial strain from 0% to 13%. In this section, to visualise the development of stress transfer and contact forces, four stages in the axial strain from 0% ~ 13% during drained monotonic compression in the *Hor_L* sample were selected and compared in Figure 5.7.

It can be observed that during the initial stage of compression, the distribution of contact forces within the sample exhibits a slight bias towards the horizontal direction. As the axial strain increases to 1%, the preferred orientation of the contact forces begins to align more closely with the vertical direction, with the anisotropic degree (*a*) reaches 0.102. This indicates that the particles are undergoing a rearrangement in response to the applied vertical stress, thereby altering the loading characteristics that are used to assess both the microstructural properties (Figure 5.6) of the sample and the volumetric strain at the macroscopic level (Figure 5.5c). When the axial strain is increased to 5%, the contacts between particles become primarily vertical, and the value of *a* further increases to 0.243. Despite this increased vertical alignment, the void ratio of the sample continues to decrease (Figure 5.6c), signifying ongoing contraction.

Meanwhile, the mean contact area between particles continues to increase, suggesting that the system has not yet reached a stable state and is still undergoing compaction and structural adjustments. At an axial strain of 11%, vertical contact forces dominate even more strongly, with the value of *a* rising to 0.323. At this stage, the void ratio begins to increase (Figure 5.6c), indicating that the sample may transition from a contracting phase to a dilation phase if vertical stress continues to apply, as shown in Figure 5.5c. This shift suggests that the internal structure of sample has reached a point where the accumulation of vertical forces induces dilation, reflecting a change in the overall mechanical behaviour of the material.

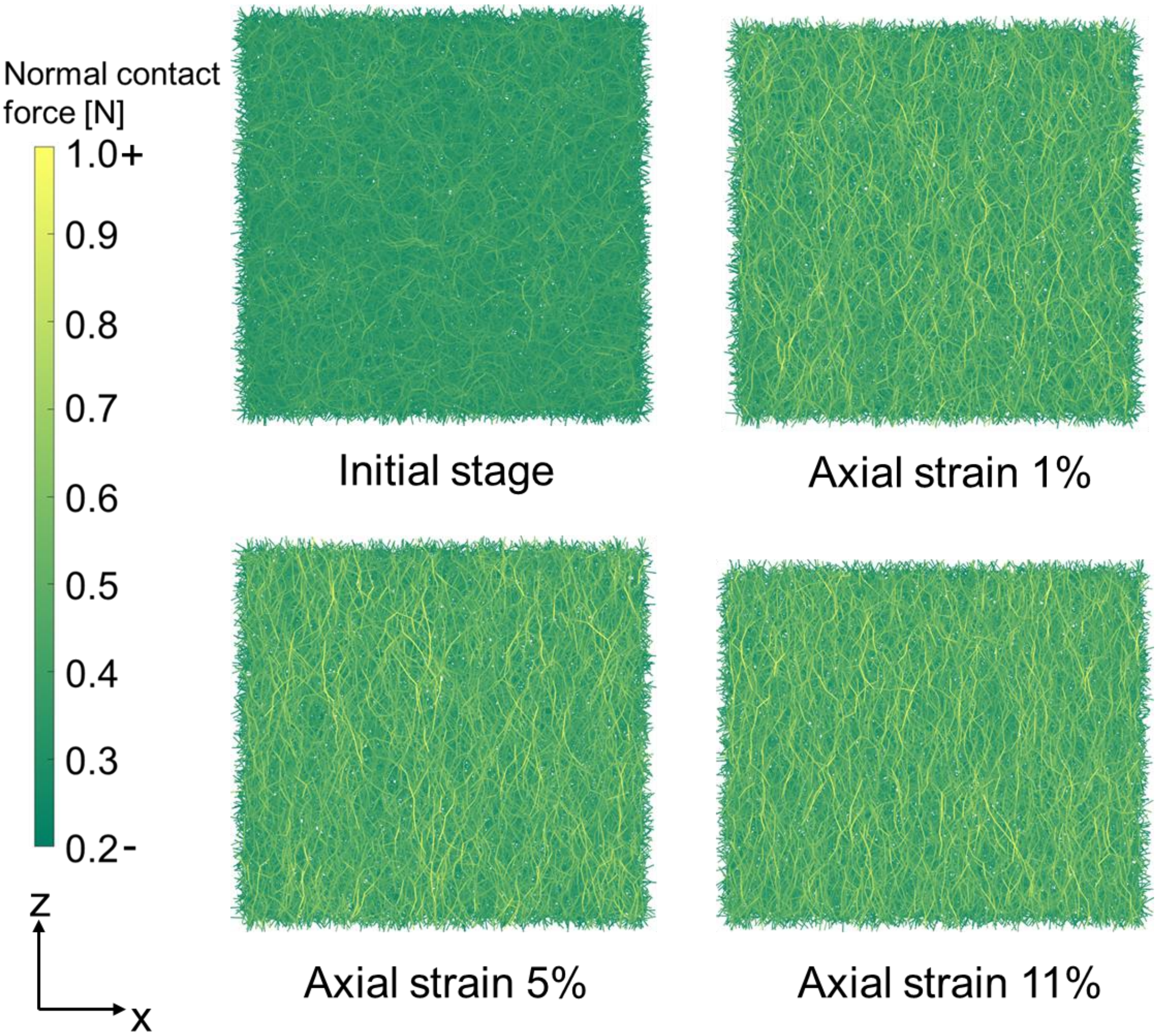

Figure 5.7 Illustration of changes in the distribution of normal contact force for *Hor-L* sample during drained monotonic compression.

5.4 Electrical Behaviour under Drained Monotonic Loading

In this sub-chapter, the electrical behaviour of three samples during drained monotonic compression was investigated. The link between the macro-mechanical responses and the electrical behaviour was assessed by quantifying the bulk resistance for three samples. Afterwards, the relationship between the microstructural responses and the electrical behaviour is analysed and the effect of packing properties at the contact-scale, such as void ratio (e), mean coordination number (CN), and mean contact area (A), on the bulk resistance of the three samples was studied. In addition, the distribution of current intensity in the orientation of the contact normal vectors was visualised for axial strain from 0% to 11%.

5.4.1 Change in Bulk Resistance under Macro-Mechanical Behaviour

Figures 5.8a and 5.8b show the overall variation of bulk resistances for *Iso_L*, *Ver_L* and *Hor_L* samples up to 45% of axial strain as well as the variation in small-strain range, respectively. It can be observed that the bulk resistances of the three samples exhibit significant differences in the range of 0% ~ 11% of axial strain. *Hor_L* sample shows the largest decrease in bulk resistance at this stage, while *Ver_L* sample shows the smallest decrease. *Iso_L* sample shows a decrease in bulk resistance that is in between the other two samples. Afterwards, the bulk resistances of the three samples tend to coincide as the monotonic compression continues.

At the small-strain stage, the *Ver_L* sample shows a significant decrease in bulk resistance, as shown in Figure 5.8b. This sharp decrease is consistent with the rapid increase in the deviatoric stress ratio (Figure 5.5b) and the average contact area (Figure 5.6f), indicating that the particle contact points are more vertically aligned with vertical loading and the contact area between the particles gradually increases, which is more conducive to the transfer of electrons within the conductive paths. In addition, the decrease in bulk resistance is further enhanced by the initial contraction observed in the volumetric strain, as shown in Figure 5.5d, which reduces the voids between particles, thereby compressing the contact points and altering the conductive network. For the *Hor_L* sample, the normal contact vectors during the initial loading phase are mainly horizontal and less resistant to vertical loading. At the small-strain range, the vertical loading leads to a redistribution of forces, weakening the horizontal force chain and reducing the bulk resistance. The volumetric strain data suggests that the initial contraction phase leads to a decrease in bulk resistance. However, as the particle contacts become less stable, they are more prone to rearrangement, which reduces the effectiveness of the conductive paths and leads to a renewed increase in bulk resistance, as shown in Figure 5.8d.

As the axial strain exceeds approximately 11%, the *Hor_L* sample shows a further decline in bulk resistance, which is closely associated with the sample transitioning from contraction to dilation (Figure 5.5c). It can be seen from Figure 5.8c that the deviator stress ratio stabilises at this point, suggesting a balance between the formation and destruction of contact points under continued loading. As the monotonic compression progresses towards 45% axial strain, the bulk resistances of all three samples converge. This convergence suggests that long-term application of axial strain leads to similar microstructures as well as restructuring of the conductive pathways in all samples, despite initial fabric and anisotropic differences.

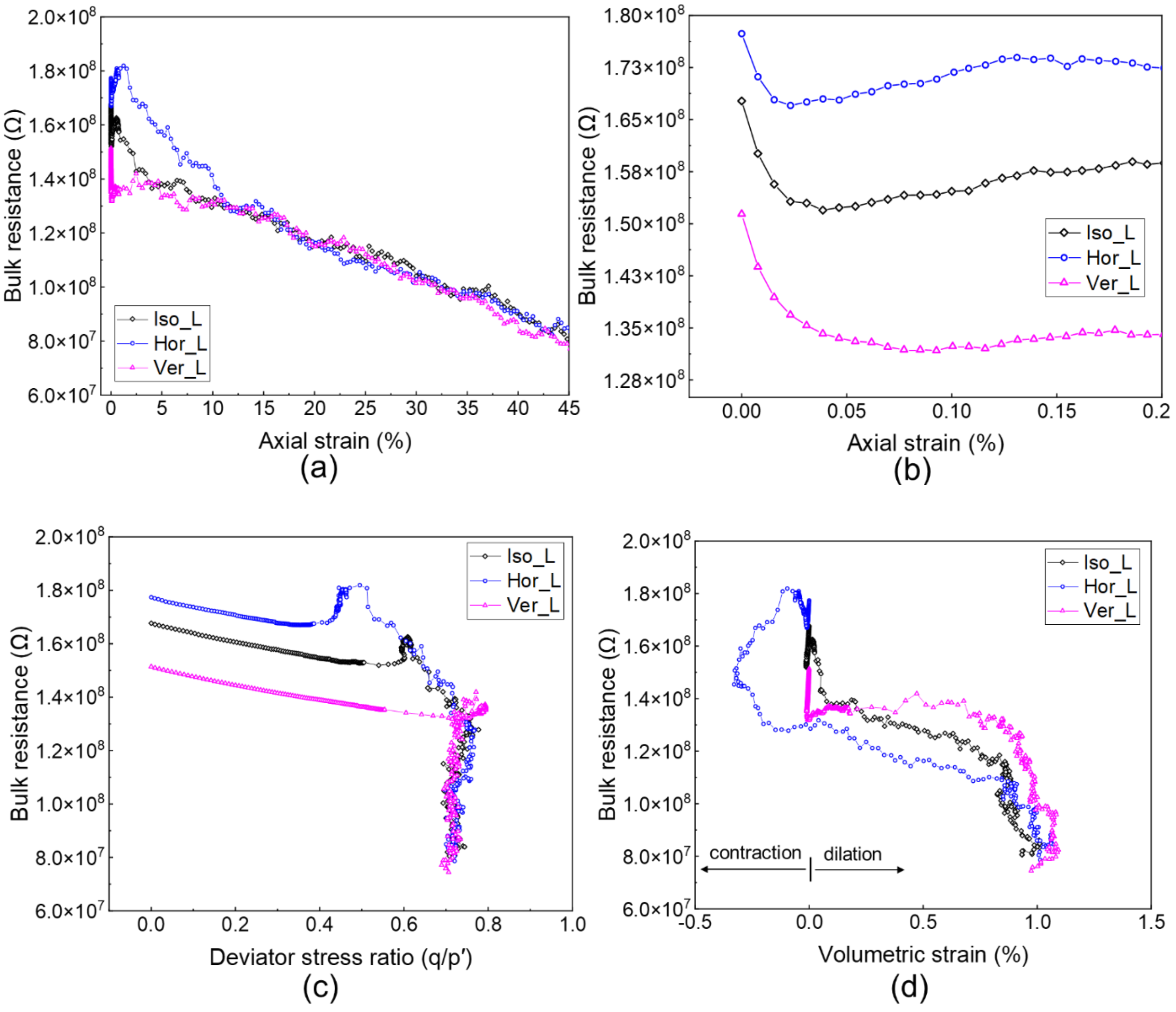

Figure 5.8 Electrical behaviour during drained monotonic compression for three samples: (a) and (b) axial strain (ε_a), (c) deviator stress ratio (q/p') and (d) volumetric strain (ε_{vol}) against bulk resistance. ((a) is overall response and (b) is response at small-strain range).

5.4.2 Relationship between Microstructural Responses and Bulk Resistance

Figure 5.9a presents the relationship between the mean coordination number (*CN*) and bulk resistance during monotonic compression for the three samples. In the initial small-strain range, the *CN* of the *Hor_L* sample decreases from 4.7 to around 4.5, representing the most pronounced reduction among the three samples. This significant decrease reflects a rapid loss of contacts due to particle rearrangement under vertical loading, resulting in fewer effective conductive paths and a slower reduction in bulk resistance. In contrast, the *Ver_L* and *Iso_L* samples exhibit a more gradual decrease in *CN* in the initial small-strain range, indicating a greater number of vertical contacts and less extensive particle rearrangement when subjected to vertical stress compared to the *Hor_L* sample. As shown in Figure 5.9b, the void ratio (*e*) of the *Ver_L* and *Iso_L* samples increase during the initial compression phase, indicating dilative behaviour. Despite this, the mean contact area (*A*) between particles within these two samples also increases at this stage (Figure 5.9c), which enhances contact between particles and allows for more efficient electron transfer, thereby reducing bulk resistance. It can also be observed that the bulk resistance of all three samples increases to some extent after an initial decrease, with a particularly notable rise in the *Hor_L* sample. This suggests that particle contacts within all three samples are not yet stabilised at this stage, and their inter-particle arrangements continue to be influenced by the vertical stress. When the axial strain reaches 11%, the *CN* and *A* for all three samples become similar (Figures 5.6a and 5.6e), with the tendency of dilative behaviour (Figure 5.6c). Meanwhile, the bulk resistance of the three samples converges, reflecting a similar structural state under the applied load.

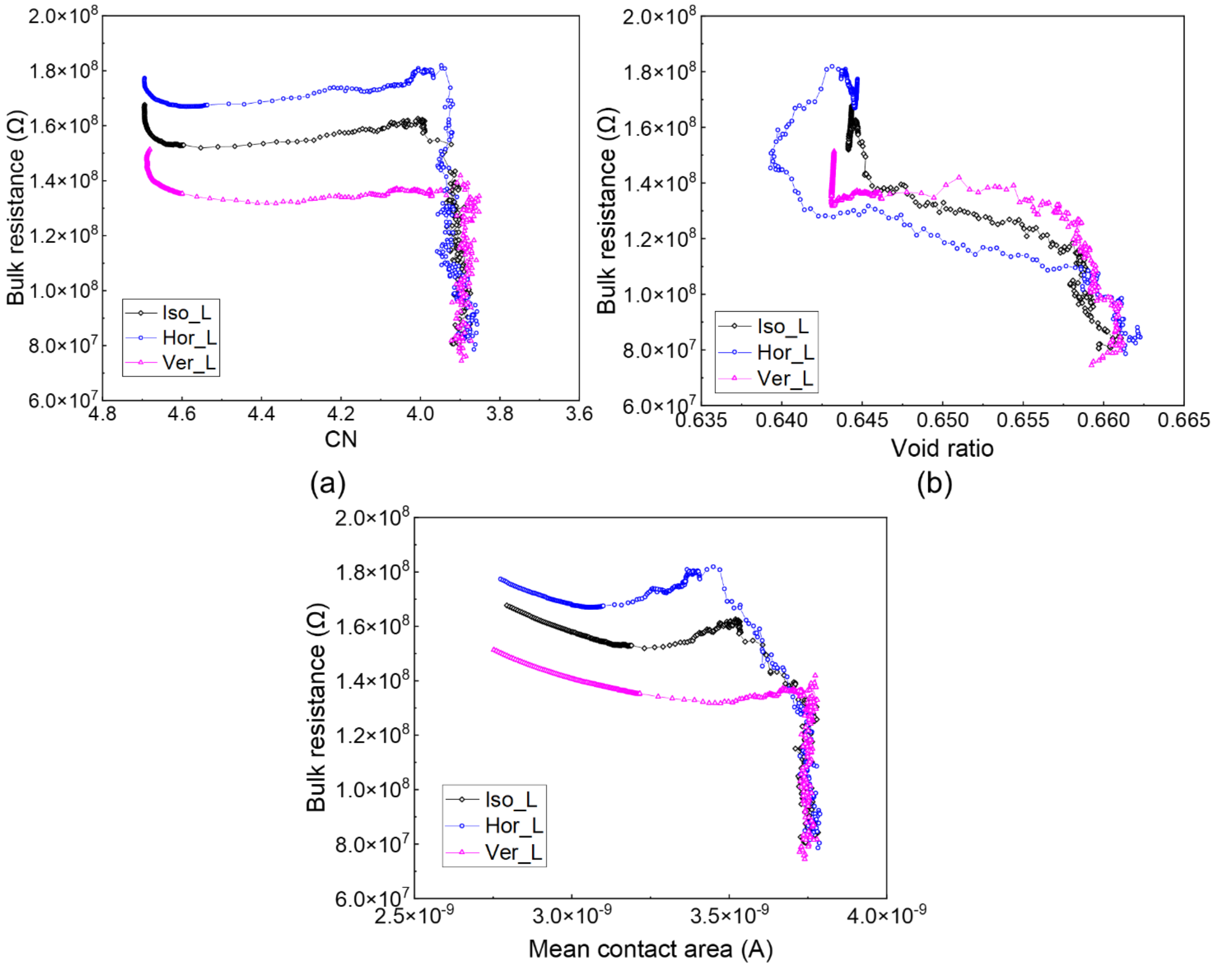

(a) (b)

(c)

Figure 5.9 Effects of packing properties on bulk resistance during drained monotonic loading: (a) mean coordination number (*CN*), (b) void ratio (*e*), and (c) mean contact area (*A*).

5.4.3 Evolution Magnitude of Current Intensity Acting on Orientations of Contact Normal Vectors

As the electrical behaviour of the three samples showed significant differences in the axial strain increase from 0% to 11%, therefore the magnitude of the current intensity acting in the orientation of the contact normal vectors was visualised for further analysis, as shown in Figure 5.10. In the initial stage, as depicted in Figure 5.10a, the maximum current is observed in the 90° direction, indicating that electrons mainly flow through vertically oriented conductive paths formed by particle contacts. In contrast, due to the boundary conditions of circuit imposed, electrons do not easily traverse horizontally oriented conductive paths composed of particles, resulting in a relatively low current. As the axial strain increases to 1%, as shown in Figures 5.10b to 5.10e, the current begins to flow more preferentially in a specific direction, particularly between 45° and 135°. This suggests the formation of more conductive paths that align with the direction of applied stress. With further increases in axial strain up to 11%, as illustrated in Figures 5.10f to 5.10j, the distribution of contact normal vectors for the three samples progressively tend to coincide. In addition, the currents in all three samples become increasingly concentrated along the vertical direction, again between 45° and 135°, which reflects a greater alignment of contacts along the loading axis. This variation in current distribution with increasing strain emphasises the gradual development of anisotropy in electrical behaviour under mechanical loading, driven by the rearrangement of particles and the evolution of the contact network. However, as monotonic loading continues beyond a certain point, the microstructure of the samples, regardless of their initial inherent anisotropy, and the orientation of the contact normal vectors between particles begin to converge. This convergence leads to similar electrical behaviours across the samples, observable at both micro- and macroscopic scales.

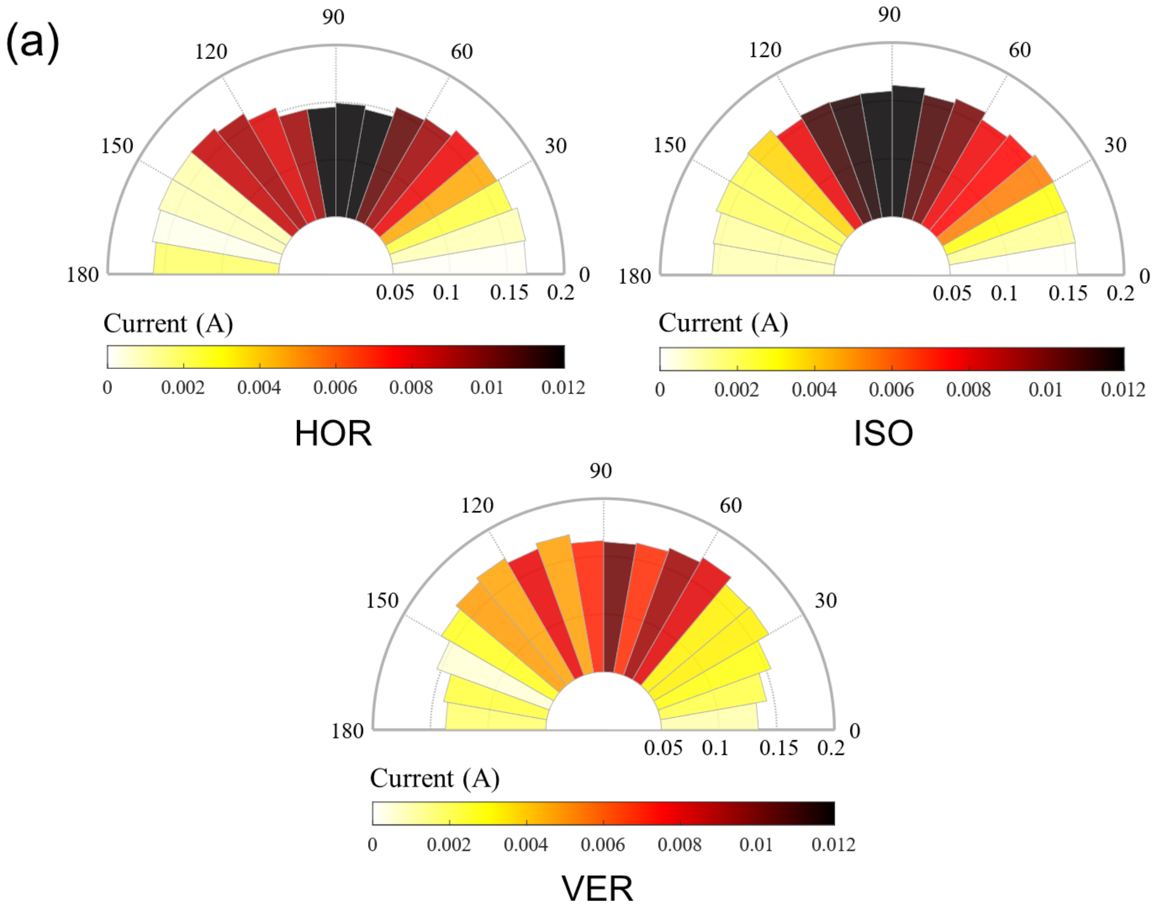

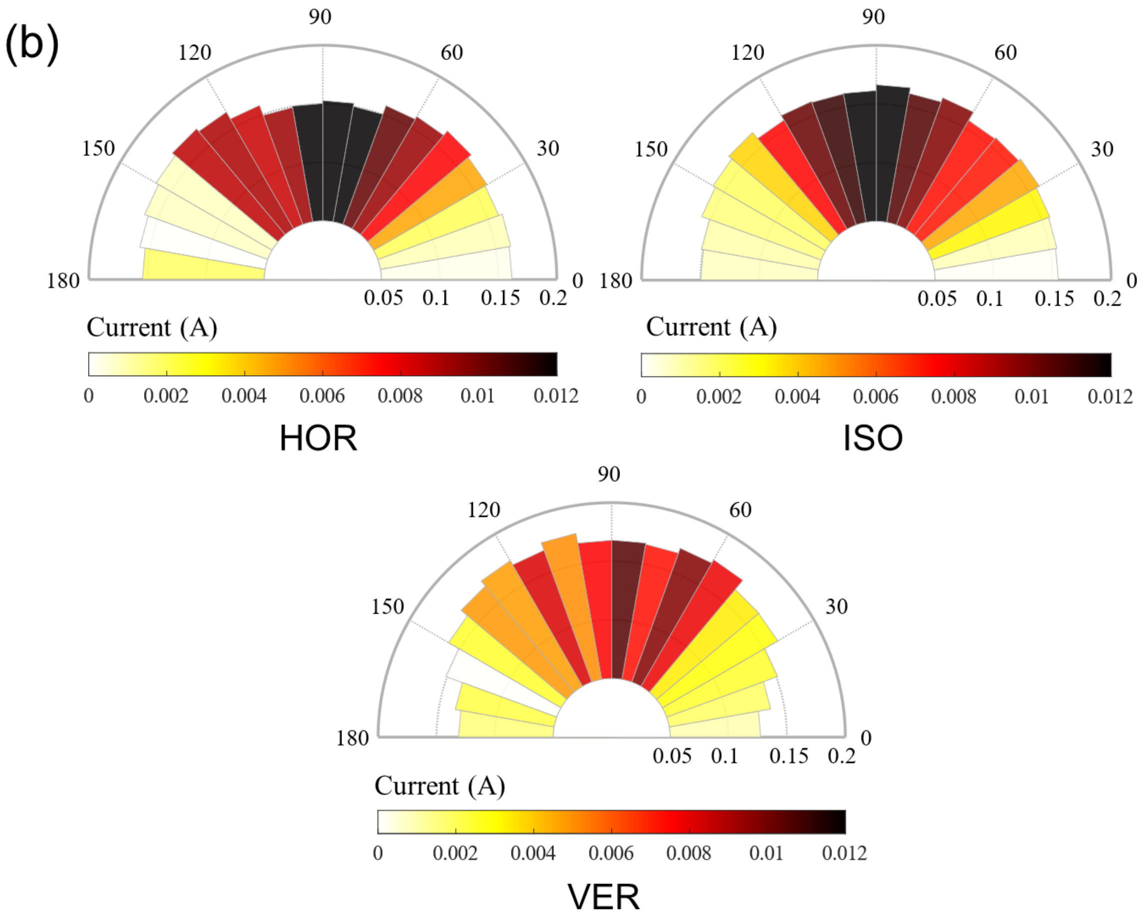
(b)
90
120
60
150
30
180
0
0.05 0.1 0.15 0.2
Current (A)
0 0.002 0.004 0.006 0.008 0.01 0.012
HOR
ISO
VER

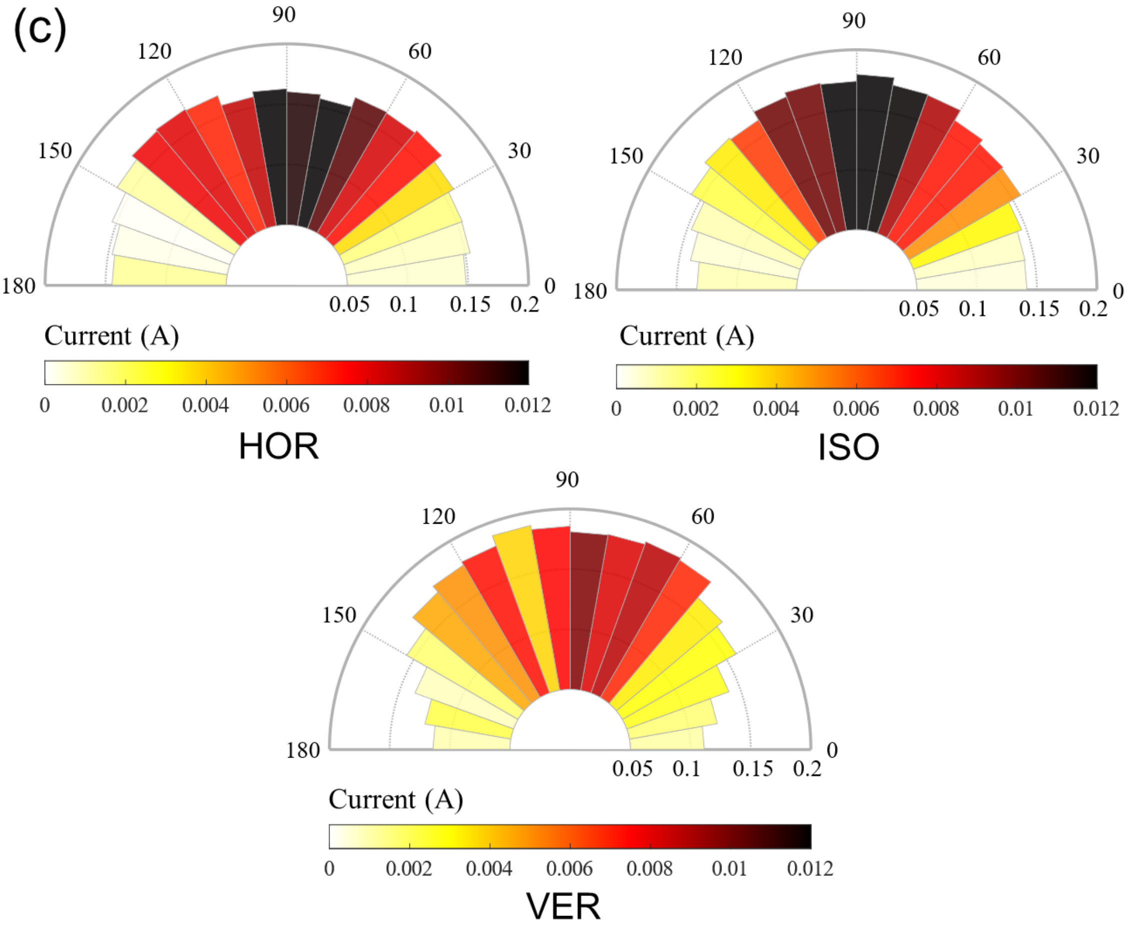
(c)
90
120
60
150
30
180
0
0.05 0.1 0.15 0.2
Current (A)
0 0.002 0.004 0.006 0.008 0.01 0.012
HOR
ISO
VER

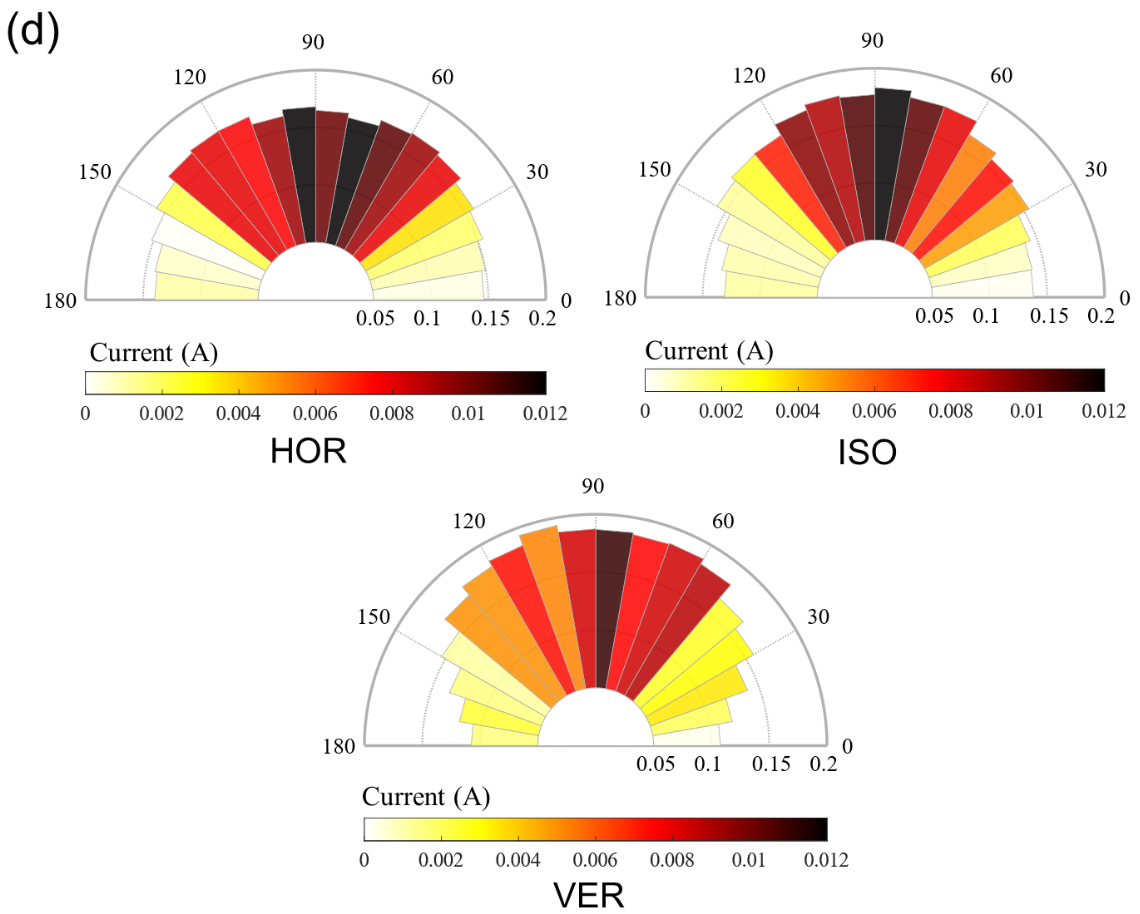
(d)
90
120
60
150
30
180
0
0.05
0.1
0.15
0.2
Current (A)
0
0.002
0.004
0.006
0.008
0.01
0.012
HOR
ISO
VER

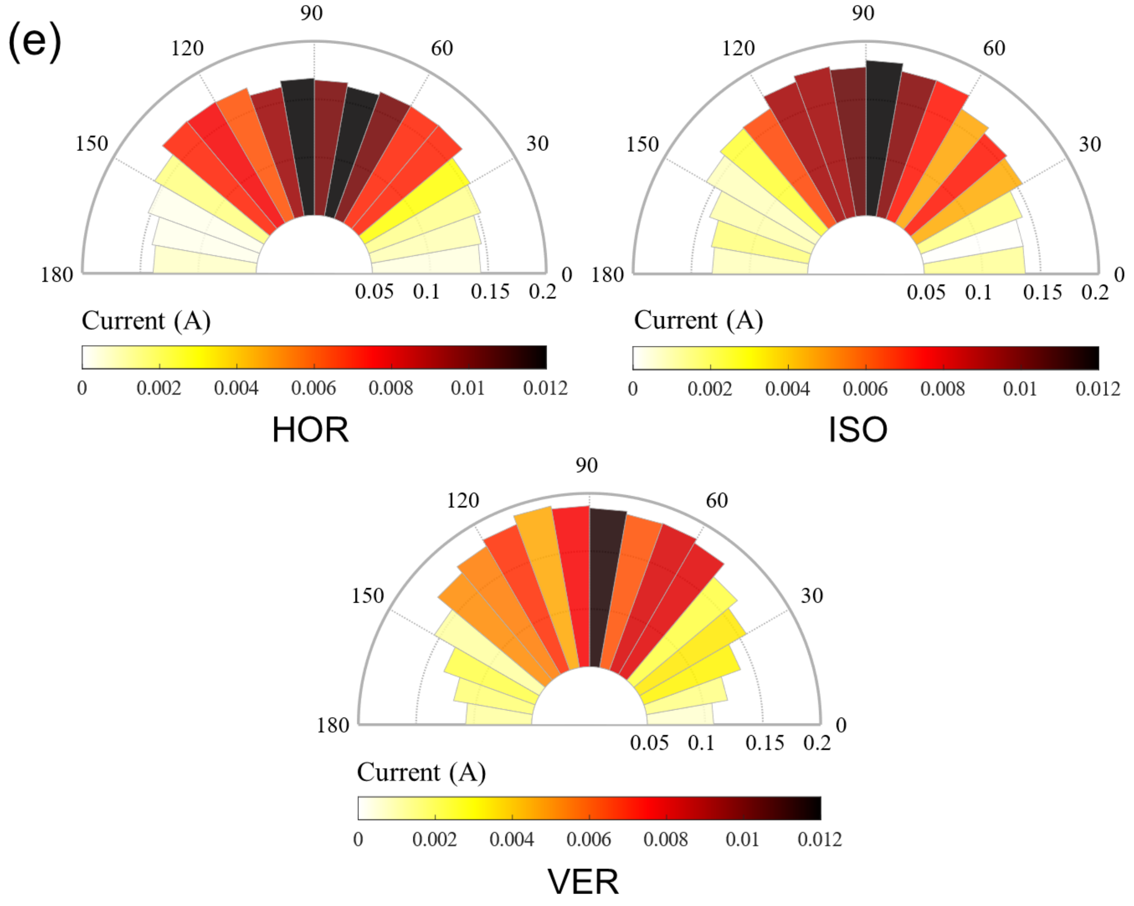
(e)
90
120
60
150
30
180
0
0.05
0.1
0.15
0.2
Current (A)
0
0.002
0.004
0.006
0.008
0.01
0.012
HOR
ISO
VER

(f)

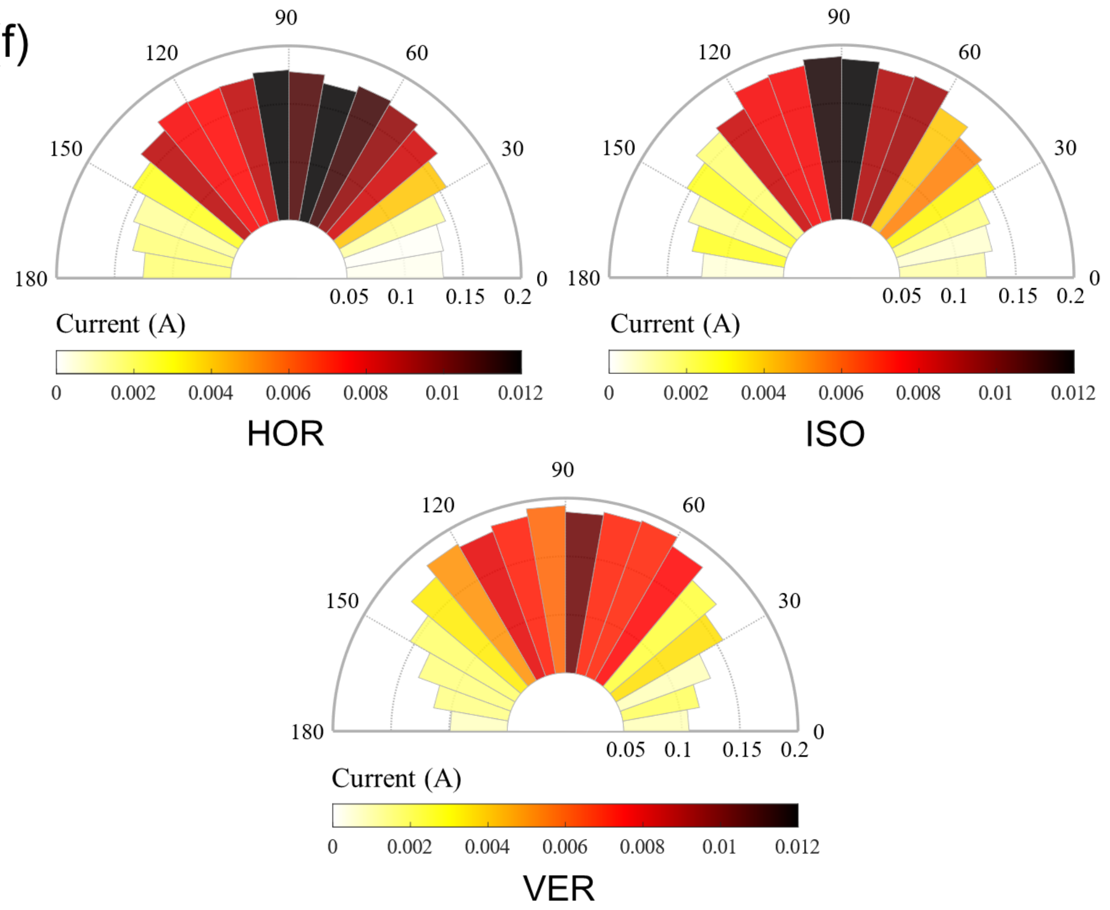
90
120
60
150
30
180
0
0.05
0.1
0.15
0.2
Current (A)
0
0.002
0.004
0.006
0.008
0.01
0.012
HOR
ISO
VER

(g)

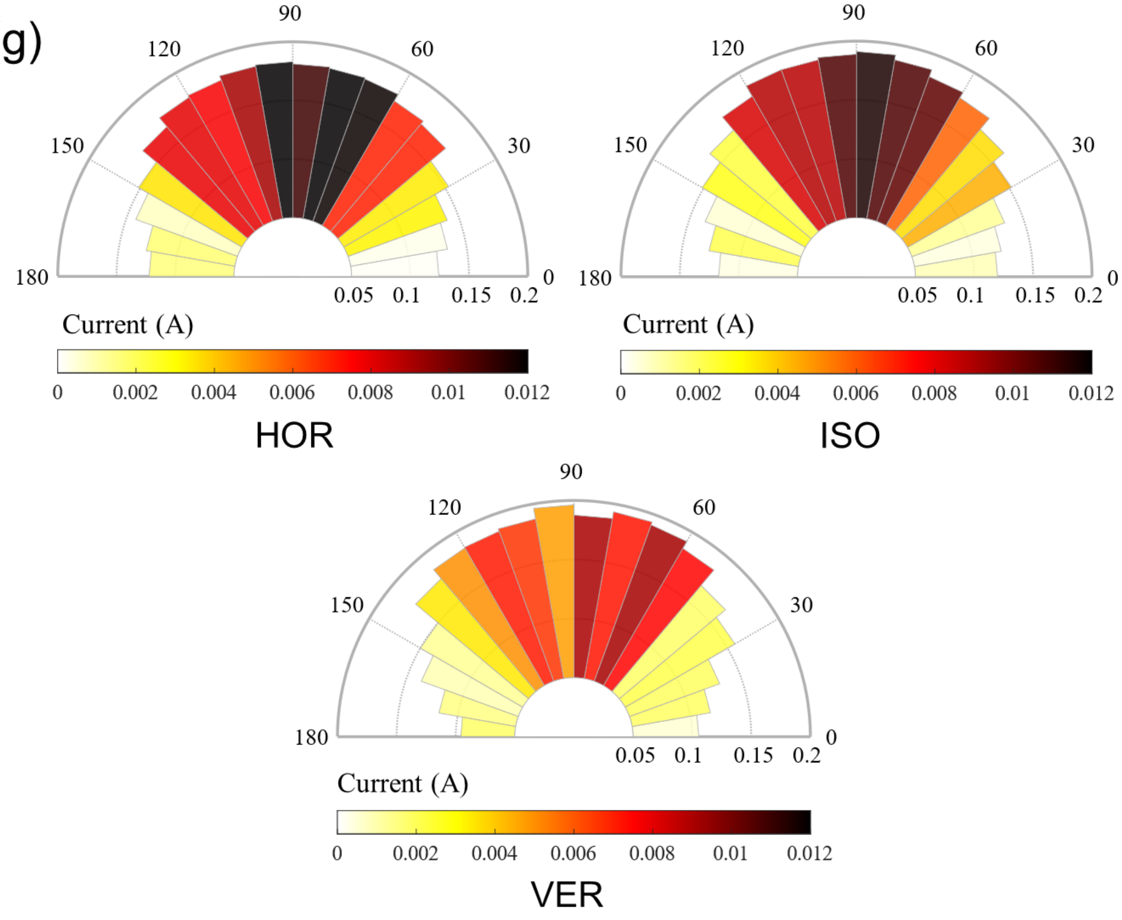
90
120
60
150
30
180
0
0.05
0.1
0.15
0.2
Current (A)
0
0.002
0.004
0.006
0.008
0.01
0.012
HOR
ISO
VER

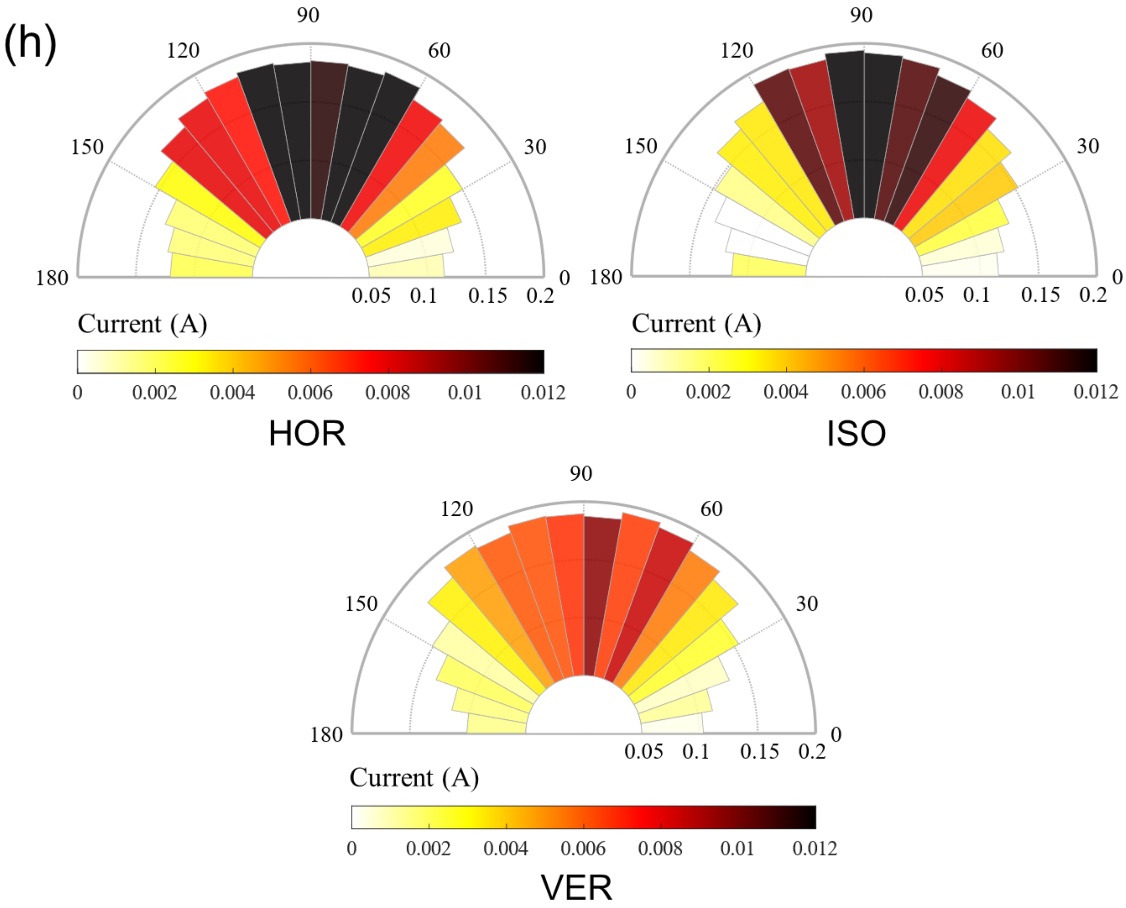
(h)
90
120
60
150
30
180
0
0.05 0.1 0.15 0.2
Current (A)
0 0.002 0.004 0.006 0.008 0.01 0.012
HOR
ISO
VER

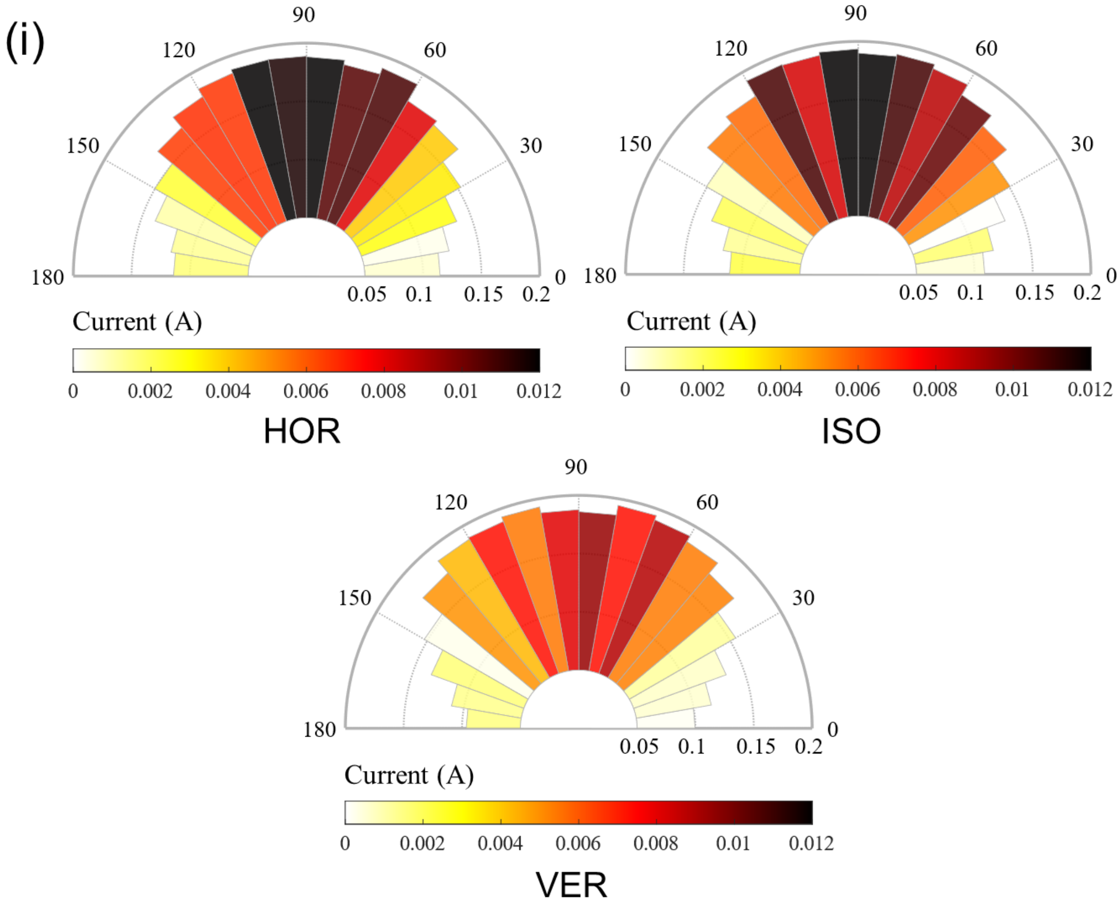
(i)
90
120
60
150
30
180
0
0.05 0.1 0.15 0.2
Current (A)
0 0.002 0.004 0.006 0.008 0.01 0.012
HOR
ISO
VER

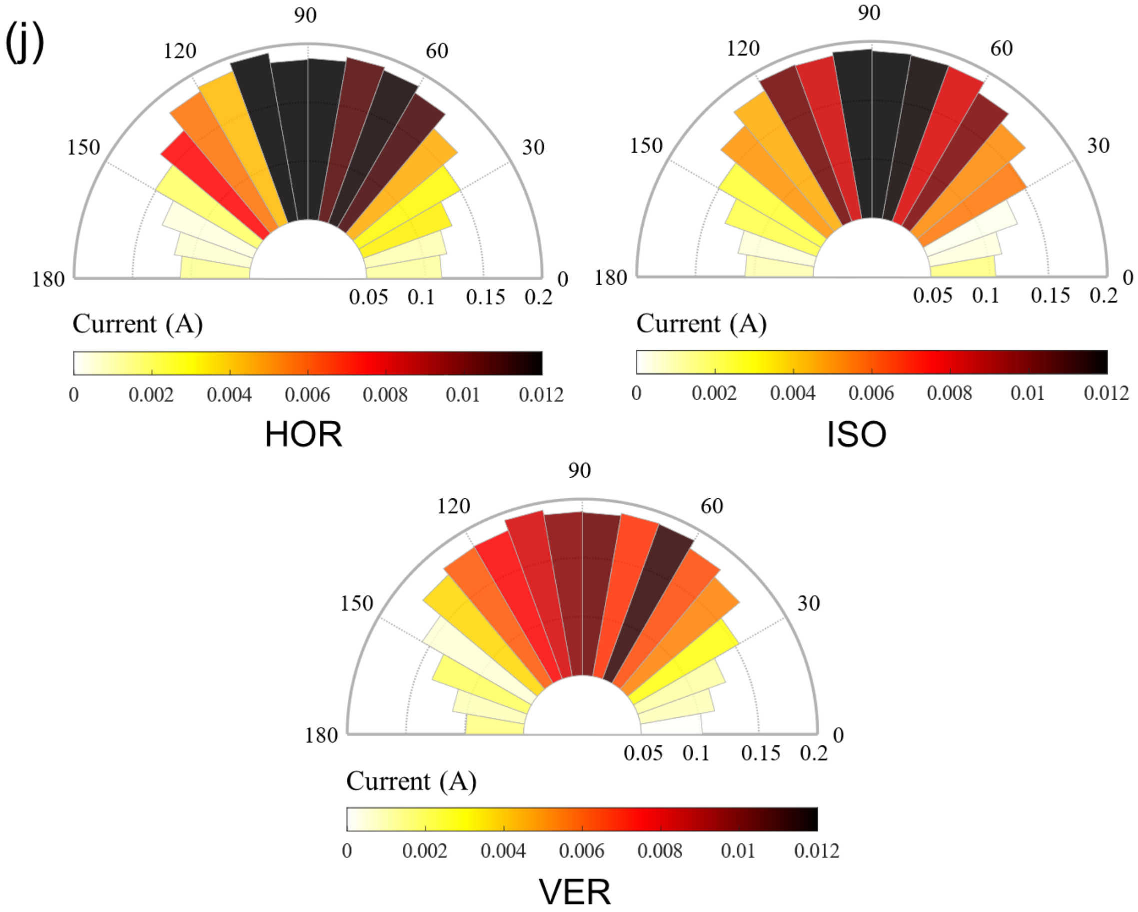

Figure 5.10 Magnitude of current intensity acting on the orientations of the contact normal vectors during drained monotonic compression: (a) axial strain 0%, (b) axial strain 0.03%, (c) axial strain 0.4%, (d) axial strain 0.8%, (e) axial strain 1%, (f) axial strain 3%, (g) axial strain 5%, (h) axial strain 7%, (i) axial strain 9%, and (j) axial strain 11% (The Probability Density Function is utilised to plot, which the length of each bin is (number of contact normal vectors in the bin)/(total number of contact normal vectors × width of bin), and the colour represents the magnitude of the average current intensity).

5.5 Evolution of Induced anisotropy during Drained Monotonic Loading

In this section, the microscopic response at the contact scale is examined for the *Iso-L*, *Ver-L*, and *Hor-L* samples, with a focus on the variation in the anisotropic degree (a). Relationships between the anisotropic degree and axial strain, deviatoric stress ratio, and bulk resistance are explored, linking the microscopic parameter to the macroscopic mechanical and electrical behaviour. Additionally, an alternative index, contact area anisotropy, is proposed to effectively track the evolution of the induced anisotropy and the mean contact area (A) in relation to the mechanical and electrical responses at macro-scale.

5.5.1 Link between Anisotropy and Electro-Mechanical Behaviour

Analyses relying solely on the mean coordination number (*CN*), as shown in Figure 5.6a, are insufficient to capture changes in fabric anisotropy during loading. Thus, the evolution of anisotropic degree (*a*), specifically induced anisotropy, is quantified to provide a more comprehensive understanding. Figure 5.11a depicts the evolution of the *a* during drained monotonic compression, while Figure 5.11b illustrates its evolution relative to the deviator stress ratio (*q*/*p'*). The variation of *a* under monotonic loading is observed to be more stable and systematic. For the *Ver_L* sample, the value of *a* increases sharply to approximately 0.3 within an initial small-strain range. As the axial strain continues to increase, it eventually reaches around 0.33, where it stabilises. In contrast, for the *Hor_L* sample, the value of *a* initially rises from approximately -0.1 to about 0.02 within the early stages of strain, indicating the onset of rearrangement between particles and a gradual increase in vertical contacts. As the axial strain reaches around 11%, the value of *a* for *Hor_L* sample approaches 0.33 and subsequently stabilises. The *Iso_L* sample exhibits an intermediate increase in *a* compared to the other two samples, with the final value of *a* also reaching approximately 0.33. This trend mirrors the relationship between the deviator stress ratio and anisotropy, where the *a* of the *Ver_L* sample increases rapidly in response to a rising *q*/*p'*, reaching 0.33. Conversely, the value of *a* for the *Hor_L* sample gradually increases to 0.33 due to a more gradual rise in the *q*/*p'*. In addition, the bulk resistances of the *Ver_L* and *Iso_L* samples decrease significantly as the *a* increases, whereas the *Hor_L* sample shows a less pronounced decrease. This suggests that conductive paths formed by particle contacts in the vertical direction are more effective in facilitating current transfer.

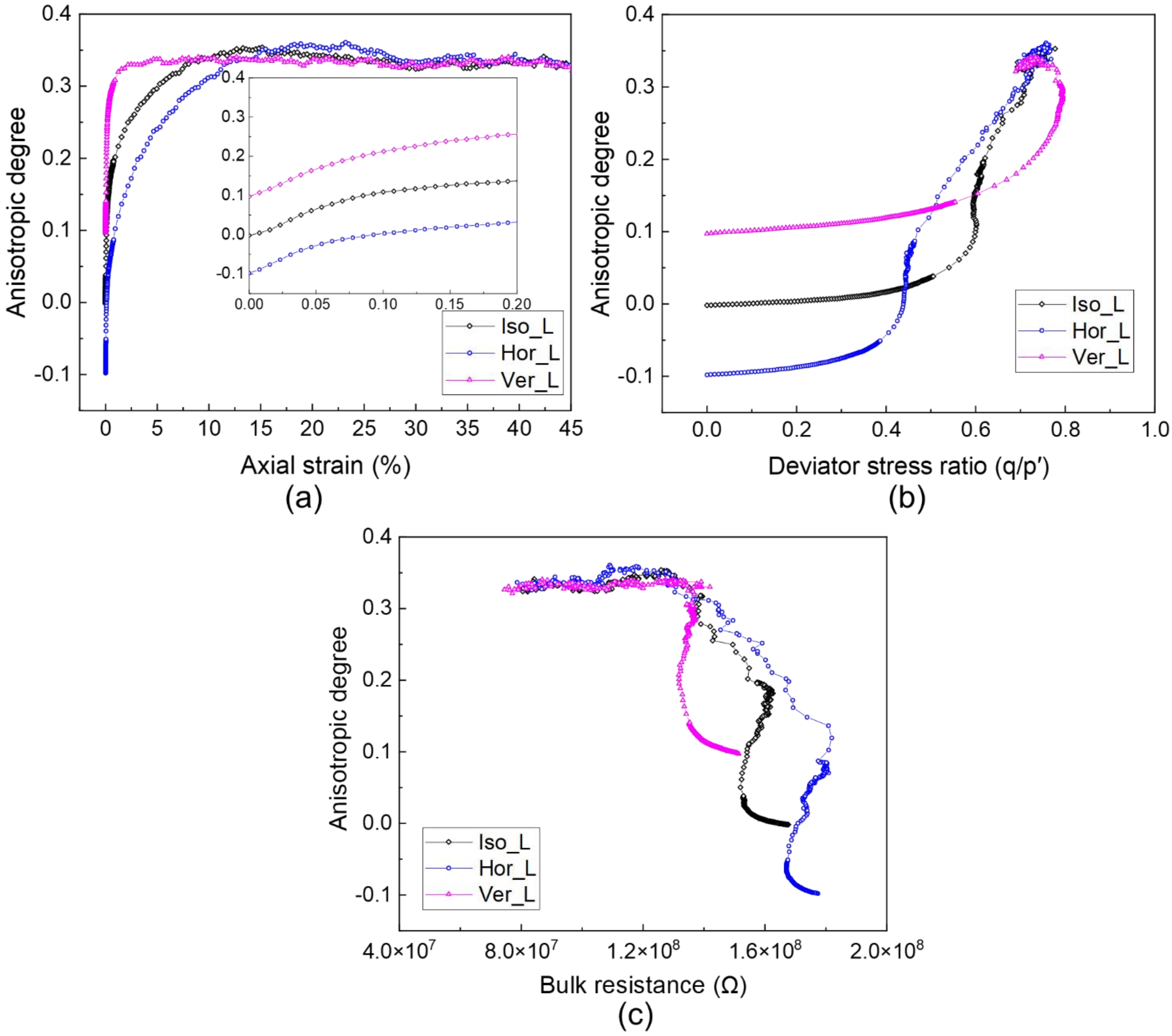

Figure 5.11 Variations in anisotropic degree (*a*) with (a) axial strain, (b) deviator stress ratio, and (c) bulk resistance under drained monotonic compression.

5.5.2 Alternative Index – Contact Area Anisotropy

The contact area between particles plays a crucial role in influencing current transfer along conductive paths (Bourbatache et al., 2012; Mikrajuddin et al., 1999; Ott et al., 2013). Building on the work of Li et al. (2021) and Otsubo et al. (2022), who utilised similar indices such as $\Phi_v \times CN$, $\Phi_h \times CN$, and $a \times CN$ for analysing drained monotonic compression and undrained monotonic loading, respectively, this study introduces an alternative index termed contact area anisotropy. This index is defined as the product of the anisotropic degree (*a*) and the mean contact area (*A*), expressed as $a \times A$. This formulation enables effective monitoring of the evolution of induced anisotropy and the contact area between particles under varying mechanical and electrical conditions.

Figures 5.12a and 5.12b illustrate the variation of $a \times A$ with axial strain and deviator stress ratio, respectively, while Figure 5.12c presents the relationship between $a \times A$ and bulk resistance. The light green lines in these figures denote the upper limits of $a \times A$, derived from the maximum values observed during the drained monotonic loading tests. Upon comparison with Figure 5.11, it is evident that the variation of $a \times A$ in response to macroscopic mechanical responses and electrical behaviour mirrors the trend observed for the anisotropy degree (a). This consistency suggests that threshold contact area anisotropy is one of the material characteristics of the given samples, independent of the loading type under drained conditions. It is important to note that the threshold value of $a \times A$ is relying on the initial void ratio (e_0), PSD, and the drainage conditions.

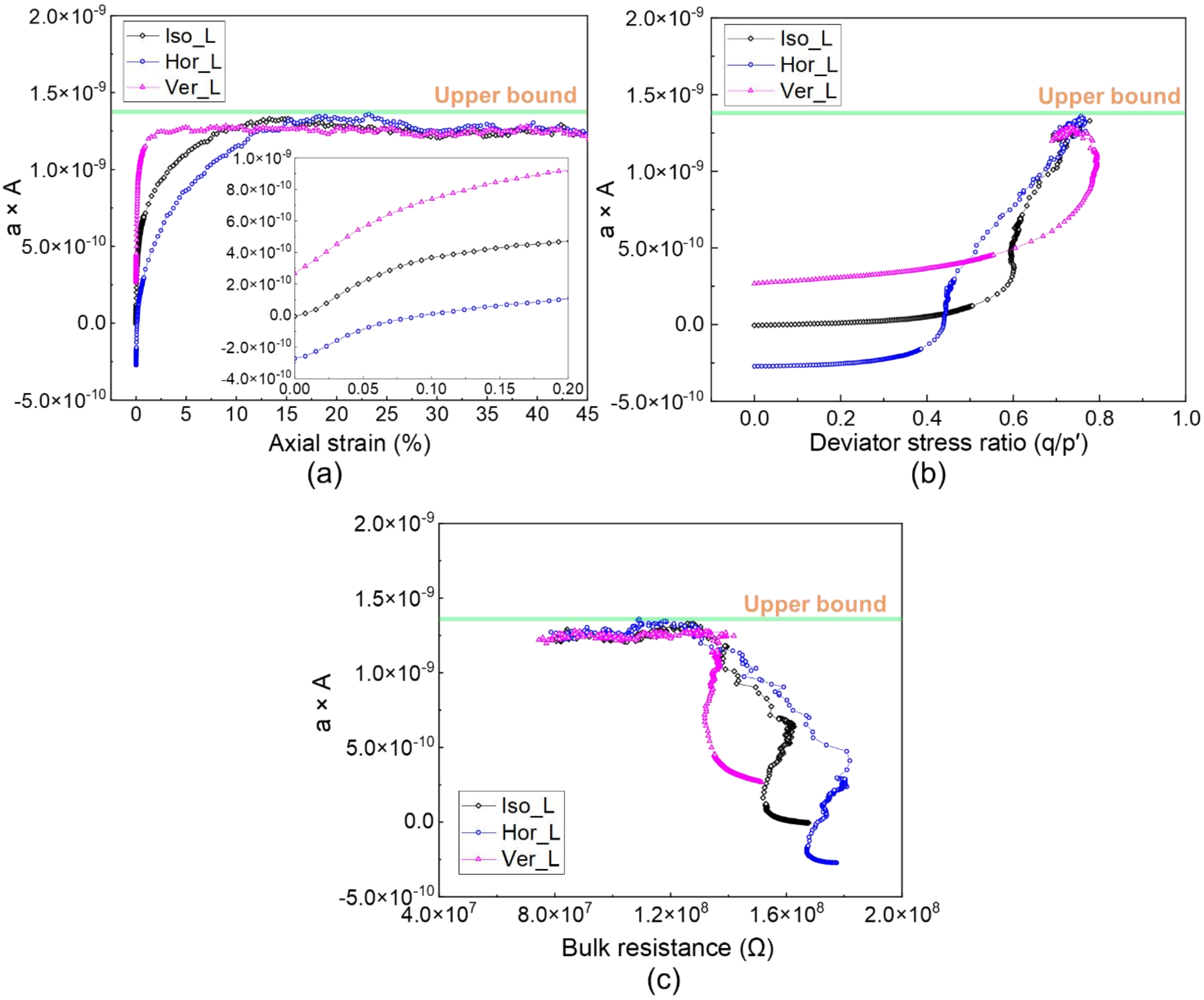

(a) (b) (c)

Figure 5.12 Variations in contact area anisotropy ($a \times A$) with (a) axial strain, (b) deviator stress ratio, and (c) bulk resistance under drained monotonic compression.

5.6 Discussion

This study investigated the macro-mechanical and microstructural responses during drained monotonic compression by examining three samples with varying inherent anisotropy: *Iso_L*, *Ver_L*, and *Hor_L*. The analysis also focused on the changes in bulk resistance of these samples under both macro-mechanical and microstructural influences. The distribution of contact forces and current intensities at different levels of axial strain (ranging from 0% to 11%) was explored to understand the interplay between mechanical deformation and electrical conduction. Furthermore, a relationship was established between the anisotropic degree (a) and the macroscopic mechanical and electrical properties, leading to the proposal of the contact area anisotropy ($a \times A$) as an alternative index to assess the evolution of induced anisotropy and contact area during monotonic compression. However, several limitations exist in this study. The DEM modelling approach does not fully capture certain critical aspects of granular soils, such as particle shape and PSD. Recent DEM studies commonly use multi-sphere clumps to represent non-spherical particles, such as Angelidakis et al. (2021) and Katagiri (2019), recognising that factors like particle shape parameters and principal axis orientation significantly influence mechanical responses. In addition, PSD is known to affect the range of achievable void ratio (e) and mean coordination number (CN) (Liu et al., 2021), which could also influence the range of initial anisotropy observed in the three loose samples presented in Table 5.2. Moreover, unlike Jiang et al. (2021), who utilised DEM to compare the dynamic responses of spherical particles under horizontally polarised shear-wave and Love-wave strain conditions, this study was limited to triaxial test conditions, highlighting a need for future research to explore a broader range of loading conditions and particle characteristics.

5.7 Conclusions

This study investigates the effect of inherent anisotropy on the mechanical and electrical behaviour of particulate systems during drained monotonic compression and relates this to induced anisotropy. Three samples with similar initial void ratio (e_0) and initial mean coordination number (CN_0) were modelled and their corresponding initial anisotropic degree (a_0) was systematically varied. The following conclusions were obtained:

(1) The initial stiffness and peak strength of the samples with inherent anisotropy, such as the *Ver_L* sample, are higher when compression is applied along the preferred contact normal direction. This is evident from the higher deviator stress ratio (q/p') observed in the *Ver_L*

sample compared to the *Hor_L* sample. The anisotropic degree (*a*) significantly influences the development of the *q*/*p'* during the initial stages of compression up to an axial strain of about 11%. However, in the residual state (at an axial strain of about 45%), the effect of anisotropic degree on the *q*/*p'* diminishes, indicating that the samples reach a similar structural state irrespective of their inherent anisotropy.

(2) The volumetric strain behaviour of the samples reflects their inherent anisotropy and contact alignment. The *Ver_L* sample, with vertically aligned contacts, exhibits a tendency to dilate more significantly during compression, while the *Hor_L* sample shows initial contraction before transitioning to dilation. This behaviour is also reflected in the changes in void ratio, where a decrease in void ratio indicates initial compaction, followed by an increase corresponding to dilation as the structure adjusts under continued loading.

(3) The mean coordination number (*CN*) and mean contact area (*A*) provide insights into the microstructural evolution of the samples under monotonic compression. A decrease in *CN* during the initial compression phase suggests particle rearrangement and loss of contacts, which is most pronounced in the *Hor_L* sample. The value of *A* increases at small to medium strain level for all samples, indicating stronger contacts are formed under compression, but eventually stabilises as the samples transition from contraction to dilation.

(4) The electrical behaviour of the samples, as quantified by bulk resistance, is closely linked to their mechanical behaviour and microstructural changes. As the anisotropy degree (*a*) increases, bulk resistance decreases, particularly in the *Ver_L* and *Iso_L* samples, due to the formation of more efficient conductive paths aligned with the vertical stress direction. The *Hor_L* sample shows a less pronounced decrease in bulk resistance, reflecting its initial horizontal alignment and subsequent particle rearrangement under vertical stress.

(5) An alternative index, contact area anisotropy ($a \times A$), to analyse induced anisotropy under drained monotonic compression. This index effectively captures the evolution of the anisotropic degree and mean contact area, providing consistent upper bound regardless of the loading conditions. This suggests that contact area anisotropy is an effective indicator of induced anisotropy and microstructural evolution, linking the micro-level changes to macroscopic mechanical and electrical responses.

Chapter 6 Conclusions

6.1 Summary

The overall aim of the research was to understand the interaction mechanisms between the mechanical response and electrical behaviour of particulate systems under loading from both macro and micro scales. The electrical properties of contacting objects were theoretically modelled and integrated into the DEM framework to simulate HPT test and drained triaxial compression test. Experimental investigations have been conducted to provide the necessary empirical data to support simulation-based findings.

Chapter 2 reviewed previous DEM studies to examine the mechanical response and electrical behaviour of particulate systems, with the aim of identifying existing research gaps. To enhance the understanding of the interplay between these two phenomena, this chapter explored the literature on the principles and modelling approaches of electrical transfer occurring during mechanical interactions between particles. Additionally, the breakage behaviour of crushable materials, such as sand particles under loading conditions, and the relevant modelling techniques were thoroughly investigated.

Chapter 3 focused on a practical application, sanding on wheel-rail interface, to investigate the effect of particle characteristics on tribological behaviour between the wheel and the rail. The HPT test, a laboratory technique for assessing wheel-rail adhesion, was modelled using DEM. Also, silica sand, a crushable material, was modelled using the BPM method. The study investigated various factors—including the bond properties (i.e., stiffness and strength) used to form silica sand particle, particle size and mass, the number of particles in the contact area, the size distribution of fragments following particle breakage, and particle shape. These effects were quantified in terms of CoT.

Chapter 3 also introduced an in-house Python code developed to regenerate size distribution data of fragments measured by laser diffraction, making them suitable for the modelling of sand particles. Samples of silica sand particles obtained via μCT scanning were modelled using this code. The accuracy of the code-generated FSD data was evaluated against the actual data using two metrics: R-squared and RMSE. In addition, the modelled silica sand particles were visualised to assess their similarity to real particles in terms of size and shape.

Chapter 4 presented an electro-mechanical contact model for investigating the electrical behaviour of a particulate system in response to mechanical loading. The model differentiates the electrical transfer within the particulate system into two types: particle-to-particle and particle-to-wall contacts. The overall electrical resistance between two contacting objects is divided into two components: contact resistance, which arises from the overlapping region, and particle resistance, which is due to the intrinsic material properties of the particles (e.g., electrical resistivity). The contact resistance is calculated using the Hertz and Holm's models, while the particle resistance is determined through the geometrical transformation of particles under mechanical stress. A one-way coupling approach in mechanical and electrical interaction is adopted, where mechanical forces influence electrical conduction, but electrical conduction does not impact mechanical behaviour. In contrast, a two-way coupling approach would involve mutual interaction, where electrical properties, such as induced currents or electromagnetic forces, could also influence the mechanical response of the granular materials. The one-way coupling assumption simplifies the analysis by focusing on how contact forces and stress distributions govern electrical conduction within the particulate system. The model was verified through analytical solutions for single-particle compression and particle-particle contact tests and validated against experimental data from stainless-steel particle chains and particle bed tests.

Chapter 4 also applied the electro-mechanical contact model to the HPT model, building on the findings from Chapter 3, to investigate how the particulate system influences the electrical behaviour between the wheel and the rail under mechanical loading. Two types of commercial coated alumina particles and non-conductive particles, silica sand, were used in the wheel-rail contact area of the HPT test. The change in electrical resistance of the HPT system was examined from a macroscopic perspective for each type of particle acting individually, and the simulation results were compared with experimental data. The distribution of electric potential and current within the particulate system at the wheel-rail interface under mechanical loading was analysed at the particle-scale. Moreover, an Electroactivity Index was proposed to quantify the contribution of different fragment sizes, generated after particle fragmentation, to the overall electrical behaviour of the particulate system.

Additional experimental and DEM studies were conducted to examine the electrical conduction properties of a mixture of conductive and non-conductive particles at the interface under loading. Compression tests were performed to explore the effect of varying the content of conductive particles with alumina coating and silica sand particles on the electrical conduction properties at the interface of two metal bodies, while maintaining a constant overall mixture mass. A specialised setup was developed and utilised to measure the changes in electrical resistance during the compression tests. Moreover, the fragment layers produced during the experiments were collected, and the microstructures of the silica sand fragment layer, the combined silica sand and conductive particles fragment layer, and the conductive particles fragment layer were observed using SEM. A DEM model of the HPT was employed to simulate each scenario involving mixtures of conductive and non-conductive particles, with the resulting electrical resistance data used to assess the electrical conduction properties at the wheel-rail interface. Additionally, the impact of the electrical resistivity of the conductive particles on the electrical resistance of the HPT system was investigated. The relationship between the content of conductive material, its electrical resistivity, and the resultant effect on electrical resistance was illustrated using a heatmap.

Chapter 5 investigated the effect of inherent anisotropy on the mechanical response of particulate systems. The LAMMPS molecular dynamic (DEM) code (Pinson et al., 1998) was utilised to model the drained triaxial compression tests. Three samples, *Iso_L*, *Ver_L*, and *Hor_L*, with different anisotropic degrees (a) were prepared. The macroscopic mechanical response of the three samples was examined from small to medium strains through to the residual state (up to 45% axial strain), including the deviator stress ratio (q/p') and volumetric strain (ε_{vol}). Simultaneously, the packing properties during drained triaxial compression process of the particulate system, with particular emphasis on the evolution of the mean coordination number (*CN*), void ratio (e_0), and mean contact area (A) under loading were investigated. Furthermore, since the contact orientation of particles in the initial stage of the *Hor_L* sample is primarily aligned in the horizontal direction (with the value of $a \approx -0.1$), this sample was selected and its distribution of contact forces from small to medium strains was visualised.

The electro-mechanical contact model was also implemented in the DEM simulations of drained triaxial compression tests to investigate the electrical behaviour of particulate system from small to medium strains until the residual state. The effect of the mechanical and microstructural responses of the three samples on their electrical properties was investigated and analysed by quantifying the evolution of the bulk resistance. Also, the current intensity in the orientation of the contact normal vectors for each sample is represented by two-dimensional rose diagrams for small and medium strain stages (0 ~ 11%). In addition, the evolution of the induced anisotropy of the three samples under the influence of macro mechanical and electrical properties was analysed. Moreover, an alternative index for assessing the induced anisotropy and the mean contact area within particulate system, the contact area anisotropy ($a \times A$), is proposed and thus can be employed to analyse the relationship between the mechanical and mechanical behaviour from the macro- to the micro-scale.

The laboratory tests and DEM simulations presented in this thesis provide valuable insights for developing design guidelines for optimising sanding strategies and balancing tribological and electrical performance at the wheel-rail interface. The findings demonstrate that while sanding recovers adhesion, excessive use of non-conductive sand can lead to electrical isolation, potentially affecting railway signalling systems. To address this, the introduction of conductive particles into the sanding mixture was explored, revealing an optimal ratio that improves traction while maintaining sufficient electrical conduction. The lab and simulation works have shown how particle size, shape, and breakage behaviour influence both mechanical response and electrical conduction. These results suggest that the selection of sanding materials should not only consider their adhesion-enhancing capabilities but also their ability to form conductive pathways in the fragment layer. Furthermore, the electro-mechanical contact model developed in this study can be used to predict how different sanding materials and mixture ratios affect both tribological and electrical properties under various loading conditions. These insights can inform railway maintenance guidelines, ensuring that sanding strategies are tailored to specific operational conditions, minimising risks related to traction loss and signal failures, and enhancing safety and efficiency in rail transport systems.

6.2 Key Remarks

The following key remarks were made in this thesis:

Sand particle characteristics

- The stiffness and density of the sand particles were appropriately scaled down to reduce the computational time, while the CoT difference was only 0.04 when compared to the results of the unscaled HPT simulation.
- The bond properties between particle fragments, particularly bond stiffness, significantly influence the tribological behaviour of wheel-rail contact, particularly as the bond stiffness is more sensitive to the CoT than bond strength.
- When bond strength exceeds a certain threshold (in this case 1×10^{10} Pa) during HPT testing, sand particles exhibit ductile behaviour instead of the expected brittle fracture.
- An increase in particle size, along with an increase in mass, decreases the CoT. Larger particles result in more fragments during compaction, which leads to the formation of particle fragment clusters that act as weak shear bands, creating a lubrication effect.
- As the number of particles in the contact area increases, the CoT at wheel-rail interface decreases, in a similar manner to the increase in particle size.
- The FSD data following sand particles fragmentation significantly affects CoT at wheel-rail interface, highlighting the need to consider this characteristic in sand particle modelling.
- No clear correlation was found between particle shape and the CoT, suggesting that shape is less critical than other particle characteristics such as particle size and FSD.

In-house Python code

- Linking the concept of weights in the Laguerre-Voronoi diagram to PSD or FSD and extending Voronoi relaxation to the Laguerre-Voronoi diagram offered a straightforward algorithm for modelling multi-sphere clustered particles.
- The code successfully modelled real sand samples as cluster particles, and the generated FSD data can be identified by R-squared and RMSE to closely matched the actual data, and the shape of cluster particles was approximately comparable to real sand particles.
- The laser diffraction data significantly improves the accuracy of the modelling for sand samples, highlighting that the code performed admirably when using finer fragment data.

Electrical behaviour of particulate systems under mechanical loading

- For both particle-particle and particle-wall contacts, electrical resistance decreased significantly as mechanical force increases until it decreased to a constant value; the contact area is a direct cause of the change in electrical resistance.

- In metallic particle systems, contact resistance was more significant than the intrinsic electrical resistance of the particles.
- In the HPT simulation, conductive coated alumina particles can significantly improve the conductivity between the wheel and rail compared to silica sand.
- The Electroactivity Index suggested that larger fragments contribute more significantly to bulk electrical conduction.
- Increasing the proportion of conductive particles in the mixture decreases the electrical resistance at the interface significantly, especially when the content reaches 5%, leading to the resistance drop sharply from around 55 kΩ to 220 Ω.
- Mixing conductive particles in silica sand will form micro-conductive channels within the fragment layer during compression to promote the electrons transfer.
- When the content of different types of conductive particles is the same, the smaller size of conductive particles mixed with silica sand can reduce the electrical resistance at the interface more effectively.
- The resistivity of the conductive material and its proportion in the mixture have a considerable effect on the resistance at the wheel-rail interface. The reasonable combination of the two factors can reduce the resistance to a very low level.

Inherent anisotropy of drained triaxial compression test

- Sample with inherent anisotropy exhibited higher initial stiffness and peak strength when stress is applied along the preferred contact normal orientation.
- The effect of inherent anisotropy on the mechanical response of the particulate system diminishes in the residual state, suggested a convergence to a similar structural status.
- The volumetric strain behaviour of the samples was influenced by their inherent anisotropy and contact alignment, and was also reflected in the variation of the void ratio.
- Changes in mean coordination number (*CN*) and mean contact area (*A*) reflected particle rearrangement and strengthening under monotonic compression.
- The electrical behaviour, measured by bulk resistance, correlates with mechanical

behaviour and microstructural changes.

- Contact area anisotropy ($a \times A$) suggested that induced anisotropy, along with an increased contact area between particles, resulted in a reduction in bulk resistance. This is mainly attributed to the vertically aligned contacts and the increase in the contact area between particles enhanced electron transfer efficiency.

6.3 Recommendations for further research

This study aimed to develop understanding of the interaction mechanisms between mechanical response and electrical behaviour of particulate systems. The following aspects should be carried out in the future research to improve the extension of the electro-mechanical contact model to more complex engineering applications.

Theoretical modelling

The electro-mechanical contact model in this thesis was undertaken under the assumption of dry contact conditions, considering only electrical transfer under two specific contact modes: particle-to-particle and particle-to-wall. However, in real railway applications, contact conditions at the wheel-rail interface are far more complex. For example, factors such as wet conditions (Buckley-Johnstone et al., 2020) or contamination (e.g., oxide, oil, and leaf layers) (Arias-Cuevas and Li, 2011), can significantly alter electrical conduction. Additionally, for three-phase materials like soil, it is necessary to consider electron transfer within the liquid phase in the voids and electrical transfer during solid-liquid contact.

During DEM simulations of metal particulate systems, it was observed that the presence of the oxide layer on the particle surfaces resulted in substantial discrepancy between the simulation results and experimental data. This discrepancy arises because the film resistance generated by the contamination layer primarily influences the overall electrical resistance between particles during the initial stages of load application (Bourbatache et al., 2012; Creyssels et al., 2017). To more accurately investigate how the contamination layer impedes metal-to-metal conductive paths at a microscopic scale, further development of the model is required to incorporate the effect of film resistance into the electro-mechanical contact framework.

Moreover, thermal effects play a crucial role in wheel-rail contact behaviour (Liu et al., 2021; Meng et al., 2024; Wang et al., 2024). Under high loads and repeated rolling-sliding interactions, frictional heating can alter surface conductivity by influencing oxide growth, material softening, and contact resistance. Thermal expansion of the wheel and rail materials may also modify contact pressure, affecting both mechanical deformation and electrical conduction pathways. In extreme cases, localised heating can lead to material phase changes or microstructural modifications, further impacting electro-mechanical interactions. To enhance the applicability of electro-mechanical contact model, future work should explore thermal influences on contact resistance, including temperature-dependent resistivity changes and heat-induced oxidation in wheel-rail interfaces.

Numerical study

The DEM simulations conducted in this thesis, both the particles and walls are assumed to have smooth surfaces. However, in real-world engineering applications, the surfaces of structures and particles are typically not smooth, as is the case with railhead surfaces in railway engineering. Surface roughness may result in the actual contact area between particles, and between particles and structures, being larger than the nominal contact area (Zhai et al., 2016). Consequently, in future DEM simulations, the effect of surface roughness will be incorporated into the modelling of both structures and particles to achieve a more accurate representation.

The DEM simulations in Chapter 5 were performed under drained monotonic loading. However, to achieve more realistic simulation of mechanical response and electrical behaviour within sand particulate system, the undrained monotonic loading and undrained cyclic loading methods need to be conducted in the future research. In addition, it is essential to consider more realistic particle shapes and PSD in future DEM studies. This is because particle shape parameters and the orientation of the major axis will contribute to the mechanical response and electrical behaviour of the particulate system. Additionally, PSD affects the range of void ratios and the mean coordination number within the particulate system, which are critical factor in determining system behaviour.

Experimental study

For future research, it is recommended to develop a comprehensive setup for measuring the electrical properties of geotechnical materials during triaxial compression testing. This setup should be capable of real-time monitoring of changes in electrical properties, such as electrical resistance and current, under different loading conditions, including drained/undrained monotonic loading, as well as undrained cyclic loading.

Additionally, while DEM simulations of the HPT test were conducted in Chapter 4 to study the effect of mixing conductive and non-conductive particles on electrical behaviour at the interface, corresponding experimental studies are needed. Conducting these experiments would provide essential data for refining the electro-mechanical contact model and validating the simulation results, thereby offering robust empirical support for the theoretical findings.

References

Abbaspour, A., Luo, J.-L., Nandakumar, K., 2010. Three-dimensional random resistor-network model for solid oxide fuel cell composite electrodes. Electrochimica Acta 55, 3944–3950.

Ai, J., Chen, J.-F., Rotter, J.M., Ooi, J.Y., 2011. Assessment of rolling resistance models in discrete element simulations. Powder Technology 206, 269–282.

Altair EDEM, 2021. https://2021.help.altair.com/2021.1/EDEM/index.htm.

Angelidakis, V., Nadimi, S., Otsubo, M., Utili, S., 2021. CLUMP: A Code Library to generate Universal Multi-sphere Particles. SoftwareX 15, 100735.

Australian Rail Track Corporation, 2017. Route Access Standard: General Information.

Antonyuk, S., Khanal, M., Tomas, J., Heinrich, S., Mörl, L., 2006. Impact breakage of spherical granules: Experimental study and DEM simulation. Chemical Engineering and Processing: Process Intensification, Particulate Processes A Special Issue of Chemical Engineering and Processing 45, 838–856.

Arias-Cuevas, O., Li, Z., 2011. Field investigations into the adhesion recovery in leaf-contaminated wheel–rail contacts with locomotive sanders. Proceedings of the Institution of Mechanical Engineers, Part F: Journal of Rail and Rapid Transit 225, 443–456.

Arias-Cuevas, O., Li, Z., Lewis, R., 2011. A laboratory investigation on the influence of the particle size and slip during sanding on the adhesion and wear in the wheel–rail contact. Wear 271, 14–24.

Arias-Cuevas, O., Li, Z., Lewis, R., 2010a. Investigating the Lubricity and Electrical Insulation Caused by Sanding in Dry Wheel–Rail Contacts. Tribology Letters 37, 623–635.

Arias-Cuevas, O., Li, Z., Lewis, R., Gallardo-Hernández, E.A., 2010b. Rolling–sliding laboratory tests of friction modifiers in dry and wet wheel–rail contacts. Wear 268, 543–551.

Arias-Cuevas, O, Li, Z., Lewis, R., Gallardo-Hernández, E.A., 2010c. Laboratory investigation of some sanding parameters to improve the adhesion in leaf-contaminated wheel—rail contacts. Proceedings of the Institution of Mechanical Engineers, Part F: Journal of Rail and Rapid Transit 224, 139–157.

Bandini, V., Coop, M.R., 2011. The Influence of Particle Breakage on the Location of the Critical State Line of Sands. Soils and Foundations 51, 591–600.

Barenblatt, G.I., 1959. The formation of equilibrium cracks during brittle fracture. General ideas and hypotheses. Axially-symmetric cracks. Journal of Applied Mathematics and Mechanics 23, 622–636.

Barrios, G.K.P., Jiménez-Herrera, N., Tavares, L.M., 2020. Simulation of particle bed breakage by slow compression and impact using a DEM particle replacement model. Advanced Powder Technology 31, 2749–2758.

Barrios, G.K.P., Tavares, L.M., 2016. A preliminary model of high pressure roll grinding using the discrete element method and multi-body dynamics coupling. International Journal of Mineral Processing, In Honor of Professor Heinrich Schubert on his 90th birthday 156, 32–42.

Beagley, T.M., McEwen, I.J., Pritchard, C., 1975. Wheel/rail adhesion—Boundary lubrication by oily fluids. Wear 31, 77–88.

Beagley, T.M., Pritchard, C., 1975. Wheel/rail adhesion — the overriding influence of water. Wear 35, 299–313.

Behjani, M.A., Rahmanian, N., Fardina bt Abdul Ghani, N., Hassanpour, A., 2017. An investigation on process of seeded granulation in a continuous drum granulator using DEM. Advanced Powder Technology 28, 2456–2464.

Belytschko, T., Liu, W.K., Moran, B. and Elkhodary, K., 2014. Nonlinear finite elements for continua and structures. John wiley & sons.

Benzeggagh, M.L., Kenane, M., 1996. Measurement of mixed-mode delamination fracture toughness of unidirectional glass/epoxy composites with mixed-mode bending apparatus. Composites Science and Technology 56, 439–449.

Birkholz, O., Gan, Y., Kamlah, M., 2019. Modeling the effective conductivity of the solid and the pore phase in granular materials using resistor networks. Powder Technology 351, 54–65.

Bolton, M.D., Nakata, Y., Cheng, Y.P., 2008. Micro- and macro-mechanical behaviour of DEM crushable materials. Géotechnique 58, 471–480.

Bourbatache, K., Guessasma, M., Bellenger, E., Bourny, V., Fortin, J., 2013. DEM ball bearing model and defect diagnosis by electrical measurement. Mechanical Systems and Signal Processing 41, 98–112.

Bourbatache, K., Guessasma, M., Bellenger, E., Bourny, V., Tekaya, A., 2012. Discrete modelling of electrical transfer in multi-contact systems. Granular Matter 14, 1–10.

Bradshaw, G., O'Sullivan, C., 2004. Adaptive medial-axis approximation for sphere-tree construction. ACM Transactions on Graphics 23, 1–26.

Branly, É., 1890. Étude des phénomènes électrostatiques dans les piles. Annales scientifiques de l'École Normale Supérieure Serie 2: 201–252.

British Standards Institution, 1990. Methods of Test for Soils for Civil Engineering Purposes. Part 2: Classification Tests. BS1377, 493.

Brodnik Zugelj, B., Kalin, M., 2020. Submicron-scale experimental analyses of the multi-asperity contact behaviour of various steels, an aluminium alloy and a polymer. Tribology International 141, 105955.

Buckley-Johnstone, L., 2017. Wheel/rail contact tribology: characterising low adhesion mechanisms and friction management products (Doctoral dissertation, University of Sheffield).

Buckley-Johnstone, L.E., Trummer, G., Voltr, P., Meierhofer, A., Six, K., Fletcher, D.I., Lewis, R., 2019. Assessing the impact of small amounts of water and iron oxides on adhesion in the wheel/rail interface using High Pressure Torsion testing. Tribology International 135, 55–64.

Buckley-Johnstone, L.E., Trummer, G., Voltr, P., Six, K., Lewis, R., 2020. Full-scale testing of low adhesion effects with small amounts of water in the wheel/rail interface. Tribology International 141, 105907.

Budynas, R.G., Nisbett, J.K., Shigley, J.E., 2015. Shigley's mechanical engineering design, Tenth edition. ed, Mcgraw-Hill series in mechanical engineering. McGraw-Hill Education, New York, NY.

Cambou, B., Dubujet, Ph., Nouguier-Lehon, C., 2004. Anisotropy in granular materials at different scales. Mechanics of Materials, Topics in Micromechanics of Heterogeneous

Materials 36, 1185–1194.

Cantor, D., Azéma, E., Sornay, P., Radjai, F., 2017. Three-dimensional bonded-cell model for grain fragmentation. Computational Particle Mechanics 4, 441–450.

Chaidee, S., Sugihara, K., 2020. Laguerre Voronoi Diagram as a Model for Generating the Tessellation Patterns on the Sphere. Graphs and Combinatorics 36, 371–385.

Chapteuil, E., Renouf, M., Zeng, C., Berthier, Y., 2018. Influence of Copper/Graphite Properties on the Tribological and Electrical Behavior of Copper-Graphite Third Body Layer. Lubricants 6, 109.

Chen, X., Qin, H., Qian, X., Zhu, W., Li, B., Zhang, B., Lu, W., Li, R., Zhang, S., Zhu, L., Domingues Dos Santos, F., Bernholc, J., Zhang, Q.M., 2022. Relaxor ferroelectric polymer exhibits ultrahigh electromechanical coupling at low electric field. Science 375, 1418–1422.

Cheng, Y.P., Nakata, Y., Bolton, M.D., 2003. Discrete element simulation of crushable soil. Géotechnique 53, 633–641.

Cho, N., Martin, C.D., Sego, D.C., 2007. A clumped particle model for rock. International Journal of Rock Mechanics and Mining Sciences 44, 997–1010.

Chicco, D., Warrens, M.J., Jurman, G., 2021. The coefficient of determination R-squared is more informative than SMAPE, MAE, MAPE, MSE and RMSE in regression analysis evaluation. PeerJ Computer Science 7, e623.

Ciantia, M.O., Arroyo, M., Butlanska, J., Gens, A., 2016. DEM modelling of cone penetration tests in a double-porosity crushable granular material. Computers and Geotechnics 73, 109–127.

Ciantia, M.O., Arroyo, M., Calvetti, F., Gens, A., 2015. An approach to enhance efficiency of DEM modelling of soils with crushable grains. Géotechnique 65, 91–110.

Cil, M.B., Buscarnera, G., 2016. DEM assessment of scaling laws capturing the grain size dependence of yielding in granular soils. Granular Matter 18, 36.

Cleary, P., 2001. Modelling comminution devices using DEM. International Journal for numerical and analytical methods in geomechanics, 25(1), 83-105.

Cleary, P.W., Sinnott, M.D., 2015. Simulation of particle flows and breakage in crushers using DEM: Part 1 – Compression crushers. Minerals Engineering 74, 178–197.

Coetzee, C.J., 2019. Particle upscaling: Calibration and validation of the discrete element method. Powder Technology 344, 487–503.

Collins, I.F., Muhunthan, B., 2003. On the relationship between stress–dilatancy, anisotropy, and plastic dissipation for granular materials. Géotechnique 53, 611–618.

Cooper P. R., 1972. An investigation into the relationship between the Particle Size and the Frictional Performance of Sand (IM-ADH-011). British Rail Report.

Creyssels, M., Laroche, C., Falcon, E., Castaing, B., 2017. Pressure dependence of the electrical transport in granular materials. European Physical Journal E 40, 56.

Cundall, P.A., Strack, O.D.L., 1979. A discrete numerical model for granular assemblies. Géotechnique 29, 47–65.

Da Rocha, R.J.B., 2016. Evaluation of different damage initiation and growth criteria in the cohesive zone modelling analysis of single-lap bonded joints (Master's thesis, Instituto Politecnico do Porto (Portugal)).

D'Addetta, G.A., Kun, F., Ramm, E., 2002. On the application of a discrete model to the fracture process of cohesive granular materials. Granular Matter 4, 77–90.

Dai, B., Yang, J., Zhou, C., Luo, X., 2016. DEM investigation on the effect of sample preparation on the shear behavior of granular soil. Particuology 25, 111–121.

DB/EBA/VDB/VDV Working Group, 2016. Supplementary Regulation No. B 011 to 'Sanding.'

De Bono, J.P., McDowell, G.R., 2016. The fractal micro mechanics of normal compression. Computers and Geotechnics 78, 11–24.

Delaney, G.W., Morrison, R.D., Sinnott, M.D., Cummins, S., Cleary, P.W., 2015. DEM modelling of non-spherical particle breakage and flow in an industrial scale cone crusher. Minerals Engineering 74, 112–122.

Deresiewicz, H., 1954. Contact of Elastic Spheres Under an Oscillating Torsional Couple. Journal of Applied Mechanics 21, 52–56.

Descartes, S., Renouf, M., Fillot, N., Gautier, B., Descamps, A., Berthier, Y., Demanche, Ph., 2008. A new mechanical–electrical approach to the wheel-rail contact. Wear, Contact Mechanics and Wear of Rail/Wheel Systems - CM2006 265, 1408–1416.

Dugdale, D.S., 1960. Yielding of steel sheets containing slits. Journal of the Mechanics and Physics of Solids 8, 100–104.

Edalati, K., Horita, Z., 2016. A review on high-pressure torsion (HPT) from 1935 to 1988. Materials Science and Engineering: A 652, 325–352.

Eidem, P.A., Runde, M., Tangstad, M., Bakken, J.A., Zhou, Z.Y., Yu, A.B., 2009. Effect of Contact Resistance on Bulk Resistivity of Dry Coke Beds. Metallurgical and Materials Transactions A B 40, 388–396.

Evans, M., Skipper, W.A., Buckley-Johnstone, L., Meierhofer, A., Six, K., Lewis, R., 2021. The development of a high pressure torsion test methodology for simulating wheel/rail contacts. Tribology International 156, 106842.

Evans, M.D., Lee, Z.S., Harmon, M., Six, K., Meierhofer, A., Stock, R., Gutsulyak, D.V., Lewis, R., 2023. Top-of-rail friction modifier performance assessment: High pressure torsion testing; creep force modelling and field validation. Wear 532–533, 205073.

Falcon, E., Castaing, B., 2005. Electrical conductivity in granular media and Branly’s coherer: A simple experiment. American Journal of Physics 73, 302–307.

Falcon, E., Castaing, B., Creyssels, M., 2004. Nonlinear electrical conductivity in a 1D granular medium. European Physical Journal B 38, 475–483.

Feki, N., Clerc, G., Velex, Ph., 2012. An integrated electro-mechanical model of motor-gear units—Applications to tooth fault detection by electric measurements. Mechanical Systems and Signal Processing 29, 377–390.

Feng, Y.T., Han, K., Li, C.F., Owen, D.R.J., 2008. Discrete thermal element modelling of heat conduction in particle systems: Basic formulations. Journal of Computational Physics 227, 5072–5089.

Feng, Y.T., Han, K., Owen, D.R.J., Loughran, J., 2009. On upscaling of discrete element models: similarity principles. Engineering Computations 26, 599–609.

Feng, Y.T., Owen, D.R.J., 2014. Discrete element modelling of large scale particle systems—I: exact scaling laws. Computational Particle Mechanics 1, 159–168.

Fischer, M., Haselsteiner, K., Szekely, F., Heinz, S. and Kröger, F., 2020. Mehr Mobilität auf der Schiene: Erhöhung der Transportkapazität Durch Optimierung des Kraftschlusses.

Fu, R., Hu, X., Zhou, B., 2017. Discrete element modeling of crushable sands considering realistic particle shape effect. Computers and Geotechnics 91, 179–191.

Fujioka, T., Horita, Z., 2009. Development of High-Pressure Sliding Process for

Microstructural Refinement of Rectangular Metallic Sheets. Materials Transactions 50, 930–933.

Fulford, C. R., 2004. Review of Low Adhesion Research (T354). RSSB Report.

Fukumoto, T., 1992. Particle Breakage Characteristics of Granular Soils. Soils and Foundations 32, 26–40.

Galindo-Torres, S.A., Pedroso, D.M., Williams, D.J., Li, L., 2012. Breaking processes in three-dimensional bonded granular materials with general shapes. Computer Physics Communications 183, 266–277.

Gao, H., Pfaff, R., Babilon, K., Ye, Y., n.d. A comprehensive wheel–rail contact model incorporating sand fragments and its application in vehicle braking simulation. Vehicle System Dynamics 0, 1–20.

Gautam, A., Green, S.I., 2021. Computational fluid dynamics–discrete element method simulation of locomotive sanders. Proceedings of the Institution of Mechanical Engineers, Part F: Journal of Rail and Rapid Transit 235, 12–21.

Glover, P.W.J., Gómez, J.B., Meredith, P.G., 2000. Fracturing in saturated rocks undergoing triaxial deformation using complex electrical conductivity measurements: experimental study. Earth and Planetary Science Letters 183, 201–213.

Glover, P.W.J., Gomez, J.B., Meredith, P.G., Boon, S.A., Sammonds, P.R., Murrell, S.A.F., 1996. Modelling the stress-strain behaviour of saturated rocks undergoing triaxial deformation using complex electrical conductivity measurements. Surveys in Geophysics 17, 307–330.

Grandin, M., Wiklund, U., 2018. Influence of mechanical and electrical load on a copper/copper-graphite sliding electrical contact. Tribology International 121, 1–9.

Gray, P., 2018. T1107 Sander Trials Dissemination Event. RSSB Report.

Guo, N., Zhao, J., 2013b. The signature of shear-induced anisotropy in granular media. Computers and Geotechnics 47, 1–15.

Haeri, S., 2017. Optimisation of blade type spreaders for powder bed preparation in Additive Manufacturing using DEM simulations. Powder Technology 321, 94–104.

Hærvig, J., Kleinhans, U., Wieland, C., Spliethoff, H., Jensen, A.L., Sørensen, K., Condra, T.J., 2017. On the adhesive JKR contact and rolling models for reduced particle stiffness discrete element simulations. Powder Technology 319, 472–482.

He, Y., Hassanpour, A., Alizadeh Behjani, M., Bayly, A.E., 2021. A novel stiffness scaling methodology for discrete element modelling of cohesive fine powders. Applied Mathematical Modelling 90, 817–844.

Hertz, H., 1882. Ueber die Berührung fester elastischer Körper. Journal für die reine und angewandte Mathematik 92, 156–171.

Hillerborg, A., Modéer, M., Petersson, P.-E., 1976. Analysis of crack formation and crack growth in concrete by means of fracture mechanics and finite elements. Cement and Concrete Research 6, 773–781.

Ho, C.-W., Ruehli, A., Brennan, P., 1975. The modified nodal approach to network analysis. IEEE Transactions on Circuits and Systems 22, 504–509.

Holm, R., 1967. The contact resistance. General theory, in: Holm, R. (Ed.), Electric Contacts: Theory and Application. Springer, Berlin, Heidelberg, 9–11.

Housecroft, C.E. and Sharpe, A.G., 2008. Structures and energetics of metallic and ionic solids. Inorganic Chemistry, pp.164-171.

Huang, X., Hanley, K.J., O’Sullivan, C., Kwok, C.-Y., 2017. Implementation of rotational resistance models: A critical appraisal. Particuology 34, 14–23.

Huang, W., Cao, X., Wen, Z., Wang, W., Liu, Q., Zhu, M., Jin, X., 2016. A Subscale Experimental Investigation on the Influence of Sanding on Adhesion and Rolling Contact Fatigue of Wheel/Rail Under Water Condition. ASME Journal of Tribology 139.

Huang, X., Hanley, K.J., O’Sullivan, C., Kwok, C.Y., 2014. Exploring the influence of interparticle friction on critical state behaviour using DEM. International Journal for Numerical and Analytical Methods in Geomechanics 38, 1276–1297.

Hubert, C., André, D., Dubar, L., Iordanoff, I., Charles, J. l., 2017. Simulation of continuum electrical conduction and Joule heating using DEM domains. International Journal for Numerical Methods in Engineering 110, 862–877.

Ishibashi, I., Capar, O.F., 2003. Anisotropy and its Relation to Liquefaction Resistance of Granular Material. Soils and Foundations 43, 149–159.

Ishizaka, K., Lewis, S.R., Lewis, R., 2017. The low adhesion problem due to leaf contamination in the wheel/rail contact: Bonding and low adhesion mechanisms. Wear 378–379, 183–197.

Ishihara, K. and Koga, Y., 1981. Case studies of liquefaction in the 1964 Niigata earthquake. Soils and foundations, 21(3), 35–52.

Itasca Consulting Group, 2019. PFC3D version 6.0 user manual.

Jakšić, Z.M., Cvetković, M., Šćepanović, J.R., Lončarević, I., Budinski-Petković, L., Vrhovac, S.B., 2017. The electrical conductance growth of a metallic granular packing. European Physical Journal B 90, 108.

J. Hanley, K., O'Sullivan, C., 2017. Analytical study of the accuracy of discrete element simulations. International Journal for Numerical Methods in Engineering 109, 29–51.

Jiang, M., Kamura, A., Kazama, M., 2021. Comparison of liquefaction behavior of granular material under SH- and Love-wave strain conditions by 3D DEM. Soils and Foundations 61, 1235–1250.

Jiang, H., Meng, D., 2018. 3D numerical modelling of rock fracture with a hybrid finite and cohesive element method. Engineering Fracture Mechanics 199, 280–293.

Jiménez-Herrera, N., Barrios, G.K.P., Tavares, L.M., 2018. Comparison of breakage models in DEM in simulating impact on particle beds. Advanced Powder Technology 29, 692–706.

Johnson, K.L., 1987. Contact mechanics. Cambridge university press.

Kawashita, L.F., Hallett, S.R., 2012. A crack tip tracking algorithm for cohesive interface element analysis of fatigue delamination propagation in composite materials. International Journal of Solids and Structures 49, 2898–2913.

Katagiri, J., 2019. A novel way to determine number of spheres in clump-type particle-shape approximation in discrete-element modelling. Géotechnique 69, 620–626.

Knoll, M.D., 1996. A petrophysical basis for ground penetrating radar and very early time electromagnetics: Electrical properties of sand-clay mixtures (Doctoral dissertation, University of British Columbia).

Kobayashi, T., Tanaka, T., Shimada, N., Kawaguchi, T., 2013. DEM–CFD analysis of fluidization behavior of Geldart Group A particles using a dynamic adhesion force model. Powder Technology, 248, 143–152.

Koch, K., Revil, A., Holliger, K., 2012. Relating the permeability of quartz sands to their grain size and spectral induced polarization characteristics. Geophysical Journal International 190, 230–242.

Kodicherla, S.P.K., Zhu, M., Gong, G., Wilkinson, S., 2024. Strength and fabric anisotropy of granular materials under true triaxial configurations using DEM. Powder Technology 446, 120179.

Kuhn, M.R., 1999. Structured deformation in granular materials. Mechanics of Materials 31, 407–429.

Kuhn, M.R., Sun, W., Wang, Q., 2015. Stress-induced anisotropy in granular materials: fabric, stiffness, and permeability. Acta Geotechnica 10, 399–419.

Kumar, S., Krishnamoorthy, P.K., Prasanna Rao, D.L., 1986. Wheel-Rail Wear and Adhesion With and Without Sand for a North American Locomotive. Journal of Engineering for Industry 108, 141–147.

Kun, F., Herrmann, H.J., 1996. A study of fragmentation processes using a discrete element method. Computer Methods in Applied Mechanics and Engineering 138, 3–18.

Kuo, H.P., Knight, P.C., Parker, D.J., Tsuji, Y., Adams, M.J., Seville, J.P.K., 2002. The influence of DEM simulation parameters on the particle behaviour in a V-mixer. Chemical Engineering Science 57, 3621–3638.

Lautensack, C., 2008. Fitting three-dimensional Laguerre tessellations to foam structures. Journal of Applied Statistics 35, 985–995.

Lewis, R., Dwyer-Joyce, R.S., 2006. Wear at the wheel/rail interface when sanding is used to increase adhesion. Proceedings of the Institution of Mechanical Engineers, Part F: Journal of Rail and Rapid Transit 220, 29–41.

Lewis, R., Dwyer-Joyce, R.S., Lewis, J., 2003. Disc machine study of contact isolation during railway track sanding. Proceedings of the Institution of Mechanical Engineers, Part F: Journal of Rail and Rapid Transit 217, 11–24.

Lewis, R., Masing, J., 2006. Static wheel/rail contact isolation due to track contamination. Part F: Journal of Rail and Rapid Transit 220, 43–53.

Lewis, S., Riley, S., Fletcher, D., Lewis, R., 2018. Optimisation of a railway sanding system for optimal grain entrainment into the wheel–rail contact. Proceedings of the Institution of Mechanical Engineers, Part F: Journal of Rail and Rapid Transit 232, 43–62.

Lewis, S.R., Lewis, R., Cotter, J., Lu, X., Eadie, D.T., 2016. A new method for the assessment of traction enhancers and the generation of organic layers in a twin-disc machine. Wear, 366–367, 258–267.

Lewis, S.R., Lewis, R., Richards, P., Buckley-Johnstone, L.E., 2014. Investigation of the isolation and frictional properties of hydrophobic products on the rail head, when used to combat low adhesion. Wear 314, 213–219.

Lewis, S.R., Riley, S., Fletcher, D.I. and Lewis, R., 2015. Optimisation of a railway sanding system, Part 2: Adhesion Tests. In The International Conference on Contact Mechanics CM.

Li, D., Wan, H., Liu, J., Jiang, H., Wang, Y., Zhang, J., Zheng, Y., 2024. Effects of calendering state on coupled electrochemical-mechanical performance of silicon based composite electrodes. Green Energy and Intelligent Transportation 100154.

Li, K., Li, X., Chen, Q., Nimbalkar, S., 2023. Laboratory Analyses of Noncoaxiality and Anisotropy of Spherical Granular Media under True Triaxial State. International Journal of Geomechanics 23, 04023150.

Li, X., Yu, H.-S., 2010. Numerical investigation of granular material behaviour under rotational shear. Géotechnique 60, 381–394.

Li, X., Yu, H.S., Li, X.S., 2009. Macro–micro relations in granular mechanics. International Journal of Solids and Structures 46, 4331–4341.

Li, X.S., Dafalias, Y.F., 2012. Anisotropic Critical State Theory: Role of Fabric. Journal of Engineering Mechanics 138, 263–275.

Li, Y., Otsubo, M., Kuwano, R., 2021. DEM analysis on the stress wave response of spherical particle assemblies under triaxial compression. Computers and Geotechnics 133, 104043.

Li, Y., Xu, Y., Thornton, C., 2005. A comparison of discrete element simulations and experiments for ‘sandpiles’ composed of spherical particles. Powder Technology 160, 219–228.

Lichter, J., Lim, K., Potapov, A., Kaja, D., 2009. New developments in cone crusher performance optimization. Minerals Engineering 22, 613–617.

Liu, D., O’Sullivan, C., Carraro, J.A.H., 2021. Influence of Particle Size Distribution on the Proportion of Stress-Transmitting Particles and Implications for Measures of Soil State. Journal of Geotechnical and Geoenvironmental Engineering 147, 04020182.

Liu, X., Hu, M., Li, Z., Zhou, C., Xiao, Q., Yang, W., Chen, D., 2021. Effect of copper contents on the current-carrying wear properties of carbon brush under different temperatures conditions. Journal of Materials Research and Technology 15, 3110–3121.

Liu, X., Tu, C., Wu, G., Gao, M., Liu, Y., Chen, Y., Cai, W., Li, R., 2024. Investigation of the enhancement in current-carrying friction performance with internal “copper network structure” constructed by pre-oxidized carbon fibers of the carbon skateboard. Tribology International 198, 109820.

Liu, Z., Wang, S., Chen, Z., Guan, W., Guo, J., Wu, S., Huang, Q., 2024. Electromechanical coupling characteristics analysis of vertical stirred mill based on ECS-MBD-DEM. Powder Technology 433, 119245.

Lloyd, S., 1982. Least squares quantization in PCM. IEEE Transactions on Information Theory 28, 129–137.

Lobo-Guerrero, S., Vallejo, L.E., 2005. Discrete Element Method Evaluation of Granular Crushing Under Direct Shear Test Conditions. Journal of Geotechnical and Geoenvironmental Engineering 131, 1295–1300.

Lommen, S., Mohajeri, M., Lodewijks, G., Schott, D., 2019. DEM particle upscaling for large-scale bulk handling equipment and material interaction. Powder Technology 352, 273–282.

Lopera Perez, J.C., Kwok, C.Y., O′Sullivan, C., Huang, X., Hanley, K.J., 2016. Assessing the quasi-static conditions for shearing in granular media within the critical state soil mechanics framework. Soils and Foundations 56, 152–159.

Lubkin, J.L., 1951. The Torsion of Elastic Spheres in Contact. Journal of Applied Mechanics 18, 183–187.

Ma, G., Zhou, W., Chang, X.-L., 2014. Modeling the particle breakage of rockfill materials with the cohesive crack model. Computers and Geotechnics 61, 132–143.

Machado, C., Guessasma, M. and Bourny, V., 2018. Electromechanical prediction of the regime of lubrication in ball bearings using Discrete Element Method. Tribology International, 127, 69-83.

Machado, C., Guessasma, M. and Bellenger, E., 2015. Electromechanical modeling by DEM for assessing internal ball bearing loading. Mechanism and Machine Theory, 92, 338-355.

Machado, C., Baudon, S., Guessasma, M., Bourny, V., Fortin, J., Bouzerar, R., Maier, P., 2019. An Original DEM Bearing Model with Electromechanical Coupling. International Journal of Computational Methods 16, 1840006.

Mahardika, H., Revil, A., Jardani, A., 2012. Waveform joint inversion of seismograms and electrograms for moment tensor characterization of fracking events. Geophysics 77, ID23–ID39.

Maramizonouz, S., Nadimi, S. and Lewis, R., 2024. CFD-DEM modelling of particle entrainment in wheel–rail interface: a parametric study on train characteristics. Acta Mechanica, 1-11.

Maramizonouz, S., Nadimi, S., Skipper, W.A., Lewis, S.R., Lewis, R., 2023a. Numerical modelling of particle entrainment in the wheel–rail interface. Computational Particle Mechanics 10, 2009–2019.

Maramizonouz, S., Nadimi, S., Skipper, W., Lewis, R., 2023b. Characterisation of physical and mechanical properties of seven particulate materials proposed as traction enhancers. Scientific Data 10, 400.

Marks E. R. C., 1996. Emergency Sanding Device: Class 159 Fleet Trial (RR-PRJESDM-RP-3). British Rail Report.

McDowell, G.R., Bolton, M.D., 2001. Micro Mechanics of Elastic Soil. Soils and Foundations 41, 147–152.

McDowell, G.R., Harireche, O., 2002. Discrete element modelling of soil particle fracture. Géotechnique 52, 131–135.

McEwen I. J., 1977. Service Experience with Sandite - South Devon Banks, Autumn 1976 (TM-TRIB-020). British Rail Report.

McEwen I. J. and Taylor R. K., 1975. Adhesion and Leaves: Wet Abrasive Blasting Tests on Southern Region 1974 (TM-TRIB-7). British Rail Report.

Mehr Mobilität auf der Schiene: Erhöhung der Transportkapazität Durch Optimierung des

Kraftschlusses.

Meierhofer, A., 2015. A new wheel-rail creep force model based on elasto-plastic third body layers. (Doctoral dissertation, Graz University of Technology).

Meng, Y., Ren, W., Han, Y., Zhang, C., 2024. Effects of current load on wear and melt erosion of electrical contacts under fretting condition. Tribology International 194, 109511.

Metzger, M.J., Glasser, B.J., 2013. Simulation of the breakage of bonded agglomerates in a ball mill. Powder Technology 237, 286–302.

Metzger, M.J., Glasser, B.J., 2012. Numerical investigation of the breakage of bonded agglomerates during impact. Powder Technology 217, 304–314.

Mikrajuddin, A., Shi, F.G., Kim, H.K., Okuyama, K., 1999. Size-dependent electrical constriction resistance for contacts of arbitrary size: from Sharvin to Holm limits. Materials Science in Semiconductor Processing 2, 321–327.

Mindlin, R.D., 1949. Compliance of Elastic Bodies in Contact. Journal of Applied Mechanics 16, 259–268.

Mindlin, R.D., Deresiewicz, H., 1953. Elastic Spheres in Contact Under Varying Oblique Forces. Journal of Applied Mechanics 20, 327–344.

Mohammadi, E., Fadaeinedjad, R., Moschopoulos, G., 2020. An electromechanical emulation-based study on the behaviour of wind energy conversion systems during short circuit faults. Energy Conversion and Management 205, 112401.

Moraru, A., Morega, A.M., Petre, M. and Cilianu, M., 2011. Magnetohydrodynamic flow simulation in an aluminum electrolysis cell. Rev. Roum. Sci. Techn., Électrotechn. et Énerg, 56(2).

Mori, Y., Takabatake, K., Tsugeno, Y., Sakai, M., 2020. On artificial density treatment for the pressure Poisson equation in the DEM-CFD simulations. Powder Technology 372, 48–58.

Morimoto, T., Otsubo, M., Koseki, J., 2021. Microscopic investigation into liquefaction resistance of pre-sheared sand: Effects of particle shape and initial anisotropy. Soils and Foundations 61, 335–351.

Nan, W., Ghadiri, M., Wang, Y., 2017. Analysis of powder rheometry of FT4: Effect of particle shape. Chemical Engineering Science 173, 374–383.

Nguyen, D.-H., Azéma, E., Sornay, P., Radjai, F., 2015. Bonded-cell model for particle fracture. Physical Review E 91, 022203.

Nguyen, V.P., Nguyen, C.T., Bordas, S., Heidarpour, A., 2016. Modelling interfacial cracking with non-matching cohesive interface elements. Computational Mechanics 58, 731–746.

Ni, X., Ma, J., Zhang, F., 2024. Mechanism of the variation in axial strain of sand subjected to undrained cyclic triaxial loading explained by DEM with non-spherical particles. Computers and Geotechnics 165, 105846.

Ni, X., Ye, B., Zhang, F., Feng, X., 2021. Influence of Specimen Preparation on the Liquefaction Behaviors of Sand and Its Mesoscopic Explanation. Journal of Geotechnical and Geoenvironmental Engineering 147, 04020161.

Niu, Q., Revil, A., Li, Z., Wang, Y.-H., 2017. Relationship between electrical conductivity anisotropy and fabric anisotropy in granular materials during drained triaxial compressive tests: a numerical approach. Geophysical Journal International 210, 1–17.

Oda, M., Kawamoto, K., Suzuki, K., Fujimori, H., Sato, M., 2001. Microstructural Interpretation on Reliquefaction of Saturated Granular Soils under Cyclic Loading. Journal of Geotechnical and Geoenvironmental Engineering 127, 416–423.

Oda, M., 1982. Fabric tensor for discontinuous geological materials. Soils and foundations, 22(4), 96-108.

Oda, M., 1972. Initial Fabrics and their Relations to Mechanical Properties of Granular Material. Soils and Foundations 12, 17–36.

Omasta, M., Machatka, M., Smejkal, D., Hartl, M., Křupka, I., 2015. Influence of sanding parameters on adhesion recovery in contaminated wheel–rail contact. Wear 322–323, 218–225.

Orefice, L., Khinast, J.G., 2020. Deformable and breakable DEM particle clusters for modelling compression of plastic and brittle porous materials — Model and structure properties. Powder Technology 368, 90–104.

Orozco, L.F., Delenne, J.-Y., Sornay, P., Radjai, F., 2019. Discrete-element model for dynamic fracture of a single particle. International Journal of Solids and Structures 166, 47–56.

O'Sullivan, C., 2011. Particulate discrete element modelling: a geomechanics perspective. CRC Press.

Otsubo, M., Chitravel, S., Kuwano, R., Hanley, K.J., Kyokawa, H., Koseki, J., 2022. Linking inherent anisotropy with liquefaction phenomena of granular materials by means of DEM analysis. Soils and Foundations 62, 101202.

Otsubo, M., Chitravel, S., Kuwano, R., Kyokawa, H., Koseki, J., 2023. Liquefaction characteristics in triaxial tests under various gravity environments – DEM analyses. Computers and Geotechnics 156, 105245.

Otsubo, M., O'Sullivan, C., Shire, T., 2017. Empirical assessment of the critical time increment in explicit particulate discrete element method simulations. Computers and Geotechnics 86, 67–79.

Otsubo, M., 2016. Particle scale analysis of soil stiffness and elastic wave propagation (Doctoral dissertation, Imperial College London).

Ott, J., Völker, B., Gan, Y., McMeeking, R.M., Kamlah, M., 2013. A micromechanical model for effective conductivity in granular electrode structures. Acta Mechanica Sinica 29, 682–698.

Pasha, M., Hare, C., Ghadiri, M., Gunadi, A., Piccione, P.M., 2016. Effect of particle shape on flow in discrete element method simulation of a rotary batch seed coater. Powder Technology, 296, 29–36.

Patwa, A., Ambrose, R.P.K., Casada, Mark.E., 2016. Discrete element method as an approach to model the wheat milling process. Powder Technology 302, 350–356.

Persson, B.N.J., 2022. On the Electric Contact Resistance. Tribology Letters 70, 88.

Pinson, D., Zou, R.P., Yu, A.B., Zulli, P., McCarthy, M.J., 1998. Coordination number of binary mixtures of spheres. Journal of Physics D: Applied Physics 31, 457.

Plimpton, S., 1995. Fast Parallel Algorithms for Short-Range Molecular Dynamics. Journal of Computational Physics 117, 1–19.

Pollicott, I.D., 1977. Review of service trails with the high velocity sander (IM-TRIB-029). British Rail Report.

Purcell, L., and Lightoller, A., 2018. Trial of Sander Configurations and Sand Laying Rates (T1107). RSSB Report.

Pöschel, T., Salueña, C., Schwager, T., 2001. Scaling properties of granular materials. Phys. Rev. E 64, 011308.

Potyondy, D.O., Cundall, P.A., 2004. A bonded-particle model for rock. International Journal of Rock Mechanics and Mining Sciences 41, 1329–1364.

Quist, J., Evertsson, C.M., 2016. Cone crusher modelling and simulation using DEM. Minerals Engineering 85, 92–105.

Rail Accident Investigation Branch, 2019. Rail accident report: near miss between a passenger train and cars at norwich road level crossing, new rackheath, norfolk. RAIB Report.

Rail Accident Investigation Branch., 2007. Autumn adhesion investigation Part 3: Review of adhesion-related incidents Autumn 2005. RAIB Report.

Radjai, F., Richefeu, V., 2009. Contact dynamics as a nonsmooth discrete element method. Mechanics of Materials, Advances in the Dynamics of Granular Materials 41, 715–728.

Rahimzadeh Oskooei, P., Mohammadinia, A., Arulrajah, A., Horpibulsuk, S., Emam, S., 2021. Crushing behavior of recycled waste materials: Experimental analysis and DEM simulation. Construction and Building Materials 299, 124226.

Rail Safety and Standards Board, 2018. New Sander Arrangements proven to dramatically reduce the impact of low adhesion conditions. RSSB Report.

Rail Safety and Standards Board, 2018. GMRT2461 Sanding Equipment (Issue 3). 1–24.

Rail Safety and Standards Board, 2013. Performance and Installation Criteria for Sanding Systems (T797). RSSB Report.

Remy, B., Khinast, J.G., Glasser, B.J., 2009. Discrete element simulation of free flowing grains in a four-bladed mixer. AIChE Journal 55, 2035–2048.

Renouf, M., Fillot, N., 2008. Coupling electrical and mechanical effects in discrete element simulations. International Journal for Numerical Methods in Engineering 74, 238–254.

Reynolds, Q., Baumgartner, S., Erwee, M., Swanepoel, S., Geldehuys, I. and Akdogan, G., 2021. Computational modelling of electrical conduction in ferroalloy furnace burdens. In Proceedings of the 16th International Ferro-Alloys Congress (INFACON XVI).

Rojek, J., Kasztelan, R., Tharmaraj, R., 2022. Discrete element thermal conductance model for sintered particles. Powder Technology 405, 117521.

Rothenburg, L., Bathurst, R.J., 1989. Analytical study of induced anisotropy in idealized granular materials. Géotechnique 39, 601–614.

Saeidi, F., Tavares, L.M., Yahyaei, M., Powell, M., 2016. A phenomenological model of single particle breakage as a multi-stage process. Minerals Engineering 98, 90–100.

Sakaguchi, H., Ozaki, E. and Igarashi, T., 1993. Plugging of the flow of granular materials during the discharge from a silo. International Journal of Modern Physics B, 7(09n10), 1949-1963.

Sakai, M., Koshizuka, S., 2009. Large-scale discrete element modeling in pneumatic conveying. Chemical Engineering Science 64, 533–539.

Sandeep, C.S., Li, S., Senetakis, K., 2021. Scale and surface morphology effects on the micromechanical contact behavior of granular materials. Tribology International 159, 106929.

Sangrós Giménez, C., Helmers, L., Schilde, C., Diener, A., Kwade, A., 2020. Modeling the Electrical Conductive Paths within All-Solid-State Battery Electrodes. Chemical Engineering & Technology 43, 819–829.

Satake, M., 1982. Fabric tensor in granular materials. In: Vermeer, P.A., Luger, H.J. (Eds.), Deformation and Failure of Granular Materials. Balkema, Rotterdam, pp. 63–68.

Schilde, C., Burmeister, C.F., Kwade, A., 2014. Measurement and simulation of micromechanical properties of nanostructured aggregates via nanoindentation and DEM-simulation. Powder Technology 259, 1–13.

Schneider, L.C.R., Martin, C.L., Bultel, Y., Bouvard, D., Siebert, E., 2006. Discrete modelling of the electrochemical performance of SOFC electrodes. Electrochimica Acta 52, 314–324.

Schofield K. G., Wayte A. C., and Waring J. R., 1995. The emergency one shot sander (RR-SAM-056). British Rail Report.

Seed, H.B., Lee, K.L., 1966. Liquefaction of Saturated Sands During Cyclic Loading. Journal of the Soil Mechanics and Foundations Division 92, 105–134.

Seladji, S., Cosenza, P., Tabbagh, A., Ranger, J., Richard, G., 2010. The effect of compaction on soil electrical resistivity: a laboratory investigation. European Journal of Soil Science 61, 1043–1055.

Sheng, Y., Lawrence, C.J., Briscoe, B.J., Thornton, C., 2004. Numerical studies of uniaxial powder compaction process by 3D DEM. Engineering Computations 21, 304–317.

Skipper, W., Chalisey, A., Lewis, R., 2020. A review of railway sanding system research:

Wheel/rail isolation, damage, and particle application. Part F: Journal of Rail and Rapid Transit 234, 567–583.

Skipper, W.A., Lewis, R. and Fletcher, D., 2023. Understanding how railhead and wheelset contamination affect track circuit performance: evaluation of datasets (T1222).

Skipper, W., Meierhofer, A., Chalisey, A., Six, K., Lewis, R., 2024. Generation of sanded creep curves using the extended creep force model with high pressure torsion data. Wear 542–543, 205278.

Skipper, W., Nadimi, S., Gutsulyak, D.V., Butterfield, J.G., Ball, T., Lewis, R., 2023. Investigating the effect of different adhesion materials on electrical resistance using a high pressure torsion rig. Wear 532–533, 205116.

Skipper, W.A., Chalisey, A., Lewis, R., 2018. A review of railway sanding system research: adhesion restoration and leaf layer removal. Tribology - Materials, Surfaces & Interfaces 12, 237–251.

Skipper, W., Nadimi, S. and Lewis, R., 2021. Sand consist changes for improved track circuit performance (COF-UOS-03).

Skipper, W.A., Nadimi, S., Chalisey, A., Lewis, R., 2019. Particle characterisation of rail sands for understanding tribological behaviour. Wear 432–433, 202960.

Skipper, W.A., Nadimi, S., Watson, M., Chalisey, A., Lewis, R., 2023. Quantifying the effect of particle characteristics on wheel/rail adhesion and damage through high pressure torsion testing. Tribology International 179, 108190.

Skipper, W., 2021. Sand particle entrainment and its effects on the wheel/rail interface (Doctoral dissertation, University of Sheffield).

Société Nationale des Chemins de fer Français, 2004. Regelwerk Infrastruktur Verfahren: Fahrzeugzulassungsspezifikation SAM S 901 Sandungsanlage.

Spettl, A., Dosta, M., Antonyuk, S., Heinrich, S., Schmidt, V., 2015. Statistical investigation of agglomerate breakage based on combined stochastic microstructure modeling and DEM simulations. Advanced Powder Technology 26, 1021–1030.

Stewart, R.L., Bridgwater, J., Zhou, Y.C., Yu, A.B., 2001. Simulated and measured flow of granules in a bladed mixer—a detailed comparison. Chemical Engineering Science 56, 5457–5471.

Suhr, B., Skipper, W.A., Lewis, R., Six, K., 2024a. DEM simulation of single sand grain crushing in sanded wheel–rail contacts. Powder Technology 432, 119150.

Suhr, B., Skipper, W.A., Lewis, R., Six, K., 2024b. DEM modelling of surface indentations caused by granular materials: application to wheel–rail sanding. Computational Particle Mechanics 1-15.

Suhr, B., Skipper, W.A., Lewis, R., Six, K., 2024a. DEM simulation of single sand grain crushing in sanded wheel–rail contacts. Powder Technology 432, 119150.

Szczotok, A., Pietraszek, J., Radek, N., International Conference on Terotechnology, 2018. Terotechnology: 10th Conference on Terotechnology, 18-19 October 2017, Kielce, Poland.

Sze, H.Y., Yang, J., 2014. Failure Modes of Sand in Undrained Cyclic Loading: Impact of Sample Preparation. Journal of Geotechnical and Geoenvironmental Engineering 140, 152–169.

Tamadondar, M.R., Rasmuson, A., 2020. The effect of carrier surface roughness on wall collision-induced detachment of micronized pharmaceutical particles. AIChE Journal 66, e16771.

Tanvir M. A., 1972. Frictional performance of abrasive fines (IM-ADG-10). British Rail Report.

Tatsuoka, F., Ochi, K., Fujii, S., Okamoto, M., 1986. Cyclic Undrained Triaxial and Torsional Shear Strength of Sands for Different Sample Preparation Methods. Soils and Foundations 26, 23–41.

Tavares, L.M., 2009. Analysis of particle fracture by repeated stressing as damage accumulation. Powder Technology 190, 327–339.

Tavares, L.M., 2007. Breakage of single particles: quasi-static. Handbook of powder technology, 12, 3-68.

Tavares, L.M., Rodriguez, V.A., Sousani, M., Padros, C.B., Ooi, J.Y., 2021. An effective sphere-based model for breakage simulation in DEM. Powder Technology 392, 473–488.

Taylor R. K. and Pollicott I. D., 1978. Assessment of the cleaning of leaf affected track on Southern region - 1977 (TM-TRIB-29). British Rail Report.

Thakur, S.C., Ooi, J.Y. and Ahmadian, H., 2016. Scaling of discrete element model parameters for cohesionless and cohesive solid. Powder Technology 293, 130-137.

Thornton, C., 2015. Granular Dynamics, Contact Mechanics and Particle System Simulations, Particle Technology Series. Springer International Publishing, Cham.

Thornton, C., Antony, S.J., 2000. Quasi-static shear deformation of a soft particle system. Powder Technology 109, 179–191.

Tordesillas, A., Muthuswamy, M., 2009. On the modeling of confined buckling of force chains. Journal of the Mechanics and Physics of Solids 57, 706–727.

Tsuji, Y., Tanaka, T., Ishida, T., 1992. Lagrangian numerical simulation of plug flow of cohesionless particles in a horizontal pipe. Powder Technology 71, 239–250.

Tunley, J., 1999. A successful approach to rail operations in low adhesion conditions. World Congress on Railway Research, Tokyo.

Vaid, Y., Sivathayalan, S., Stedman, D., 1999. Influence of Specimen-Reconstituting Method on the Undrained Response of Sand. Geotechnical Testing Journal 22, 187–195.

Wang, G., Wei, J., 2016. Microstructure evolution of granular soils in cyclic mobility and post-liquefaction process. Granular Matter 18, 51.

Wang, L., Park, J.-Y., Fu, Y., 2007. Representation of real particles for DEM simulation using X-ray tomography. Construction and Building Materials 21, 338–346.

Wang, P., Arson, C., 2016. Discrete element modeling of shielding and size effects during single particle crushing. Computers and Geotechnics 78, 227–236.

Wang, W.J., Liu, T.F., Wang, H.Y., Liu, Q.Y., Zhu, M.H., Jin, X.S., 2014. Influence of friction modifiers on improving adhesion and surface damage of wheel/rail under low adhesion conditions. Tribology International 75, 16–23.

Wang, W.J., Zhang, H.F., Wang, H.Y., Liu, Q.Y. and Zhu, M.H., 2011. Study on the adhesion behavior of wheel/rail under oil, water and sanding conditions. Wear 271(9-10), 2693-2698.

Wang, Y., Mora, P., Liang, Y., 2022. Calibration of discrete element modeling: Scaling laws and dimensionless analysis. Particuology 62, 55–62.

Wang, Z.-X., Liao, W.-Q., 2022. Giant electromechanical effects in polymers. Science 375, 1353–1354.

Wang, P., Wu, K., Wu, W., Pan, A., Guo, Z., Chen, S., 2024. Current-carrying wear behavior of CoCrFeNiW0.2 and CoCrFeNiW0.2+3at%C high entropy alloys. Tribology International 197, 109749.

Waring J. R., 1996. Sanding to Assist Braking in Low Adhesion: Class 318 Feasibility Study (RR-SAM-158). British Rail Report.

Washino, K., Chan, E.L., Miyazaki, K., Tsuji, T., Tanaka, T., 2016. Time step criteria in DEM simulation of wet particles in viscosity dominant systems. Powder Technology 302, 100–107.

Washino, K., Chan, E.L., Tanaka, T., 2018. DEM with attraction forces using reduced particle stiffness. Powder Technology 325, 202–208.

Washino, K., Nakae, S., Yamagami, R., Chan, E.L., Tsuji, T., Tanaka, T., 2024. Scaling of attraction force and rolling resistance in DEM with reduced particle stiffness. Chemical Engineering Research and Design 203, 501–519.

Weerasekara, N.S., Powell, M.S., Cleary, P.W., Tavares, L.M., Evertsson, M., Morrison, R.D., Quist, J., Carvalho, R.M., 2013. The contribution of DEM to the science of comminution. Powder Technology 248, 3–24.

Wei, J., Huang, D., Wang, G., 2018. Microscale Descriptors for Particle-Void Distribution and Jamming Transition in Pre- and Post-Liquefaction of Granular Soils. Journal of Engineering Mechanics 144, 04018067.

Wei, J., Wang, G., 2017. Discrete element method analysis of initial fabric effects on pre- and post-liquefaction behavior of sands. Géotechnique Letters 7, 161–166.

Wetscher, F., Vorhauer, A. and Pippan, R., 2005. Strain hardening during high pressure torsion deformation. Materials Science and Engineering: A, 410, 213-216.

Wing, O., 1972. Circuit theory with computer methods. Holt, Rinehart and Winston, New York.

Wright, S., 1921. Correlation and causation. Journal of agricultural research 20, 557.

Wu, C.-Y., Ruddy, O.M., Bentham, A.C., Hancock, B.C., Best, S.M., Elliott, J.A., 2005. Modelling the mechanical behaviour of pharmaceutical powders during compaction. Powder Technology 152, 107–117.

Wu, M., Wang, J., Zhao, B., 2022. DEM modeling of one-dimensional compression of sands incorporating statistical particle fragmentation scheme. Canadian Geotechnical Journal 59, 144–157.

Yang, Y., Fei, W., Yu, H.-S., Ooi, J., Rotter, M., 2015. Experimental study of anisotropy and non-coaxiality of granular solids. Granular Matter 17, 189–196.

Yang, Z.X., Li, X.S., Yang, J., 2008. Quantifying and modelling fabric anisotropy of granular soils. Géotechnique 58, 237–248.

Yang, Y.L., Zhang, T. and Liu, S.Y., 2020. Influence factor analysis and calculation model for thermal/electrical resistivity of geomaterials. Measurement 152, p.107373.

Yao, G., Mo, X., Yin, C., Lou, W., Wang, Q., Huang, S., Mao, L., Chen, S., Zhao, K., Pan, T. and Huang, L., 2022. A programmable and skin temperature–activated electromechanical synergistic dressing for effective wound healing. Science Advances, 8(4), p.eabl8379.

Yim, S., Aoyagi, K., Yanagihara, K., Bian, H., Chiba, A., 2023. Effect of mechanical ball milling on the electrical and powder bed properties of gas-atomized Ti–48Al–2Cr–2Nb and elucidation of the smoke mechanism in the powder bed fusion electron beam melting process. Journal of Materials Science & Technology 137, 36–55.

Yim, M.J. and Paik, K.W., 1997. Design and understanding of anisotropic conductive films (ACFs) for LCD packaging. In Proceedings. The First IEEE International Symposium on Polymeric Electronics Packaging, PEP'97, 233-242.

Yimsiri, S., Soga, K., 2010. DEM analysis of soil fabric effects on behaviour of sand. Géotechnique 60, 483–495.

Yuan, Z., Li, F., Xue, F., He, M., Hussain, M.Z., 2014. Analysis of the stress states and interface damage in a particle reinforced composite based on a micromodel using cohesive elements. Materials Science and Engineering: A 589, 288–302.

Zeng, Y., Mao, B., Jia, F., Han, Y., Li, G., 2022. Modelling of grain breakage of in a vertical rice mill based on DEM simulation combining particle replacement model. Biosystems Engineering 215, 32–48.

Zhai, C., Hanaor, D., Proust, G., Brassart, L., Gan, Y., 2016. Interfacial electro-mechanical behaviour at rough surfaces. Extreme Mech Lett, Mechanics of Energy Materials 9, 422–429.

Zhang, B., Nadimi, S., Lewis, R., 2024. Modelling the adhesion enhancement induced by sand particle breakage at the wheel-rail interface. Wear 538–539, 205232.

Zhang, B., Nadimi, S., Eissa, A., Rouainia, M., 2023. Modelling fracturing process using cohesive interface elements: theoretical verification and experimental validation. Construction and Building Materials 365, 130132.

Zhang, C., Nadimi, S., Maramizonouz, S., Milledge, D., Lewis, R., 2024a. A Discrete Element Model of High-Pressure Torsion Test to Assess the Effect of Particle Characteristics in the Interface. ASME Journal of Tribology 146, 081501.

Zhang, C., Maramizonouz, S., Milledge, D., Nadimi, S., 2024b. An electro-mechanical contact model for particulate systems. Powder Technology 440, 119759.

Zhao, M., Chen, S., Wang, K., Liu, G., 2023. Analysis of Electrical Resistivity Characteristics and Damage Evolution of Soil–Rock Mixture under Triaxial Shear. Materials 16, 3698.

Zhou, L., Brunskill, H., Pletz, M., Daves, W., Scheriau, S., Lewis, R., 2019. Real-Time Measurement of Dynamic Wheel-Rail Contacts Using Ultrasonic Reflectometry. ASME Journal of Tribology 141.

Zobel, F.G.R., 1974. Development of Remedies for Poor Adhesion (IM-ADH-019). British Rail Research.

Zobel F. G. R., 1972. Effect of ‘slipmaster’ on track circuit operation. Tests using the ‘silica gun’ and high speed tribometer train (IM-ADH-004). British Rail Report.

Appendix A

Referring to Section 3.6.3, the figures provided in this appendix show the comparison between the fragment size distribution data predicted by the code against the desirable input distribution obtained by laser diffraction for the rest of the sand particle samples. Label (a) presents sand particles from Source 1 and label (b) from Source 2.

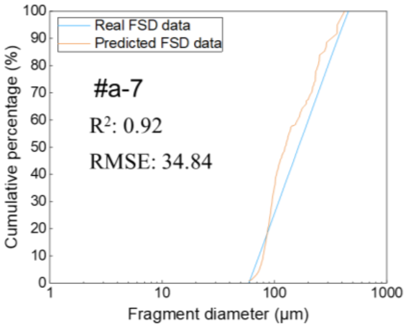
Real FSD data
Predicted FSD data
#a-7
R²: 0.92
RMSE: 34.84
Cumulative percentage (%)
Fragment diameter (μm)
0 10 20 30 40 50 60 70 80 90 100
1 10 100 1000

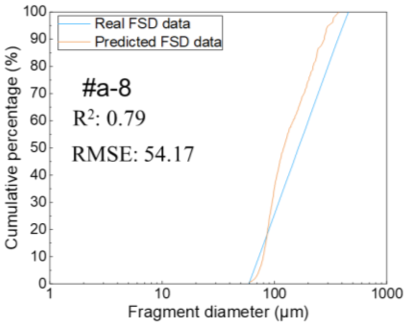
Real FSD data
Predicted FSD data
#a-8
R²: 0.79
RMSE: 54.17
Cumulative percentage (%)
Fragment diameter (μm)
0 10 20 30 40 50 60 70 80 90 100
1 10 100 1000

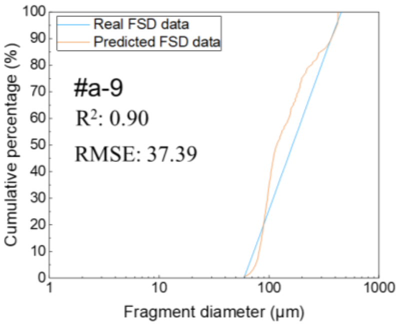
Real FSD data
Predicted FSD data
#a-9
R²: 0.90
RMSE: 37.39
Cumulative percentage (%)
Fragment diameter (μm)
0 10 20 30 40 50 60 70 80 90 100
1 10 100 1000

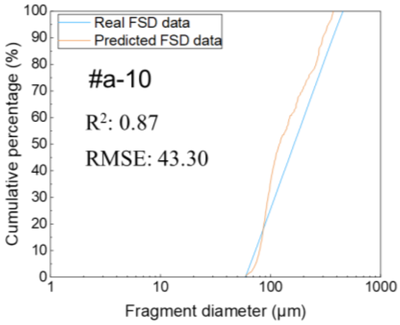
Real FSD data
Predicted FSD data
#a-10
R²: 0.87
RMSE: 43.30
Cumulative percentage (%)
Fragment diameter (μm)
0 10 20 30 40 50 60 70 80 90 100
1 10 100 1000

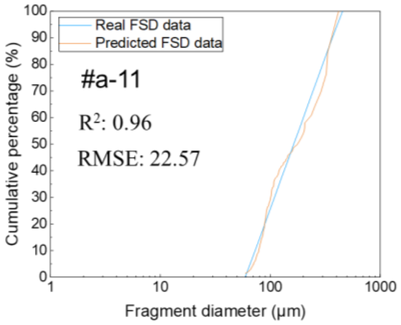
Real FSD data
Predicted FSD data
#a-11
R²: 0.96
RMSE: 22.57
Cumulative percentage (%)
Fragment diameter (μm)
0 10 20 30 40 50 60 70 80 90 100
1 10 100 1000

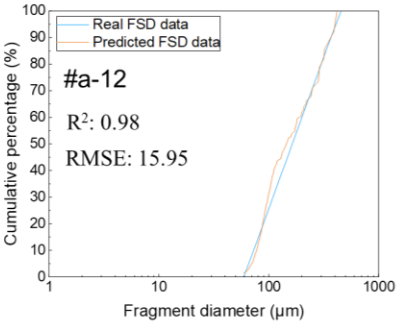
Real FSD data
Predicted FSD data
#a-12
R²: 0.98
RMSE: 15.95
Cumulative percentage (%)
Fragment diameter (μm)
0 10 20 30 40 50 60 70 80 90 100
1 10 100 1000

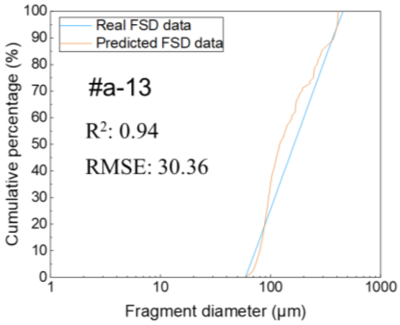
Real FSD data
Predicted FSD data
#a-13
R²: 0.94
RMSE: 30.36
Cumulative percentage (%)
Fragment diameter (μm)
0 10 20 30 40 50 60 70 80 90 100
1 10 100 1000

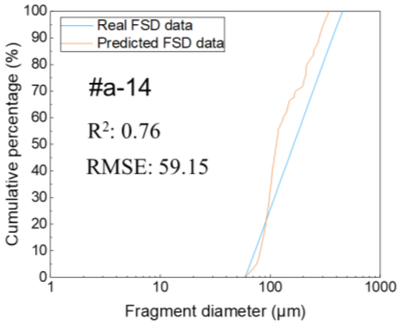
Real FSD data
Predicted FSD data
#a-14
R²: 0.76
RMSE: 59.15
Cumulative percentage (%)
Fragment diameter (μm)
0 10 20 30 40 50 60 70 80 90 100
1 10 100 1000

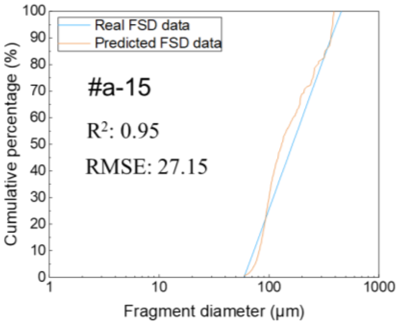
Real FSD data
Predicted FSD data
#a-15
R²: 0.95
RMSE: 27.15
Cumulative percentage (%)
Fragment diameter (μm)
0 10 20 30 40 50 60 70 80 90 100
1 10 100 1000

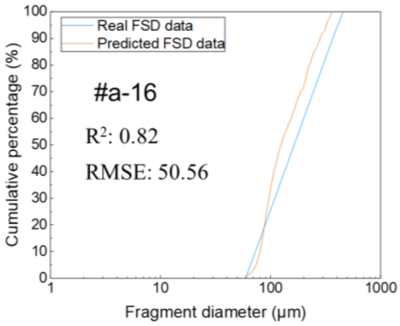
Real FSD data
Predicted FSD data
#a-16
R²: 0.82
RMSE: 50.56
Cumulative percentage (%)
Fragment diameter (μm)
0 10 20 30 40 50 60 70 80 90 100
1 10 100 1000

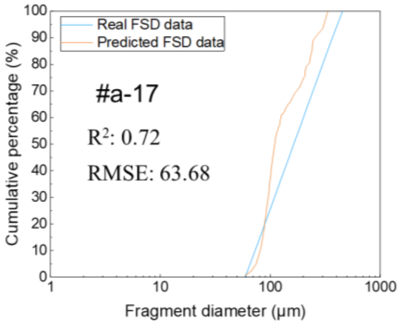
Real FSD data
Predicted FSD data
#a-17
R²: 0.72
RMSE: 63.68
Cumulative percentage (%)
Fragment diameter (μm)
0 10 20 30 40 50 60 70 80 90 100
1 10 100 1000

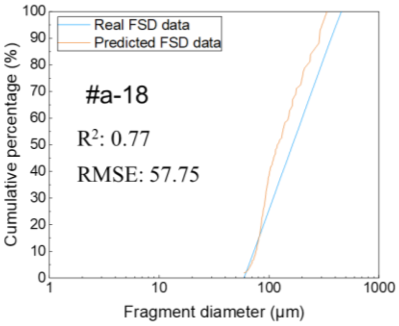
Real FSD data
Predicted FSD data
#a-18
R²: 0.77
RMSE: 57.75
Cumulative percentage (%)
Fragment diameter (μm)
0 10 20 30 40 50 60 70 80 90 100
1 10 100 1000

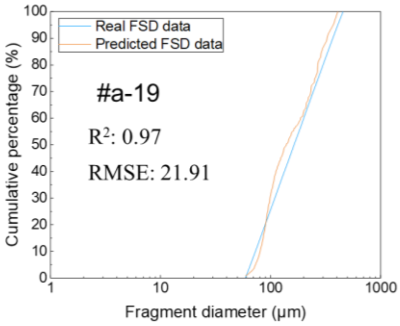
Real FSD data
Predicted FSD data
#a-19
R²: 0.97
RMSE: 21.91
Cumulative percentage (%)
Fragment diameter (μm)
0 10 20 30 40 50 60 70 80 90 100
1 10 100 1000

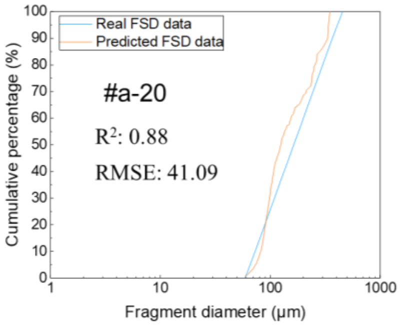
Real FSD data
Predicted FSD data
#a-20
R²: 0.88
RMSE: 41.09
Cumulative percentage (%)
Fragment diameter (μm)
0 10 20 30 40 50 60 70 80 90 100
1 10 100 1000

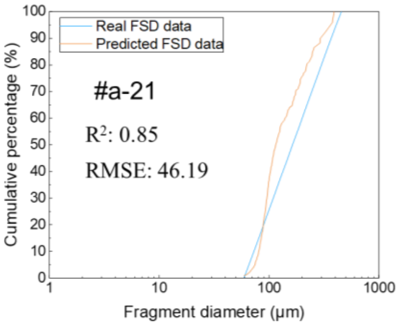
Real FSD data
Predicted FSD data
#a-21
R²: 0.85
RMSE: 46.19
Cumulative percentage (%)
Fragment diameter (μm)
0 10 20 30 40 50 60 70 80 90 100
1 10 100 1000

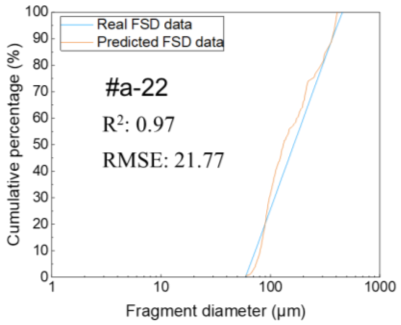
Cumulative percentage (%)
0 10 20 30 40 50 60 70 80 90 100
Real FSD data
Predicted FSD data
#a-22
R^2: 0.97
RMSE: 21.77
1 10 100 1000
Fragment diameter (μm)

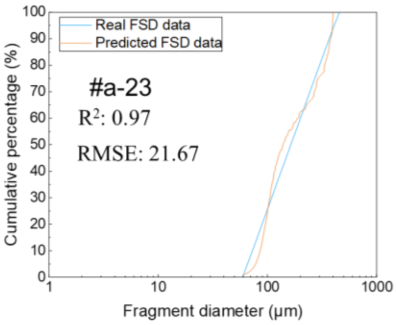
Cumulative percentage (%)
0 10 20 30 40 50 60 70 80 90 100
Real FSD data
Predicted FSD data
#a-23
R^2: 0.97
RMSE: 21.67
1 10 100 1000
Fragment diameter (μm)

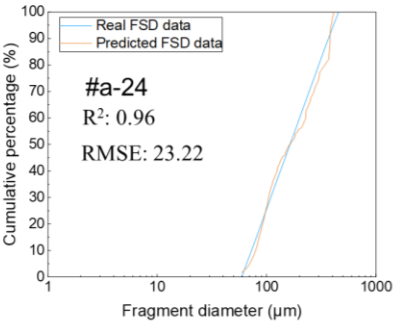
Cumulative percentage (%)
0 10 20 30 40 50 60 70 80 90 100
Real FSD data
Predicted FSD data
#a-24
R^2: 0.96
RMSE: 23.22
1 10 100 1000
Fragment diameter (μm)

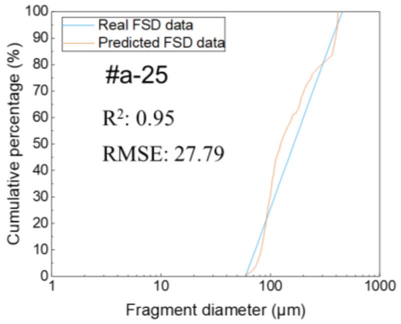
Cumulative percentage (%)
0 10 20 30 40 50 60 70 80 90 100
Real FSD data
Predicted FSD data
#a-25
R^2: 0.95
RMSE: 27.79
1 10 100 1000
Fragment diameter (μm)

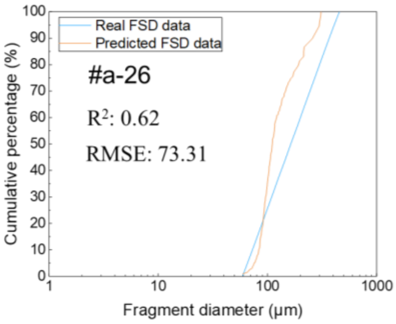
Cumulative percentage (%)
0 10 20 30 40 50 60 70 80 90 100
Real FSD data
Predicted FSD data
#a-26
R^2: 0.62
RMSE: 73.31
1 10 100 1000
Fragment diameter (μm)

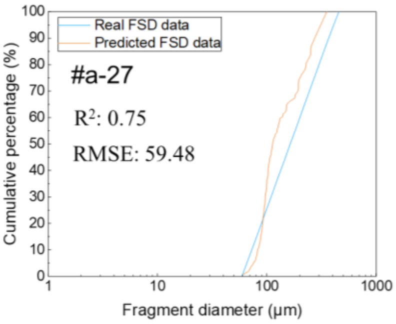
Cumulative percentage (%)
0 10 20 30 40 50 60 70 80 90 100
Real FSD data
Predicted FSD data
#a-27
R^2: 0.75
RMSE: 59.48
1 10 100 1000
Fragment diameter (μm)

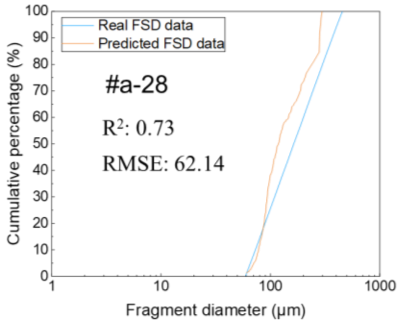
Cumulative percentage (%)
0 10 20 30 40 50 60 70 80 90 100
Real FSD data
Predicted FSD data
#a-28
R^2: 0.73
RMSE: 62.14
1 10 100 1000
Fragment diameter (μm)

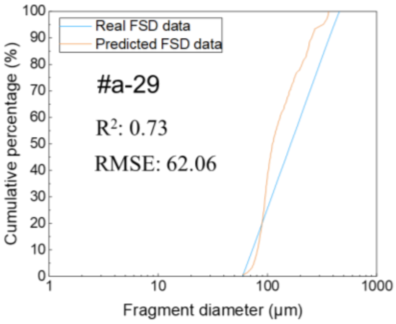
Cumulative percentage (%)
0 10 20 30 40 50 60 70 80 90 100
Real FSD data
Predicted FSD data
#a-29
R^2: 0.73
RMSE: 62.06
1 10 100 1000
Fragment diameter (μm)

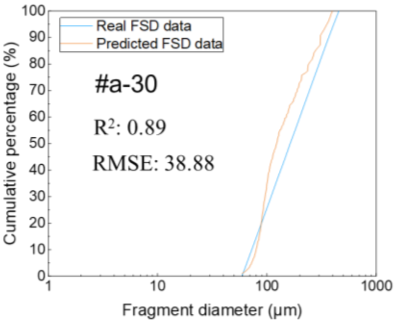
Cumulative percentage (%)
0 10 20 30 40 50 60 70 80 90 100
Real FSD data
Predicted FSD data
#a-30
R^2: 0.89
RMSE: 38.88
1 10 100 1000
Fragment diameter (μm)

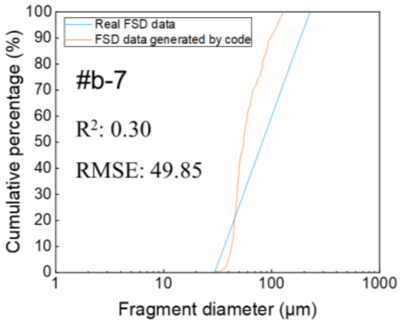
Cumulative percentage (%)
0 10 20 30 40 50 60 70 80 90 100
Real FSD data
FSD data generated by code
#b-7
R^2: 0.30
RMSE: 49.85
1 10 100 1000
Fragment diameter (μm)

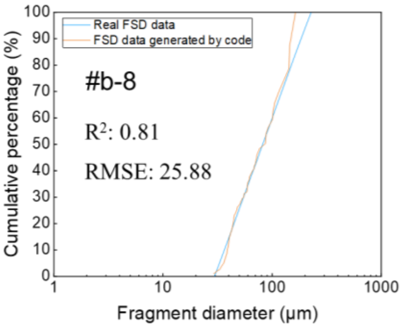
Cumulative percentage (%)
0 10 20 30 40 50 60 70 80 90 100
Real FSD data
FSD data generated by code
#b-8
R^2: 0.81
RMSE: 25.88
1 10 100 1000
Fragment diameter (μm)

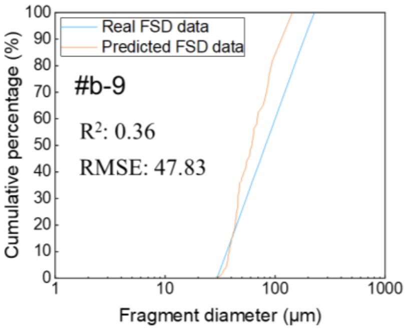
Cumulative percentage (%)
0 10 20 30 40 50 60 70 80 90 100
Real FSD data
Predicted FSD data
#b-9
R^2: 0.36
RMSE: 47.83
1 10 100 1000
Fragment diameter (μm)

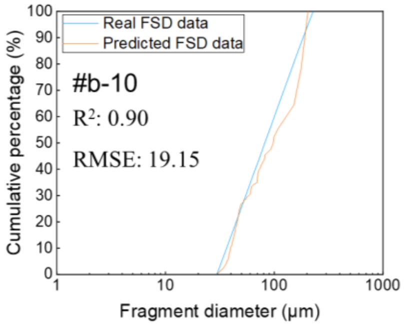
Cumulative percentage (%)
0 10 20 30 40 50 60 70 80 90 100
Real FSD data
Predicted FSD data
#b-10
R^2: 0.90
RMSE: 19.15
1 10 100 1000
Fragment diameter (μm)

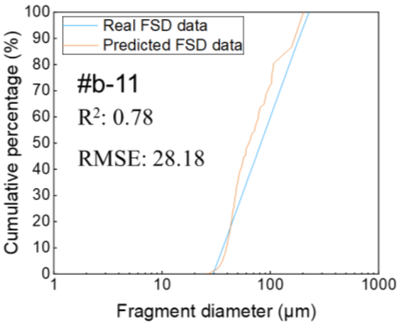
Cumulative percentage (%)
0 10 20 30 40 50 60 70 80 90 100
Real FSD data
Predicted FSD data
#b-11
R^2: 0.78
RMSE: 28.18
1 10 100 1000
Fragment diameter (μm)

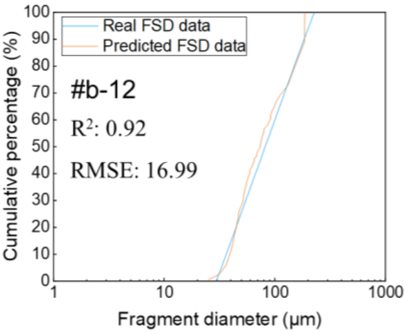
Cumulative percentage (%)
0 10 20 30 40 50 60 70 80 90 100
Real FSD data
Predicted FSD data
#b-12
R^2: 0.92
RMSE: 16.99
1 10 100 1000
Fragment diameter (μm)

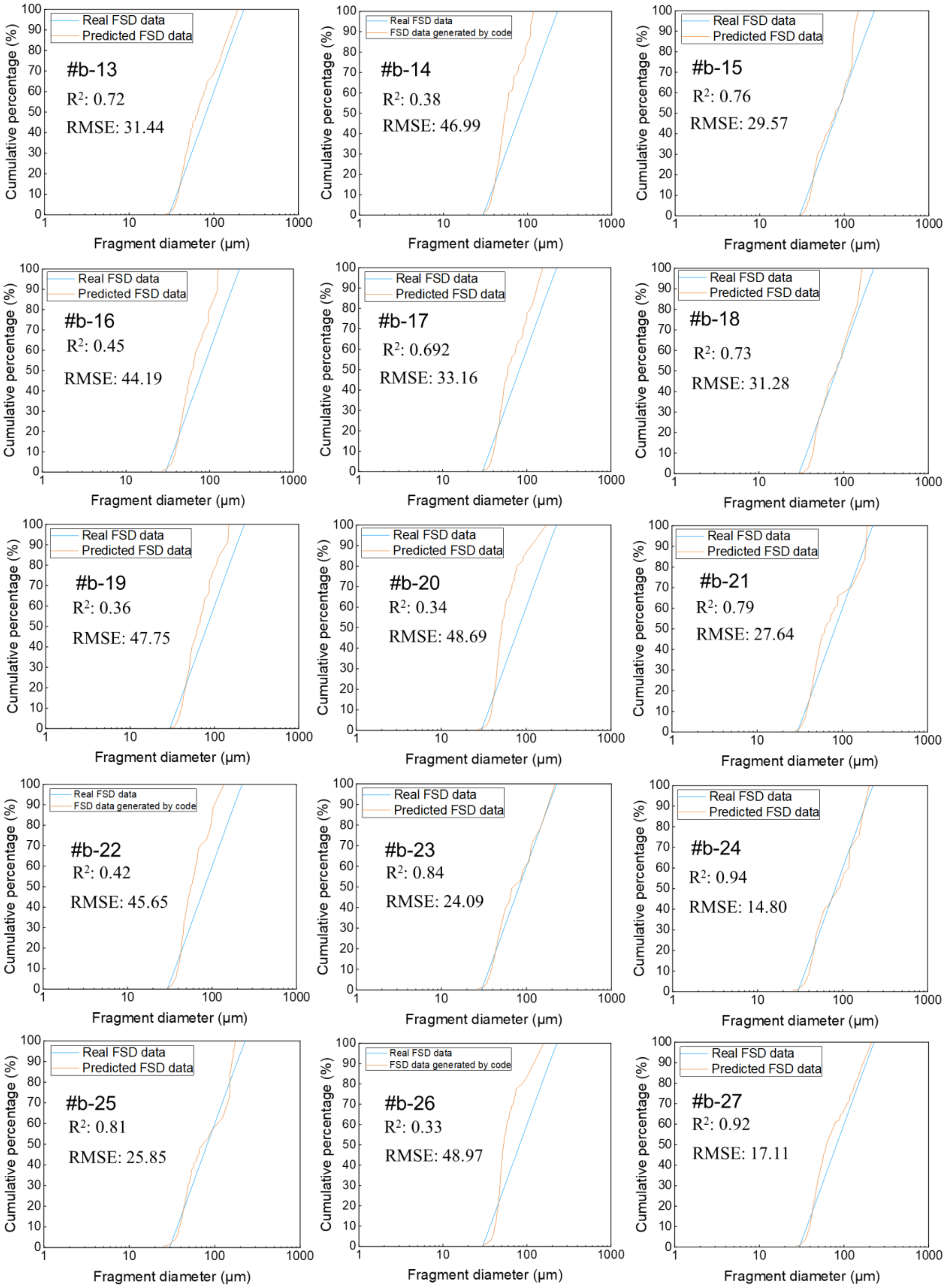
Cumulative percentage (%)
Fragment diameter (µm)
0
10
20
30
40
50
60
70
80
90
100
1
10
100
1000
Real FSD data
Predicted FSD data
FSD data generated by code
#b-13
R²: 0.72
RMSE: 31.44
#b-14
R²: 0.38
RMSE: 46.99
#b-15
R²: 0.76
RMSE: 29.57
#b-16
R²: 0.45
RMSE: 44.19
#b-17
R²: 0.692
RMSE: 33.16
#b-18
R²: 0.73
RMSE: 31.28
#b-19
R²: 0.36
RMSE: 47.75
#b-20
R²: 0.34
RMSE: 48.69
#b-21
R²: 0.79
RMSE: 27.64
#b-22
R²: 0.42
RMSE: 45.65
#b-23
R²: 0.84
RMSE: 24.09
#b-24
R²: 0.94
RMSE: 14.80
#b-25
R²: 0.81
RMSE: 25.85
#b-26
R²: 0.33
RMSE: 48.97
#b-27
R²: 0.92
RMSE: 17.11

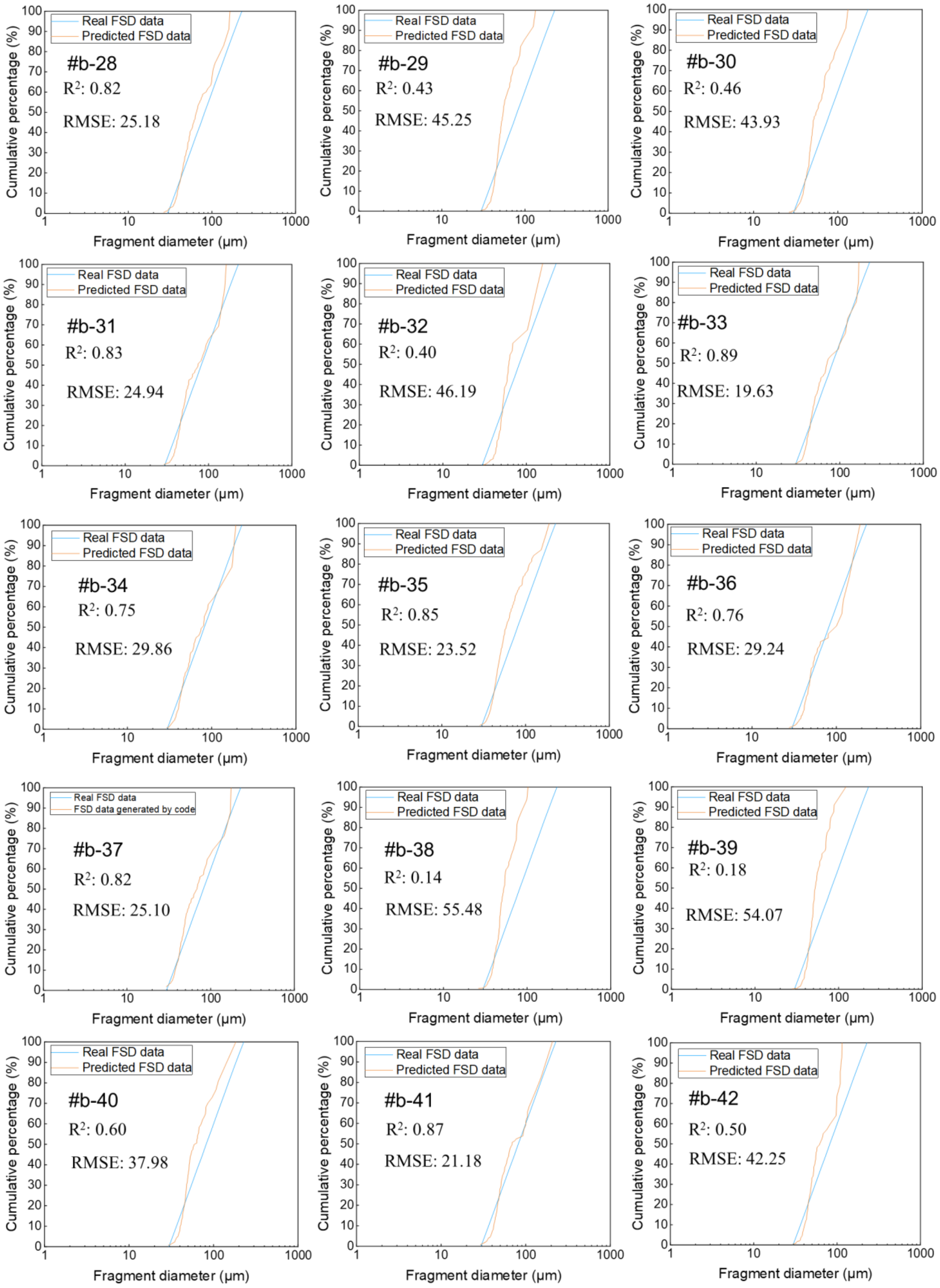
#b-28
R²: 0.82
RMSE: 25.18
#b-29
R²: 0.43
RMSE: 45.25
#b-30
R²: 0.46
RMSE: 43.93
#b-31
R²: 0.83
RMSE: 24.94
#b-32
R²: 0.40
RMSE: 46.19
#b-33
R²: 0.89
RMSE: 19.63
#b-34
R²: 0.75
RMSE: 29.86
#b-35
R²: 0.85
RMSE: 23.52
#b-36
R²: 0.76
RMSE: 29.24
#b-37
R²: 0.82
RMSE: 25.10
FSD data generated by code
#b-38
R²: 0.14
RMSE: 55.48
#b-39
R²: 0.18
RMSE: 54.07
#b-40
R²: 0.60
RMSE: 37.98
#b-41
R²: 0.87
RMSE: 21.18
#b-42
R²: 0.50
RMSE: 42.25
Real FSD data
Predicted FSD data
Cumulative percentage (%)
Fragment diameter (μm)
0
10
20
30
40
50
60
70
80
90
100
1
10
100
1000

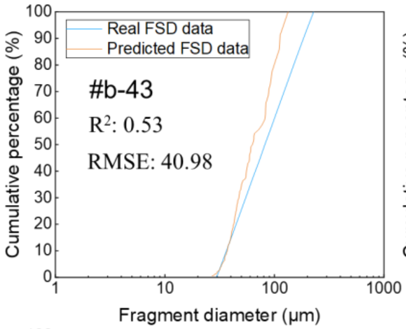
Real FSD data
Predicted FSD data
#b-43
R²: 0.53
RMSE: 40.98
Cumulative percentage (%)
0
10
20
30
40
50
60
70
80
90
100
1
10
100
1000
Fragment diameter (μm)

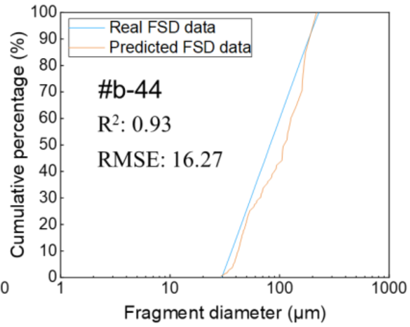
Real FSD data
Predicted FSD data
#b-44
R²: 0.93
RMSE: 16.27
Cumulative percentage (%)
0
10
20
30
40
50
60
70
80
90
100
1
10
100
1000
Fragment diameter (μm)

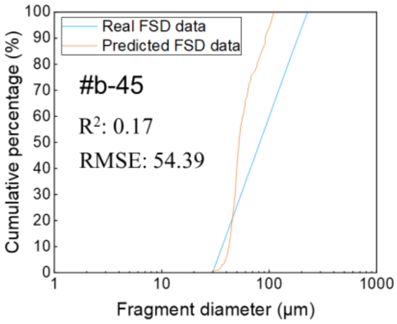
Real FSD data
Predicted FSD data
#b-45
R²: 0.17
RMSE: 54.39
Cumulative percentage (%)
0
10
20
30
40
50
60
70
80
90
100
1
10
100
1000
Fragment diameter (μm)

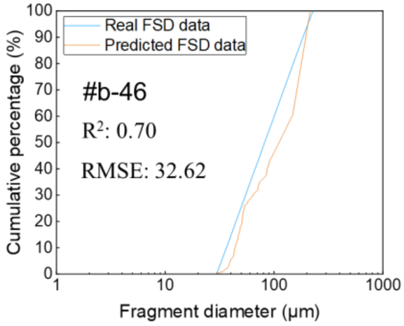
Real FSD data
Predicted FSD data
#b-46
R²: 0.70
RMSE: 32.62
Cumulative percentage (%)
0
10
20
30
40
50
60
70
80
90
100
1
10
100
1000
Fragment diameter (μm)

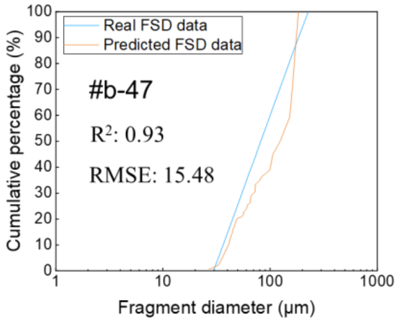
Real FSD data
Predicted FSD data
#b-47
R²: 0.93
RMSE: 15.48
Cumulative percentage (%)
0
10
20
30
40
50
60
70
80
90
100
1
10
100
1000
Fragment diameter (μm)

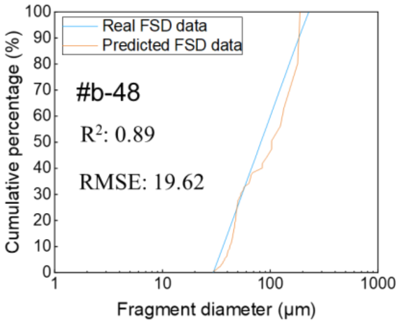
Real FSD data
Predicted FSD data
#b-48
R²: 0.89
RMSE: 19.62
Cumulative percentage (%)
0
10
20
30
40
50
60
70
80
90
100
1
10
100
1000
Fragment diameter (μm)

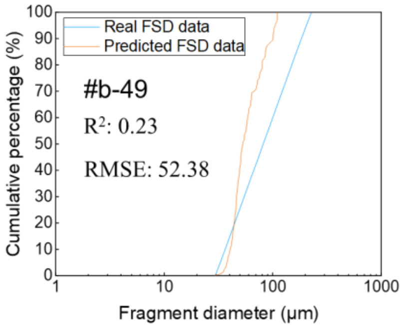
Real FSD data
Predicted FSD data
#b-49
R²: 0.23
RMSE: 52.38
Cumulative percentage (%)
0
10
20
30
40
50
60
70
80
90
100
1
10
100
1000
Fragment diameter (μm)

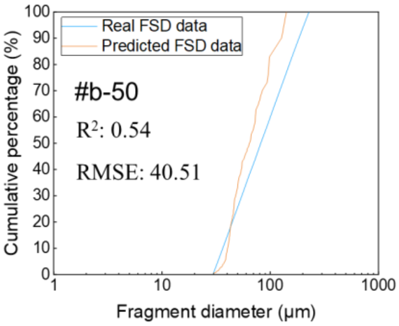
Real FSD data
Predicted FSD data
#b-50
R²: 0.54
RMSE: 40.51
Cumulative percentage (%)
0
10
20
30
40
50
60
70
80
90
100
1
10
100
1000
Fragment diameter (μm)

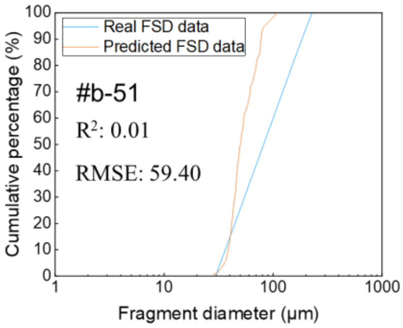
Real FSD data
Predicted FSD data
#b-51
R²: 0.01
RMSE: 59.40
Cumulative percentage (%)
0
10
20
30
40
50
60
70
80
90
100
1
10
100
1000
Fragment diameter (μm)

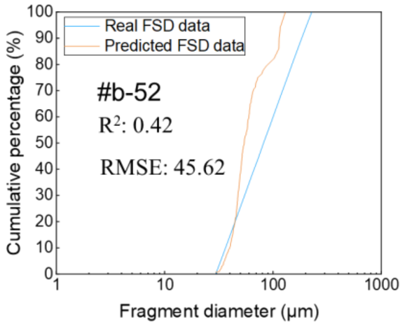
Real FSD data
Predicted FSD data
#b-52
R²: 0.42
RMSE: 45.62
Cumulative percentage (%)
0
10
20
30
40
50
60
70
80
90
100
1
10
100
1000
Fragment diameter (μm)

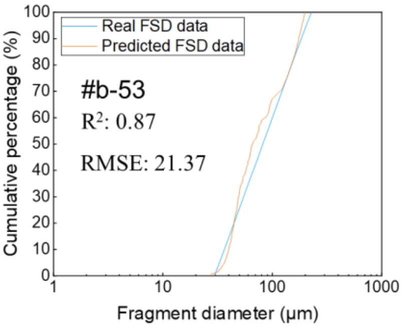
Real FSD data
Predicted FSD data
#b-53
R²: 0.87
RMSE: 21.37
Cumulative percentage (%)
0
10
20
30
40
50
60
70
80
90
100
1
10
100
1000
Fragment diameter (μm)

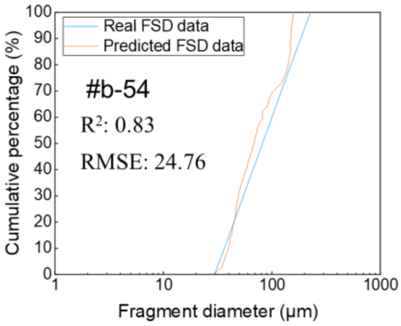
Real FSD data
Predicted FSD data
#b-54
R²: 0.83
RMSE: 24.76
Cumulative percentage (%)
0
10
20
30
40
50
60
70
80
90
100
1
10
100
1000
Fragment diameter (μm)

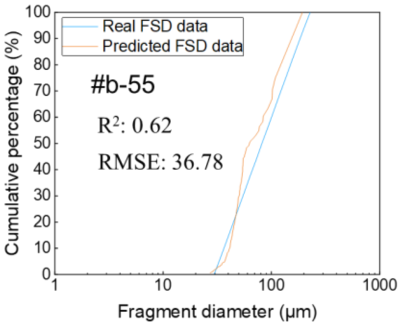
Real FSD data
Predicted FSD data
#b-55
R²: 0.62
RMSE: 36.78
Cumulative percentage (%)
0
10
20
30
40
50
60
70
80
90
100
1
10
100
1000
Fragment diameter (μm)

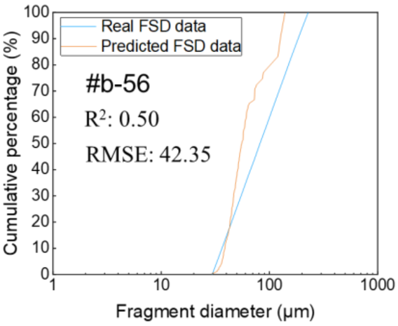
Real FSD data
Predicted FSD data
#b-56
R²: 0.50
RMSE: 42.35
Cumulative percentage (%)
0
10
20
30
40
50
60
70
80
90
100
1
10
100
1000
Fragment diameter (μm)

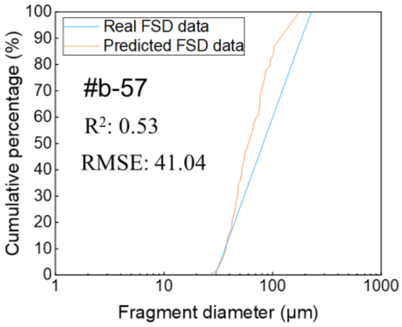
Real FSD data
Predicted FSD data
#b-57
R²: 0.53
RMSE: 41.04
Cumulative percentage (%)
0
10
20
30
40
50
60
70
80
90
100
1
10
100
1000
Fragment diameter (μm)

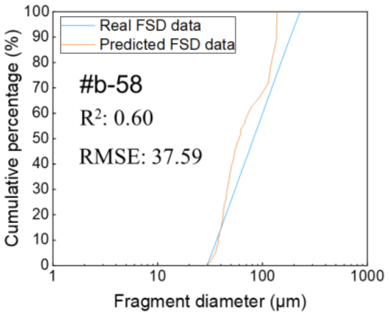
Real FSD data
Predicted FSD data
#b-58
R^2: 0.60
RMSE: 37.59
Cumulative percentage (%)
Fragment diameter (μm)
0 10 20 30 40 50 60 70 80 90 100
1 10 100 1000

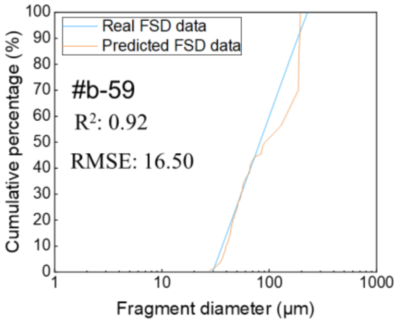
Real FSD data
Predicted FSD data
#b-59
R^2: 0.92
RMSE: 16.50
Cumulative percentage (%)
Fragment diameter (μm)
0 10 20 30 40 50 60 70 80 90 100
1 10 100 1000

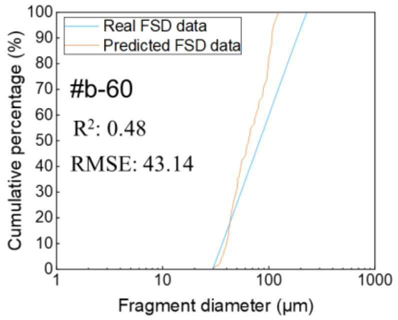
Real FSD data
Predicted FSD data
#b-60
R^2: 0.48
RMSE: 43.14
Cumulative percentage (%)
Fragment diameter (μm)
0 10 20 30 40 50 60 70 80 90 100
1 10 100 1000

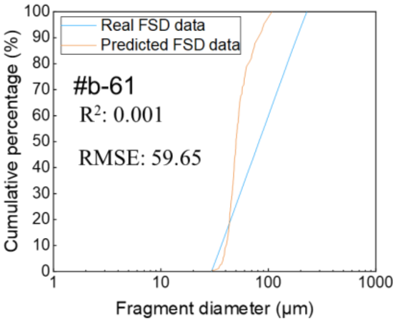
Real FSD data
Predicted FSD data
#b-61
R^2: 0.001
RMSE: 59.65
Cumulative percentage (%)
Fragment diameter (μm)
0 10 20 30 40 50 60 70 80 90 100
1 10 100 1000

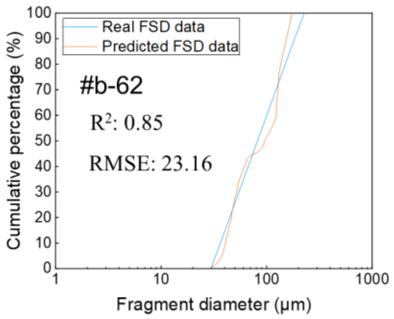
Real FSD data
Predicted FSD data
#b-62
R^2: 0.85
RMSE: 23.16
Cumulative percentage (%)
Fragment diameter (μm)
0 10 20 30 40 50 60 70 80 90 100
1 10 100 1000

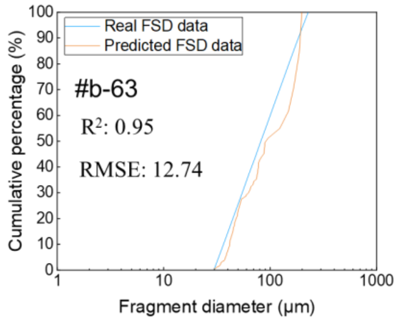
Real FSD data
Predicted FSD data
#b-63
R^2: 0.95
RMSE: 12.74
Cumulative percentage (%)
Fragment diameter (μm)
0 10 20 30 40 50 60 70 80 90 100
1 10 100 1000

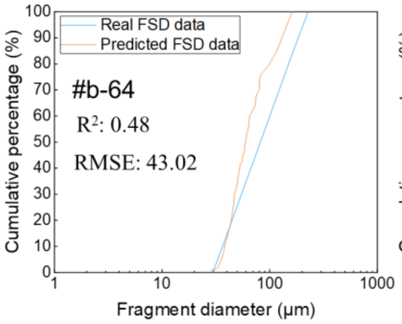
Real FSD data
Predicted FSD data
#b-64
R^2: 0.48
RMSE: 43.02
Cumulative percentage (%)
Fragment diameter (μm)
0 10 20 30 40 50 60 70 80 90 100
1 10 100 1000

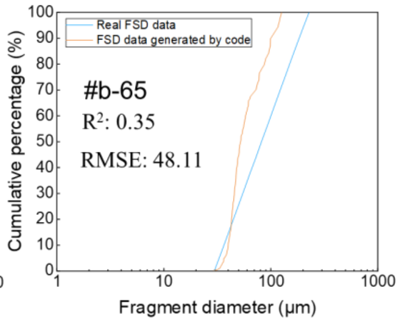
Real FSD data
FSD data generated by code
#b-65
R^2: 0.35
RMSE: 48.11
Cumulative percentage (%)
Fragment diameter (μm)
0 10 20 30 40 50 60 70 80 90 100
1 10 100 1000

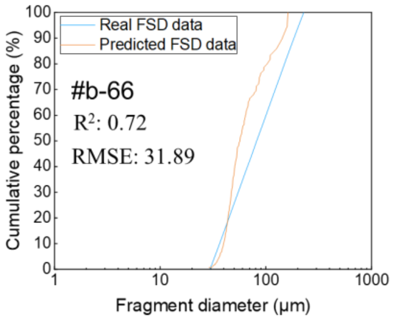
Real FSD data
Predicted FSD data
#b-66
R^2: 0.72
RMSE: 31.89
Cumulative percentage (%)
Fragment diameter (μm)
0 10 20 30 40 50 60 70 80 90 100
1 10 100 1000

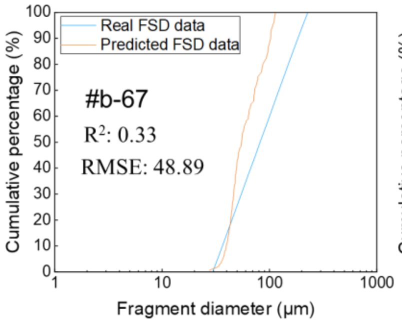
Real FSD data
Predicted FSD data
#b-67
R^2: 0.33
RMSE: 48.89
Cumulative percentage (%)
Fragment diameter (μm)
0 10 20 30 40 50 60 70 80 90 100
1 10 100 1000

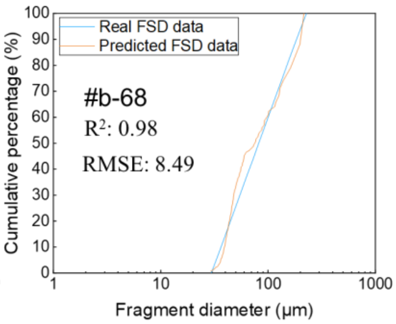
Real FSD data
Predicted FSD data
#b-68
R^2: 0.98
RMSE: 8.49
Cumulative percentage (%)
Fragment diameter (μm)
0 10 20 30 40 50 60 70 80 90 100
1 10 100 1000

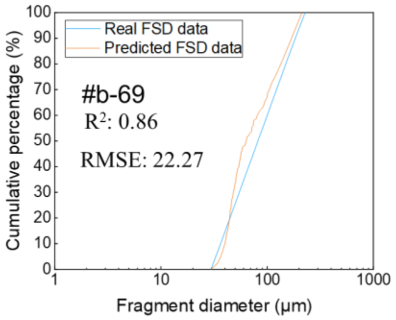
Real FSD data
Predicted FSD data
#b-69
R^2: 0.86
RMSE: 22.27
Cumulative percentage (%)
Fragment diameter (μm)
0 10 20 30 40 50 60 70 80 90 100
1 10 100 1000

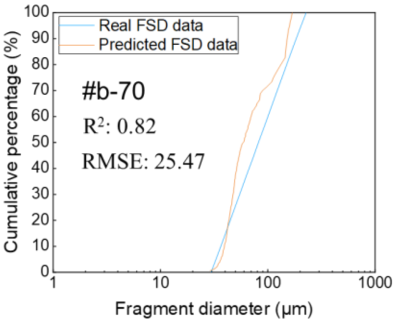
Real FSD data
Predicted FSD data
#b-70
R^2: 0.82
RMSE: 25.47
Cumulative percentage (%)
Fragment diameter (μm)
0 10 20 30 40 50 60 70 80 90 100
1 10 100 1000